DIMUON PRODUCTION BY 0-600 GEV NEUTRINOS IN THE FERMILAB 15 FT. BUBBLE CHAMBER

A DISSERTATION SUBMITTED TO THE GRADUATE DIVISION OF THE UNIVERSITY OF HAWAII IN PARTIAL FULFILLMENT OF THE REQUIREMENTS FOR THE DEGREE OF

DOCTOR OF PHILOSOPHY

IN PHYSICS

AUGUST 1988

By

Vivek Jain

Dissertation Committee

Frederick A. Harris, Chairman
Robert J. Cence
Charles S. Fadley
Charles F. Hayes
Michael D. Jones
Sandip Pakvasa

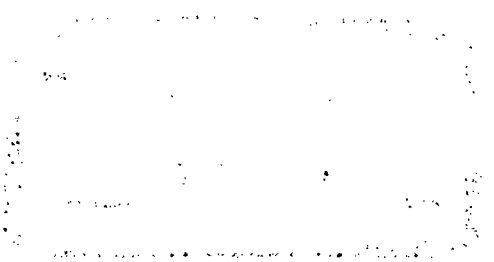

We certify that we have read this dissertation and that, in our opinion, it is satisfactory in scope and quality as a dissertation for the degree of Doctor of Philosophy in Physics.

DISSERTATION COMMITTEE

Frederick A Harris

Chairman

Michael D. Jones

Robert J. Cence

Sandip Pakvasa

ACKNOWLEDGEMENTS

I would first like to thank my advisor Fred Harris for his patience and sound advice throughout my stay in Hawaii and the time I spent at Fermilab. I would also like to thank Mike Jones for all his help and guidance. I have greatly benefitted from the many useful discussions with Jeremy Lys (Berkeley).

I would like to thank Howie Rubin (Ill. Inst. Tech.) and Steve Sewell for their critical assistance in processing the EMI data tapes and collecting the scan files from the various groups in our collaboration. I would also like to acknowledge Kevin Varvell's (Birmingham) help in coordinating the flow of data from Europe, and ironing out all the problems.

I would like to thank everbody I worked with at Fermilab during 1984 and 1985, especially Dan Chapman (Berkeley), Ron Campbell, Liz Quigg (Fermilab) and Peter Heinecke (Fermilab). I would particularly like to thank Stephen Pordes (Fermilab) and Sten Hansen (Fermilab) for their crucial assistance and guidance during the construction of the EMI (and their friendship). I would like to thank all the members of this collaboration for their assistance and friendship, especially Phil Allport, Harry Bingham, Christian Coutures and Peter Kasper.

This experiment would not have been possible without the hard work of the crew of the 15 Ft. Bubble Chamber, Facilities Support

Group, and the film analysis staff at the collaborating groups for scanning and measuring the difficult film.

I would like to thank all my friends and fellow graduate students in Hawaii without whom life would not have been as much fun.

I would also like to thank the High Energy Group at University of Hawaii for providing a conducive atmosphere for research.

Finally, I would like to thank my parents who have always supported me in my endeavours, and who taught me the ethic of hard work and perseverance.

ABSTRACT

Neutrino (and anti-neutrino) induced events with multi-muons in the final state are studied using the Fermilab 15 Ft. Bubble Chamber. The neutrino beam is made by 800 GeV protons incident on a Beryllium target, and the secondaries are focussed by a quadrupole triplet train tuned to 300 GeV/c. The bubble chamber, filled with a 74% molar Ne-H_2 mix, has been equipped with a new External Muon Identifier/Internal Picket Fence system. 44 $\mu^-\mu^+$ (neutrino induced), 8 $\mu^+\mu^-$ (anti-neutrino induced), 11 $\mu^-\mu^-$, 1 $\mu^+\mu^+$, and 0 trimuons are observed. After subtracting background and correcting for detection losses, the opposite sign rate (per charged current event) is 0.62±0.13%, for $P_\mu \geq$ 4 GeV/c, the like sign events are consistent with background, and the 90% confidence level upper limit for $\mu^-\mu^-/\mu^-$ is $1.1*10^{-3}$. Eight neutral strange particles are observed in the opposite sign sample, leading to a corrected rate for $\mu\mu V^0X/\mu\mu X$ of 0.50±0.21. One neutral strange particle is observed in the like-sign sample, and the raw neutral strange particle rate per like-sign event is consistent with the raw rate in charged current events. We present kinematic distributions of the event samples, where the opposite sign sample is compared with the predictions of a charm Monte Carlo and background predictions, and the like-sign event sample is compared with the predictions of a background calculation.

TABLE OF CONTENTS

LIST OF TABLES

LIST OF FIGURES

Chapter 1

Introduction

Neutrinos were "invented" by Wolfgang Pauli, to explain the continuous energy spectrum of electrons emitted during nuclear beta decay. They were postulated to be neutral particles with spin 1/2 and mass less than 1% of the proton mass. In the "standard model" of particle interactions, there are at least three neutrino flavors, two of them (ν_e and ν_μ) having been observed by their interactions with matter[1]. The third flavor, ν_τ, has not been observed directly, but is required by lepton flavor conservation arguments, and by the agreement between experimental results on τ decay[2] and theoretical predictions, which assume the former's existence. Apart from some controversy about the mass of ν_e, the masses of the other two neutrino flavors are only bounded from above[3]. The standard model assumes that the mass of all neutrinos is zero, however, massive neutrinos can also be accommodated[4]. Measuring the Z^0 width and 'neutrino counting' experiments[5], at SLC and LEP, will provide answers about the number of neutrino flavors (where the mass of the new neutrino flavor(s) is $< M_Z/2$). At present, the best limit on the number of neutrino flavors (from UA1 and UA2)[6] is $N_\nu \leq 6$, at the 90% C.L. limit.

In this chapter, we present a brief description of the standard model with emphasis on multi-muon production. We also discuss the

possibility of using multi-muon events as a tool for probing beyond the standard model.

1.1 The Standard Model

According to current belief, matter is composed of quarks, leptons and gauge bosons. For instance, atoms are made up of a nucleus, containing protons and neutrons (which are themselves made up of quarks), surrounded by electrons (one kind of a lepton). Quarks and leptons interact with each other via gauge bosons, e.g., the photon. At present, we know of six quarks (including the top quark, which has not been detected experimentally, but whose existence is required in current models), six leptons (including ν_τ) and twelve gauge bosons. The quarks and leptons are arranged in three families of two quarks and two leptons each. It is not known how many more such fundamental particles exist in nature.

The standard model is a field theory, based on underlying symmetry principles (also called gauge invariances) which predict the presence of gauge bosons, and describe the nature of their interactions with each other, and with quarks and leptons. In the standard model, the underlying symmetry is given by $SU_C(3) \times SU_L(2) \times U_Y(1)$ group. These groups describe the transformations of the fundamental fields of the theory under which the Lagrangian is invariant (this invariance is called gauge invariance). For example, we consider the Lagrangian for a free fermion field, and require it to be invariant under a transformation of the fermion field, where the

latter, $\phi(x)$, transforms as $e^{i\alpha(x)}\phi(x)$, i.e., α is a function of x, implying that the phase changes are local. Requiring the free Lagrangian to be invariant under these (local) transformations, described by the U(1) group, we are led to an expression for the Lagrangian, which not only describes the free field but also describes the interaction between the fermion and a massless gauge field. The latter field is identified with the photon field. Thus, requiring the free fermion Lagrangian to be locally gauge invariant leads to the theory of electromagnetic interactions.

In the standard model, strong interactions are described by the $SU_C(3)$ group, and, the electromagnetic and weak interactions are given by the $SU_L(2) \times U_Y(1)$ group. Gravity is not included in the standard model.

1.2 Strong Interactions

Strong interactions are based on the $SU_C(3)$ group, which gives the transformations between the three quark (and antiquark) colors. This means that quarks can change their "color" without affecting the strong Lagrangian. The theory of strong interactions, also called quantum chromodynamics (QCD), has eight massless bosons (gluons) mediating the force between different colored quarks (and anti-quarks). The strong coupling constant is large, $\alpha_s \sim 1$, at small Q^2 (invariant momentum transfer), which is why strong interactions are strong. A large coupling constant also means that perturbation techniques cannot be used easily (unlike, for example, in quantum

electrodynamics where the coupling constant, α, is 1/137, and the theory can be used for calculations to any order in α). However, QCD has had many qualitative successes.

QCD can be tested quantitatively in the high Q^2 limit, and it has met with success. Quarks at high Q^2 behave as essentially free particles (i.e., $\alpha_s \to 0$), and QCD can be used to make predictions (the property that $\alpha_s \to 0$ as $Q^2 \to \infty$ is also called asymptotic freedom). For instance, the observation of scaling and scaling violation in deep inelastic scattering of nucleons by leptons[7], hard scattering processes[8] (e.g., direct photon production in pp and $p\bar{p}$ collisions), and jet production[8,9] (in e^+e^-, pp, $p\bar{p}$ and νN interactions) are consistent with QCD predictions.

Quarks are also believed to be confined, and there is no confirmed experimental evidence for free quarks[10]. It is also believed that all colored quantities are confined, and that all observable matter containing quarks (and gluons) has to be colorless.

1.3 Electromagnetic and Weak Interactions

Electromagnetic (EM) interactions of quarks and leptons are described by quantum electrodynamics (QED), and as mentioned previously, arise by requiring the Lagrangian for a free fermion to be locally gauge invariant. QED is generated by the gauge group U(1). The EM interactions are mediated by the massless photon. QED has had enormous success[11]. For instance, the (Lamb) shift in the energy of the $2s_{1/2}$-$2p_{1/2}$ levels of the Hydrogen atom has been calculated via

QED, and confirmed experimentally; the anomalous magnetic moment of the electron has been calculated and experimentally confirmed with an accuracy of roughly 0.0002%. Weak interactions are responsible for nuclear β-decay, decays of the $\pi^{\pm}$ and μ mesons, ν and $\bar{\nu}$ interactions with matter, etc. We now have a single theory which incorporates both weak and EM interactions.

The Glashow-Weinberg-Salam gauge theory (GSW)[12], based on symmetries described by the $SU_L(2) \times U_Y(1)$ group, is one such theory. The Lagrangian for leptons (and quarks) is required to be invariant under transformations given by the $SU_L(2) \times U_Y(1)$ group. The $SU_L(2)$ group describes transformations between the electron and the electron neutrino (and, μ and ν_μ etc.), and those between the up and down quarks (also, c and s quarks etc.). These particles are arranged in left-handed doublets and right-handed singlets, as

$$\begin{pmatrix} \nu_e \\ e \end{pmatrix}_L \quad \begin{pmatrix} u \\ d' \end{pmatrix}_L \quad e_R \;\; u_R \;\; d_R \cdots$$

This pattern repeats over the known families. The $U_Y(1)$ group describes transformations between all quarks and leptons. Requiring this theory to be locally gauge invariant under SU(2) X U(1) predicts the presence of four massless gauge bosons, whereas in reality there is only one such boson (apart from the strongly interacting gluons), the photon. Therefore, the symmetry group has to be "spontaneously broken" to yield $U_{EM}(1)$[13], which leads to the result that three of the previous four massless gauge bosons become massive, and only one remains massless (identified as the photon). If, we give mass to the

vector bosons by explicitly putting a mass term in the Lagrangian, then the Lagrangian is no longer invariant under SU(2) X U(1) transformations. Two of the massive bosons are the $W^{\pm}$ which mediate the charge changing reactions like β decay, μ decay, etc., while the third boson (Z^0) mediates the neutral weak current interactions, and the fourth boson (photon) mediates the electromagnetic interactions. The spontaneous breaking of symmetry predicts the presence of yet another particle, a neutral scalar called the Higgs particle. The neutral gauge bosons, Z^0 and γ, are linear combinations of the generators of $U_Y(1)$ and the neutral part of $SU_L(2)$, and the mixing is described by the angle θ_W.

The GSW theory has had spectacular success. It predicted the existence of weak neutral currents, which were confirmed by the observation of elastic $\nu_\mu e^-$ scattering in the Gargamelle bubble chamber[14]. Among the other successes of this theory is the prediction and experimental confirmation of forward-backward asymmetry in the cross-section of $e^+e^- \rightarrow e^+e^-$ (or, to $\mu^+\mu^-$, $\tau^+\tau^-$), arising due to Z^0 and γ interference in the s-channel[15]. Finally, the weak bosons, $W^{\pm}$ and Z^0, were directly observed in $p\bar{p}$ collisions[16], with masses predicted by the GSW theory.

1.4 Glashow-Iliopoulos-Miani (GIM) mechanism

The GIM[17] mechanism very successfully predicted the existence of the charm quark which, as will see later, explains the phenomena of

opposite sign dimuons (in $\nu(\bar{\nu})$ interactions). We briefly describe the reasons which lead to the formulation of the GIM mechanism.

In the late 1960's, it was believed that there were only three quarks, u, d and s, and that all hadrons could be constructed out of them on the basis of SU(3) flavor symmetry[18]. In this model, the quarks were grouped together as a SU(3) triplet, with u and d as an isospin doublet, and the s as an isospin singlet

$$\begin{pmatrix} u \\ d' \end{pmatrix}_L \text{ and } s \qquad 1.1$$

where $d' = d\cos\theta_C + s\sin\theta_C \quad (\sin\theta_C = 0.22)$

In equation 1.1, d' is the weak eigenstate, whereas d and s are mass eigenstates. The reason d' was written as a linear combination of d and s quarks was to explain the difference in G_F (Fermi coupling constant) determined in β-decay and μ decay, and the different rates for non-strangeness and strangeness changing reactions like $\pi \to \mu\nu$ and $K \to \mu\nu$[19]. Such a scheme, however, gave rise to strangeness changing neutral interactions where a s quark could transform to a d quark, with the amplitude proportional to $\sin\theta_C\cos\theta_C$, but the experimental limits on such interactions were very stringent (branching ratios of $K^+ \to \pi^+\nu\bar{\nu} < 1.4\text{X}10^{-7}$ and $K^0_L \to \mu^-\mu^+ < 9\text{X}10^{-9}$)[20]. The GIM mechanism solved this problem by proposing the existence of a fourth quark, charm. We now identify the first two quark doublets as

$$\begin{pmatrix} u \\ d' \end{pmatrix}_L \text{ and } \begin{pmatrix} c \\ s' \end{pmatrix}_L, \quad (1.2) \quad \text{where,} \quad \begin{aligned} d' &= s\sin\theta_C + d\cos\theta_C \\ s' &= -d\sin\theta_C + s\cos\theta_C \end{aligned}$$

(actually the existence of a fourth quark had been proposed in 1964, on the basis of SU(4) flavor symmetry[21]). Writing the quarks as in 1.2, we get two strangeness changing (neutral) terms which cancel each other, in agreement with data. The two terms are,

$s \to u \to d$ with amplitude $\sin\theta_c\cos\theta_c(\bar{d}\gamma^\mu(1-\gamma^5)s)Z_\mu$, and

$s \to c \to d$ with amplitude $-\sin\theta_c\cos\theta_c(\bar{d}\gamma^\mu(1-\gamma^5)s)Z_\mu$

The interactions $u \to d$ and $c \to s$ are "Cabibbo-favored" (since their strength is $\alpha \cos^2\theta_c \sim 0.95$), and $u \to s$ and $c \to d$ are "Cabibbo-suppressed" (since they are $\alpha \sin^2\theta_c \sim 0.05$).

The charm quark was first observed as a bound $c\bar{c}$ state[22], and subsequently charmed mesons (bound states of c and u(or d) quarks)[23] were detected. Since then, charmed mesons and baryons have been produced and detected in very different environments (e^+e^-, pp, $p\bar{p}$, νN, γN, πN interactions). An exhaustive review can be found elsewhere[24].

With the discovery of the bottom quark and τ lepton, the quark and leptons are now arranged in three families,

$$\begin{pmatrix} \nu_e \\ e \end{pmatrix}_L \quad \begin{pmatrix} \nu_\mu \\ \mu \end{pmatrix}_L \quad \begin{pmatrix} \nu_\tau \\ \tau \end{pmatrix}_L \quad e_R \, , \, \mu_R \text{ and } \tau_R$$

$$\begin{pmatrix} u \\ d' \end{pmatrix}_L \quad \begin{pmatrix} c \\ s' \end{pmatrix}_L \quad \begin{pmatrix} t \\ b' \end{pmatrix}_L \quad u_R \, , \, d'_R \, , \, c_R \, , \, s'_R \, , \, t_R \, , \, b'_R$$

The weak eigenstates, d', s' and b', are expressed in terms of the mass eigenstates, d, s and b, via the Kobayashi and Maskawa matrix,

$$\begin{pmatrix} d' \\ s' \\ b' \end{pmatrix} = \begin{pmatrix} c_1 & -s_1c_3 & -s_1s_3 \\ s_1c_2 & c_1c_2c_3+s_2s_3e^{i\delta} & c_1c_2c_3+s_2c_3e^{i\delta} \\ s_1s_2 & c_1s_2c_3+c_2s_3e^{i\delta} & c_1s_2s_3-c_2c_3e^{i\delta} \end{pmatrix} \begin{pmatrix} d \\ s \\ b \end{pmatrix}$$

where $c_i = \cos\theta_i$, $s_i = \sin\theta_i$, δ is a complex phase angle (responsible for CP violation in weak interactions), and θ_1 is the Cabibbo angle.

1.5 Neutrino Interactions

Neutrinos (and anti-neutrinos) interact with matter via both charged and neutral current weak interactions, with the charged current (CC) structure being purely V-A, while the neutral current (NC) structure has a small V+A component in addition to the V-A component. The amount of V+A component depends on the nature of the target.

Neutrino interactions at currently accessible accelerator energies are well described by the V-A theory, which is the low energy limit ($Q^2 \ll M_W^2$) of the GSW theory. In the following discussion all cross-sections are computed in this limit. We use the quark parton model[61] to describe neutrino interactions, since in our energy regime the neutrino probe is small enough to "see" the partons which make up the nucleon. The neutrino is assumed to interact with a quark via a W or Z boson, and the struck quark (and the other quarks in the nucleon)

convert to hadrons through the fragmentation process. The final state in this (deep inelastic) process is an outgoing lepton accompanied by a hadronic shower. This is schematically shown in Fig. 1.1. Neutrinos which interact coherently with an entire nucleus have been observed in both previous experiments and this experiment. However, this process accounts for only about 1% of all neutrino interactions at high energy.

1.6 Multi-muon production models

1.6.1 Opposite Sign Dimuons (OSD)

Neutrino events, with two oppositely charged muons in the final state, were first observed[25] at Fermilab, and soon confirmed by other neutrino experiments[26]. OSD were explained to be charged current neutrino events where a charm quark was produced, which hadronized mainly as a charmed meson (at times as a baryon) that subsequently decayed semileptonically to produce the second muon, as shown in Fig. 1.2 (a) and (b). Events, where the second lepton is an electron, have also been seen[27] with the same rate as OSD. Some other models were also put forward to explain OSD, but the data best agrees with charm production and decay hypothesis[28]. Fig. 1.3 (a) and (b) show the $\mu^- l^+/\mu^-$ and $\mu^+ l^-/\mu^+$ rates (the solid line is the charm excitation function, as calculated by Lai[65]). The increase with energy is due to the momentum cut on the second lepton and a threshold effect due to the large charm quark mass. In Chapter 6 we will compare kinematic

distributions of the present event sample with predictions of a (charm) Monte Carlo. If a charm quark is produced in approximately 10% of neutrino charged current events and the observed charm (meson) semi-leptonic branching fraction is roughly 10%, then one would observe OSD at a level of 1% (of charged current events). This rate is approximately what is experimentally observed.

In neutrino events, a charmed quark can only be produced by the interaction of the W^+ boson with a d or a s quark (the latter being "Cabibbo-favored"), while in anti-neutrino events, charm is produced by the action of a W^- boson on a $\bar{d}$ or $\bar{s}$ anti-quark (which only exist in the 'sea'). Therefore, one would expect one or two strange particles per event in neutrino induced OSD, and two strange particles per event in most anti-neutrino induced OSD. One strange particle is produced by the decay of the charmed particle, and the second one is due to the remaining s (or $\bar{s}$) quark in the sea (in case the $W^{\pm}$ interacts with $\bar{s}$ or the s quark in the sea). In anti-neutrino induced OSD, one expects two strange particles per dimuon event because charm is produced mainly by interaction with the $\bar{s}$ quark (being "Cabibbo-favored"). The average number of strange particles per neutrino induced OSD depends on the fraction of the strange quarks (relative to d quarks), and can be expressed as $1+10\eta$, where $\eta = \int xs(x)/\int xd(x)$ (η is the ratio of strange to down quarks in a nucleon). Thus if η is 2% to 6%, one would expect 1.2 to 1.6 strange particles/event. Studies of neutral strange particle production in bubble chamber experiments support this hypothesis[29].

The kinematic variables used to describe deep inelastic processes are

$\nu = E - E'$	where E and E' are the initial and final lepton energies in the lab. frame
$Q^2 = -q^2 \cong 4EE'\sin^2(\theta/2)$	This is the 4-momentum transferred between the neutrino and the struck quark. θ is the lepton scattering angle in the lab frame. Masses of the two leptons are assumed to be zero.
$x = Q^2/2M_N\nu$	In the quark parton model, x is the fraction of the nucleon momentum carried by the struck parton. M_N is the nucleon mass. This is also referred to as x_{Bj} or Bjorken x).
$y = \nu/E$	Fraction of the initial lepton's energy loss (in the lab frame). This is related to the scattering angle in the center-of-mass frame. This is referred to as y_{Bj} (or Bjorken y).
$W^2 = M_N^2 + 2M_N\nu - Q^2$	Mass of the hadronic system recoiling against the outgoing lepton.

In the high energy limit ($E \gg m$, i.e., particles are massless), quarks can be treated as left-handed particles, and anti-quarks as right-handed. In this limit, ν_L interactions with a quark are isotropic in the center-of-mass system, and hence uniform in y, while ν_L interactions with anti-quarks are not isotropic and have a $(1-y)^2$ dependence. The reverse is true for $\bar{\nu}_R$ interactions with quarks and anti-quarks. If we assume the charm producing current to be left-handed (i.e., V-A), we can write the cross-section for interactions with isoscalar nuclei as (in the limit $Q^2 \ll M_W^2$)

$$\frac{d\sigma^{\nu}}{dx\,dy} = \frac{G_F^2\, M_N\, E_\nu\, x}{\pi}\left[\, |V_{cd}^2|\,(u(x) + d(x)) + |V_{cs}^2|\, 2s(x)\,\right] \qquad 1.7$$

and,

$$\frac{d\sigma^{\bar{\nu}}}{dx\,dy} = \frac{G_F^2\, M_N\, E_{\bar{\nu}}\, x}{\pi}\left[\, |V_{cd}^2|\,(\bar{u}(x) + \bar{d}(x)) + |V_{cs}^2|\, 2\bar{s}(x)\,\right] \qquad 1.8$$

The terms in the bracket are written using the quark parton model, where a nucleon is represented as the sum of the parton density functions. In equations 1.7 and 1.8 the terms u(x), d(x) and s(x) represent the probability of finding a u,d and a s quark respectively, with momentum fraction x. Also, in writing 1.7 and 1.8 we have assumed the Callan-Gross relation ($2xF_1=F_2$), and maximal V-A interference[30], i.e., $-2F_1(x) = F_3(x)$. We see in equations 1.7 and 1.8 that the cross-sections are uniform in y, and have no $(1-y)^2$ term, the latter being due to either ν_L interactions with d_R (s_R) or $\bar{\nu}_R$ interactions with $\bar{d}_L$ ($\bar{s}_L$). If the experimental results have a dependence on y, then it would mean that charm is not produced by pure V-A currents, but has some mixture of V+A currents.

Equations 1.7 and 1.8 have to be corrected for the large charm quark mass (mass $\cong$ 1.5 GeV/c^2), because it introduces a threshold into the d (s) $\rightarrow$ c process. This kinematical effect is taken into account via the slow re-scaling procedure[30], where x is replaced by $\xi = x + (m_c^2/2M_N\nu)$, and the structure functions $f_1(x)$ are replaced by $f_1(\xi)$ (where m_c is related to the charm quark mass, and is usually taken to be 1.5 GeV/c^2). The corrected cross-sections are[31],

$$\frac{d\sigma^{\nu}}{dx\,dy} = \frac{G_F^2 M_N E_\nu \xi}{\pi}\left(1 - y + \frac{xy}{\xi}\right)\left[|V_{cd}^2|(d(\xi) + u(\xi)) + |V_{cs}^2|2s(\xi)\right] \quad 1.9$$

$$\frac{d\sigma^{\bar{\nu}}}{dx\,dy} = \frac{G_F^2 M_N E_{\bar{\nu}} \xi}{\pi}\left(1 - y - \frac{xy}{\xi}\right)\left[|V_{cd}^2|(\bar{d}(\xi) + \bar{u}(\xi)) + |V_{cs}^2|2\bar{s}(\xi)\right] \quad 1.10$$

We use equations 1.9 and 1.10 in the charm Monte Carlo (described in chapter 6).

OSD have been studied in great detail and have yielded information about various aspects of the standard model :

(1) Anti-neutrino induced OSD occur by interaction with anti-quarks, and since $\bar{s} \rightarrow \bar{c}$ transition is "Cabibbo-favored" they provide a clean measurement of the structure function of strange quarks, s(x). This has been studied, and the fraction $2s(x)/(\bar{u}(x)+\bar{d}(x))$ is estimated to be between 0.4 and 0.5 (with roughly 20% errors)[31,32].

(2) The energy spectrum of the secondary lepton can be used to study the fragmentation function of charm quarks (D(z), where z is the fraction of the charmed quark energy carried off by the charmed hadron). It is believed that quark fragmentation functions should be the same, regardless of the environment in which it fragments, and thus a comparison of results from νN and e^+e^- interactions serve as a test of this hypothesis. The shape of the fragmentation function cannot be measured directly in OSD, and is consistent with many different functional forms, however, the mean, $\langle z \rangle$, is determined with good accuracy ($\langle z \rangle = 0.68 \pm 0.08$)[31]. The result is consistent with results from e^+e^- interactions and theoretical predictions[15,33].

(3) Combining neutrino and anti-neutrino induced OSD results, one can estimate the element V_{cd} of the Kobayashi-Maskawa matrix. The CDHS group[31] has done this analysis, and calculate $|V_{cd}| = 0.24\pm0.03$. The CCFR group[33] calculate $|V_{cd}| = 0.25\pm0.07$. Using this estimate, the two groups have calculated $\cos\theta_2$ (in the KM matrix) to be 1.05 ± 0.14 and 1.14 ± 0.35 respectively.

(4) A mechanism for OSD, not associated with charm production, has been discussed in a recent calculation[34]. The Feynman diagrams for the processes are shown in Fig. 1.4 (a) and (b). Such a mechanism enables us to study the interference between W and Z propagators. The experimental signature would be the presence of two oppositely charged muons and nothing else (not even nuclear fragments). The rate (per charged current event) is calculated for $\langle E_\nu \rangle = 50$ GeV and an iron detector, and is $\sim 10^{-5}$. Since bubble chamber experiments have low statistics, these reactions can only be detected in electronic counter experiments. One collaboration did do such an analysis and obtained a signal of 1.7 ± 1.7 events[34], whereas the theoretical calculation predicts (for their experimental cuts) 10 ± 2.6 events. The reason for the discrepancy is not understood. The same mechanism can be used to produce μ^-e^+ events with a rate which is roughly ten times higher. There have been no searches reported for this mode.

(5) A study of OSD, especially at low neutrino energies, is important for estimating the value of the parameter m_c (used in slow rescaling). Some experiments[31,35] claim a deficiency of OSD at low energy (compared to the rate at higher energies) even after correcting for the slow rescaling threshold effect, as in Fig. 1.5. One way to

remove this deficiency would be to increase the value of m_c beyond the commonly used value of 1.5 GeV/c^2 (in fact, $>$ 1.9 GeV/c^2). This, however, causes problems when the value of $\sin^2\theta_W$ determined from deep inelastic scattering experiments is compared with that from $p\bar{p}$ collider results. Another explanation, that the strange sea structure function s(x) is a function of Q^2, is also ruled out by data[35,36]. It has been proposed[36], that at low Q^2 and W there is enhanced Λ_c production, and since the Λ_c semi-leptonic branching ratio is believed to be lower than the D semi-leptonic branching ratio, this would lead to a suppression of OSD. Λ_c production can be studied in bubble chamber experiments by comparing Λ^0/K^0 rates (Λ_c may decay to Λ^0 or pK^0, whereas D decays to K^0). The statistics at low energies are poor, but there is some evidence that for 2.1 $<$ W $<$ 2.7 GeV/c^2 there is enhanced Λ_c production (in this particular experiment[37] ($\langle E_\nu \rangle$ = 2 Gev). Some experiments, at higher energy, do not see any excess of Λ_c in dilepton events (compared to ordinary charged current interactions), whereas some others see an excess of Λ^0, but do not see any dependence with neutrino energy[27,29]. However, the latter experiments are all done with much higher energy neutrino beams ($\langle E_\nu \rangle$ $>$ 25 GeV), and hence may not probe the low energy region. The counter experiments which claim to see a deficiency at low E_ν are also done with high energy beams ($\langle E_\nu \rangle$ $>$ 25 GeV). One explanation could be that the Λ_c has a significant semi-leptonic branching ratio into states not containing a Λ^0. This would explain why bubble chamber experiments see no excess of Λ^0, whereas the counter experiments are affected by

the small Λ_c semi-leptonic decay fraction. It is also possible that the counter experiment results are in error.

(6) As discussed above, OSD are produced via charm decay, and if the decay is visible then one could study exclusive decay modes and lifetimes. Even though charm meson (and baryon) lifetimes are well measured, bubble chambers can make a significant contribution in the study of new and exotic decay modes (this becomes easier when one has a large event sample).

It is in the study of strange particle production (and unusual behavior around the event vertex) that bubble chamber experiments have a distinct advantage over high statistics electronic counter experiments.

1.6.2 Like sign dimuons (LSD)

The presence of OSD can be easily explained by the charm hypothesis, but LSD have been controversial ever since they were first observed. The experimental evidence is confusing and uncertain at best (see Fig. 1.6). Most electronic counter and some bubble chamber experiments claim a signal at the 1-3σ level[29,38], whereas most bubble chamber experiments see no excess above the predicted background[39]. A recent result from a counter experiment[51] claims no LSD signal (an earlier experiment by the same collaboration did see a signal at the 1-2σ level). The reason that LSD are controversial is that the first order perturbative QCD calculations fall short of the observed signal by 1-2 orders of magnitude[40].

Many models have been proposed that claim to explain the LSD signal seen by some of the experiments, however, they predict too large a rate for charm in photo-production and hadro-production experiments. These include: (1) The proton's structure function is assumed to have charm component at the 1% level[41]. On interaction with the W boson, the c ($\bar{c}$) quark transforms to a b quark, as in Fig. 1.7 (a), which then decays in a cascade process (b → c → s) producing a muon, and giving rise to LSD. In addition, this model predicts large b and t quark production cross-sections in hadronic interactions. Lowering the intrinsic charm fraction gives too low a LSD rate[42]. (2) The quark (in the nucleon) struck by the W boson is postulated to undergo a non-perturbative transition[43] (Fig. 1.7 (b)), and give off a $c\bar{c}$ pair. One of the charm quarks decays semileptonically to give LSD. The results from a previous bubble chamber experiment[49] contradict the predictions of this model. (3) Another model includes QCD and non-perturbative effects[44] (Fig. 1.7 (c)), and appears to give rates and kinematic distributions consistent with results from some of the experiments, but results from a previous bubble chamber experiment[49] contradicts its predictions. Some other models also exist, but they predict a rate which is too low compared to the observed signal. These include : (4) Gluon fusion processes[42], as shown in Fig. 1.7 (d). (5) Gluon bremstrahlung. This is the first order QCD calculation[40] mentioned above (Fig. 1.7 (e)). (6) D^0 - $\bar{D}^0$ mixing, as in Fig. 1.7 (f). A D^0 produced in a normal (ν) charged current reaction converts to a $\bar{D}^0$ which then decays semileptonically to give off the second μ^-. D^0's which do not convert to $\bar{D}^0$ contribute

towards producing OSD. This model is ruled out by experimental limits[60] on the amount of mixing.

These models also predict a large strange particle production rate in LSD, since there are two charm quarks (except for model 6, which has only one c quark) in the final state. Most bubble chamber experiments[45,46] see no anomalous neutral strange particle rate in their like-sign dilepton samples (which are consistent with background, anyway), however, one experiment[47] did observe neutral strange particles along with a LSD signal, although with poor statistics. (7) Another model[48] has been proposed (Fig. 1.7 (g)), which tries to account for the LSD rate and the lack of strange particles in such events by postulating the existence of a new neutral, low mass (< 5 Gev/c^2) and non-strange particle which decays weakly. Such a particle would be produced either in W decays or in $p\bar{p}$ collisions, depending on whether it couples directly to the W or is produced in the hadronic debris and is unrelated to the W. However, there is no evidence for such a particle[48,49].

The LSD signal seen by some counter experiments is only 1-3σ effect, and it is possible that the background calculations, which are complicated and model dependent, are wrong[50]. The major source of background is the decay of π's and K's that are produced in charged current reactions (the decay background is at least 60% of the event sample). The background calculations[51] have to estimate the π/K production at the event vertex and in the hadronic shower. This is done by using quark fragmentation data from muon experiments and bubble chamber ν experiments. Assumptions have to be made in

extrapolating results from ν interactions in H_2 to heavier targets. On the other hand, bubble chamber experiments have backgrounds which are easier to calculate, but they suffer from a lack of statistics. In Fig. 1.6 one can see that the upper limits from bubble chamber experiments are comparable to the signals reported by the counter experiments. Bubble chambers do offer the opportunity for studying the event vertex to search for anomalous behavior. However, the recent result from a counter experiment[51] and one from a previous high statistics bubble chamber experiment[52] (along with upper limits set by other bubble chamber experiments[39]) seem to suggest that there is no discrepancy between experiment and theory (first order QCD calculations[40]).

1.6.3 Tri-leptons and Tetraleptons

Multi-muon (and multi-lepton) events have been observed by both electronic counter and bubble chamber experiments, in ν and $\bar{\nu}$ interactions, and the final states[53] include $\mu^-\mu^-\mu^+$, $\mu^+\mu^+\mu^-$ and $\mu^-e^-e^+$ (and one report of $\mu^-\mu^-e^+$). Two tetralepton[54] events have also been reported ($\mu^-\mu^-\mu^+\mu^+$ and $\mu^+e^-e^+e^-$). The production rate per charged current event for ν induced trimuons is $(3.1\pm0.4)*10^{-5}$ (averaged over two experiments where $P_\mu>4.5$ GeV/c), $\bar{\nu}$ induced trimuons $(1.8\pm0.6)*10^{-5}$, and for ν induced $\mu^-e^-e^+$ is $(3.1\pm1.9)*10^{-4}$ ($P_\mu>4.5$ GeV/c and $P_e>0.3$ GeV/c). The energy dependence for ν induced trimuons is shown in Fig. 1.8. The difference in the $\mu\mu\mu$ and μee rate is due

to the cut on the lepton momentum. Due to poor statistics, no rate has been calculated for the tetra-leptons events.

Many models[55] have been proposed to explain the existence of tri-leptons : (1) Production of a heavy charged lepton, which decays to a neutral heavy lepton which decays further with muons being produced in each decay. This is shown in Fig. 1.9 (a). The limit[6] on the mass of a new heavy charged lepton is $M_L > 41$ GeV/c^2, and since the center of mass energy available in fixed target neutrino experiments is less than 40 GeV, this model can be ruled out as a possible source. (2) Radiative production of $\mu^-\mu^+$ pair by either the leading muon or the quark, as shown in Fig. 1.9 (b). (3) Hadronic production of a $\mu^-\mu^+$ pair during the hadronization of quarks, as in Fig. 1.9 (c). (4) Production of a heavy quark, like b, which then decays to lighter quarks semi-leptonically, producing a muon at each step.(5) Electromagnetic production of vector mesons, that decay producing a $\mu^-\mu^+$ pair. (6) Diffractive production of a $\bar{b}c$ meson which then decays in a cascade process; (7) Non-perturbative production of a $c\bar{c}$ pair, each of which decays semi-leptonically. Some of these models also have implications for the production of like sign dimuons (e.g. models 3, 6, and 7).

The data best agrees with a combination of models 1 and 2 (in the ratio 1:3)[56]. However, to explain the trimuon rate, it is assumed that hadronic production of muon pairs in νN interactions (model 2) is enhanced compared to πN interactions[57] (by a factor of 2.5). This led to a calculation[58] which proposed that the observed production rate is best reproduced by a mixture of 20% $c\bar{c}$ production (model 7), 30%

radiative production (model 1) and the rest hadronic production (model 2). This proposal also explains the LSD rate observed by some experiments[43], but overestimates charm production in hadronic interactions, and cannot explain the lack of neutral strange particles in LSD samples (as mentioned in 1.6.2). The other models underestimate the production rate, and the (kinematic) characteristics of the events do not follow the predictions made by these models[55]. Considering all these factors, it seems the data is is best explained by a mix of models 1 and 2 only.

Although, tetraleptons are produced in the standard model with very small rates[54], ~ 10^{-5} - 10^{-7} per CC event, it is quite likely that it can explain the two observed tetralepton events. However, some of the models discussed for trimuon production can also produce tetraleptons (for example, models 3 and 6), but with only two events it is not possible to draw any conclusions.

1.7 Can multimuons be used to probe beyond the standard model?

Although the standard model explains the current data very well, it has a lot of unattractive features[59], some of which are: (1) There are too many free parameters in the theory, e.g., all quark and lepton masses have to be put in by hand. (2) The theory does not explain why the proton and electron charges have exactly the same magnitude. (3) There is no explanation for the replication of quark and lepton families, nor can it predict the total number of such families (in nature). (4) The bare mass of the Higgs bosons has to be fine-tuned

with extraordinary precision. (5) It does not include gravity. Considering all these "problems", it is believed that there has to be be something beyond the standard model. Possibilities include grand unified theories, supersymmetric theories, superstring theories, horizontal symmetric models, models incorporating composite W, Z and Higgs bosons, composite fermions, etc. Each of them solve some of the problems with the standard model (but have problems of their own).

We discuss two specific cases which, in principle, can be tested by studying dimuon (or multi-muon) production in ν interactions: (1) Production of supersymmetric particles, e.g., the scalar-neutrino, and its subsequent decay to produce dileptons. (2) Production and decay of heavy neutral leptons to produce multi-lepton events. The latter have been searched for, both in bubble chamber experiments and high statistics counter experiments, with no success[62]. Bubble chamber experiments, however, suffer from lack of statistics, though have the advantage of being able to study anomalous events in greater detail.

Supersymmetry is a theory in which bosons and fermions can be transformed into each other, due to the presence of a new symmetry. Thus, all the presently known particles have supersymmetric partners, e.g., the electron's partner is a scalar-electron, the photon's partner is a photino, etc. Since these supersymmetric particles have not been detected, it is believed that if supersymmetry is indeed true, then their masses have to be rather large. The present discussion is based on arguments presented in a recent review article[63].

We consider here the production of a scalar-neutrino, and study its decay modes. Current limits[6] on the mass of the scalar-neutrino and the scalar quark make it impossible for us to actually produce them in present day fixed-target experiments. A scalar-neutrino can be produced via a neutral current interaction, as depicted in Fig. 1.10. The rate of this reaction depends on the mass of the supersymmetric gauge boson, masses of the final state scalar particles, e.g., the scalar quark, energy of the incident neutrino, etc. If the scalar-neutrino is assumed to be unstable it can have decay modes involving 2, 3 or 4 particles in the final state. In most scenarios, the 2-body decay modes dominate. However, in some circumstances the scalar-neutrino can have 4-body decay modes, producing opposite sign dimuons (or dileptons), some of which are depicted in Fig. 1.11 (a) - (e). If the scalar-neutrino is lighter than the scalar-lepton (its weak partner) or scalar quarks, the 2-body decays ($\tilde{\nu} \rightarrow \nu\tilde{\gamma}$, assuming the photino is the lightest supersymmetric particle) dominate, whereas if the scalar-neutrino is nearly degenerate with the scalar-lepton (or scalar-quark) or heavier than them, then 4-body decays have significant branching ratios. The cleanest experimental signature would be that the angle between the two muons, when projected on a plane perpendicular to the neutrino direction, would peak at small angles when compared to ordinary dimuon production, where the same angle peaks at large values (suggesting that the second muon is anti-correlated with the primary muon, which is indeed the case). One must point out that the experimental

evidence for the presence (or absence) of supersymmetry is most likely to come from high energy colliders.

In some grand unified theories, neutral heavy leptons are predicted to exist which can mix with the lighter neutrinos. These are not members of a new lepton family, but are isosinglets under the weak SU(2) group. The present discussion is based on arguments presented in a recent article[62]. Such leptons can have masses as low as 1 GeV/c^2, and we restrict ourselves to the case where the mass is in the range $1 \leq M_N \leq 2$ GeV/c^2. In such a case one might expect that these leptons are produced in decays of charm and bottom mesons, e.g., $D^{\pm,0}$, and $B^{\pm,0}$. A beam-dump experiment[64] searched for such leptons by looking for the decay process $N_e \rightarrow e^+e^-\nu_e$, where the heavy lepton N_e is produced in the decay of D^+, the latter being produced in the target region far upstream of the detector. They observed no signal, enabling them to set limits on the mixing between the heavy lepton and ν_e, as a function of the heavy lepton mass. The signature of such a process would be the presence of a dilepton event with low invariant mass, and no accompanying hadronic shower. There are other decay modes of the heavy lepton, including $\mu^-\mu^+\nu$, $\mu^-e^+\nu$ and single leptons in the final state. The single lepton final states also include hadrons. Thus, one can search for long-lived heavy lepton decays by searching for events with unusual lepton signatures, and for short-lived heavy lepton decays by looking for decay vertices in opposite sign dimuon events, since the latter are due to the decay of the D meson. Big bubble chambers compete very well with counter experiments

in searching for long-lived heavy leptons, but not for short-lived leptons.

1.8 Motivation for the present Experiment

The present experiment was initially proposed in 1980. The major aims outlined in the proposal[66] were the search for new phenomena, study of charm and heavy quark production, τ lepton production, and study of fragmentation and structure functions. The focus was on the search aspect, since this was the first big bubble chamber experiment to be operated in a new energy regime, available at Fermilab's new Tevatron. Also, this would be the first big bubble chamber to be equipped with holographic optics, which would improve resolution by a factor of 4-5 over conventional photography. With holographic optics, one hoped to see particles with lifetimes of the order of 10^{-12} - 10^{-13} sec.

We expected to obtain roughly 28,000 charged current events, which would imply that about 280 charm particles would be observable within the holographic fiducial volume (roughly 1/3 of the fiducial volume used in conventional photography). This would allow a good lifetime determination, search for unexpected decay modes, etc. There was also a small possibility that one could produce b-quarks, and actually see the b-particle decaying. This was an exciting prospect since at that time there was uncertainty in the b-quark lifetime (estimates ranged from 10^{-15} to 10^{-13} sec). There was also a possibility that one could see a τ lepton decaying at the primary

vertex, thereby indicating that the incoming neutrino was a ν_τ for which there is still no direct evidence.

The study of like-sign dileptons was given high priority too. As has been pointed out in Chapter 1.6.2, the rate at which these events were being observed by some experiments was higher than theoretical predictions by a factor of 10-100. If a signal did exist at this level, then bubble chambers could make a unique contribution by studying strange particle production in such events, and perhaps discriminate between the various models proposed to explain like-sign dileptons.

1.9 Organization of the present work

In Chapter 2, we present a description of the experimental setup, with emphasis on the External Muon Identifier/Internal Picket Fence hardware and the online data acquisition system. In Chapter 3, we describe the procedure to select multi-muon candidates, i.e., the raw event sample. In Chapter 4, we describe cuts designed to remove some of the background events from the event sample, and estimate the background due to events which cannot be removed from the sample. In Chapter 5, efficiency of the various cuts, and the geometrical and electronic acceptance of the EMI is calculated. In Chapter 6, we calculate rates for the various multi-muon categories, compare kinematic distributions for the event sample with Monte Carlo predictions. A summary of our conclusions is presented in Chapter 7.

References

1) F. Reines and C. Cowan, Science 124, 103 (1956).
G. Danby et al., Phys. Rev. Lett., 9, 36 (1962).

2) M.G.D. Gilchriese, XXIIIrd Intl. Conf. on High Energy Physics, Berkeley, July 16 - 23, 1986.

3) G. Altarelli, Ref. 2.

4) S.M. Bilenky and S.T. Petcov, Rev. Mod. Phys., Vol. 59, No. 3, Part 1, p. 671 (1987)

5) E. Ma and J. Okada, Phys. Rev. Lett. 41, 287 (1978);
P. Langacker, Proceedings of the 1985 International Symposium on Lepton and Photon Interactions at High Energies, Kyoto, August 19 - 24, 1985;
L. DiLella, in same proceedings as Langacker's talk.

6) S. Geer, Talk at International Europhysics Conference on High Energy Physics, Uppsala, 25 June - 1 July, 1987 and preprint CERN-EP/87-163.

7) F. Dydak, Proceedings of the 1983 International Symposium on Lepton and Photon Interactions at High Energies, Cornell, August 4 - 9, 1983.

8) J.F. Owens, Rev. Mod. Phys., Vol. 59, No. 2, p. 465 (1987).

9) M.D. Sokoloff, Ph.D. thesis, Univ. of California, Berkeley, May 1983 (unpublished).

10) See reference list in Review of Particle Properties (Particle Data Group), Phys. Lett. 170B, p. 168 (1986).

11) F. Halzen and A.D. Martin, Quarks and Leptons, An Introductory Course in Modern Particle Physics, pp. 158 - 162, John Wiley & Sons (1984).

12) S. Glashow, Nucl. Phys. 22, 579 (1961).
S. Weinberg, Phys. Rev. Lett. 19, 1264 (1964).
A. Salam, Elementary Particle Theory, ed. N. Svartholm, Almquist and Wisell, Stockholm (1968).

13) C. Quigg, Gauge Theories of the Strong, Weak and Electromagnetic Interactions, pp. 106 - 118, Benjamin/Cummings (1983).

14) F.J. Hasert et al., Phys. Lett. 46B, 121 (1973);
F.J. Hasert et al., Nucl. Phys. B73, 1 (1974).

15) H. Yamamoto, Lepton and Photon Interactions, (1985) (Ref. 5).

16) G. Arnison et al., Phys. Lett. 129B, 273 (1983).
P. Bagnaia et al., Phys. Lett. 129B, 130 (1983).

17) Glashow, Ilipoulos and Miani, Phys. Rev. D2, 1285 (1970).

18) M. Gell-Mann, Phys. Lett. 8, 214 (164).

19) F. Halzen and A.D. Martin, Ref. 11, pp. 279 - 283.

20) Particle Data Group, Ref. 10.

21) J.D. Bjorken and S. Glashow, Phys. Lett. 11, 255 (1964).

22) J.J. Aubert et al., Phys. Rev. Lett. 33, 1404 (1974).
J.E. Augustin et al., Phys. Rev. Lett., 33, 1406 (1974).

23) G. Goldhaber et al., Phys. Rev. Lett., 37, 255 (1976).
I.Peruzzi et al., Phys. Rev. Lett., 37, 569 (1976).

24) S.P.K. Tavarnier, Ph.D. thesis, Inter-University Institute for High Energy Physics, Brussels, Belgium, October 1984 (unpublished).

25) A. Benvenuti et al., Phys. Rev. Lett. 34, 419 (1975).
A. Benvenuti et al., Phys. Rev. Lett. 35, 1199 (1975).
A. Benvenuti et al., Phys. Rev. Lett. 41, 1204 (1978).

26) The counter experiments are :
M. Holder et al., Phys. Lett. 69B, 377 (1977).
B.C. Barish et al., Phys. Rev. Lett. 36, 939 (1976).
B.C. Barish et al., Phys. Rev. Lett. 39, 981 (1977).
T. Trinko et al., Phys. Rev. D23, 1889 (1981).
H. Abramowicz et al., Z. Phys. C15, 19 (1982).
The bubble chamber experiments are:
P.C. Bosetti et al., Phys. Lett. 73B, 380 (1978).
N. Armenise et al., Phys. Lett. 86B, 115 (1979).
C. Ballagh et al., Phys. Rev. D21, 569 (1980).
N. Armenise et al., Phys. Lett. 94B, 527 (1980).
G. Gerbier et al., Z. Phys. C29, 15 (1985).

27) C. Ballagh et al., Phys. Rev. Lett. 39, 1650 (1977).
C. Baltay et al., Phys. Rev. Lett., 39, 62 (1977). Also see Ref. 29.
H. Deden et al., Phys. Lett., 67B, 474 (1977).
P.C. Bosetti et al., Ref. 26.
J.P. Birge et al., Phys. Lett. 81B, 89 (1979).
O. Erriquez et al., Phys. Lett. 77B, 227 (1979).
C. Ballagh et al., Phys. Rev. D24, 7 (1981).
A. Haatuft et al., Nucl. Phys. B222, 365 (1983).
G. Gerbier et al., Ref. 26.

28) J. Orthel, Ph.D. thesis, University of California, Berkeley, Sept. 1979 (unpublished).

29) M. Murtagh, Proceedings of the International Symposium on Lepton and Photon Interactions at High Energies, Fermilab, August 23 - 29, 1979.
For experiments after 1979 see Refs. 26 & 27.

30) Leo B. Pilachowski Jr., Ph.D. thesis, University of Hawaii, Honolulu, Dec. 1976 (unpublished).

31) H. Abramowicz et al., Ref. 26.

32) K. Lang, Ph.d. thesis, University of Rochester, New York, 1985.

33) T. Nash, Lepton and Photon Interactions, 1983 (Ref. 7).

34) R. Belusevic and J. Smith, Preprint Fermilab-Pub-87/124-T, Aug. 1987.

35) F. Sciulli, Lepton and Photon Interactions, 1985 (Ref. 5).

36) A. Bodek, Talk at Physics in Collisions VI (Quark-Lepton), Chicago, Sept. 3 - 5, 1986 and University of Rochester, New York preprint UR969 (ER13065-462), Sept. 1986.

37) H. Deden et al., Ref. 27.

38) M. Holder et al., Phys. Lett. 70B, 396 (1977).
A. Benvenuti et al., Phys. Rev. Lett. 41, 1204 (1978).
J.G.H. Groot et al., Phys. Lett. 86B, 103 (1979).
V. V. Ammosov et al., Phys. Lett. 106B, 151 (1981).
M. Jonker et al., Phys. Lett. 107B, 241 (1981).
T. Trinko et al., Ref. 26.
A. Haatuft et al., Ref. 27.
K. Nishikawa et al., Phys. Rev. Lett. 54, 1336 (1985).
H. Burkhardt et al., Z. Phys. C31, 39 (1986).
V.V. Ammosov et al., Phys. Lett. 189B, 245 (1987).
K. Lang et al., Z. Phys. C33, 483 (1987).

39) C. Ballagh et al., Ref. 26.
C. Ballagh et al., 1981, Ref. 27.
C. Baltay et al., Phys. Rev. Lett. 55, 2543 (1985).
G. Gerbier et al., Ref. 26.
F. Merritt et al., Talk (by M. Oreglia) at Div. Part. and Fields meeting, 14 - 17 January, 1987, Salt Lake City, UT and University of Rochester, New York, preprint UR 999 ER 13065-487, April 1987.

40) B.L. Young et al., Phys. Lett. 74B, 111 (1978).

41) S. Brodsky et al., Phys. Rev. D23, 2745 (1981).

42) V. Barger et al., Phys. Rev. D24, 244 (1981).

43) D.P. Roy and R.M. Godbole, Z. Phys. C22, 39 (1984).
J.R. Cudell et al., Phys. Lett. 175B, 227 (1986).

44) E.A. Choban, Z. Phys. C25, 269 (1984).

45) A. Haatuft et al., Ref. 27.

46) All references in 39 except F. Merritt et al.

47) V.V. Ammosov et al., 1981, Ref. 38.

48) D.B. Cline, Lett. Nuovo Cimento 40, 377 (1984).

49) G. Gerbier et al., Ref. 27.

50) H. Burkhardt et al., Ref. 38.

51) F. Merritt et al., Ref. 39.

52) C. Baltay et al., Ref. 39.

53) B.C. Barish et al., Phys. Rev. Lett. 38, 577 (1977).
T. Hansl et al., Nucl. Phys. B142, 381 (1978).
A. Benvenuti et al., Phys. Rev. Lett. 42, 1024 (1979).
J.G.H. Groot et al., Phys. Lett. 85B, 131 (1979).
A. Haatuft et al., Ref. 27.

54) M. Holder et al., Phys. Lett. 73B, 105 (1978).
R.J. Loveless et al., Phys. Lett. 78B, 505 (1978).

55) C. Albright et al., Phys. Rev. D18, 108 (1979).

56) T. Hansl et al., Ref. 53.

57) V. Barger et al., Phys. Rev. D18, 2308 (1978).
A. Haatuft et al., Ref. 27.

58) J. Smith and G. Valenzuela, Phys. Rev. D28, 1071 (1983).

59) P. Langacker, Ref. 5.

60) E.H. Thorndike, Lepton and Photon, 1985 (Ref. 5).
61) J.D. Bjorken and E.A. Paschos, Phys. Rev. 158, 175 (1969).

62) M. Gronau, C.N. Leung and J.L. Rosner, Phys. Rev. D29, 2539 (1984).

63) H.E. Haber and G.L. Kane, Phys. Rep., Vol. 117, Nos. 2-4 (1985).

64) K. Winter, Lepton and Photon Interactions, 1983 (Ref. 7).

65) C. H. Lai, Phys. Rev. D18, 1422 (1978).

66) Tevatron Proposal No. 632, An Exposure of the 15-Ft. Bubble Chamber with a Ne-H_2 mixture to a Wideband Neutrino beam from the Tevatron, May 6, 1980;
Addendum to Tevatron Proposal No. 632, Feb. 12, 1982.
(1) University of California, Berkeley, (2) University of Birmingham, U.K., (3) University Libre De Brussels, Belgium, (4) CERN, Switzerland, (5) Panjab University, Chandigarh, India, (6) Fermilab, (7) University of Hawaii, (8) Imperial College, U.K. (9) Illinois Institute of Technology, (10) University of Jammu, Jammu, India, (11) Department of Nuclear Physics, Oxford, U.K., (12) Max-Planck Institute, Munich, W. Germany, (13) Rutherford Appleton Laboratory, U.K., (14) Rutgers University, (15) CEN-SACLAY, France, (16) Stevens Institute of Technology, (17) Tufts University.

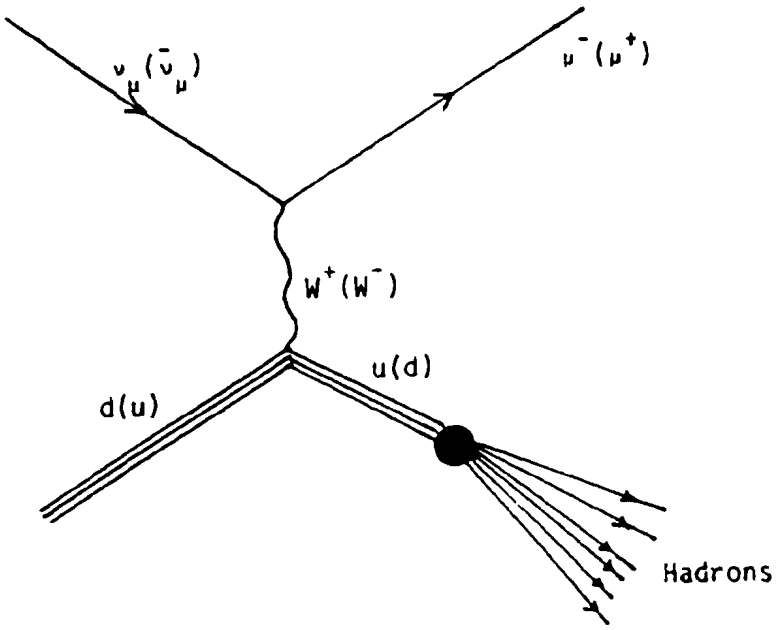

Fig. 1.1. Feynman diagram for deep inelastic scattering.

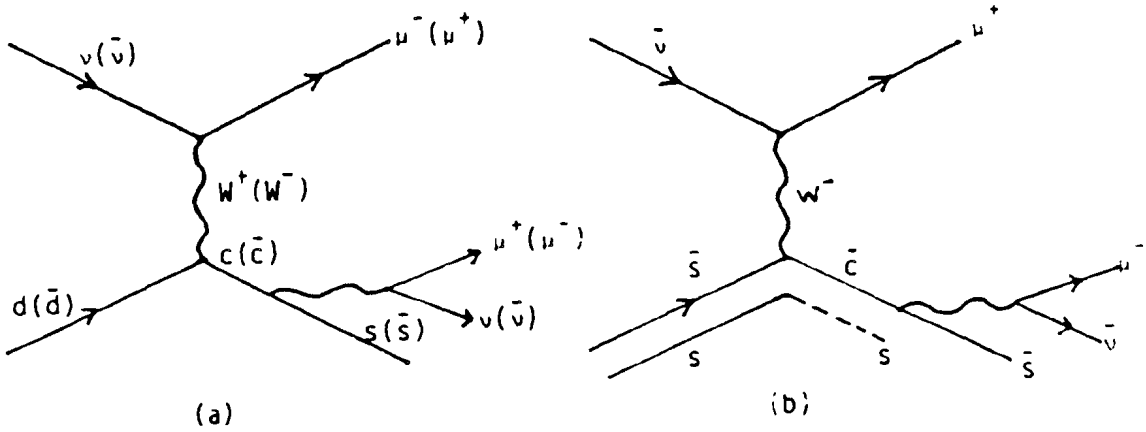

Fig. 1.2. Production of opposite sign dimuons by ν and $\bar{\nu}$ off (a) non-strange quarks, (b) strange quarks.

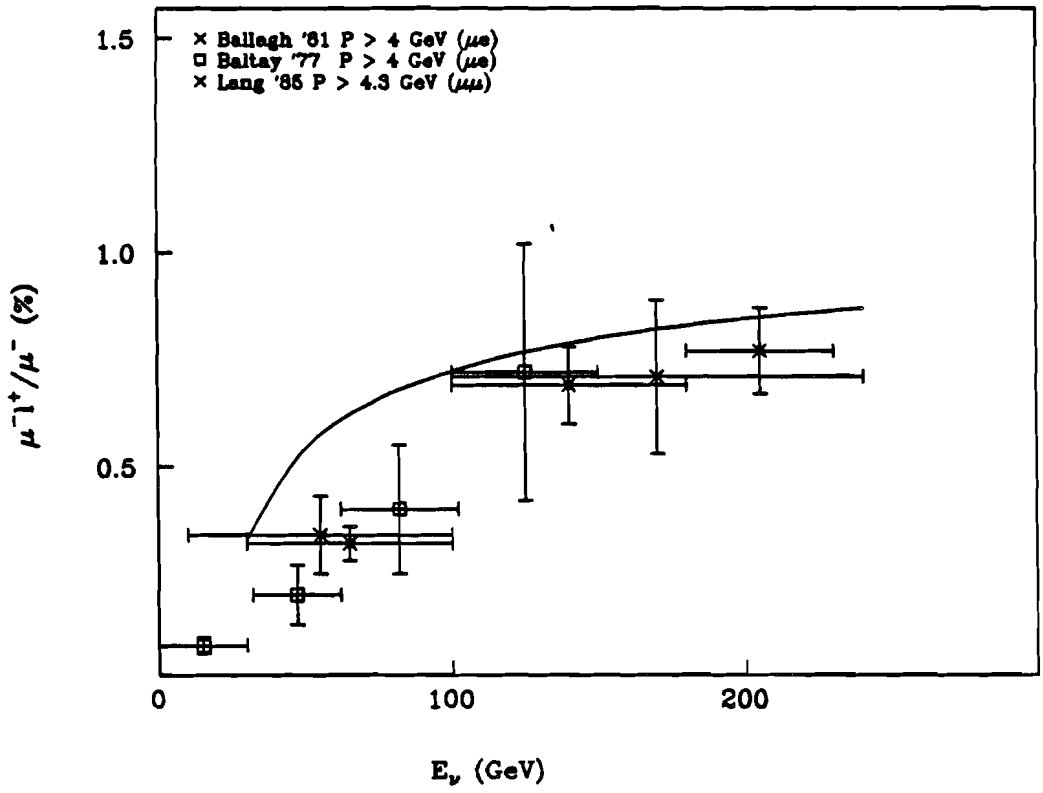

Fig. 1.3a. Experimental rate for $\mu^- l^+/\mu^-$ vs. neutrino energy (GeV).

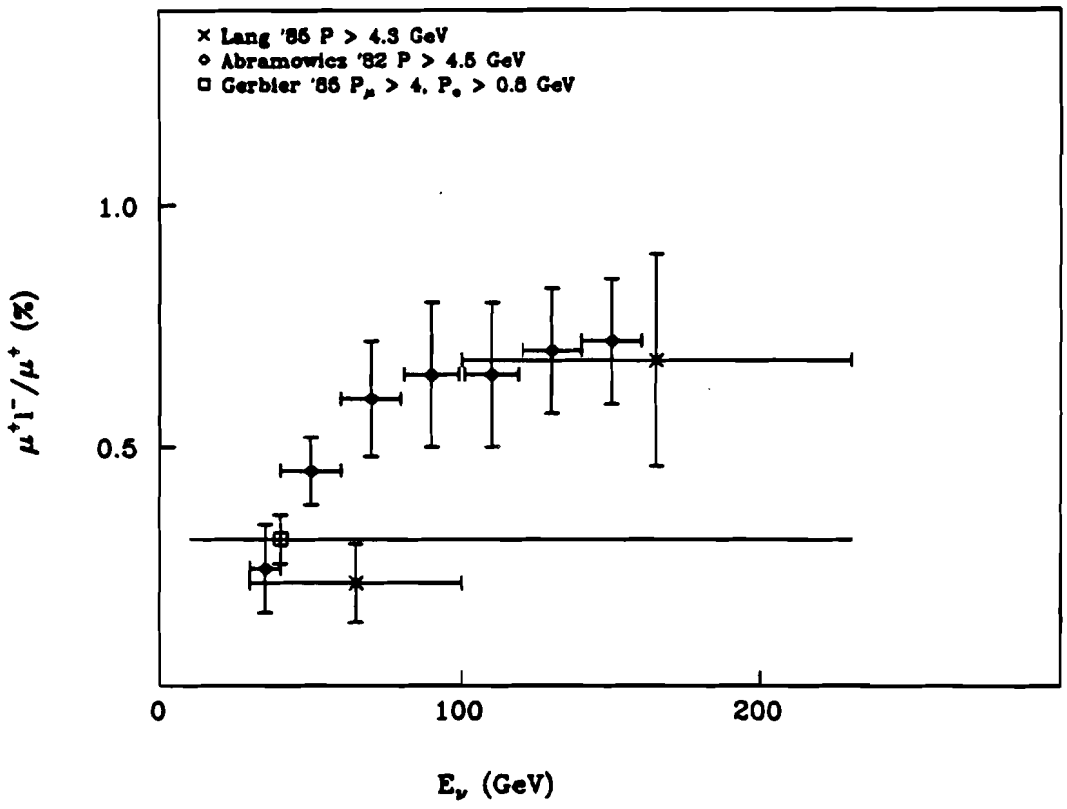

Fig. 1.3b. Experimental rate for μ^+l^-/μ^- vs. anti-neutrino energy (GeV).

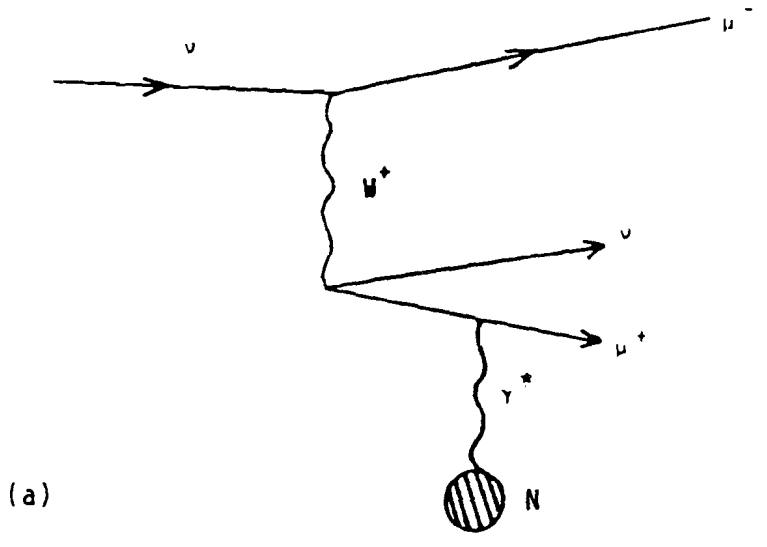

(a)

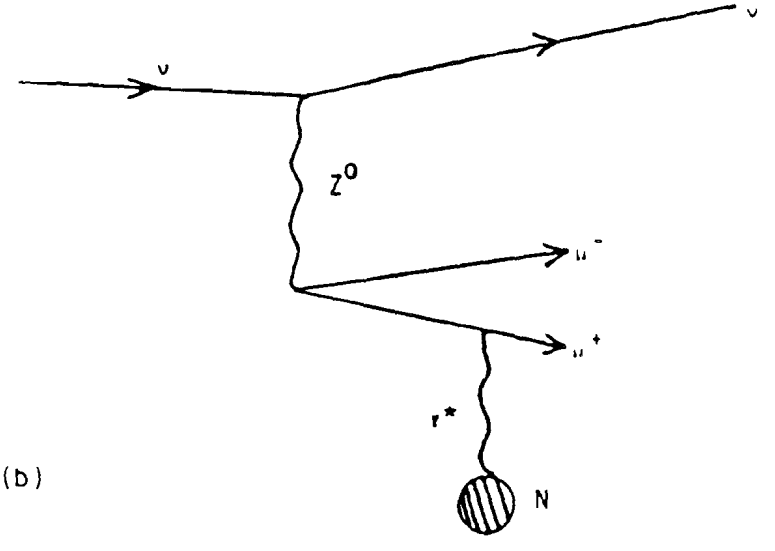

(b)

Fig. 1.4. Production of Opposite sign dimuons off the Coulomb field of a nucleus.

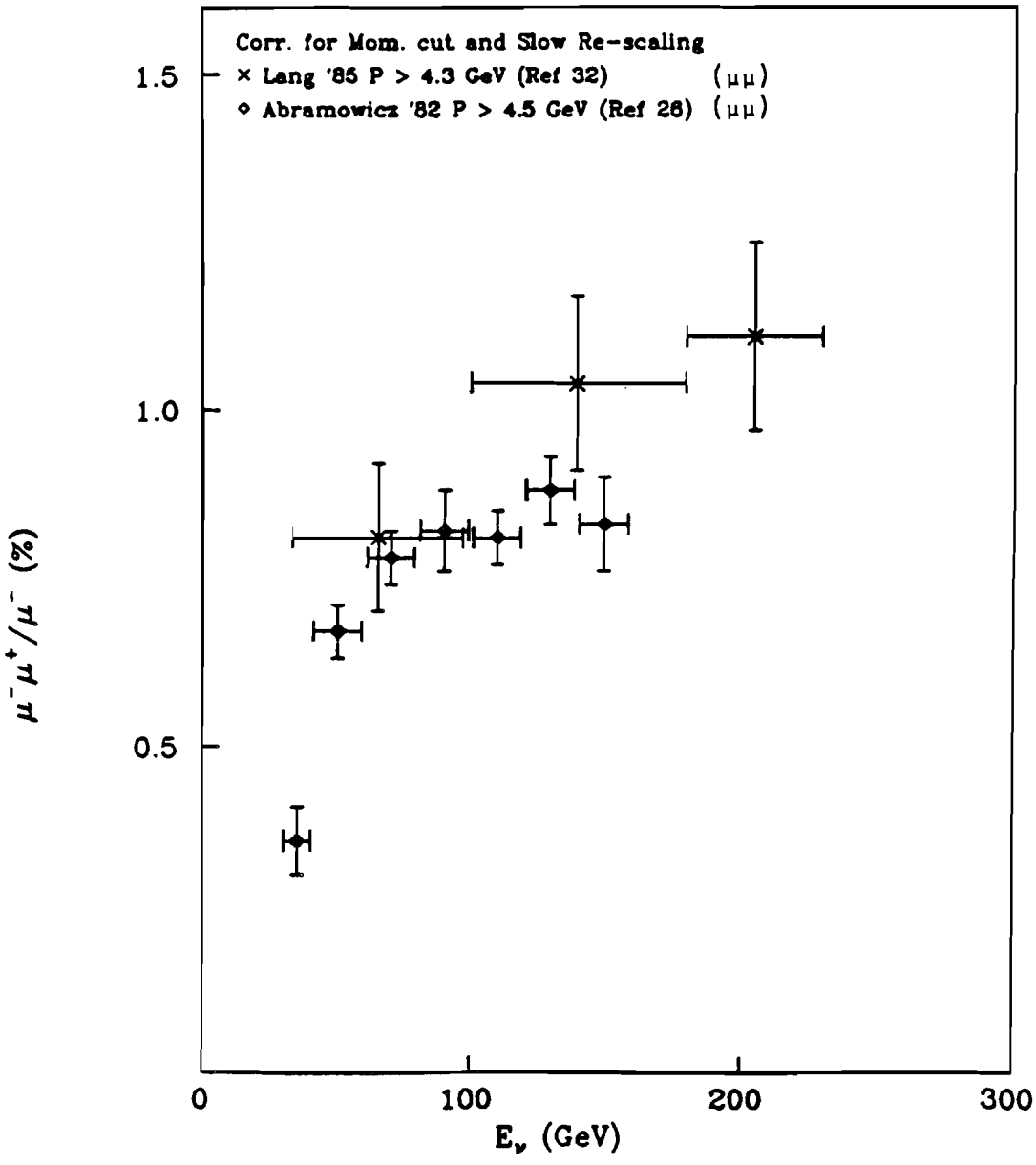

Fig. 1.5. $\mu^-\mu^+/\mu^+$ rate corrected for slow-rescaling and momentum cut on the second lepton, vs. neutrino energy (GeV).

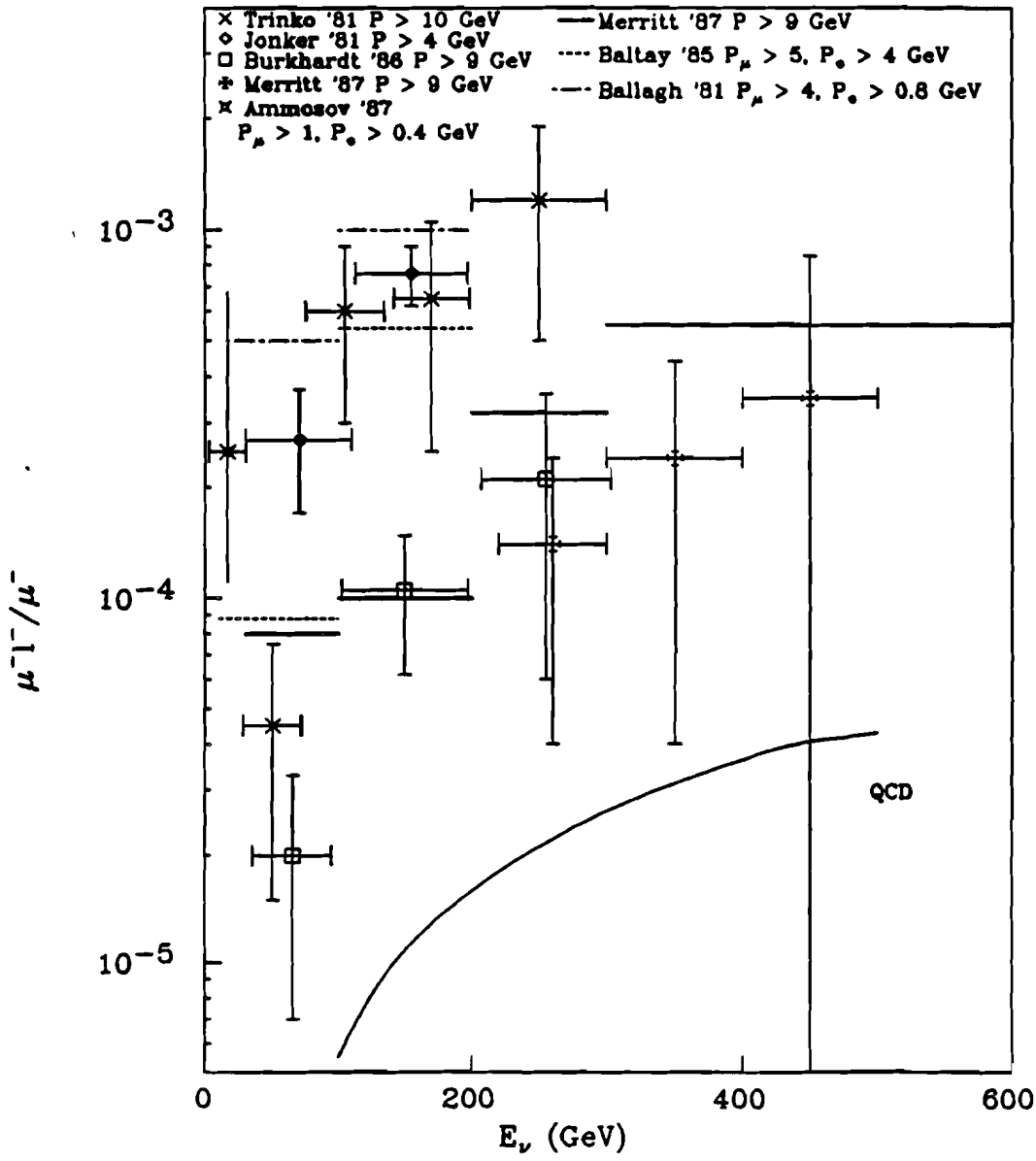

Fig. 1.6. Experimental rates for $\mu^-\mu^-/\mu^-$ vs. neutrino energy (GeV).

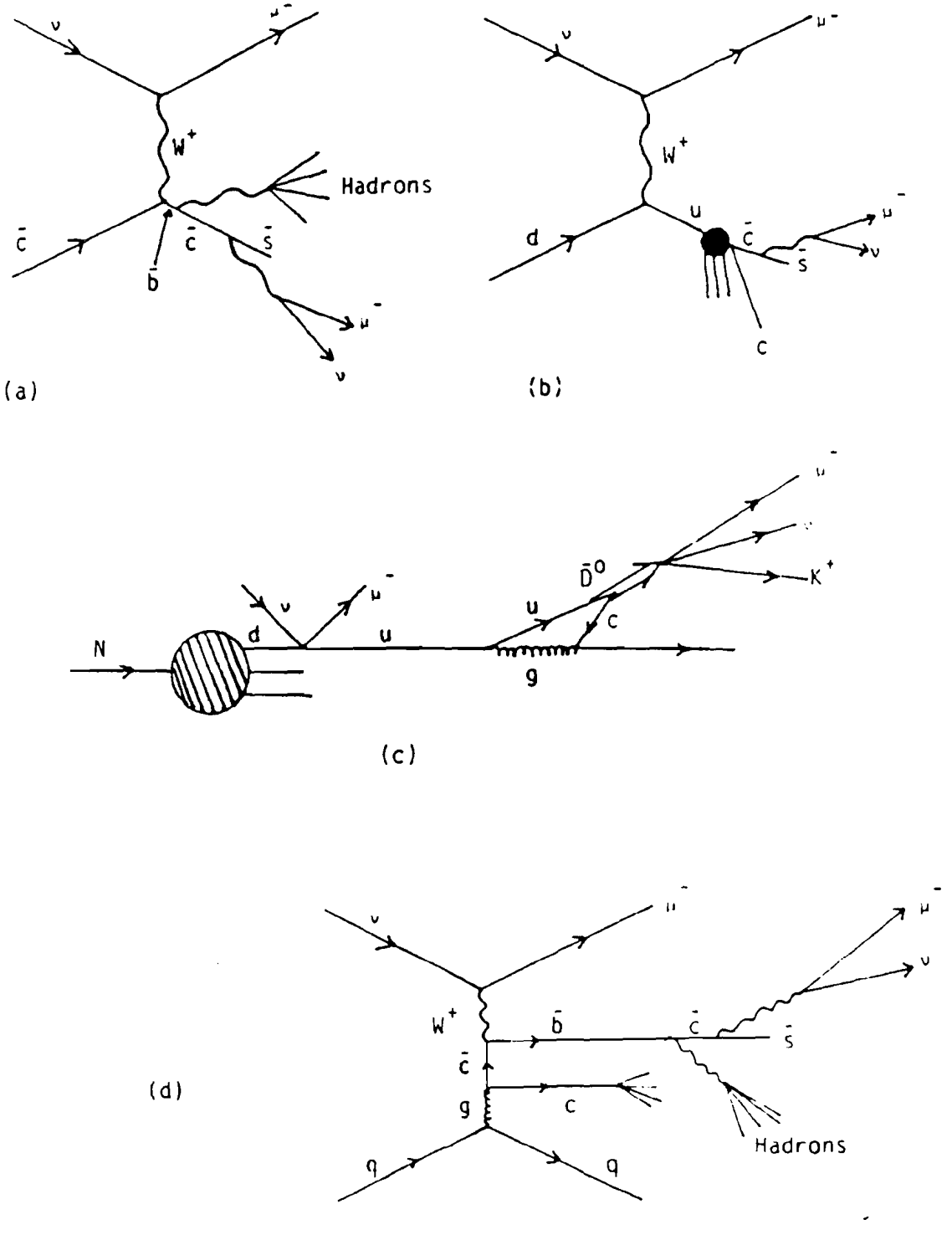

Fig. 1.7. Production models for like-sign dimuons.

(e)

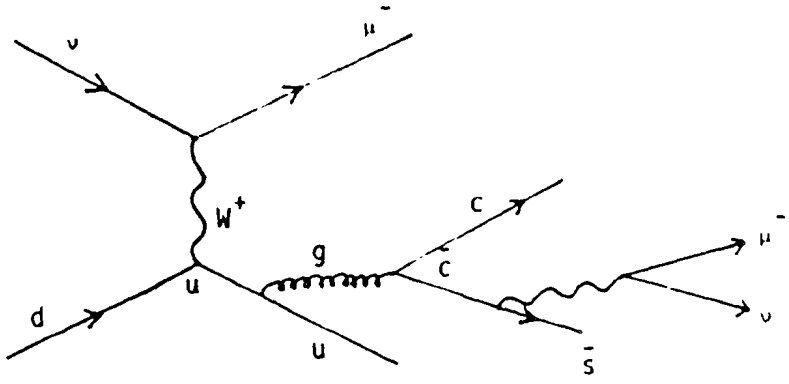

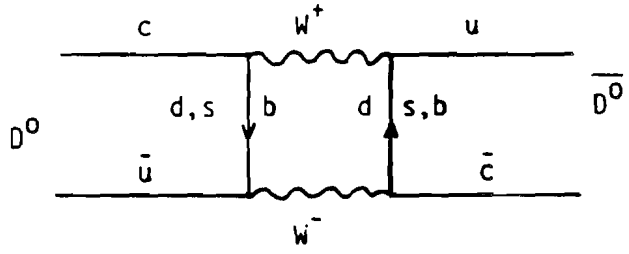

(f)

(g)

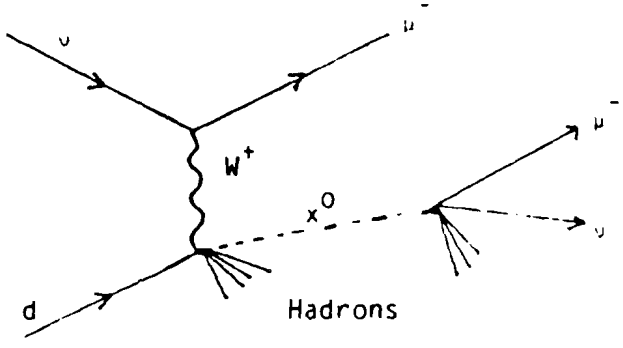

Fig. 1.7 contd. Production models for like-sign dimuons.

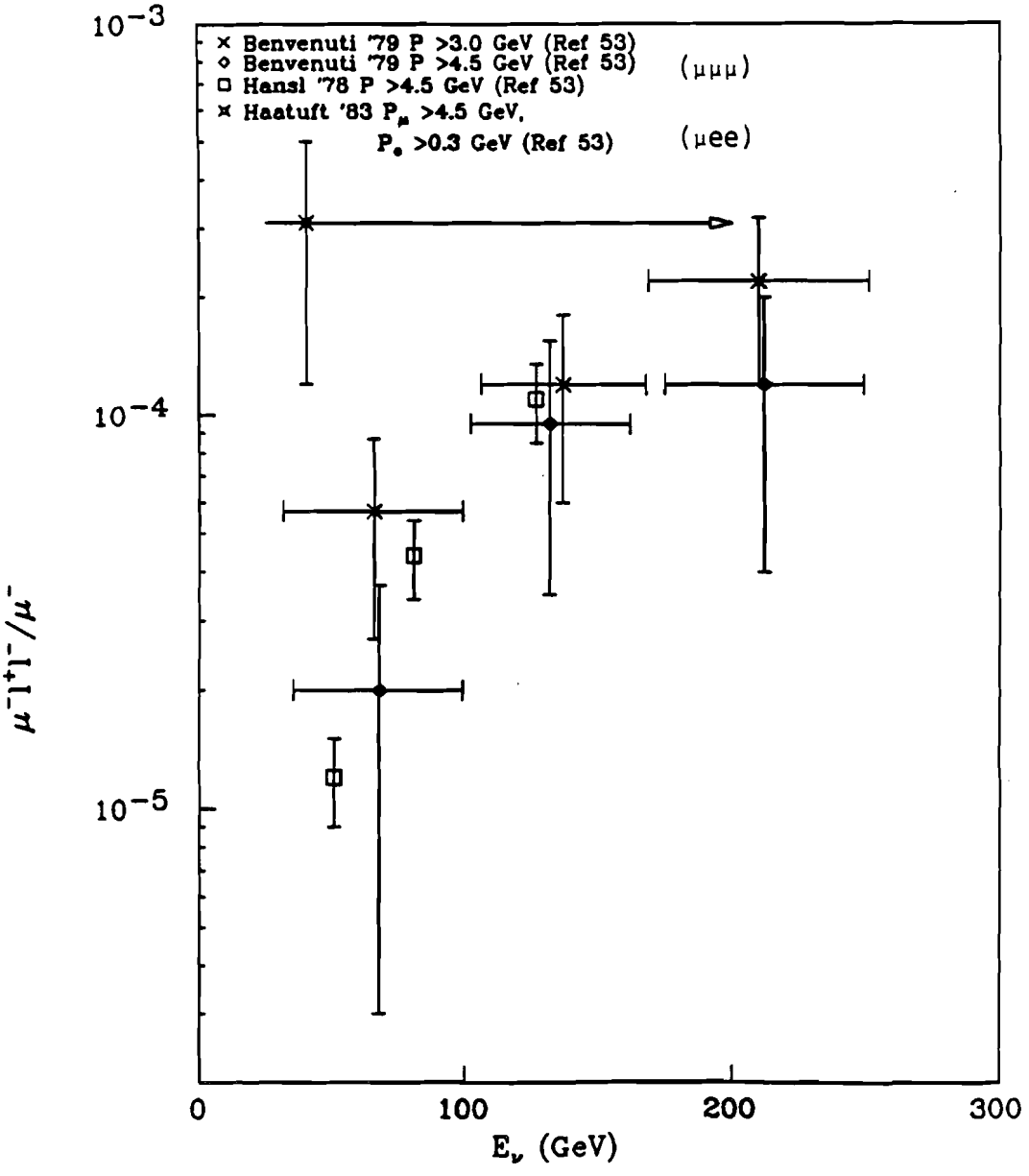

Fig. 1.8 Experimental rates for $\mu^-l^-l^+/\mu^-$ vs. neutrino energy (GeV).

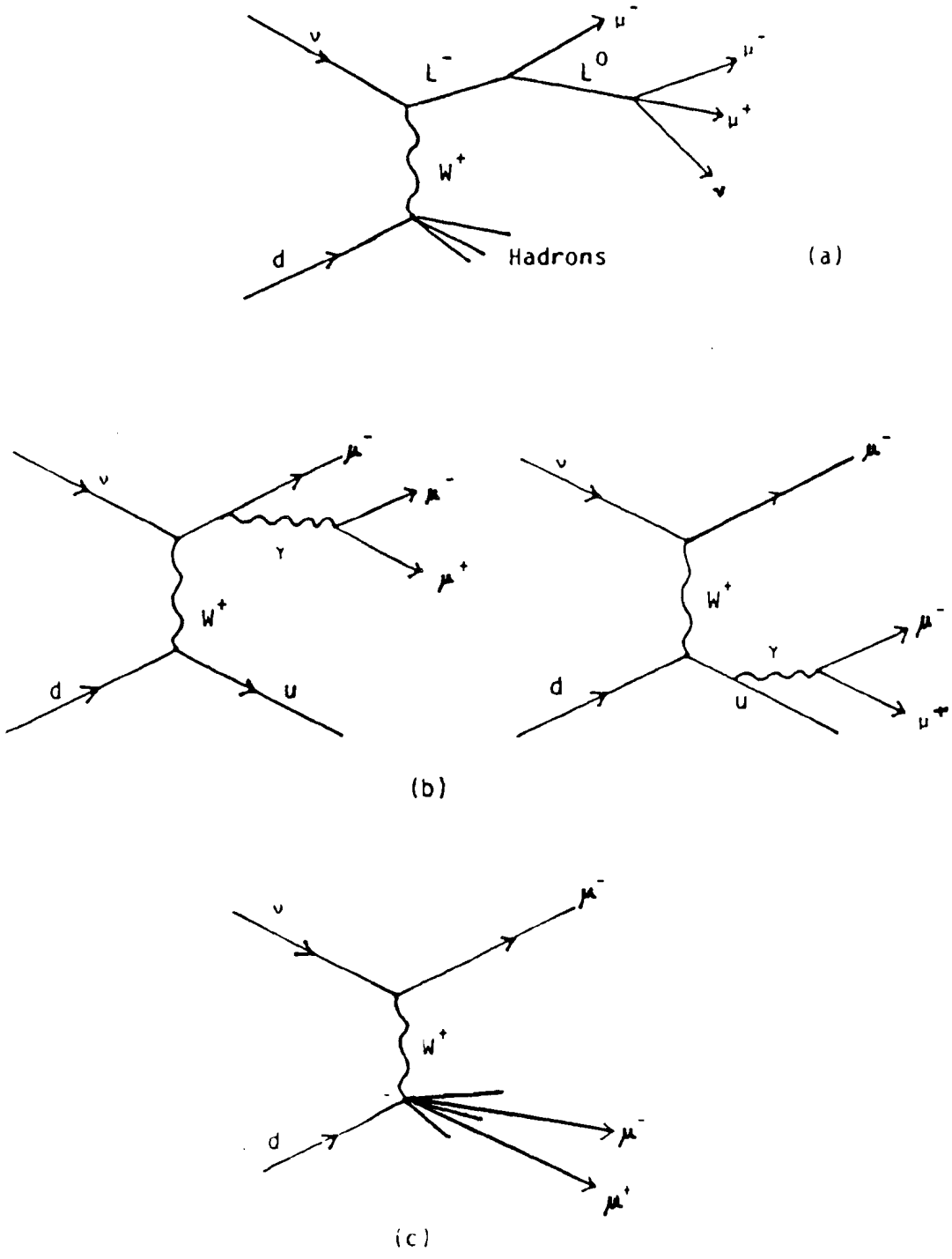

Fig. 1.9. Production models for trimuon events.

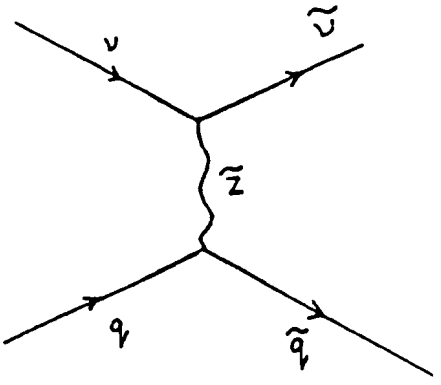

Fig. 1.10. Production of scalar-neutrino in neutrino interactions.

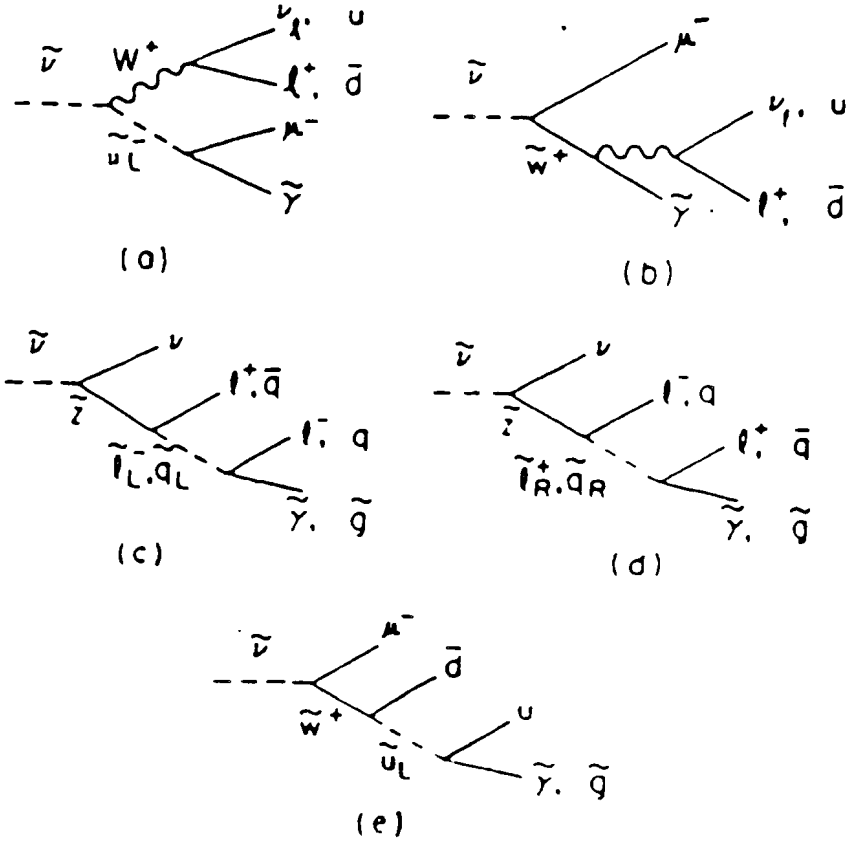

Fig. 1.11. Four body decay modes of the scalar-neutrino.

Chapter 2

Experimental Apparatus

2.1 Neutrino Beamline

The data for this work was collected at an experiment (E632) conducted at the neutrino facility at the Fermi National Accelerator Laboratory. The neutrino beam was produced by the Quadrupole Triplet train. This beam, compared to a wideband beam, enhances the relative amount of the high energy flux by suppressing the low energy component. The QT produces both ν's and $\bar{\nu}$'s, but the $\bar{\nu}$ flux is down by, roughly, a factor[1] of 2.5. One could choose the Sign Selected Triplet to reduce the $\bar{\nu}$ component further, but keeping in mind the primary aim of the experiment, the search for new phenomena, the QT train was chosen. The ν (and $\bar{\nu}$) yields of some neutrino beams[2] are shown in Fig. 2.1.

A typical accelerator cycle lasted 65 seconds. After the protons were accelerated to 800 GeV in the Tevatron they were extracted over a 23 sec period, known as the 'flat-top', as shown in Fig. 2.2. For producing the neutrino beam the protons were extracted from the Tevatron by the fast ejection method. The extraction was done in 3 'spills', each spill being 2 - 3 msec long and containing $1.5\text{-}2*10^{12}$ protons. During the rest of the 'flat-top' protons were

extracted for experiments in other beamlines. The three spills were 10 seconds apart because the laser used for holography could not be pulsed faster (the bubble chamber could be pulsed every 7-8 seconds).

The neutrino beam was formed by targeting 800 GeV protons onto a water-cooled, D-shaped Beryllium cylinder. The charged secondaries, primarily pions and kaons, were then 'focussed' by a train of quadrupole magnets. A schematic of the neutrino beamline is shown in Fig. 2.3. The high energy secondaries are produced in the very forward direction[2]. The optics of the quadrupoles was set such that 300 GeV/c is point to parallel, i.e., secondaries with $P \geq 300$ GeV/c travelled parallel to the beam line, whereas the lower energy secondaries, usually produced at larger angles, diverged out of the beam. After the secondaries were 'focussed' they were allowed to decay in a 520 meter long decay tunnel. At the end of the decay tunnel a hadron dump was placed to absorb the undecayed secondaries, protons from the primary beam, etc. Beyond the dump was a 1000 meter earth shield, which also contained lead, concrete, and iron to filter out the muons produced, along with the ν's and $\bar{\nu}$'s, in the decay of the π's and K's.

The beam was monitored at various points along the beamline using Segmented Wire Ion Chambers (SWIC), which provided a X-Y readout of the beam profile, and Split Plate Ion Chambers, which measured the beam intensity in four D-shaped plates placed symmetrically around the beam axis, thereby giving a measure of the beam symmetry. The SWICs were placed before the Beryllium target to measure the incident proton beam and in the earth shielding to measure the muons, whereas, the

Split Plate Ion Chambers were placed after the Beryllium target to measure the secondary beam profile. Any deviation from the expected Gaussian shape of the beam meant that part of the beam was being lost due to mis-steering. The primary proton current was measured by an inductance toroid counter placed upstream of the target.

The mean energy of ν-component of the beam is 80 GeV, and the mean event energy of ν-induced charged current events is 155 GeV. The corresponding numbers for the $\bar{\nu}$ component are 70 and 130 GeV respectively.

2.2 Bubble Chamber

The detector used was the 15 Ft. bubble chamber filled with a heavy neon/hydrogen mix (74% molar Neon mix corresponding to ρ = 0.72). The general features of the bubble chamber are shown in Fig. 2.4. The total target volume was 30 m^3 with the fiducial volume being ~ 15 m^3. Events which occurred between ± 110 cm along the vertical axis, at least 70 cm from the downstream wall, and at X (measured along the neutrino axis) ≥ -160 cm were counted as being in the fiducial volume (the origin of the coordinate system was at the center of the bubble chamber). Also, the event vertex was required to be at least 2 cm away from the bubble chamber walls. The radiation length was 40 cm and the interaction length was 153 cm, and since both these lengths were smaller than the bubble chamber radius (= 1.8 m), most γ's converted inside the chamber, and many of the hadrons interacted before leaving the chamber. Two superconducting coils, in

the Helmholtz configuration, supplied a 3 T field in the vertical direction, causing charged particles to bend in the horizontal plane, thereby providing a measure of their momenta. A 4 GeV charged particle had, approximately, a 4 m radius of curvature.

The bubble chamber had six camera ports with three being used for conventional cameras, one for a conventional high resolution and one for holographic camera (one port was not used). The three conventional cameras viewed the bubble chamber interior from different angles to provide stereoscopic views. The field of view of each camera was 108°. The wide-angle lens and the camera body were separated from the liquid by three hemispherical, concentric 'fish-eye' lenses. The inner two 'fish-eye' lenses were made of quartz, whereas the outermost lens was made of BK 7 glass.

The liquid in the bubble chamber was kept at 30 K and a static pressure of 8.3 bars. The operating conditions were such that the pressure on the liquid was just above the equilibrium vapor pressure at 30 K. The cycle to reduce the chamber pressure (by about 3 bars) started 40-50 msec before the beam was due to enter it. The expansion was timed so that the beam arrived at the bottom of the pressure curve. The pressure-time curve is shown in Fig. 2.5. After beam injection, chamber pressure was brought back to its original value over the next 50 msec. The sudden expansion causes the liquid to become superheated, and when charged particles traverse the liquid they ionize the atoms, and cause them to give off extremely low energy δ-rays[3], which travel a short distance, producing more ionization. This secondary ionization reaches a maximum just before the δ-rays

come to a rest, thus depositing a large amount of energy in a very small volume. The ions in the small volume then recombine giving off energy, largely as heat, which causes bubbles to be formed. The charged particles are therefore identified by the stream of tiny bubbles they leave behind. Neutral particles cannot be identified in a bubble chamber unless they decay or interact producing charged particles.

Bubble diameter increases at a rate proportional to $t^{0.5}$, where t is the growth time, with the constant of proportionality depending on chamber operating conditions like temperature, vapor pressure etc. One, however, cannot wait for too long to take a picture as turbulence in the liquid moves the bubbles randomly, thus spoiling track quality. In the current experiment one aimed to achieve a bubble size of 100 μm for holography and 400 μm for the conventional pictures with an adequate bubble density in both cases. The chamber conditions were such that the holographic picture was taken 1 msec after beam injection (or an event trigger, whichever occurred earlier) and the conventional pictures 12 msec after injection. The high resolution photograph was taken 2 msec after beam injection.

A unique feature of the experiment was that holography was tried, in a production mode, for the first time in a big bubble chamber. This technique has already been used in small bubble chambers[4]. The main motivation of holography was to have high resolution over a large volume ($\sim$ 4 m^3). In contrast the fiducial volume in focus for the conventional high resolution camera was only 0.5 m^3. The large holographic fiducial volume implies that approximately 10% of charm

decays, which have lifetimes of the order of 10^{-12} sec, can be detected[5].

Since there is no aperture to focus the image on the holographic film the (diffraction limited) resolution is determined by the physical dimensions of the film. The theoretical limit is

$$d = \frac{1.22\lambda L}{D}$$

where d is the bubble image diameter, λ the laser wavelength, D the film size and L is the distance from the bubble to the film plane. For a ruby laser, λ = 694 nm, and if the object to be imaged is at a distance of 2 m from the film (the distance between the bubble chamber midplane and the film), and the film is 50X50 mm, then the limit is 34 μm. Thus one can, in principle, separate two bubbles, or equivalently two tracks, which are at least 70 μm apart. This figure is very sensitive to imperfections in the recording system, turbulence in the bubble chamber etc. It was hoped to achieve a two track resolution of 100 μm. This is to be compared to a 400 μm for conventional photography and 150-200 μm for the conventional high resolution camera. Unfortunately, holography did not yield any useful physics results in the 1985 Spring run but a lot of the problems were understood, and many good holograms were taken during the run in Summer-Fall 1987.

For making holograms, a pulsed ruby laser was used. The light from the laser was brought into the lower hemisphere of the bubble chamber. The light, before entering the chamber, passed through a

specially designed dispersing lens which had the property of directing more energy at wider angles than at smaller angles as shown in Fig. 2.6 (b)[6]. This was done to counter the effect of the sharply decreasing scattering amplitude, $G(\alpha)$, in the direction of the holographic camera, as a function of scattering angle, as shown in Fig. 2.6 (a)[6]. The light rays passing through the central part of the dispersing lens served as the reference beam (for making the hologram) and the light scattered by the bubbles served as the object beam. A schematic of the recording scheme is shown in Fig. 2.4.

For the playback of the holograms, three machines are in use. They are situated at Fermilab, Rutherford Appleton Laboratory, and the University of Hawaii. The latter two machines use a time reversed beam to create a real image, whereas the Fermilab machine creates a virtual image and was mainly used to check the quality of the holograms. Details of the holographic recording and playback system can be found elsewhere[6].

2.3 External Muon Identifier/ Internal Picket Fence and Readout System

2.3.1 EMI/IPF

2.3.1.1 Theory of Proportional Counters

The bubble chamber was also equipped with an External Muon Identifier and an Internal Picket Fence. The EMI (as the name suggests) is used to identify muons produced in neutrino events and

the IPF is used to aid in determining the time of these events. Both the EMI and IPF were newly built for the experiment.

Both the EMI and the IPF were made of drift tubes that were operated in the proportional mode. The aim was to detect the position of minimum ionizing particles. The passage of a minimum ionizing particle through a drift tube (filled with 80-20 mix of Ar-CO_2) produces about 30 ion pairs/cm[7]. The electrons from these primary ionizations produce more secondary ionization leading to the liberation of about 90 ion pairs/cm[7]. If this charge is collected at an electrode, it would lead to a detected signal V=ne/C, which for n=90 and a typical system capacitance, C=10 pF, would be ~ 2 μV. This signal is too small to be detected. A strong electric field applied between the electrodes of the drift tube leads to avalanche multiplication, thus boosting the signal.

The avalanche multiplication depends on the value of the applied electric field. Far from the anode wire (diameter of 50 μm), the electric field (which goes as 1/r), only causes the electrons to drift towards the anode and the ions towards the cathode. But at distances very close to the wire (~ few wire radii), the field gets so strong that electrons gain enough energy to further ionize the argon atoms, and an avalanche develops. As the avalanche drifts in the electric field, it assumes a tear-drop shape[7], where the electrons are in the front part and the positive ions are in the tail. Because of lateral diffusion and the small anode radius the avalanche surrounds the wire as shown in Fig. 2.7[7]. The electrons are collected at the anode and the ions drift towards the cathode. To operate the system without

causing a breakdown and yet have good gain, the avalanche multiplication has to be in the range 10^5 - 10^6. The maximum gain that can be obtained without breakdown depends on the gas used.

The typical drift velocity of electrons in the avalanche region is 5 cm/μsec[7]. This implies that the whole process of multiplication will take place in less than 1 nsec and electrons will be collected at the anode in that time interval. The signal induced in the system is due to the change in the energy caused by charges drifting in an electric field, electrons to the anode and ions to the cathode, and is proportional to the distance through which the charge is moved. Hence the signal due to electrons, which only have to travel a few wire radii, is much smaller (~ 1%) than the signal due to the ions. The signal develops slowly in time, and all the ions are collected at the cathode in a few hundred microseconds. However, the rise time of the signal is extremely fast, and a significant fraction (~ 50%) of the signal develops within the first few hundred nanoseconds[7]. Therefore, one can terminate the output signal from the drift tube with a small resistance, giving a time constant, τ = RC, and thus very short pulses can be achieved, thereby decreasing the dead time of the counter.

The gas mix used in a proportional counter is such that it allows avalanche multiplication without breakdown. Counters are usually filled with a noble gas, for economic reasons argon, because multiplication occurs at lower fields than for gases with complex molecules[7]. However, argon alone cannot be used because it breaks down at low gains (~ 10^3 - 10^4). This is because when an excited argon atom returns to ground state it does so by a radiative process,

releasing a photon with E ≥ 11.6 eV. This is greater than the ionization potential of the cathode (6 eV for aluminum), and hence photoelectrons can be extracted initiating a new avalanche very soon after the original avalanche. Also, argon ions are neutralized at the cathode by electrons extracted from the electrode surface, and the excess energy is dissipated by the atom either by radiating a photon or extracting another electron from the metal surface, thus starting a delayed avalanche. To avoid the early breakdown, argon is usually mixed with a polyatomic gas (organic or inorganic). This is because polyatomic molecules have many non-radiative excited states (rotational and vibrational) which can absorb photons generated with a wide energy spectrum. The polyatomic gases dissipate the excess energy either by elastic collisions or by dissociation into simpler molecules, thus acting as 'quenchers'[7]. Some efficient 'quenchers' are methane, isobutane, freons, CO_2 etc. Carbon dioxide was used in the EMI/IPF system.

To keep the anode wire stable against electrostatic forces, it is strung in the drift tube under tension. The tension also reduces the catenary sag of the wire. For the EMI the tensions were 325 gm for the 22' wires and 250 gm for all the other lengths.

2.3.1.2 Description of the EMI/IPF

The IPF surrounds the inner tank of the bubble chamber (see Fig. 2.8) and is physically fastened to the bubble chamber magnet coils. The region where the IPF is situated, between the inner and the outer

tanks of the bubble chamber, is in vacuum and at an extremely low temperature. Also, the IPF is subjected to a 3T magnetic field. No repairs can be made once it is installed in place. All these factors have to be kept in mind while designing the system. The IPF covers approximately 290° in azimuth.

The IPF consists of 96 cans with each can 220 cm long, 11.0 cm wide and 2.2 cm thick. They are grouped in 4 quadrants of 24 cans. The cans are symmetrically placed with respect to the mid-plane of the bubble chamber. The cans upstream of the bubble chamber are labeled IPFA, whereas the cans downstream are labeled IPFB. A cross-section of one IPF can is shown in Fig. 2.9. A single can contains 24 stainless steel tubes glued together to form two layers. Each tube is 2.2 m long with an inner diameter of 7 mm and 0.5 mm wall thickness. Inside each tube is a 50 μm gold plated tungsten wire. The two layers are staggered with respect to each other to increase geometric and electronic efficiency of the system. High voltage cables, heater control cables, gas tubes and signal cables are fed to each can via 'umbilicals' shown in Fig. 2.10. Six tubes in each layer in a can are ganged together to form one signal channel. Hence each can provides four output signals. Twelve signals from each layer are multiplexed before being sent to the control room.

The EMI is placed outside the bubble chamber and is downstream from it. A schematic of the EMI/IPF is shown in Fig. 2.8. The first EMI plane (EMIB) is separated from the bubble chamber by 3-5 hadronic interaction lengths (chamber vessel, magnet coils, support structure and zinc). The magnet coils are slightly over two interaction lengths

thick, and the zinc is 3-5 interaction lengths thick[8]. The second plane (EMIC) is separated from the first one by another 4-6 hadronic interaction lengths (lead and shielding blocks).

Hadrons which leave the chamber interact in the absorber, whereas muons going through it undergo only multiple Coulomb scattering. All charged particles produced in a neutrino event, which leave the chamber without interacting, are extrapolated through the magnetic field and the absorber. The extrapolation program (XTRAP) includes the energy loss in the bubble chamber liquid and the absorber (assuming that the tracks are muons), and predicts where the particles will hit the EMI (i.e., X, Y and Z coordinates). These positions are then compared with the hits recorded in the EMI, and tracks which pass cuts on the fit are labeled muons. The algorithm to tag muons is described in detail in Chapter 3.

The EMI planes are made of proportional drift tubes which are formed out of aluminum extrusions as shown in Fig. 2.11. The extrusions are fastened together to form a plane. The proportional drift tubes are 7/8" on the side (inside dimension), with wall thickness of 1/8". Each tube contains a 50 μm gold plated tungsten wire. Two layers are staggered with respect to each other by half a tube width to increase electronic and geometric efficiency of the system. The layers were labelled H-H', V-V' or U-U' (at 36.5° to the vertical) depending on their orientation. The primed layer was downstream of the unprimed layer. Planes with wires running in horizontal and vertical directions were physically fastened to each other to provide a X-Y readout at one location. In the case of EMIB,

a plane with wires at an angle to the vertical was also provided (U coordinate). Each tube was counted as a single channel, and fifteen channels from each layer were multiplexed onto one signal cable. An Amplifier/ Discriminator/ Multiplexer card (described later on), physically mounted on the extrusion itself, multiplexed the signals before sending them to the control room. On the opposite end of the extrusion a distribution card was mounted which supplied high voltage to the same 15 wires.

The wires in the IPF were kept at a positive potential of 1750 Volts and those in the EMI at 2400 Volts. Thresholds for the discriminators differed from layer to layer (0.5-1 Volt), although the voltage supplied by the threshold power supply was about 20 times higher. There was a resistive drop of 50% along the cables carrying the threshold signals and another factor of 10 was due to a 10 to 1 voltage dividing circuit on the electronic cards. The entire EMI/IPF system was fed with a 80-20 mixture of Ar-CO_2. The EMI was built and installed by the Facilities Support Group at Fermilab while the IPF was built at CERN but installed by the above group and the 15 Ft. Bubble Chamber crew.

2.3.1.3 Online Event Trigger for Holography Using the EMI/IPF

The amplified signals from all tubes in a single layer (before being discriminated) were connected in parallel to provide a signal which was available earlier than the multiplexed signal. This signal, called a 'fast OR', was used in an event trigger for holography.

To make holograms of bubbles which were of the same size as the resolution (~ 100 μm), it was necessary to flash the laser 1 msec after an event occurred. If the hologram was taken at the end of the beam spill, which was typically 2 - 3 msec wide, the bubbles would be between 100-200 μm, for an event occurring 1 msec after the start of the beam spill. It was thus decided to construct a trigger which would generate a signal available immediately after an event occurred. Also, the laser used in the recording scheme had an inherent delay of ~ 1 msec between the time it received a signal to fire and the time there was light output. Thus, if a signal from the event trigger was made available to the laser firing circuit immediately after the event occurred a hologram could be taken at a time when the bubble size was of the order of 100 μm.

The fast 'OR' signal stayed on for as long as the signal from the EMI/IPF stayed above threshold. The pulse height was a measure of the number of tubes hit coincidentally, allowing one to distinguish between 1, 2 and $\geq$ 3 tubes hit in coincidence (in the EMI layer). For the IPF, signals were grouped in units of six cans, called a 'segment'. A 'segment hit' was registered when there was a hit (in time coincidence) in both the inner and outer layers. The event trigger was activated for different event topologies. The event topologies used in the trigger were :

(1) 1 or 2 IPFA segments, $\geq$ 3 IPFB segments and $\geq$ 1 EMIB four-fold (time coincidence hits in H, H', V and V').

(2) 0 IPFA segments, $\geq$ 2 IPFB segments and $\geq$ 1 EMIB four-fold.

(3) 0 IPFA segments, $\geq$ 1 IPFB segments and $\geq$ 2 EMIB four-folds.

(4) $<$ 2 IPFA segments and $\geq$ 3 IPFB segments.

(5) A default trigger, 1.3 msec after beam arrival, was generated in case there was no event which matched the chosen topologies. After generating one signal the trigger logic was disabled from generating anymore triggers during a beam spill. The trigger logic is detailed elsewhere[9].

2.3.2 Readout System

The entire EMI/IPF system contained 2600 individual electronic channels, and, to avoid having as many signal cables, it was decided to use a multiplexing scheme. The amplifier/discriminator and the multiplexer for the IPF were on different cards unlike the EMI where all three components were on one card. However, the principle of operation for both the IPF and the EMI was the same. A 16 MHz clock was used for multiplexing. The clock pulse train was 'divided' into 1 μsec time slots and thus each slot contained sixteen clock pulses. Therefore, a maximum of fifteen bits of data were encoded in one such slot (the sixteenth bit was reserved as a timing bit). For the IPF, however, one encoded only 12 bits/slot. The clock module was triggered by a signal indicating arrival of the neutrino beam, and it generated a 4 msec pulse train. The passage of a particle through a EMI/IPF tube was recorded by a single channel of the electronics. The signal was amplified, discriminated and a latch was set. At the end of the time slot (1 μsec wide), the contents of the latch were loaded into a shift register (each multiplexer card has two 8-bit registers).

The clock pulse train shifted the information out and a reset signal cleared the latches enabling them to read in data during the next 1 μsec time slot. In this manner the data was conveniently divided into 1 μsec time slots. Moreover, the EMI/IPF had no dead time (although electronic interference from a nearby experiment caused the EMI/IPF to be saturated, rendering it useless for roughly 3-4 μsec during the 2-3 msec long beam spill). One of the sixteen bits of the shift register was connected to +5 Volts and thus was always on (this was the timing bit). The output from each ADM card during one time slot consisted of the first bit always set high and the trailing 15 bits (12 for IPF) set high or low depending on whether there were any hits in the tubes corresponding to those bits.

At the other end of the 600' cable, the signal was demultiplexed by using the same clock train which multiplexed the data. The bits which were set were translated into a spatial position (since we know the extrusion of the EMI or the group of cans of the IPF to which the cable is connected and the tube which is associated with that bit). The temporal information was obtained by noting the ordinal number of the time slot in which the bit was on. The timing bit was used to keep the data signals and the clock pulses synchronized. The electronics to do the demultiplexing was built by Nanometric Systems Inc. There were 20 12-channel digitizers. Each channel was fed data from one ADM card or one IPF multiplexer. The entire Time Digitizing System, including the clock module, was housed in one CAMAC crate. A correspondence table mapped the spatial positions of the EMI/IPF tubes onto the digitizer channels that received their data.

A second CAMAC crate contained additional modules for the online system. Input gates were used to obtain the bubble chamber roll/frame number, and the bubble chamber magnet current. A 16-bit Gated Register was used to store the event type of the event which was being read out. A 032/036 module was used to communicate with the beam line system so that beam monitoring data could be read into our computer. A scalar was used as a counter to store the ordinal number of the beam spill. Other scalars counted the fast 'ORs', the number of clock pulses in the clock burst and the various trigger topologies. Another 16-bit Gated Register was used to store additional information about the laser trigger. The data was read from CAMAC modules by a PDP 11/45 computer and stored on 9-trk 1600 BPI tape.

2.3.3 Event Interrupts

A device called the Bison Box, designed and built by Fermilab, acted as an interface between the hardware and the PDP 11/45. The Bison Box had an input register, output register and two special inputs called Interrupt A and B. Interrupt A was used to indicate to the software that a beam spill was about to occur so that one could halt interspill processing (described later), and was generated by a pulse synchronized with the accelerator clock. Interrupt B was used to indicate to the data acquisition software that data had been collected by the TDS and was ready to be read out and written to tape. The signal that generated Interrupt B was issued by the master clock

module of the TDS, after all the data had been read into the digitizers. The timing sequence is shown in Fig. 2.12.

2.4 Data Acquisition and Online Analysis Software

The standard Fermilab data acquisition package, RTMULTI[10], was customized for the present experiment. RTMULTI consists of two parts, DA and MULTI, as shown in Fig. 2.13. The DA part handles the Bison Box event interrupts, reads CAMAC, controls data buffers, writes tape and passes the events to MULTI for analysis. MULTI contains some analysis software, and in addition, has lots of 'hooks' to add on extra analysis software.

The reading of CAMAC and the format of the event record is controlled by the CAMAC list. The list is read from the disk at the time MULTI is initialized. The commands in the list are processed whenever an interrupt is generated. Different branches are followed depending on the kind of interrupt, Interrupt A, B or C (described later), and on the event type.

Since bubble chamber events cannot be scanned and measured quickly (compared to electronic counter experiments), it is very important to check the data quality as soon as possible. The performance of the EMI/IPF was continuously monitored by analyzing online cosmic rays going through the system. In addition, the demultiplexers were subjected to online hardware tests to ensure that they were working as expected. This monitoring was done in the period

between beam spills and was called 'interspill monitoring'. More detailed information on the online system can be found elsewhere[11].

2.4.1 Hardware Tests

The first hardware test was the MUX pattern test which tests the Time Digitizing System. The second test pulses all wires in the EMI (the test did not work for the IPF) and checks that data is recorded for all channels. These tests were done once automatically after the beginning of a run.

2.4.1.1 MUX Pattern Test

Since information from one EMI/IPF tube was encoded as one bit in a digitizer, it was necessary to ensure that the digitizers were working properly. A MUX Pattern Test CAMAC module was built for this purpose. A bit pattern, corresponding to which of the 15 possible tubes are hit was generated by the module. The pattern could be generated in a single 1 μsec timeslot or for a number of timeslots. The starting timeslot, number of timeslots and the pattern were under computer control.

The pattern unit was synchronized with the master clock. The output from the unit was fed to the entire TDS. The digitizers had a special input for the MUX test pattern.

To allow MUX pattern tests to be treated differently from other neutrino events they were given a different event type. The data read out from a digitizer had a simple format if it was working well. For each one μsec time bin selected all the bits in the wire pattern corresponding to the test pattern would appear for all 12 digitizer channels. The software tests performed on the data were straight forward:

1.) Check if all selected and no extra time bins appeared.

2.) Check that the correct bits appeared in all 12 digitizer channels in the selected time bins and that there are no extras.

Any errors occurring were logged on the terminal.

2.4.1.2 Anode Pulsing Test

To check the complete EMI (not the IPF) readout system, a test was devised where all the wires were simultaneously pulsed twice during one TDS clock cycle. A signal was distributed to the EMI via the high voltage distribution cards. This induced a signal in the anode wires which was then picked up by the ADM cards. The data read out contained a lot of hits in the anode pulse time slots and also hits for some wires in a few extra time slots since the EMI/IPF was also sensitive to cosmic rays during the test. Once the data was analyzed, information was printed out about dead tubes and extra time slots (not anode pulsing time slots). This test was heavily used

while debugging the EMI since it provided a quick check of the dead ADM and high voltage cards, broken wires etc. To treat such events differently from neutrino events and MUX events, they were given a different event type.

2.4.2 Cosmic Ray Monitoring

Cosmic rays provided another check of the EMI/IPF. The beam spills were at least 10 sec apart and so the intervening time was utilized to collect cosmic rays. Cosmic ray events occur at a rate of approximately 100 Hz/(sq. m.)[11]. For an EMI plane of dimensions 22' X 12' this implies 10 cosmic ray events/plane/livetime (of 4 msec). This rate is quite large, and no special cosmic ray trigger was needed to collect data. Each such event was fully analyzed before 'triggering' the EMI to collect more cosmic ray data. The cosmic ray data was distinguished from other kinds of events by giving it a different event type.

Cosmic rays pass through the EMI/IPF from all angles at all times. This meant that a histogram (binned according to tube numbers) of the raw hits in a layer, during cosmic ray events, should be uniformly filled. This was a very simple way to monitor the EMI. Dead wires, non-functioning electronic cards, lack of Ar-CO_2 in the EMI/IPF all showed up as non-uniformities in the histogram. Over-active wires showed up as spikes.

Cosmic rays were also used to provide a measure of the efficiency of the EMI. When a cosmic ray goes through an EMI plane it registers

hits in the efficient layers. Time slots were selected by demanding that they have between two and eight hits in two adjoining time slots (adjacent tubes were counted as a single hit)[11]. For the IPF plane, there had to be at least one and less than five hits in each layer, and spatial coincidence between a tube in one layer and one of the tubes in the other was required. For the EMI plane, there had to be at most one hit in each layer. Efficiencies were calculated for each layer separately, by counting how often that layer fired in coincidence with the other layers in that plane. Spatial coincidence between the primed and the unprimed layers (H-H' or V-V') was demanded. Hits in the orthogonal layers of a EMI plane were correlated by demanding that all hits occur within two adjacent time slots.

For efficiency calculations, it was required that at least three out of the four layers (four out of six in the region where the U layer was present) register hits. If, for example, there were hits in H, H' and the V layers of a plane then the efficiency counters for the hit tubes in H, H' and V were incremented whereas the inefficiency counter for V', using the tube number in the V layer, was incremented. This information was also displayed in histograms, binned according to tube numbers. Since spatial coincidence was demanded between the primed and unprimed layers, holes (15 tubes wide) in the efficiency histograms could imply that signal cables from the multiplexing cards had been fed to the wrong digitizer channels. This problem did not show up in the raw number histograms (described earlier) since they plotted all hits in the event.

Each IPF plane had only two adjacent layers, and hence the above algorithm was not appropriate for calculating efficiencies, and only the efficiency histograms were filled. A subroutine analyzed the contents of the EMI's efficiency and inefficiency histograms to calculate layer efficiencies. This information was printed out at regular intervals. A sample printout is shown in Fig. 2.14. The singles/spill column was the average number of hits/4 msec for that layer. This number provided a quick check of the activity in the EMI/IPF planes. A active tube in a layer would boost the number of hits per spill.

2.4.3 Other aspects of the Online system

It is crucial to associate the neutrino beam data with the correct bubble chamber roll/frame number. The roll/frame was read from the bubble chamber data box and included in the record with the rest of the neutrino beam data. The roll/frame number was read in, via the CAMAC list, at Interrupt A time and again at Interrupt B time. No change in the frame number meant that no picture had been taken and hence the data was not written to tape. If the frame number changed by one, it implied that a picture had been taken and the data was written to tape. If the change was greater than one, then an error message was logged on the terminal. A bubble chamber photograph was taken only if the proton intensity, as measured by the toroid counter, was above a threshold of $2.0*10^{10}$ protons.

Other changes made to MULTI included new software for beam line monitoring. The software was written by the Fermilab Computing Department but was later modified. The list of beam line devices, like the proton counter, total ionization from SWICS, was specified by us in a file resident on the beam line computer. A terminal, hooked to the beam line computer, was located in the EMI control room. The beam line devices were read at the end of a beam spill and information for all three spills came together in one record after the third spill. The data arrived via the 032/036 module, which generated a Look At Me signal. This was processed, and the data read into memory. After this, a software interrupt, Interrupt 'C', was generated, causing the data to be read into a buffer and written to tape. Beam line records were given a different event type to distinguish them from other kinds of events. The bubble chamber roll/frame number was also included in the beamline record.

During the run in Spring-Summer 1985 155,000 conventional pictures and 90,000 holograms were taken. These corresponded to a total of $2.5*10^{17}$ protons on target, yielding 15,000 ν (plus $\bar{\nu}$) induced charged current events in the bubble chamber fiducial volume (as defined in 2.2). In the present analysis, we only used data corresponding to $2.25*10^{17}$ protons on target (or 13,000 charged current events).

References

1) D.C. Carey, NUADA - A Neutrino Flux Computer Program, June 1975 (unpublished).

2) A. Malensak and L. Stutte, Fermilab TM 1190, April 1983 (unpublished).

3) Gert G. Harigel, CERN/EF 87-3, May 1987 (unpublished).

4) Stefaan P.K. Tavernier, Ph.D. Thesis, Inter-University Institute for High Energy Physics, Brussels, Belgium, October 1984 (unpublished).

5) Addendum to Tevatron Proposal No. 632, An Exposure of the 15-Ft. Bubble Chamber with a Ne-H_2 mix to a Wideband Neutrino beam from the Tevatron, Feb. 12, 1982 (unpublished).

6) H. Akbari, Ph.D. Thesis, Tufts University, 1987 (unpublished). P. Nailor, Ph.D. Thesis, Imperial College, London, 1986 (unpublished).

7) F. Sauli, CERN Yellow Report 77-09, 1977.

8) R.J. Cence et al, Nuclear Instruments and Methods, 138,245 (1976).

9) P.P. Allport, Ph.D. Thesis, Wolfson College, Oxford University, 1986 (unpublished).

10) L. Taff, D. Ritchie and T. Lagerlund, Fermilab PN-98, July 1979; PN-110, July 1979 (unpublished).

11) R. Campbell, F.A. Harris and V. Jain, University of Hawaii at Manoa, UH-511-542-84, Feb. 1985 (unpublished).

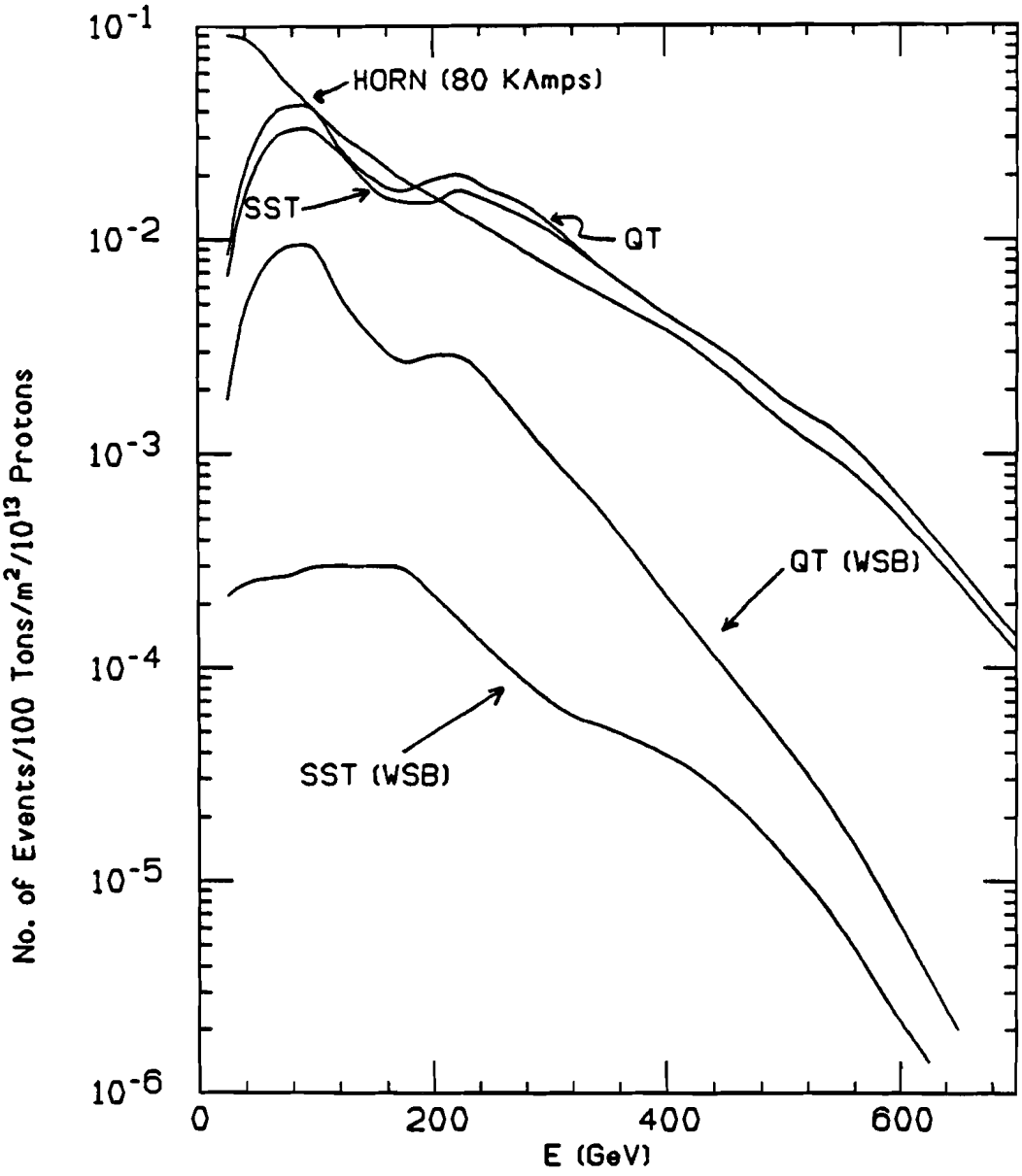

Fig. 2.1. Comparison of different neutrino beams. The horn beam is set to produce only neutrinos. The curves labeled WSB represent the anti-neutrino background in the beam.

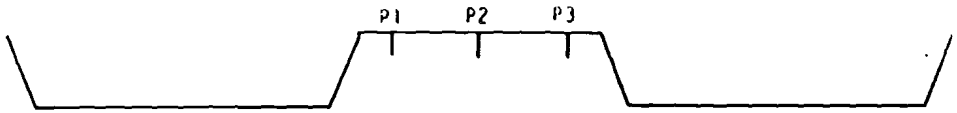

Fig. 2.2. Schematic of a typical accelerator cycle. The fast spills occur at P1, P2 and P3. The time between P1 and P3 is roughly 23 sec, and duration of cycle is 65 sec.

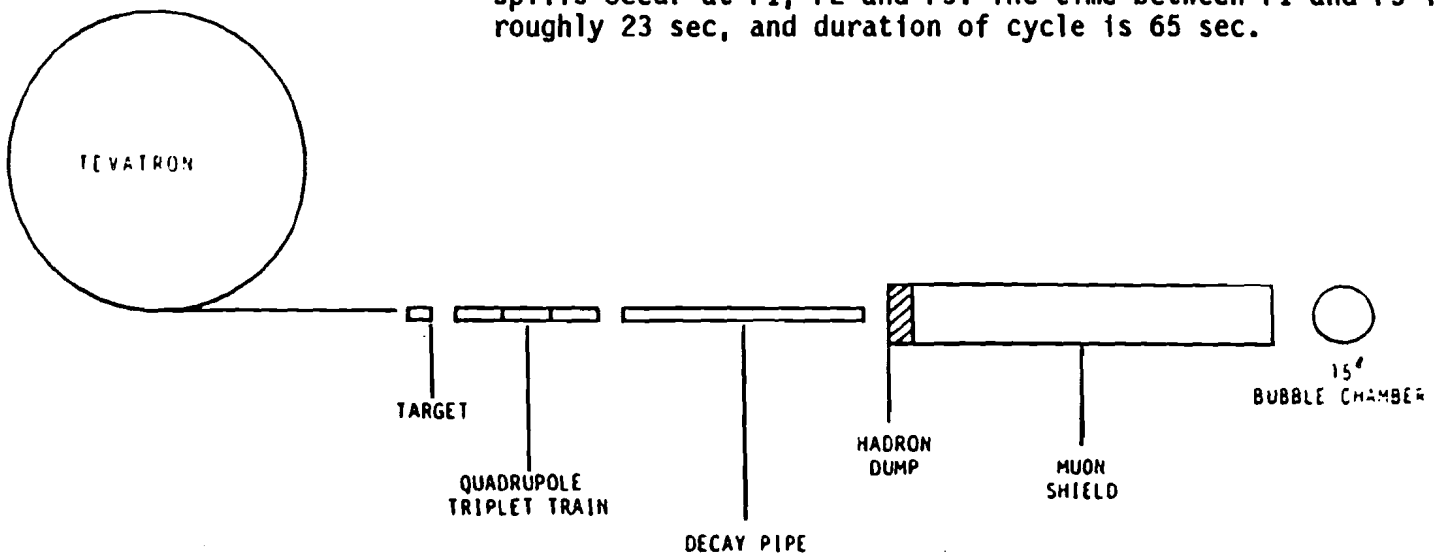

Fig. 2.3. Schematic of neutrino beamline at Fermilab.

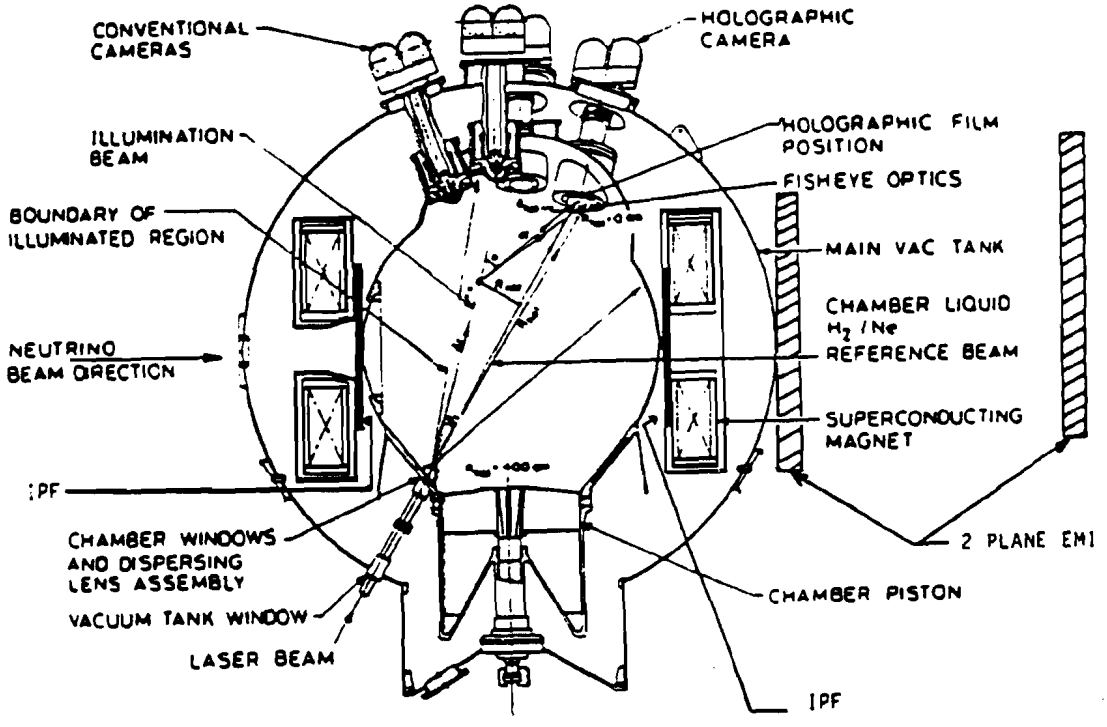

Fig. 2.4. Side view of the 15 Ft. Bubble Chamber. The EMI/IPF and the holographic recording system is shown.

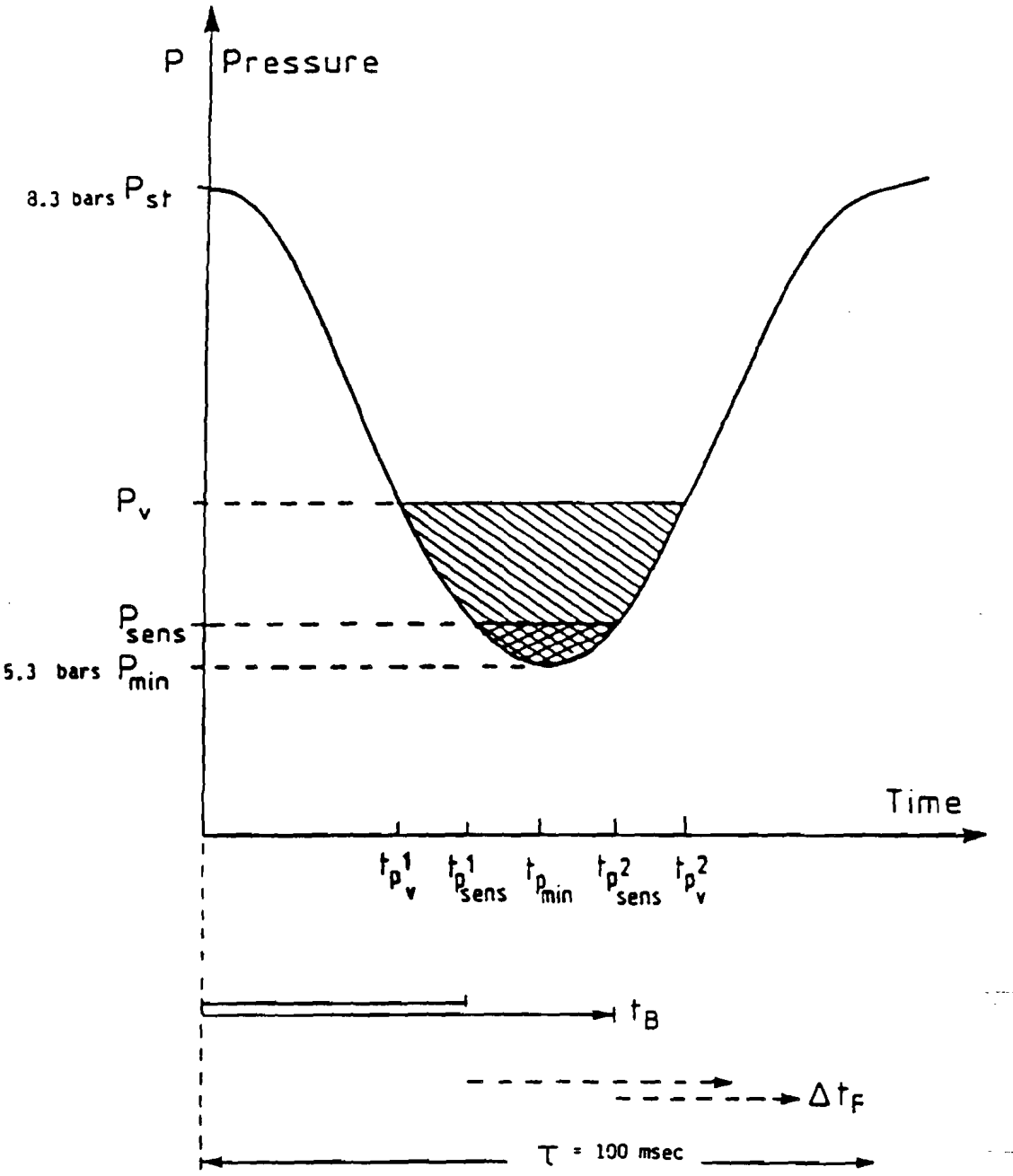

Fig. 2.5. Pressure-time curve of the bubble chamber. P_{st} = static pressure prior to expansion, P_v = vapor pressure at equilibrium temperature T, P_{sens} = pressure at which liquid is sensitive to ionizing particles, t_B = range over which particle beam is injected, Δt_F = time between beam injection and photography, τ = expansion cycle.

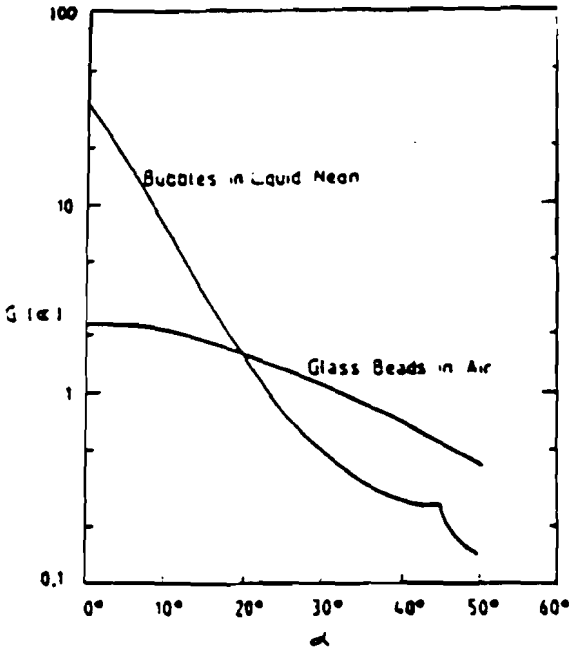

Fig. 2.6a. Geometrical scattering function, $G(\alpha)$, as a function of scattering angle, α, for bubbles ($n_b = 1.0$) in Neon ($n_{Ne} = 1.085$), and glass beads ($n_g = 1.5$) in air ($n_a = 1.0$).

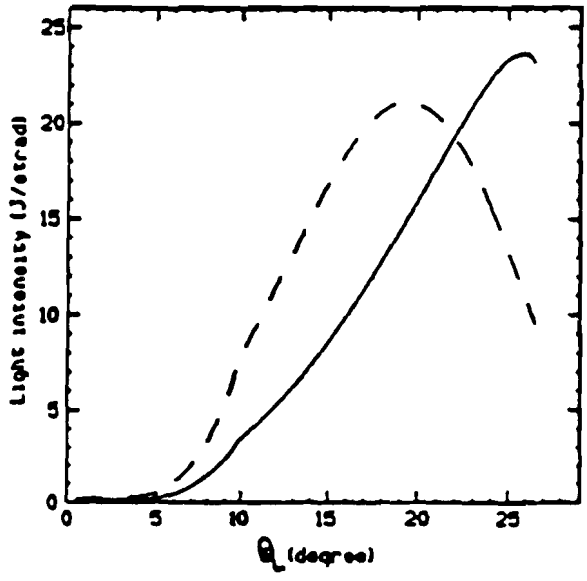

Fig. 2.6b. Design values for distribution of light intensity by the dispersing lens. The angular distribution is for liquid Ne-H_2. Laser energy is 10J. The dashed curve is for a Gaussian beam profile, solid curve to a flat profile.

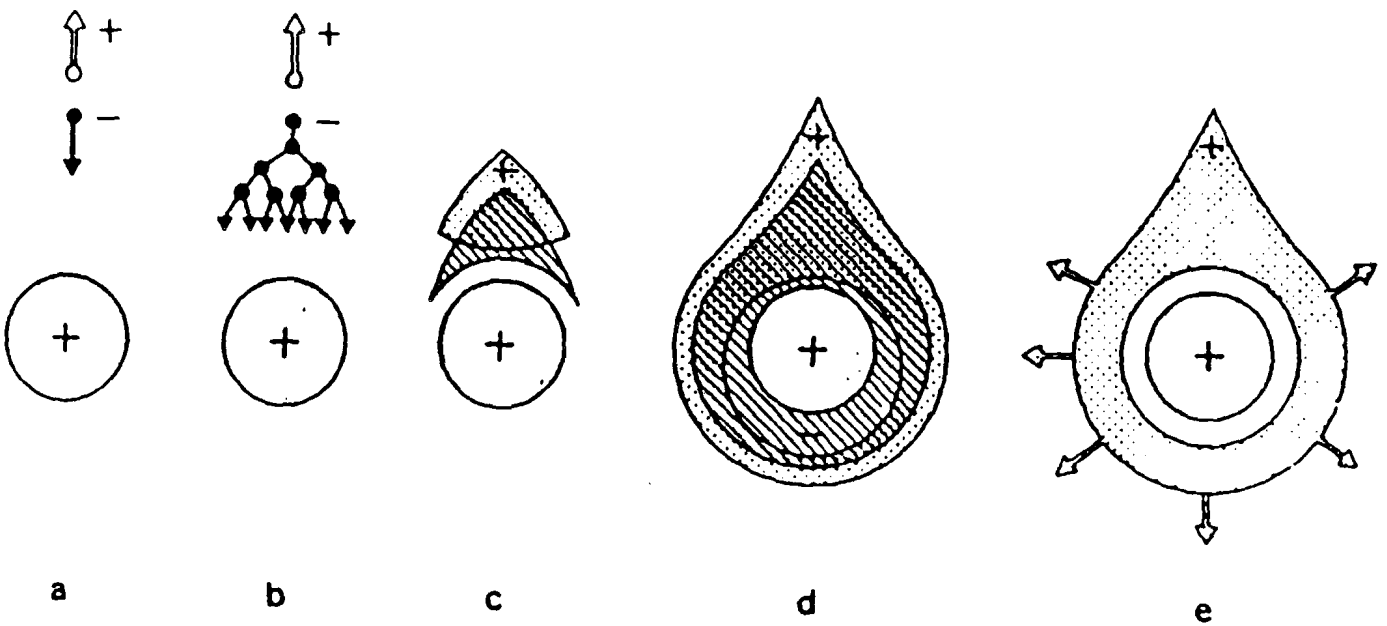

Fig. 2.7. Time development of an avalanche in a proportional tube.

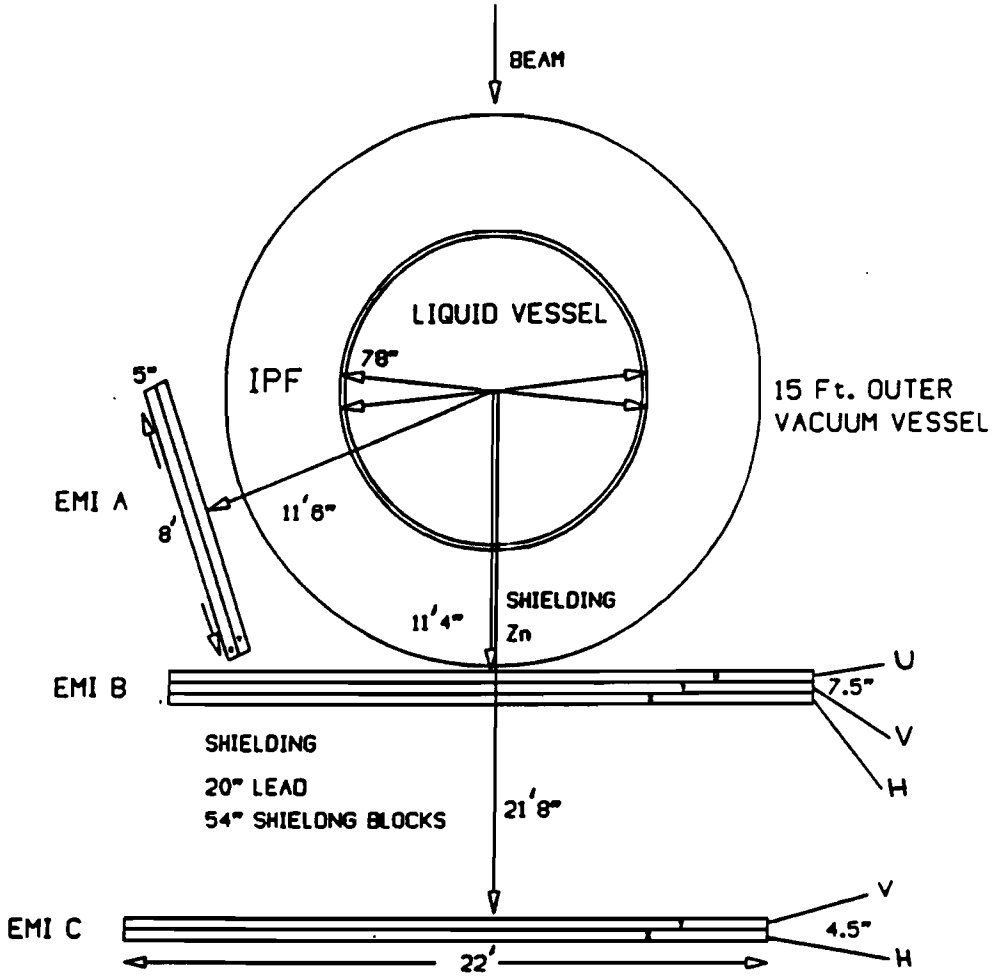

Fig. 2.8. Top view of the EMI/IPF with dimensions of various planes. Not to scale.

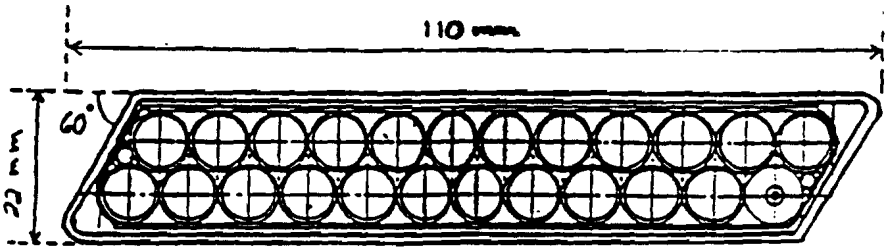

Fig. 2.9. Cross-section of an IPF can.

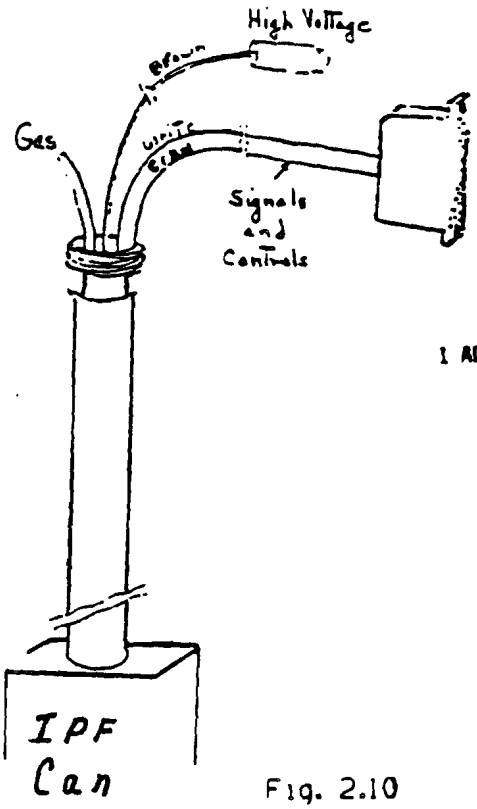

Fig. 2.10

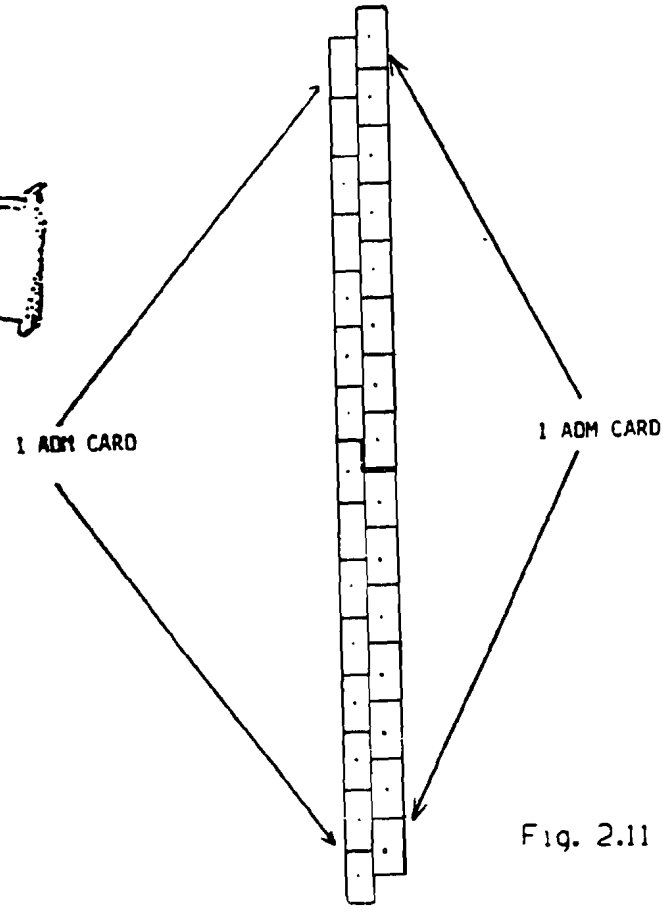

Fig. 2.11

Fig. 2.10. 'Umbilicals' carrying cables to a IPF can.

Fig. 2.11. View of two EMI extrusions.

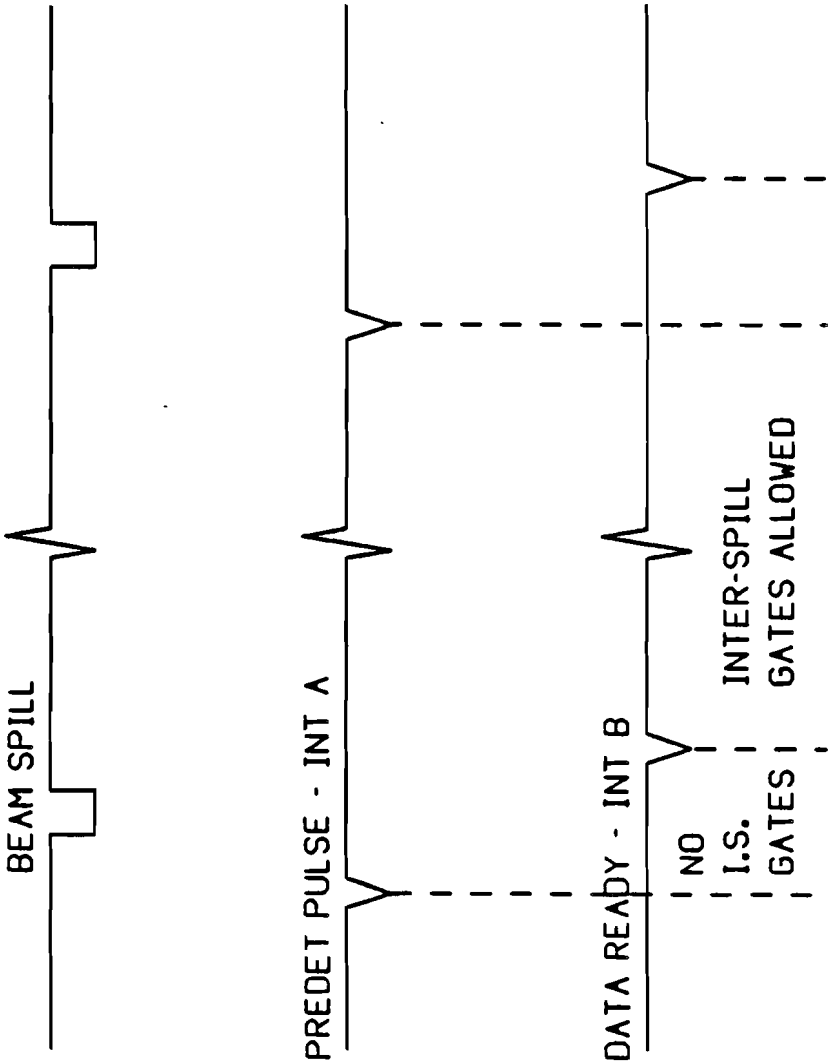

Fig. 2.12. Timing sequence for Interrupt A and B.

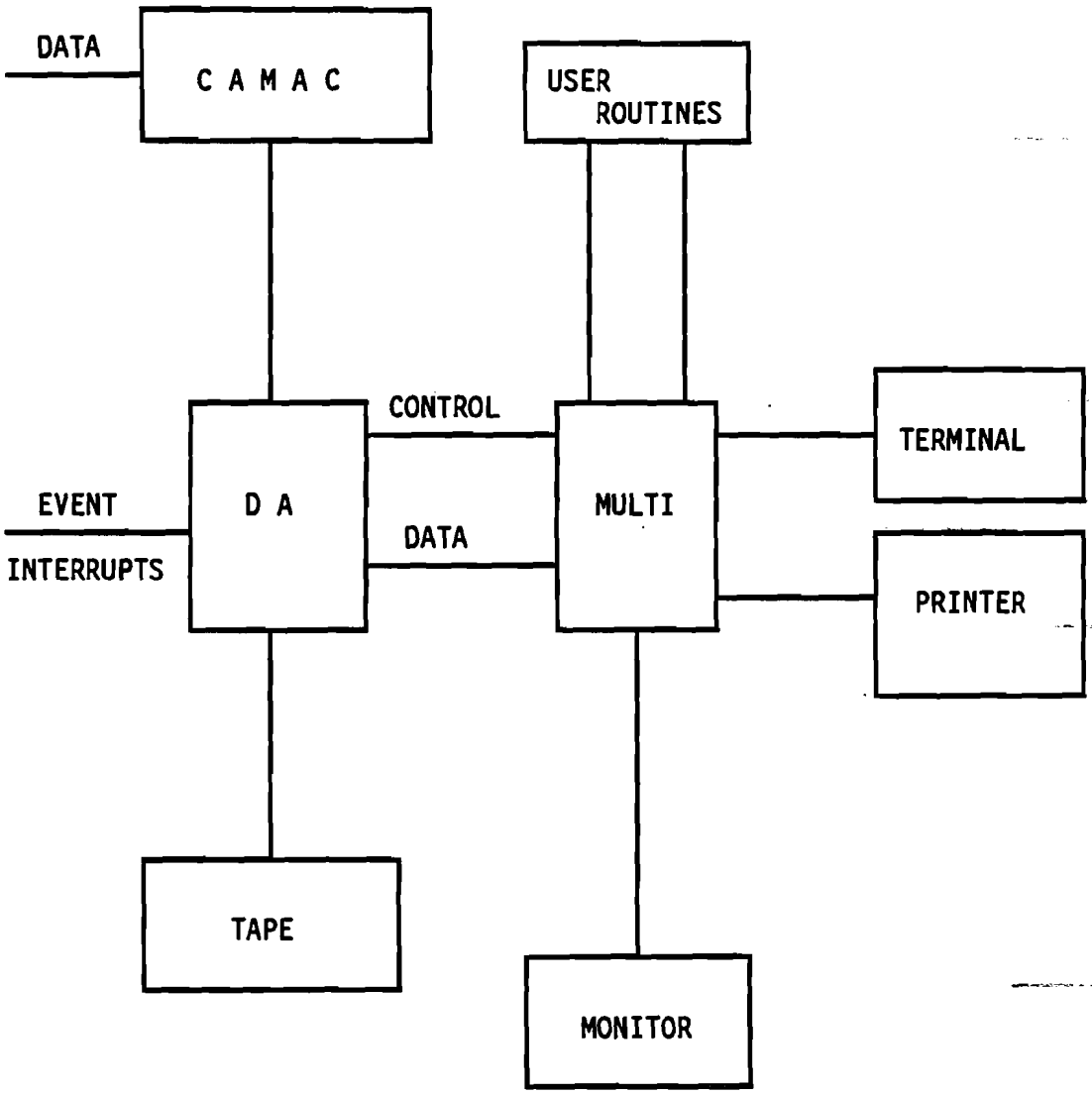

Fig. 2.13. RTMULTI Organization

EFFICIENCIES AND SINGLES RATES BY LAYER
DATE: 23-JUN-85 TIME: 07:46:21

LAYER	EFF(%)	DEFF(%)	SINGLES/SPILL
IAH	0	0	2.9
IAH1	0	0	2.7
IBH	0	0	2.5
IBH1	0	0	3.4
EAH	86	0	11.2
EAH1	80	0	11.6
EAV	91	0	14.2
EAV1	92	0	13.8
EBH	82	0	28.8
EBH1	73	0	27.1
EBV	82	0	38.0
EBV1	89	0	40.6
EBU	73	1	20.6
EBU1	70	1	18.0
ECH	80	0	26.8
ECH1	84	0	28.9
ECV	87	0	34.7
ECV1	87	0	35.3

Fig. 2.14 Cosmic Ray Efficiency printout

Chapter 3

The Data Sample

The analysis procedure used in the search for multimuon events consisted of five distinct steps, as shown in Fig. 3.1: (1) All frames are scanned for events, and the event vertices noted down. (2) Event vertices are used in conjunction with the EMI/IPF data, in program DIMUON, to tag events as possible multimuon candidates. (3) Events tagged in step 2 are re-scanned to ensure that they have at least two tracks originating from the event vertex, and leaving the chamber without undergoing any visible interactions. All such tracks, referred to as 'leaving' tracks, that have momentum $\geq$ 3 GeV/c are measured for these events. (4) 'Leaving' track measurements are processed by program PROB632 to select events which have two or more muons. (5) All events with at least two muons are completely measured. At the end of the chain, the data sample contains both genuine multimuon candidates and background events.

Some of the groups bypassed step 2, and measured all 'leaving' tracks in events that had at least one 'leaving' track. Table 3.1 shows the number of events passing each step. The numbers shown in Table 3.1 (except the last line) and below are only for those groups which followed all the steps.

3.1 Scanning

The film was distributed, for scanning and measuring, among the groups in the collaboration[1]. In the first scan, all frames were looked at, and vertices for all events found were noted down. An event is defined as a neutral-induced interaction, visible in all three views and one which has no obvious association with interactions in the upstream bubble chamber wall and support structure. A second scan was also done on a subset of the film to determine a scan efficiency for the first scan. The event vertices are also used in searching for events on the holographic film. In this step 35700 events were found.

3.2 Search For Multi-muons using Event Vertices and EMI/IPF Data

Usually, in bubble chamber experiments, one measures all 'leaving' tracks in all events and then determines which of them are muons. However, in the present analysis, in order to reduce the measuring load, this measurement was done on a sub-sample of the events found above. The basic idea was to use event vertices and EMI/IPF data, in program DIMUON, to tag possible candidates. Only those events which are in the fiducial volume (as defined in 2.2) are considered here - 25100 events pass this cut. We loop over timeslots (that pass cuts described in 3.2.1), combining them with an adjacent time slot. 'Tracks' are constructed using hits in horizontal and

vertical layers of the EMI. Only those tracks that pass cuts (described in 3.2.2) are kept. Events, with at least two tracks in each view, are tagged as multi-muon candidates.

3.2.1 Timeslot Selection

The data on the raw EMI tapes is processed and put in HYDRA format[2] by program MUCKEMI[3]. The data in a timeslot is arranged in 'bunches'. 'Bunches' are made for each layer pair in an EMI/IPF plane, for eg., EMIBH-H', EMIBV-V' and so on. A 'bunch' is defined as a group of consecutively hit tubes in a layer pair, where tubes in the primed layer of a layer pair have even numbers, and those in the unprimed layer have odd numbers. For instance, if tubes 72 and 74 are hit in EMIBH', and 73 and 75 hit in EMIBH then the bunch 72-75 is made for EMIBH-H'.

The timeslots that are present in a data record are divided into four classes: (1) Timeslots that contain hits in the IPF, EMIA or EMIB, and EMIC. (2) Timeslots that contain hits in the IPF, EMIA or EMIB, and none in EMIC. (3) Timeslots that contain at least two IPF bunches, or one IPF bunch that is at least three tubes wide, and which otherwise do not fit in classes 1 and 2. (4) Timeslots that do not fit into classes 1 through 3. In this classification scheme, it is reasonable to expect that event timeslots for charged current events would fall into class 1, whereas those for neutral current events would fall into classes 2 and 3. Class 4 timeslots are usually generated by electronic noise in the EMI/IPF, cosmic rays passing

through the detector, background associated with the beam, or hits spilling over from timeslots belonging to class 1, 2 and 3.

In the present analysis, only those timeslots that belong to classes 1 through 3 are considered. However, since hits in the EMI/IPF can span two timeslots, all timeslots belonging to classes 1 through 3 are combined with adjacent timeslots. Two adjacent timeslots are combined by adding all the 'bunches' present in both timeslots. The combined timeslots have to satisfy additional criteria before they are used for constructing 'tracks'. Firstly, they have to have less than 200 hits in the entire EMI/IPF system. This is done to avoid including timeslots which have a lot of 'electronic noise'. Secondly, the timeslots have to have at least three bunches in EMIC, with each layer pair i.e., EMICH-H' and EMICV-V', contributing at least one bunch.

3.2.2 Algorithm to construct tracks

Tracks are constructed separately in the top and side views, as shown in Figs. 3.2 (a) and (b). The figures explain the various quantities described below.

a) Top View

We choose one EMICH and EMIBH bunch from a combined timeslot. A straight line, with slope SLP(1), is constructed using the mean position of the two bunches. This line is extrapolated back till it intersects a cylinder of radius (RIPF) equal to that of the IPF. The magnetic field outside this cylinder is assumed to be negligible

compared to the field inside (see Fig. 3.2(c)[4]), and hence straight lines can be drawn between EMIC and IPFB. A circle, of radius RAD, is drawn between the above intersection point and the event vertex, requiring that the line with slope SLP(1) is tangential to the circle at the intersection point. The circle represents the approximate path of a charged particle inside the bubble chamber. The slope of the tangent to the circle, at the event vertex, is SLOPET. Also, another line is constructed, with slope SLP(2), between the above intersection point and the event vertex.

A IPFB tube number is calculated corresponding to the intersection point, although only for vertices which lie between ≥ 95 cm (along the vertical axis). The predicted IPFB tube number is compared with the IPFB data in the combined timeslot, and the difference between it and the closest IPFB bunch is stored in IPFDIF. The closest tube in the bunch is used in calculating this difference. We then impose cuts on RAD, SLOPET, SLP(1)-SLP(2), IPFDIF. Tracks which pass these cuts are kept. We loop over all bunches in EMICH and EMIBH in the combined time slot.

b) Side View

As above, we choose one bunch in EMICV and EMIBV. We then fit a straight line, using the least squares method, to the bunch means and the vertex position. A chi-square is calculated for the fit. The slope of the line and chi-square are stored in SLOPES and CHIS. Cuts are imposed on them, and tracks passing them are kept. We loop over all EMICV and EMIBV bunches in the combined timeslot.

c) U - Coordinate

In the previous two steps, we generate lists of tubes, in EMIBH and EMICH (also, in EMIBV and EMICV), used in constructing 'tracks'. Each combination of tubes, in EMIBH and EMICH, represents one 'track' in the top view (similarly for the side view). Since the two views are treated separately, the 'tracks' constructed in each view are independent of each other. We use the U coordinate in EMIB to correlate the two views by requiring that for each EMIBH tube there is at least one EMIBV tube such that the U tube, corresponding to the (H,V) combination, exists in the EMI data. The expression relating the three coordinates is,

$$U = 0.813*H - 0.582*V + 5.6$$

We compare the predicted U tube number with the bunches hit in EMIBU, and difference to the closest is stored in UDIF. A cut is then imposed on UDIF. If the calculated U tube number is less than 1 or greater than 270 (the range of U tube numbers in EMIBU), no cut is made on UDIF. If a tube in EMIBH cannot be matched with any of the tubes in EMIBV, we decrease the number of 'tracks' in the top view by one. By looping over all EMIBH tubes, we keep only those which can be matched with at least one EMIBV tube. Similarly, we demand that each EMIBV tube be matched with at least one EMIBH tube. We now require, that there be at least two tracks in the top and side views, or else the timeslot is rejected.

To further reduce background, we require that if one 'bunch' is used for all 'tracks' in both EMIBH and EMIBV or in EMICH and EMICV, then the bunch widths in both H and V layers have to be greater than two tubes.

3.2.3 Determination of Cuts

To determine the cuts that are imposed on the geometrical quantities calculated above, we use measured tracks which are extrapolated to hit both EMIB and EMIC. The extrapolation is done by program XTRAP. Hadrons and muons (defined by a method described in 3.4.1) are treated separately. Tracks are also divided according to their charge. No significant difference was found for the different categories. When a track is extrapolated by XTRAP, the output consists of tube numbers that are predicted to be hit in the various EMI/IPF layers, and the multiple Coulomb scattering errors associated with the predictions. We generate fake hits in the EMI by scattering the predicted positions of the tracks using a Gaussian distribution generator and the multiple Coulomb scattering error. In this manner we simulate multiple Coulomb scattering in the absorber. We then process these fake hits and the vertex positions of the events (which produce these tracks) through the algorithm described above. Cuts are chosen such that most of the tracks pass them. Table 3.2 lists the cuts and their efficiency for tracks with momentum $\geq$ 4 GeV/c. The typical uncertainty on these efficiencies is 1%.

From Table 3.2 it is clear that the efficiency for picking real tracks is very high. This algorithm is tested using an unbiased event sample. The Munich group has measured 'leaving' tracks for all events which had at least one such track. This sample is processed through a 'muon tagging' program, PROB632 (described in 3.4.2), which picked a very small number of events as possible multimuon candidates (8 out of 2300), and all events found in the unbiased sample were also picked by the algorithm described above. However, this algorithm also picks a lot of background; for instance, in the Munich sample, 464 out of 2300 events were tagged as possible multi-muon candidates .

Vertex positions for 25100 events were processed through this algorithm, and 4900 events were tagged as interesting events.

3.3 Measurement of 'leaving' tracks

The events tagged in the previous step are re-scanned to ensure that they have at least two 'leaving' tracks. A momentum template is used while scanning to discard tracks with momentum < 3 GeV/c. All 'leaving' tracks are then measured and processed through geometry. The 'leaving' tracks are extrapolated, by XTRAP, through the absorber to the EMI/IPF layers, and multiple Coulomb scattering errors are calculated. EMI/IPF information, corresponding to the roll/frame number on which the event is found, is added to the data structure.

Out of the 4900 events passing the previous step only 2300 events satisfy the above two criteria. However, there are losses associated with this step and some 'leaving' tracks are missed. The losses can

be due to the tracks being too faint or out of focus or simply being missed by the scanner. The event itself can have a complicated topology making measurements unreliable. We will estimate these losses and correct for them in Chapter 5.

3.4 Search for multi-muon candidates in the 'leaving' track measurements

To decide if a 'leaving' track is a muon or not, we compare the tubes that the track is predicted to hit with the tubes present in a timeslot. We have to loop over all timeslots in the data record. A chi-square, using multiple Coulomb scattering errors, is calculated for the fit. Using the number of EMI layers the track actually hits, we calculate a probability corresponding to this chi-square (this is a pseudo-probability, since true probability corresponds to the case where the EMI has infinite spatial resolution). Tracks that pass cuts on the number of layers hit by the track and on the probability are labeled muons. The probability calculated here is the probability of getting a χ^2 worse than the one observed.

One approach to this problem is the minimum χ^2 method, as developed by Jeremy Lys[5]. The European groups in the collaboration used a modified version of this approach (by Peter Kasper[6]). However, in the present analysis we use another method, based on Bayes' theorem, to calculate probabilities. The motivation for a different approach was to find an alternative method where we could calculate a

probability distribution, whose shape would enable us to check the extrapolation, multiple Coulomb scattering errors, optical constants etc.

3.4.1 Minimum χ^2 Method

In this method each layer of an EMI/IPF plane is treated separately. If a track hits the tube it is predicted to pass through, χ^2 is set to zero. If the track hits a tube that is different from the tube it is predicted to hit, the distance between the extrapolated position and the closest wall of the hit tube is used to calculate a χ^2. The tube which is closest to the predicted tube such that the probability, corresponding to 1 degree of freedom, is better than 0.05 is chosen as the hit tube. If both layers of a layer pair fire, say H and H', then the minimum of the two χ^2's is used for that layer pair. Adding up the χ^2's for the H and V layers of an EMI plane gives a 2-degree of freedom χ^2. The χ^2's for the hits in EMIBH(V) and EMICH(V) are combined together after taking correlations between them into account. The correlations depend upon the momentum, errors in the azimuthal and dip angle of the track, and on multiple Coulomb scattering in the absorber before EMIB. This leads to a χ^2 corresponding to 4 degrees of freedom (see appendix A.1 for the necessary formulas). We then calculate a probability corresponding to this χ^2. Tracks which have a probability greater than 0.0001 are labeled muons, and all other tracks are labeled hadrons. The distribution of probabilities calculated by this method is strongly

peaked at the high end. A typical probability distribution is shown in Fig. 3.3 (a).

In order to reduce the effect of systematic biases in the extrapolation and matching procedure, an offset (or floor) of 3 cm is added in quadrature to the multiple Coulomb scattering error before calculating a χ^2. This has the effect of increasing the efficiency for detecting muons, but, at the same time it increases the background too. This algorithm effectively picks up almost all the muons which strike the efficient area of the EMI.

Peter Kasper modified the above approach, and in his version, the 3 cm floor is not used. Also, the probability cutoff for selecting hits in a single layer is 0.002, rather than 0.05 used above. Thirdly, correlations are not used in the 2-plane probability calculation. A typical distribution is shown in Fig. 3.3 (b). The efficiency of these two methods to detect muons is discussed in Chapter 5.2

3.4.2 Method based on Bayes' Theorem (Program PROB632)

Since the EMI consists of 1" square tubes, we only know a track's position, when it hits the EMI, with an accuracy of 1/2" - 1". We use the present method to predict the hit position more accurately, and to calculate a 2-plane probability.

The first difference, between this method and the previous one, is that we consider both the layers in a layer pair simultaneously. If a track hits tubes in both layers of a layer pair, then assuming

that it is travelling normal to the EMI plane, its position is constrained to be within half a tube width (since the two layers are offset by half a tube width). This happens for approximately 80% of the tracks. For the rest of the tracks, only one layer fires and the track position is constrained to be within a full tube width i.e., 22.2 mm. Therefore, for 80% of the tracks the spatial resolution of the EMI improves by a factor of 2.3. Another difference is that while calculating χ^2's we use only the multiple Coulomb scattering error (i.e., the 3 cm floor is not added).

Bayes' theorem[7] is used to estimate the position of the track within this half tube or full tube wide region. Bayes' theorem is useful in cases where the a priori probability of the occurrence of an event is known. In the present case, the a priori knowledge is the extrapolated position of the track and the posteriori knowledge is the hit region. The error in the predicted position of the track is due to multiple Coulomb scattering and measurement errors, and is assumed to be Gaussian. We now define the position of the track within the hit region to be the mean of that part of the Gaussian distribution which lies within this region. If we had a large number of such tracks, all going through the hit region, then the average of their hit positions would correspond to this mean. Appendix A.2 contains the appropriate formulas.

Comparing this estimated position with the extrapolated position and using the multiple Coulomb scattering error we are able to calculate a χ^2 and a probability. In this manner, we calculate a probability for every layer pair. For low momentum tracks, which have

large errors as compared to the resolution of the EMI, the coarseness of the EMI becomes less important, and the calculated χ^2 approaches the true χ^2 (calculated assuming infinite resolution). However, this is not true for high momentum tracks, where the width of the error distribution is small compared to the EMI's resolution, and for such tracks, the estimated position is very close to the extrapolated position. This leads to a small χ^2 and consequently a large probability. Thus, even this method leads to a probability distribution peaked towards the high end but not as much as in the minimum χ^2 method, as will be shown later.

Before using this method on 'leaving' tracks to decide which of them are muons, we have to calibrate it using a known sample of muons. Muons are generated in neutrino interactions upstream of the bubble chamber, in the earth shielding etc. They are sometimes referred to as 'beamtracks'. Some of them go through the bubble chamber and the EMI and can be used to calibrate the EMI. However, the momentum distribution of 'beamtracks' is quite different from that of muons produced by interactions inside the bubble chamber. To check our method, we first use a Monte Carlo to predict the shape of the probability distributions and compare them with distributions generated for a sample of 'beamtracks'. A clean sample of 'beamtracks' is chosen by requiring that (1) they have an entry point (along the Z axis) in the bubble chamber between $\pm$ 110 cm, (2) they are measured in all three views, (3) a muon mass fit exists for the track, (4) momentum of the track is greater than 4 GeV/c, and, (5)

they have a probability greater than 0.0001, as calculated by the minimum χ^2 method.

In the Monte Carlo, hits are generated around the extrapolated position according to a Gaussian distribution, and probabilities are calculated. The width of the Gaussian distribution is given by the multiple Coulomb scattering error. The input to the Monte Carlo is a distribution of multiple Coulomb scattering errors corresponding to this sample of 'beamtracks'. In this manner, the Monte Carlo calculates probabilities for the momentum spectrum of the 'beamtrack' sample. Figs. 3.4 (a)-(d) show the various probability distributions. The plots for H and V layers in any one plane are similar.

We now use this algorithm on 'beamtracks'. Before we do so we adjust the position of the EMI with respect to measurements in the bubble chamber. This is done by plotting the difference between the extrapolated position and the hit position for the 'beamtracks' and requiring that the plot be centered at zero. Each layer pair has to be shifted separately. Fig. 3.5 shows a typical plot.

For the data we calculate probability distributions for a single layer (1 degree of freedom), one plane (2 d.o.f.) and both planes (4 d.o.f.). Since the H and V layers in any one plane are independent of each other, one plane χ^2 (and hence probability) is calculated by simply adding the single layer χ^2's. The calculation for two plane probability is not as simple because the hits in EMICH(V) and EMIBH(V) are correlated, and one has to take correlations into account when calculating a χ^2. Taking the coarseness of the EMI into account, some assumptions are made regarding the use of correlations. Firstly, we

use correlations only if the tube that is hit is different from the one predicted by XTRAP. Secondly, we use correlations only if the multiple Coulomb scattering error is greater than the width of the hit region (in both planes). This is done because if the error is less than the tube width, and if the hit tube is different from the one predicted by XTRAP, then it is more likely that this difference is due to a random fluctuation rather than actual Coulomb scattering. As it turns out correlations are not used for almost 80% of the tracks. Figs 3.6 (a) - (e) show the results for the various probability distributions. The plots for H and V layers in any one plane are similar. Comparing the two plane probability distributions for the minimum χ^2 method and our method, Fig. 3.3 and 3.6 (e), shows the difference between the two methods.

Comparing probability distributions for the Monte Carlo and data, Figs 3.4 and 3.6, it is clear that the agreement is good. This was not the case for part of the data where a problem was found in the geometrical reconstruction program. After correcting the problem the agreement between that part of the data and the Monte Carlo became good for all layers except EMICH. At present the probability distribution for EMICH has a peak at low probabilities, as shown in Fig. 3.7 (a). This causes the 2-plane probability distribution also to have a peak at low probabilities, as in Fig. 3.7 (b). Consequently, a cut on the 2-plane probability leads to a loss of real muons, which is larger than for that part of the data where this problem does not exist (Fig. 3.6 (e)).

This problem exists only for that part of the data where 'beamtracks' are chosen using Jeremy Lys' version of the minimum χ^2 method. The cause of the problem is that the difference between the extrapolated position of a 'beamtrack' and the actual hit position increases as we go towards larger values of the Y coordinate (as measured by the H layers of the EMI), and this translates into more 'beamtracks' not having a match in EMICH. Since EMIB is much closer to the end point of the track (which is used as the starting point of the extrapolation procedure) than EMIC, the effect of this problem is much smaller for the former. The reason that only those 'beamtracks' which are chosen using Jeremy Lys' version of minimum χ^2 method are affected by this problem is that a 3 cm floor is added in quadrature to the multiple Coulomb scattering and measurement errors, and this makes the selection procedure rather insensitive to any systematic effects (this was the original reason to use a floor). As a result, more of the 'beamtracks' chosen using Jeremy Lys' version fail the 1% cut, since the latter does not use a 3 cm floor. On the other hand, Peter Kasper's version of the minimum χ^2 method does not use a 3 cm floor to begin with, and thus it already weeds out such tracks before we apply the 1% cut. A probable source of this problem is a non-optimal set of optical constants being used by the geometrical reconstruction program. Since we pre-select muons (see 3.4.3) with the minimum χ^2 method, this problem will have an effect on the efficiency to detect muons. We will correct for this in a later chapter (5.2).

From the probability distribution in Figs. 3.6 (e) and 3.7 (b), it is clear that if we require probability of tracks to be greater than 0.01 then the loss of real muons is small. The reason for using this cut is that the tracks which constitute the background usually pile up at low probabilities, and making a cut on probability gets rid of a significant amount of the background.

3.4.3 Muon Detection in the 'Leaving' Track sample

The muon tagging algorithm (based on Bayes' theorem) is now used on the sample of 2300 events which passed through steps 1 through 3 (see the introductory paragraph at the start of Chapter 3), and on the unbiased sample of events measured by some of the groups that contains all events with $\geq$ 1 'leaving' track. Tracks are required to have momentum $\geq$ 4 Gev/c. Only those tracks are considered for which a match (according to the minimum χ^2 method) exists in any EMI/IPF layer. Since the minimum χ^2 algorithm has looser criteria for tagging muons, it is used as a trigger for pre-selecting muon candidates. Also, only those timeslots are considered in which these pre-selected tracks have a match. Thus, only for these tracks and timeslots the 2-plane probability is recalculated in program PROB632. Tracks which have a 2-plane probability greater than 0.01 are labeled muons. Events with two or more such tracks which pass these criteria in the same time slot (or in timeslots within 1 μsec of each other) are tagged as multi-muon candidates.

Events tagged at this stage have to satisfy certain criteria before they are kept in the raw sample. Firstly, the muons have to have distinct 'bunches' in either EMICV or EMICH. This cut is made to weed out cases where hadrons are predicted to hit EMIC near the actual muon, and by virtue of their large multiple Coulomb errors (because of low momentum) can make a match using the hits due to the actual muon. Demanding independent hits in at least one coordinate gets rid of a lot of background events.

Secondly, the 'event timeslots' are required not to have too many hits. One source of too many hits in the EMI/IPF was electronic interference from an experiment in a nearby experimental hall. A signal, in time coincidence with the onset of this interference, was available for part of the data. Using that part of the data where the signal was available, a set of cuts were determined to pick out these 'noise' timeslots. A timeslot is labeled as a 'noise' timeslot if it has more than 95 bunches in all EMI/IPF layers, with EMIA contributing at least 25 bunches and EMIBH and EMIBV contributing at least 50 bunches and EMIC contributing at least 8 bunches. All multi-muon event timeslots are required not to satisfy this noise criterion.

After using the muon tagging algorithm and the two cuts described above, we are left with 125 multimuon candidates. This sample contains both real multimuons and background events. The background will be estimated in Chapter 4, and the effect of various cuts made to clean up the raw sample will be estimated in Chapter 5.

3.5 Complete Measurement of Multimuon Candidates

The events tagged as multimuons have to be completely measured. In a complete measurement, one measures everything which could be associated with the primary vertex. This includes γ's and neutral strange particles which decay in the bubble chamber and neutral hadronic interactions.

References

1) The data used in this work is from all the groups except the two Indian groups.

2) Program MUCKEMI, developed by Jim Hanlon and Howie Rubin (unpublished).

3) HYDRA Topical Manual, Book MQ version 3.4, 1981, CERN.

4) 15 Ft. Bubble Chamber Safety Report, Vol. 2 p. 221, National Accelerator Laboratory, Illinois, 1972.

5) Jeremy Lys (private communication).

6) Peter Kasper, Performance of the 15 Ft. Bubble Chambers New EMI and IPF, D.Ph.P.E SACLAY, 1985 (unpublished).

7) B. Roe, Lectures on Probability and Statistics for Physicists, UM HE 85-15 (unpublished).
Frodeson, Skjeggestad and Tøfte, Probability and Statistics in Particle Physics, Universitetsforlaget 1979.

Table 3.1. Number of events passing each step of analysis chain.

Events found in Scan 1	35700	
Events within fiducial volume	25100	(20% of frames
Events tagged as multimuon candidates by DIMUON	4900	(19.5%)
Events with ≥ 2 'leaving' tracks, that have momentum ≥ 3 GeV/c	2300	(9%)
Events tagged as multimuons by program PROB632	93	(0.4%)
Total number of multimuon candidates tagged by PROB632, including those from the unbiased event sample	116	(0.4%)

Table 3.2. Efficiency of various cuts used in program DIMUON.

	Cuts	Efficiency of cuts for track with momentum ≥ 4 GeV/c
Top View		
	RAD ≥ 2 m	98.4%
	ABS{SLP(1)-SLP(2)} ≤ 0.6	100.0%
	ABS(SLOPE) ≤ 0.51	100.0%
	ABS(IPFDIF) ≤ 9	100.0%
Side View		
	ABS(SLOPE) ≤ 0.15	100.0%
	CHIS ≤ 7.0	100.0%
U - View		
	ABS(UDIF) ≤ 3	100.0%

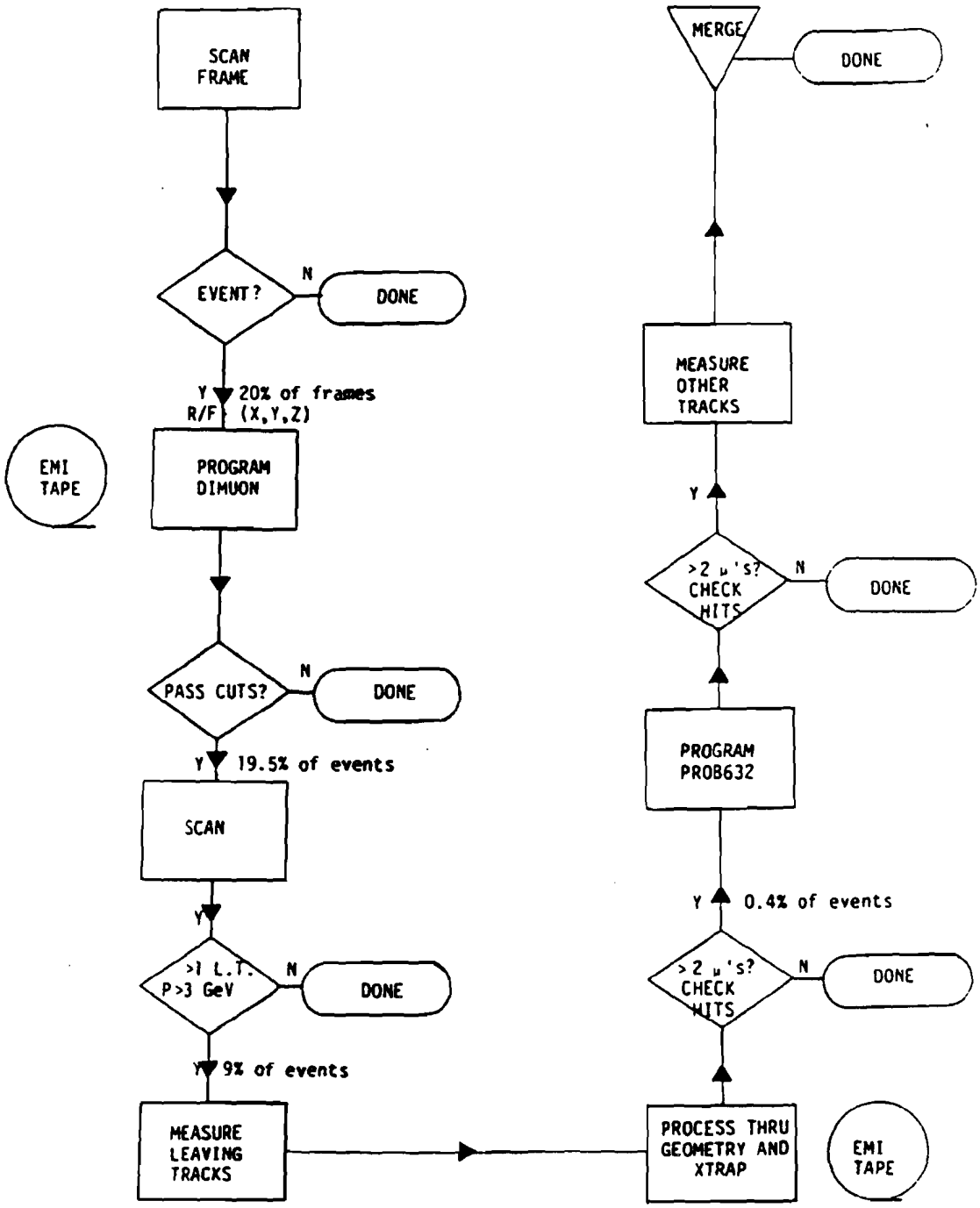

Fig. 3.1. Flow chart detailing the steps in the search for multi-muons. The % of events passing each step is indicated.

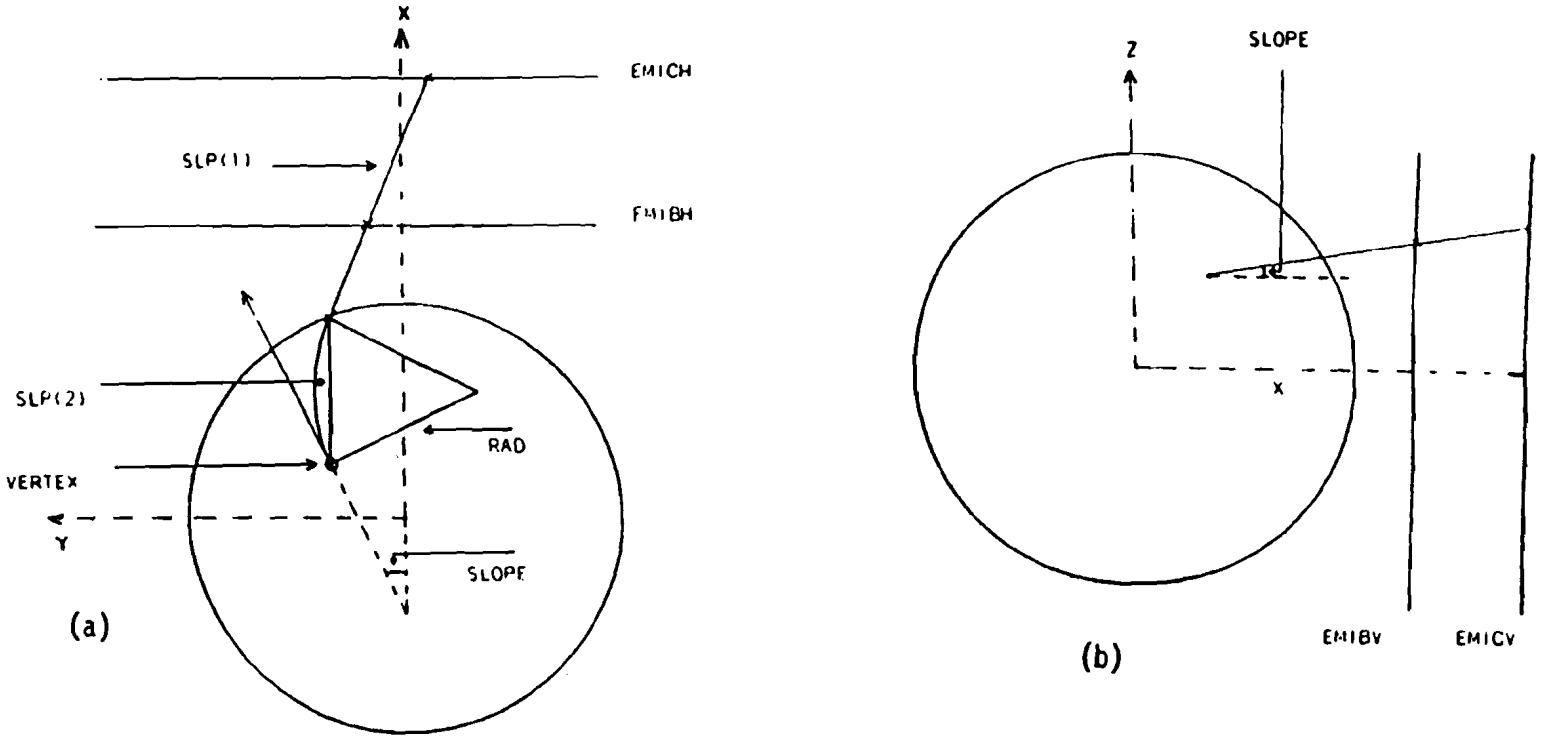

Fig. 3.2. The geometrical quantities used in the construction of 'tracks' in (a) Top View, SLP(2) refers to the slope of the line indicated; (b) Side view.

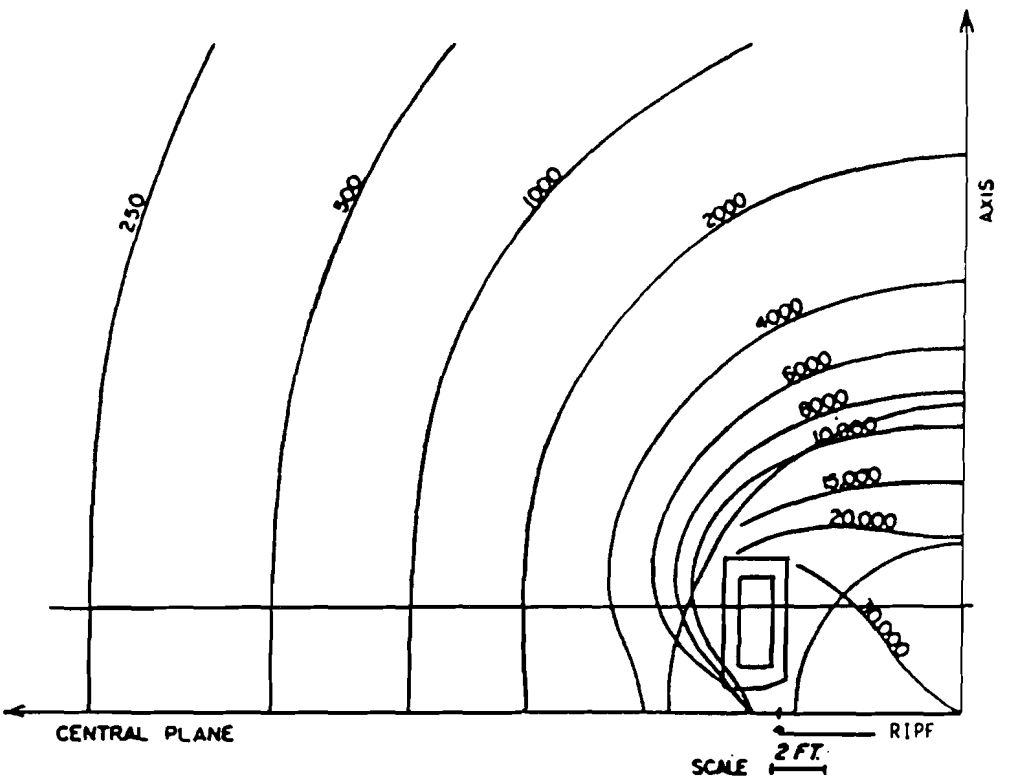

Fig. 3.2c. Stray magnetic field due to bubble chamber magnet. The horizontal line corresponds to the fiducial volume cutoff along the vertical axis. RIPF, radius of the IPF, is shown on the plot.

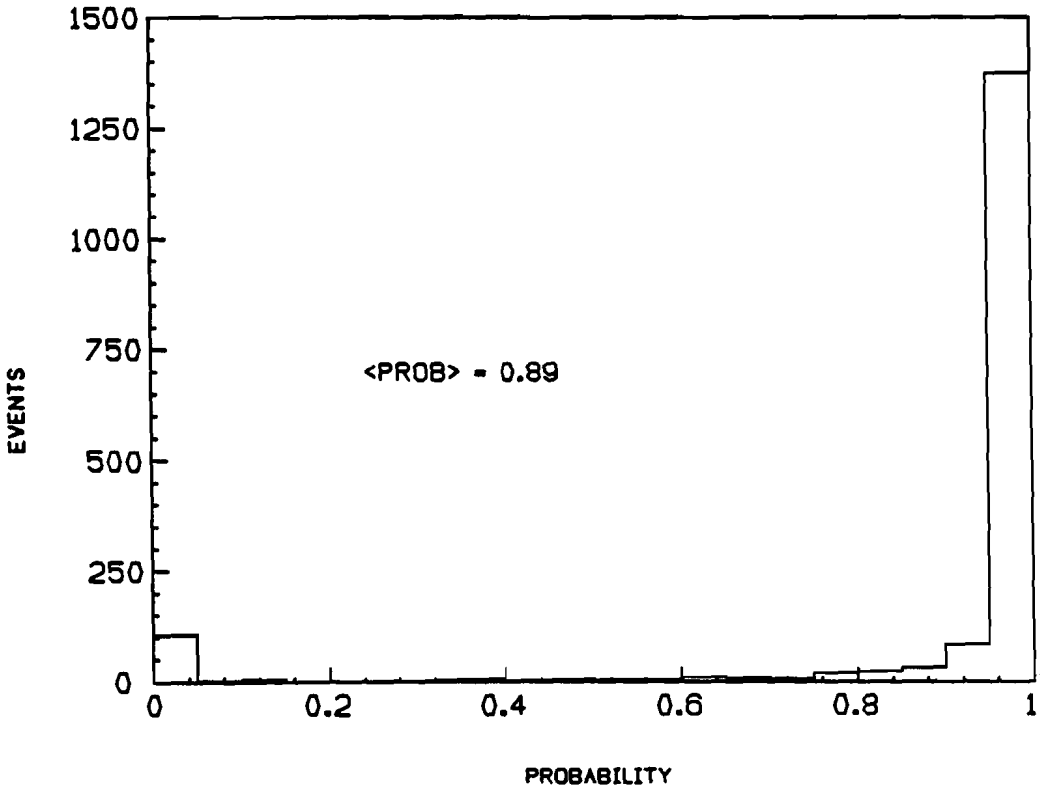

Fig. 3.3a. 2-plane probability distribution of 'beamtracks' according to Jeremy Lys' version of minimum chi-square method.

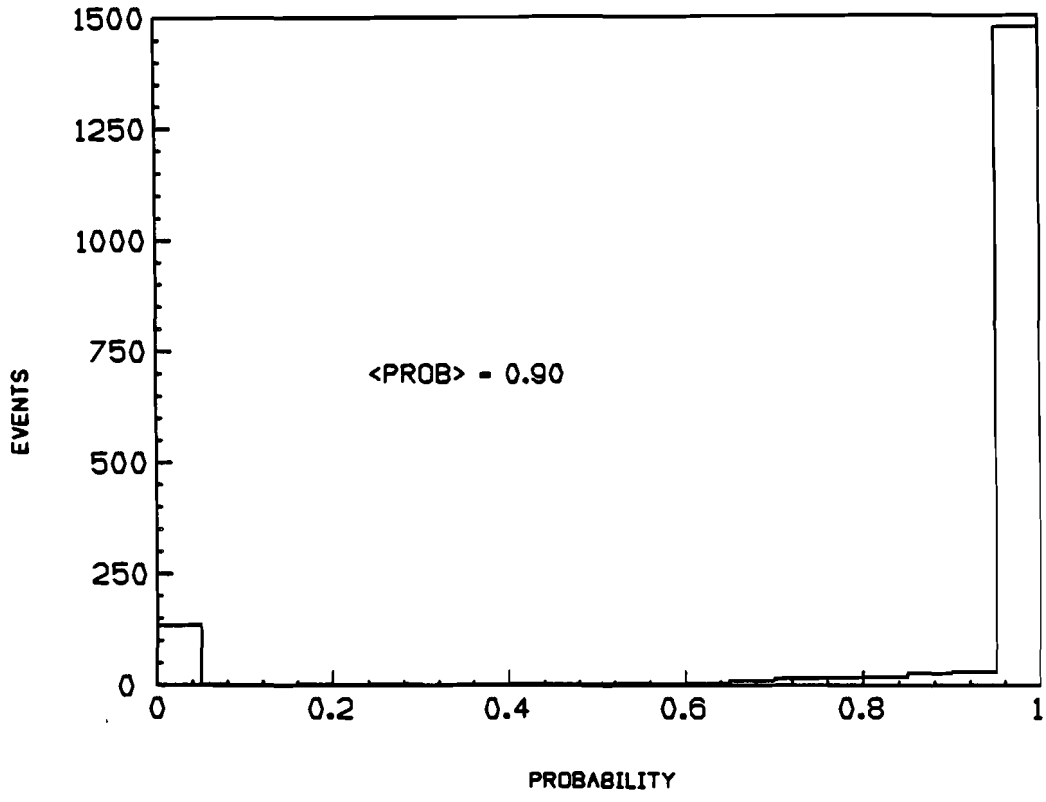

Fig. 3.3b. 2-plane probability distribution of 'beamtracks' according to Peter Kasper's version of minimum chi-square method.

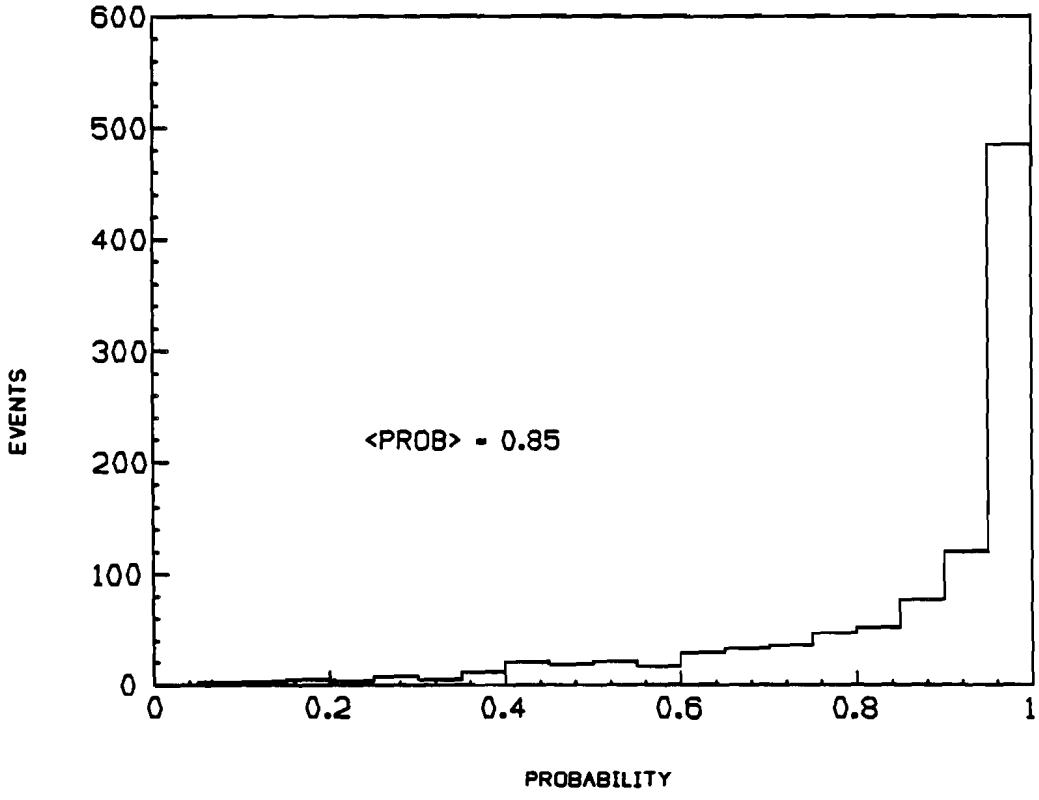

Fig. 3.4a. Monte Carlo generated probability distribution using Bayes' theorem for single layer (1 degree of freedom) in EMIB.

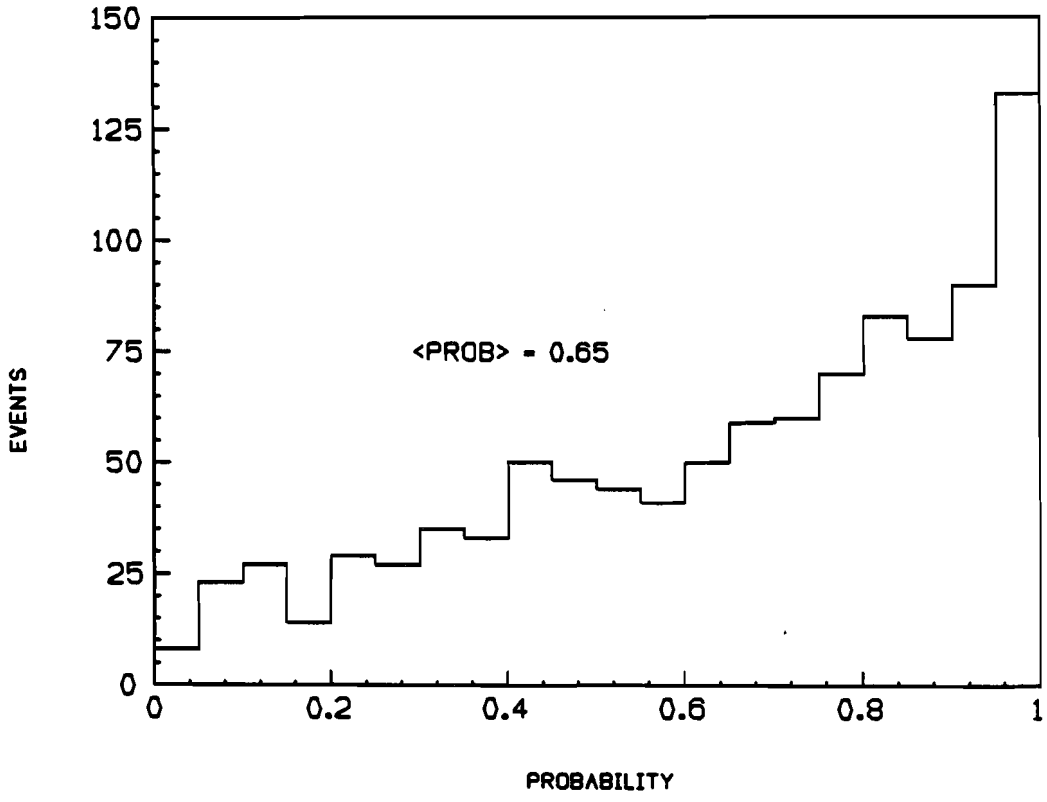

Fig. 3.4b. Monte Carlo generated probability distribution using Bayes' theorem for single layer (1 degree of freedom) in EMIC

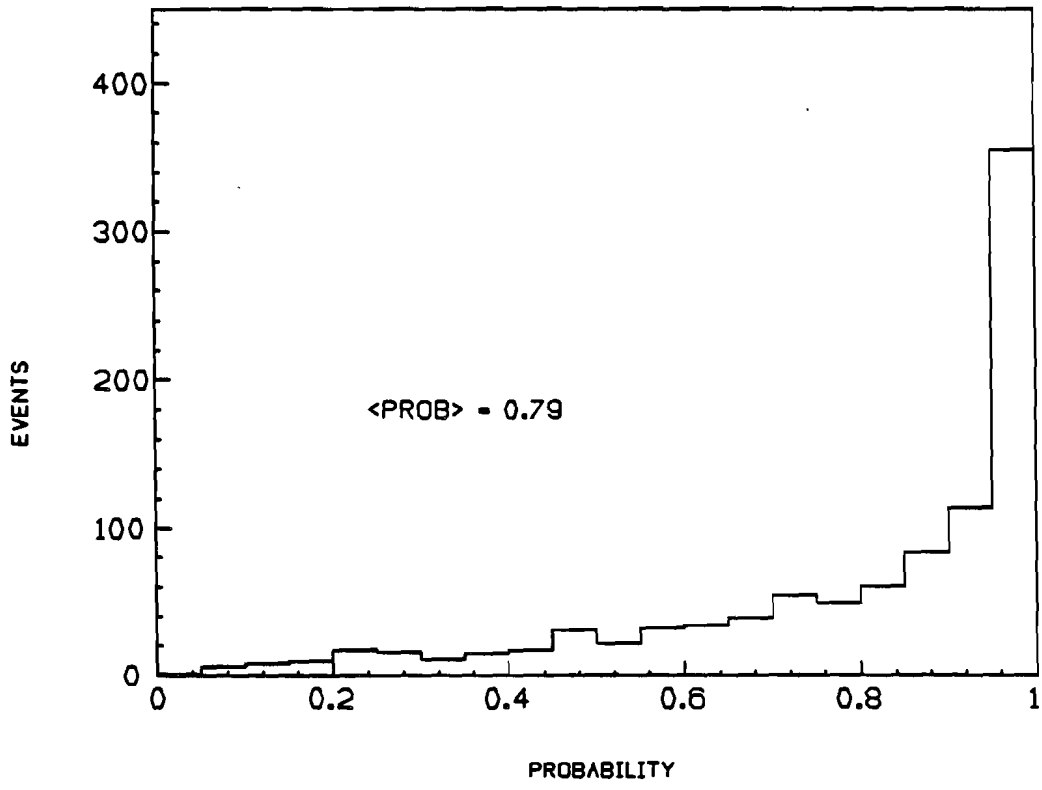

Fig. 3.4c. Monte Carlo generated probability distribution using Bayes' theorem for EMIB (2 degrees of freedom, H + V).

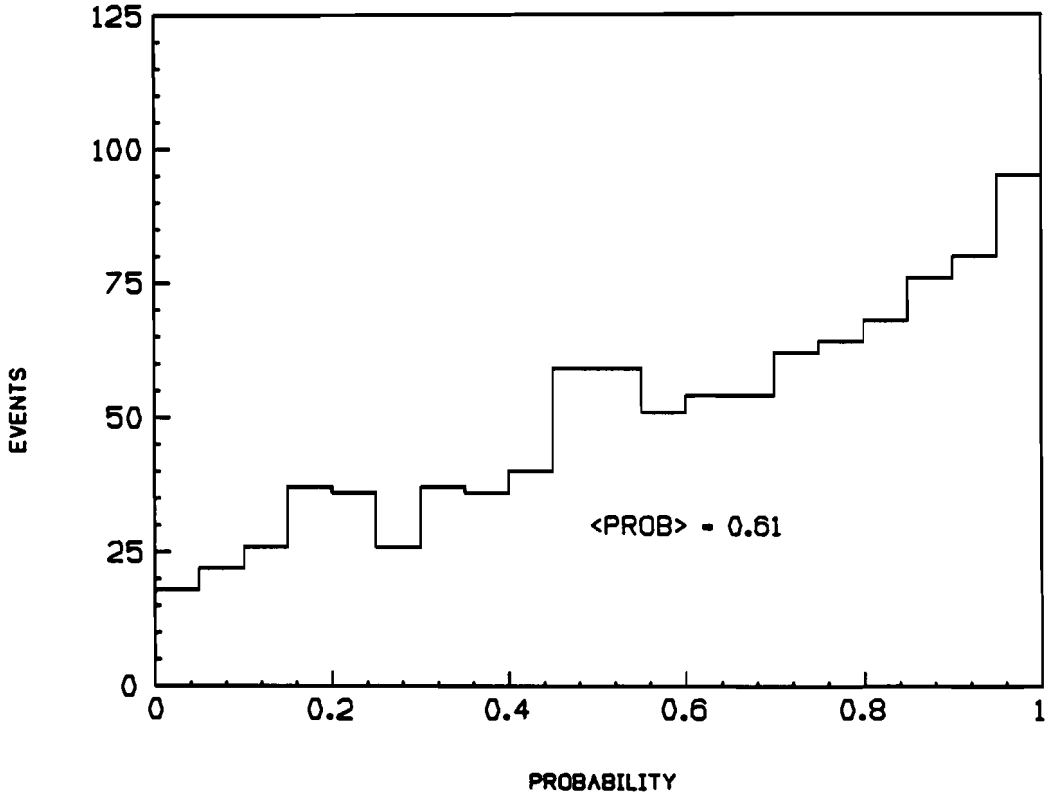

Fig. 3.4d. Monte Carlo generated probability distribution using Bayes' theorem for EMIC (2 degrees of freedom, H + V).

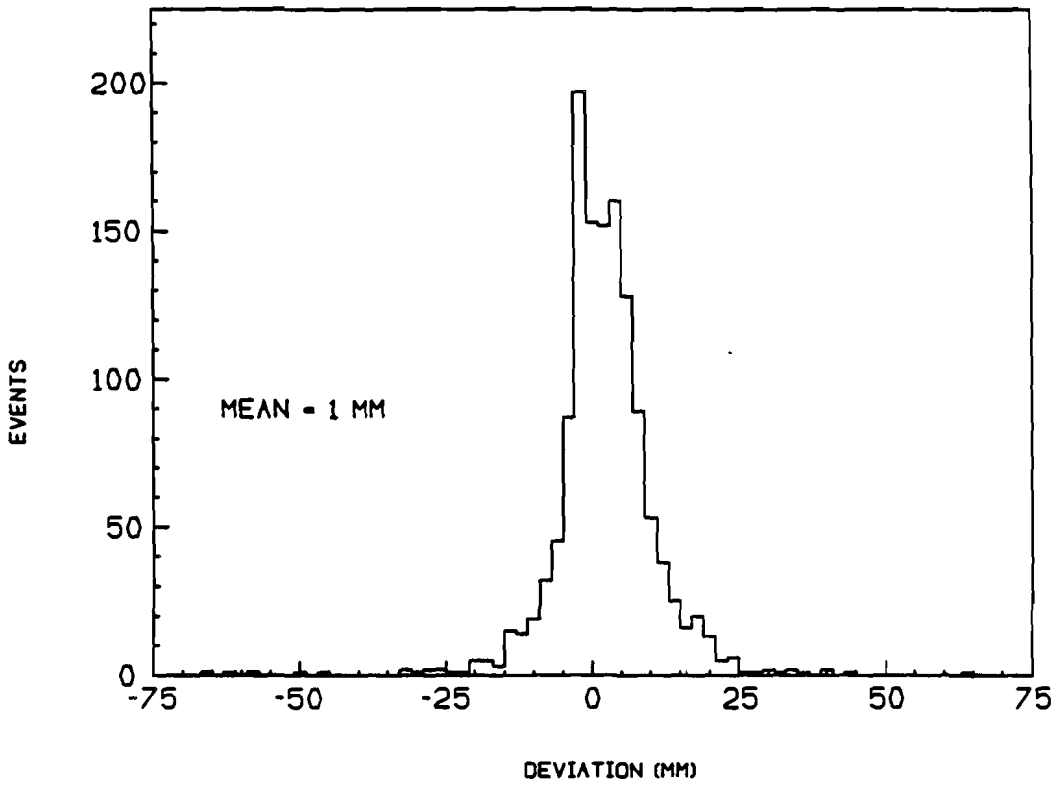

Fig. 3.5. Difference between extrapolated and hit positions at an EMI layer. The scale of the horizontal axis is in mm.

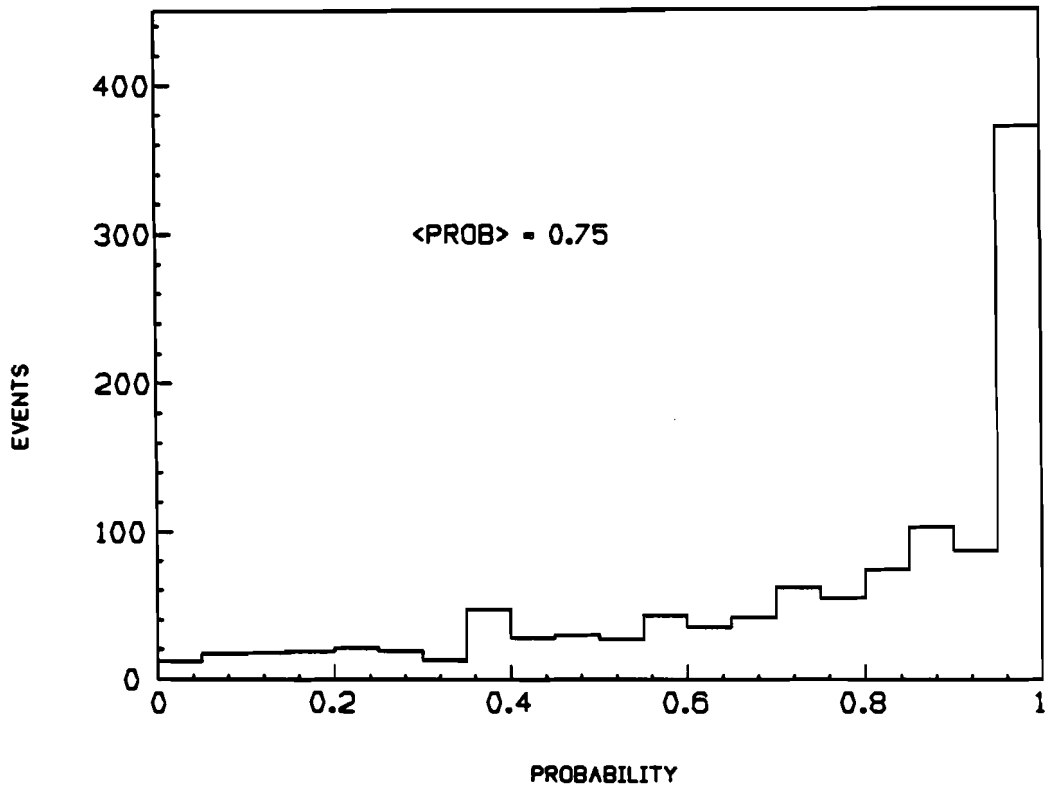

Fig. 3.6a. Probability distribution for data for 'beamtracks' for EMIBV (or EMIBH, 1 degree of freedom) using Bayes' theorem.

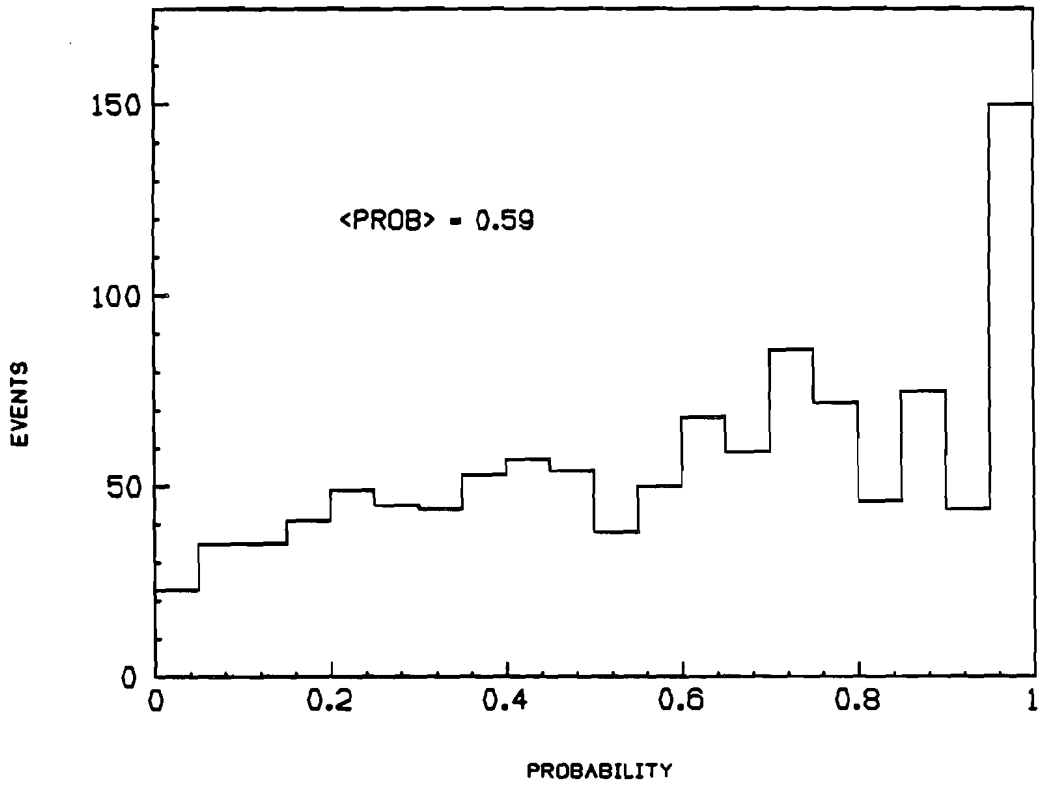

Fig. 3.6b. Probability distribution for data for 'beamtracks' for EMICV (or EMICH, 1 degree of freedom) using Bayes' theorem.

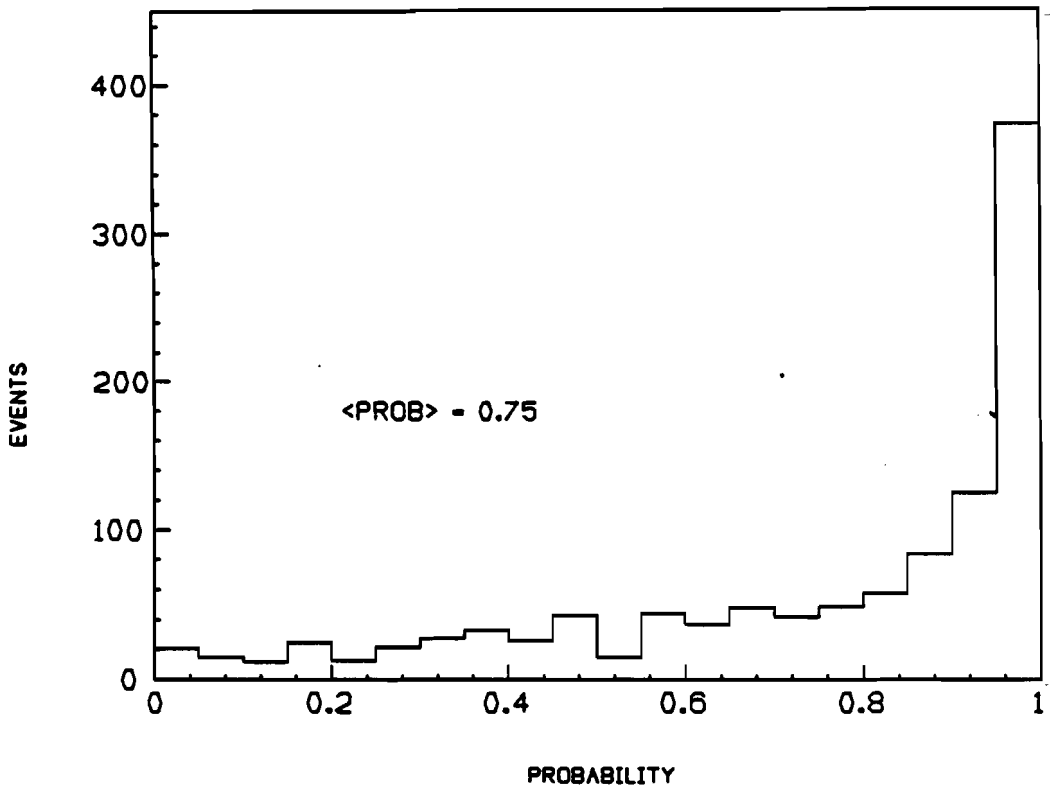

Fig. 3.6c. Probability distribution for data for 'beamtracks' for EMIB (2 degrees of freedom) using Bayes' theorem.

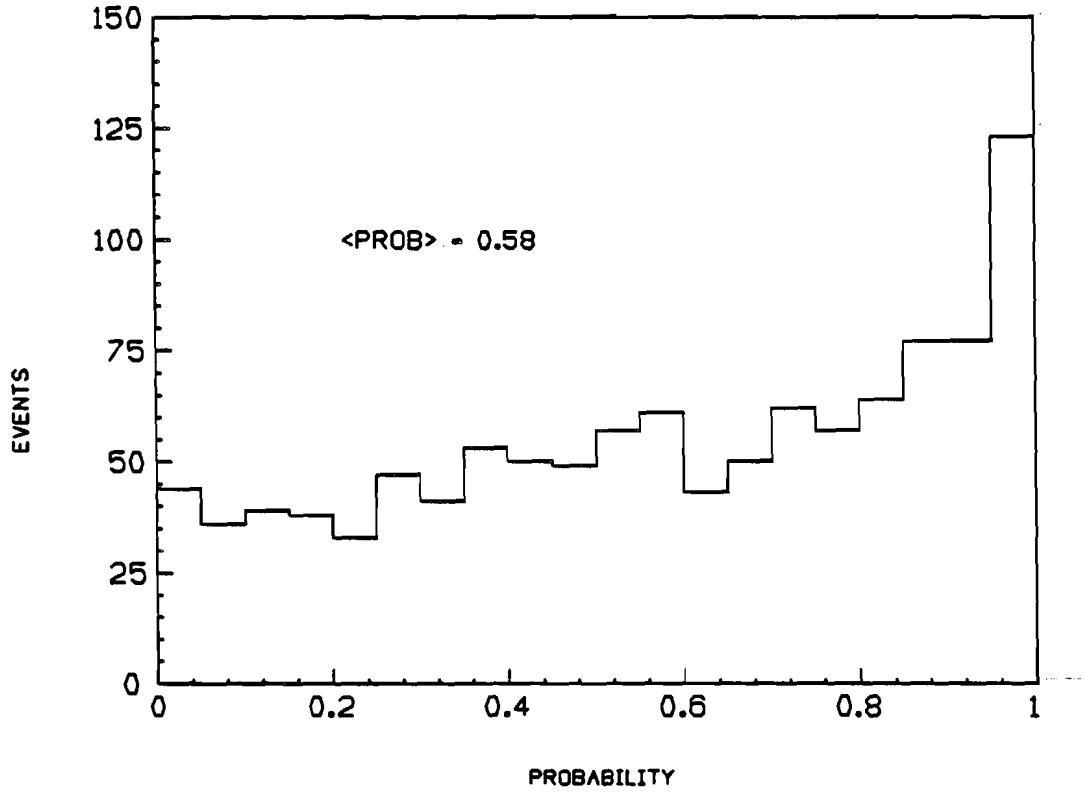

Fig. 3.6d. Probability distribution for data for 'beamtracks' for EMIC (2 degrees of freedom) using Bayes' theorem.

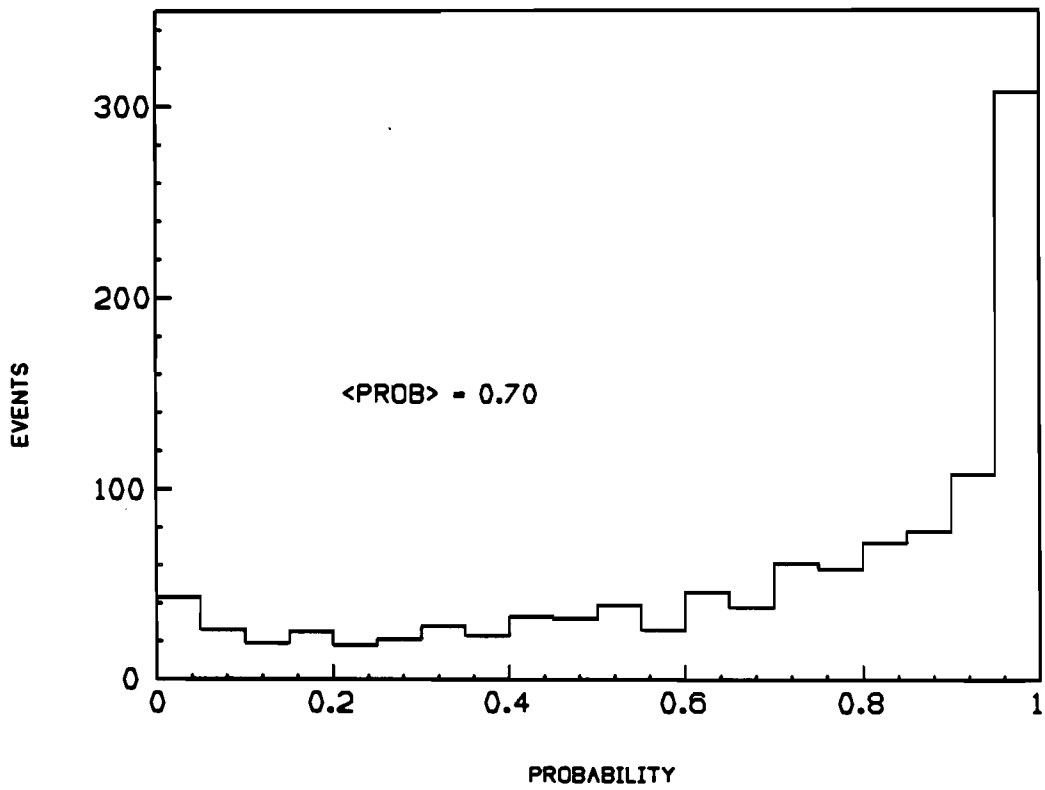

Fig. 3.6e. 2- plane probability distribution for data for 'beamtracks' (4 degrees of freedom) using Bayes' theorem.

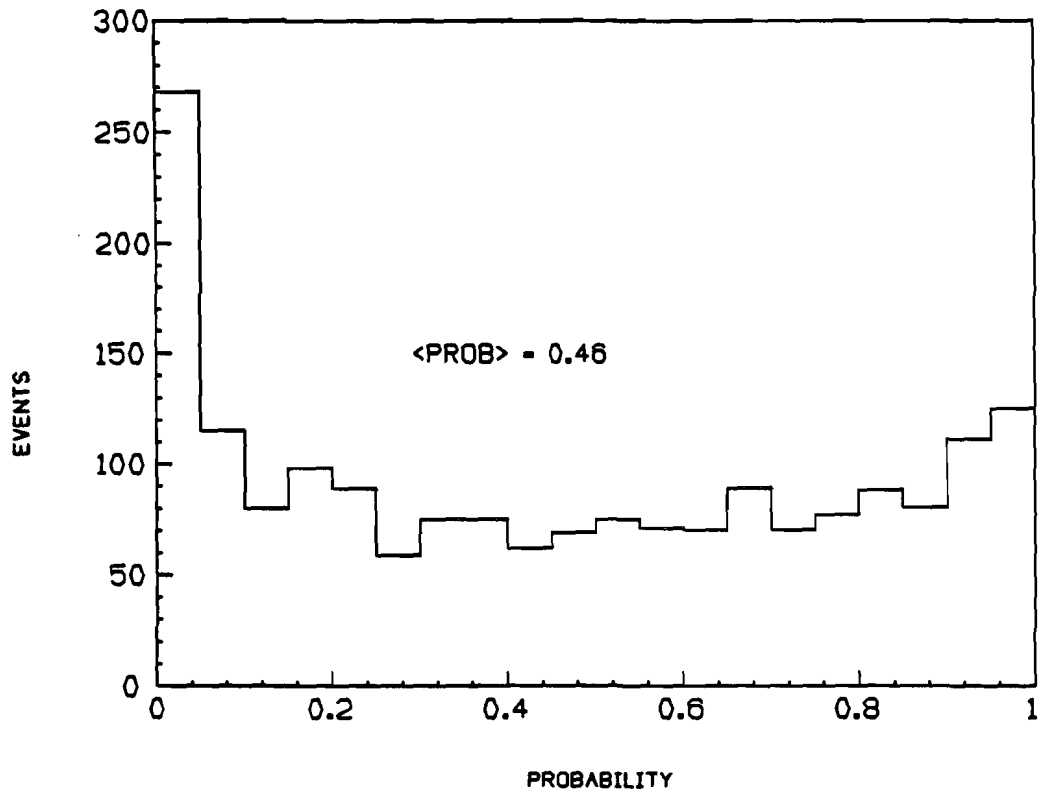

Fig. 3.7a. Single layer probability distribution for EMICH for 'beamtracks' using Jeremy Lys' minimum chi-square method.

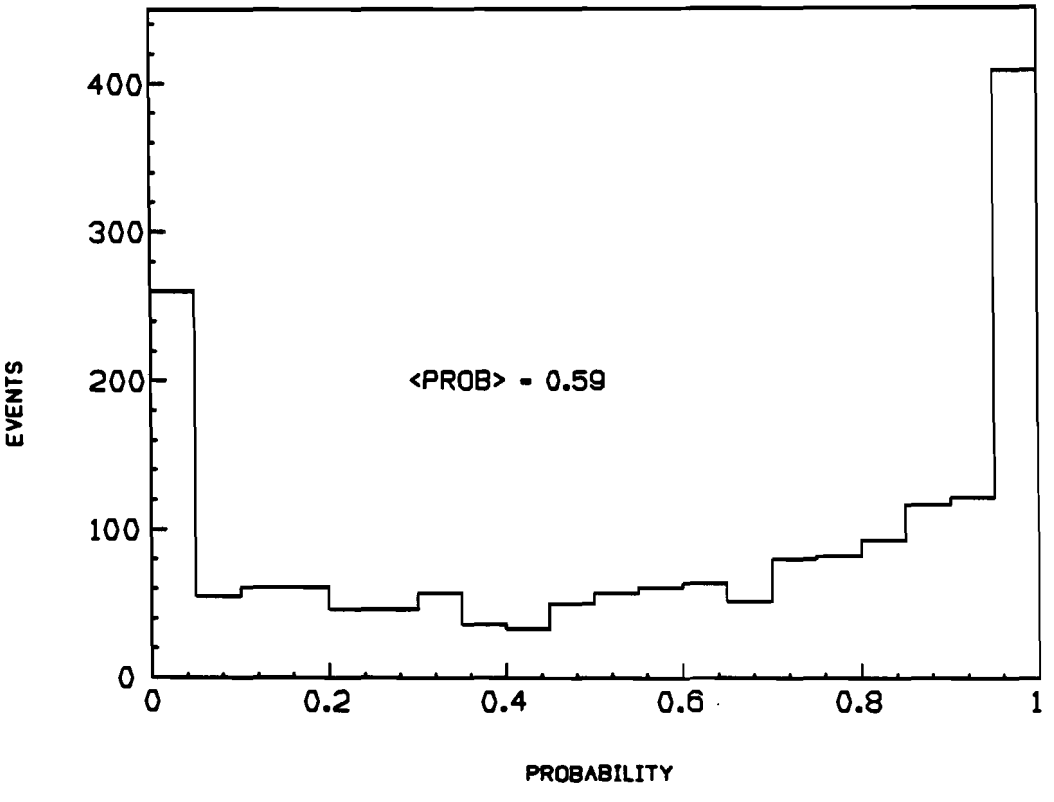

Fig. 3.7b. 2-plane probability distribution for the same data set as in Fig. 3.7 (a).

Chapter 4

Estimation of Background in Data Sample

The raw sample, obtained by the method described in the previous chapter, contains both genuine multimuons and background events. Some of these background events can be removed from the raw sample by additional cuts designed to keep the loss of genuine events small, i.e., requiring, (a) a minimum number of hits in IPFB in the event timeslot, (b) that each 'muon' have a match in EMIBU, and (c) that all the 'muons' in the event have distinct hits in EMICH and EMICV. The last requirement is more restrictive than the one in 3.4.3.

Even after making these cuts the sample still contains background: (a) Some of the pions and kaons, produced in charged current events, can decay in flight to produce a muon (along with a ν ($\bar{\nu}$)). The decay muon can make a good match in the EMI causing a hadron to be wrongly tagged as a muon. (b) Hadrons, produced in charged current events, which interact in the absorber and produce a spray of secondary particles some of which can hit EMIC. A hadron which is predicted to hit EMIB and EMIC can be associated with these hits and be wrongly labeled a muon. This background is loosely referred to as punch-through. (c) Hadronic 'leaving' tracks in an event can be associated with random, background hits in the EMI, thus producing a fake multimuon event (called accidental associations).

The background due to these sources will be estimated and subtracted from the event sample.

4.1 Cuts which remove background events from the raw sample

4.1.1 Activity in IPFB

The IPF at the downstream end of the bubble chamber, i.e., IPFB, is used in the determination of the event timeslot. Figs. 4.1 (a) and (b) show, respectively, the number of IPFB 'bunches' in timeslots corresponding to 'beamtracks' going straight through the bubble chamber and neutrino events occurring inside the chamber. Comparing the two figures, it is clear that the activity in IPFB is significantly greater during event timeslots. Therefore, IPFB can be used to discriminate against possible event timeslots where the EMI has a lot of hits, but IPFB is inactive. These cases can be due to electronic noise in the EMI (the EMI was more sensitive than IPFB) or due to unrelated neutrino events in the absorber which give hits in the EMI but not the IPF.

Since IPFB was less sensitive than the EMI, we do not require that each 'muon' in a multimuon event have a IPFB match, but rather that either each 'muon' have a match in IPFB such that χ^2 for the match is ≤ 5 or the event timeslot have ≥ 2 'bunches' in IPFB.

This algorithm was calibrated on a sample of ν and $\bar{\nu}$ charged current events, culled from a minimum bias sample of events. $91\pm1\%$ of the events have ≥ 2 'bunches' in IPFB, while $90\pm1\%$ of the muons

predicted to hit IPFB have a match such that $\chi^2 \leq 5$. If we require that either of the two conditions hold, then 95.7±0.8% of the events pass this criteria. The loss of real dimuons, due to this cut, can be calculated using these numbers, and is estimated to be 4±1%. The effect of this cut on the raw data sample is shown in Table 4.1. A discussion of results is in 4.1.4.

4.1.2 Match in EMIBU

The U-coordinate in EMIB is used to improve the track quality of each muon in a multimuon event by removing ambiguous combinations of hits in EMIBH and EMIBV. Each muon is required to have a hit in EMIBU, close to the tube number predicted by the combination of H,V tubes hit by the track - just how close the hit has to be depends upon the momentum of the track. If the predicted U tube falls outside the area which is covered by EMIBU, then this cut is not required. In this analysis, we require that tracks with momentum < 10 GeV/c have hits within 6.5 tubes of the predicted tube, whereas tracks with momentum ≥ 10 GeV/c must have hits within 4 tubes. The momentum dependence of the cut arises due to the geometrical construction of EMIB. The expression which relates the H,V and U coordinates (U = 0.813*H - 0.582*V +5.6) assumes that all three coordinates occupy the same region in space, whereas in reality the three planes of wires are separated from each other by a few inches. Therefore, the lower the momentum of the track, the worse is the effect of the separation.

The above mentioned limits are determined using measured tracks which have been extrapolated to hit EMIB. Using the tube numbers predicted by XTRAP in EMIBH and EMIBV, we calculate a U tube (by the above expression), and compare its value with the U tube number predicted by XTRAP. A scatter plot of track momentum versus the difference in these two U tube numbers is shown in Fig. 4.2. Since EMIBU had more inactive channels than the other EMI layers, the limits on the difference between the U tube numbers were increased somewhat to insure a high efficiency for accepting muons in charged current events. Requiring this criteria for muons in a minimum bias sample of charged current events results in a loss of $4.0\pm0.8\%$. Therefore, requiring both muons in a dimuon event to have matches in EMIBU results in a net efficiency of $93.0\pm1.6\%$. The effect of this cut on the raw sample is shown in Table 4.1. A discussion of results is in 4.1.4.

4.1.3 Independent hits in EMIC

The criterion in 3.4.3, that the muons in a multimuon event have to hit independent 'bunches' of tubes in either EMICH or EMICV, is now made more restrictive by requiring that the muons have to have independent hits in both CH and CV. The tighter cut is made to further improve the quality of the events in the sample. The motivation behind the more restrictive cut is to remove cases where a hadron is predicted to hit EMIC near the muon and it uses the latter's

hits to make a match in one view and uses background hits in the other view.

The loss of real dimuon events due to this cut is estimated by using opposite sign dimuon events generated by a Monte Carlo (described in Chapter 6). It is assumed that the loss of like sign dimuon candidates is the same.

To estimate the loss of real dimuons, the following procedure is used. Firstly, the muons in the Monte Carlo dimuon events are extrapolated, and only those events are retained where both muons are predicted to hit the EMI. Secondly, the predicted positions of the two muons are scattered, using the multiple Coulomb scattering errors, according to a Gaussian distribution. Thirdly, muons in a minimum bias sample of charged current events are used to determine the distribution of 'bunch' widths of tubes hit (by them) in EMICH and EMICV. This distribution is then used for the muons in the Monte Carlo dimuon events, to simulate their hits in EMIC. We then try to combine the 'bunches hit' by the two muons in both EMICH and EMICV. If the two 'bunches' overlap in either view, the event is rejected. Using a sample of 2450 Monte Carlo dimuon events, it is determined, that requiring independent 'bunches' in both CH and CV, the loss is $5.6\pm0.5\%$. Out of this $4.1\pm0.4\%$ of the events are lost due to muons sharing 'bunches' in CV, while $1.5\pm0.2\%$ are lost due to sharing in CH.

A Monte Carlo has been written to investigate how often hadrons, that are produced in charged current events, can fake a dimuon event by sharing the muon's hits in either EMICV or EMICH. This Monte Carlo checks, in essence, the effect of accidental 'in-time' background.

Only those charged current events are considered which have at least two 'leaving' tracks, including the muon, predicted to hit EMIB and EMIC. In the Monte Carlo we make the assumption that all extra hits in EMIC during the event timeslot, i.e., hits other than those caused by the muon, depend only weakly on the actual event topology but are more strongly related to the event energy. By making this assumption we can substitute the extra hits in one event timeslot with those in another event timeslot (associated with a different charged current event that has similar energy). Even though the Monte Carlo was written to estimate how often hadronic 'leaving' tracks would share 'bunches' with the muon, it can also be used to estimate how often hadronic 'leaving' tracks, in a charged current event, would not share any 'bunches' with the muon, thereby producing a fake dimuon event. This method provides a lower limit to the accidental 'in-time' background, and can be compared with the results of the calculation described in 4.2.

In this procedure, the hits due to the muon in the first event are left unchanged. However, since the second charged current event could have occurred at a different point in the bubble chamber, we have to move the extra hits, taken from the second event, so that they occupy the region around the muon in the first event. Thus, the new set of extra hits are translated by the same distance as that between the muons in the two events. This is done separately for hits in EMIBV, EMIBH, EMICV and EMICH. This fake event is then run through the EMI analysis program. Whenever a dimuon event is faked, it is classified as opposite sign or like sign, according to the charge of

the muon and the hadronic track. To improve statistics each event was used a number of times by substituting hits from many different events.

The energy correlation cannot be done exactly since this exercise is performed on a sample of events where only the 'leaving' tracks are measured. However, since the spatial position of EMIB corresponds approximately to the hadronic shower maximum, the number of hits in EMIB is used as a rough guide to the event energy. All the charged current events are binned according to the total number of hits in EMIB during the event timeslot. They are then divided into three groups, with the total number of hits in EMIB (1) between 0 and 20, (2) between 20 and 64, and (3) greater than 64. Each event is used only with those events which are in the same category.

The results from this exercise showed that we can expect, in the dimuon event sample, for opposite sign events, at least 5 events where the two tracks share 'bunches' in EMICV and 2 events where they share bunches in EMICH. The corresponding numbers for like-sign events were 4 and 2, respectively. We can also expect, for both opposite sign and like-sign events, at least 4 events (each) where the two tracks do not share any bunches, in either EMICH or EMICV. The last result is consistent with the background calculation in Chapter 4.2. The errors on these numbers are roughly 10%.

The effect of making this cut on the raw data sample is shown in Table 4.1. See below for a discussion of the results.

4.1.4 Discussion of results

From the results in Table 4.1, it is clear that the above cuts remove a significant fraction of events from the raw data sample. Some events fail more than one of the above criteria. Some of the tri-muon candidates which fail to pass the cuts are often labeled as dimuons. For instance, if one of the muons in a tri-muon event does not have a U match then it is rejected, and the event is classified as a dimuon on the basis of the two surviving muons. Similarly, if two muons in a tri-muon event share hits in either EMICH or EMICV then again the event is classified as a dimuon.

It is clear that the effect of requiring independent hits in EMIC is the largest. The attempt to calculate a lower limit, described in Chapter 4.1.3, on fake dimuon events shows that such a background is possible. Though the method followed there is quite approximate, it still predicts that the accidental in-time associations account for approximately half of what is actually removed by the cut. This gives us confidence to say that most of the events removed by this cut are really background. This exercise is necessary because the fraction of genuine dimuon events lost by this cut is predicted to be only 5.6% (using the charm Monte carlo), whereas the raw data sample is reduced by at least 25%.

After making these cuts we are left with 52 opposite sign candidates (44 $\mu^-\mu^+$ and 8 $\mu^+\mu^-$), 12 like-sign candidates (11 $\mu^-\mu^-$ and

1 $\mu^+\mu^+$)and 0 tri-muon candidates. These candidates still contain background, and that will be estimated below.

4.2 Decay and Punch-through background, Accidental associations

4.2.1 Decay background

This background is due to pions and kaons that are produced in charged current events. Some of these can decay before interacting, giving rise to a muon and a (anti-)neutrino. The decay muon usually follows the direction of the parent particle closely enough such that it hits the EMI near the parent's predicted position. In most instances, the EMI match can pass the cut on 2-plane probability, thereby producing a fake muon. The fake muon in conjunction with the muon from the charged current event can thus fake a dimuon event. A major fraction of this background is due to decays inside the bubble chamber, rather than outside, because the pions and kaons interact once they reach the absorber outside, which has a much smaller hadronic interaction length than the bubble chamber liquid.

4.2.1.1 Decays inside the bubble chamber

The estimation of this background is carried out according to the procedure followed in a previous bubble chamber experiment[1]. The basic idea is very simple, as illustrated in Fig. 4.3. A hadronic 'leaving' track in a charged current event is allowed to decay inside

the bubble chamber, using a Monte Carlo program. The decay distribution depends on whether we treat the 'leaving' track as a pion or a kaon. A composite track is fitted to the parent track and the decay muon, processed through the geometry reconstruction program, and extrapolated to the EMI. In this manner, the composite track simulates the original 'leaving' track which has decayed in flight. The decay muon is also extrapolated to the EMI. The predicted position of the decay muon is scattered, using multiple Coulomb scattering errors, according to a Gaussian distribution. The decay muon's scattered position is then compared with the predicted position of the composite track, and a 2-plane probability is calculated. If the match passes the cut on 2-plane probability, then the 'leaving' track is said to fake a muon and thus produce a fake dimuon event.

A Monte Carlo[1] had been written which took 'leaving' tracks and allowed them to decay, and fitted composite tracks to them. Two tapes containing these composite tracks and decay muons were produced, one where the pion lifetime and the other where the kaon lifetime was used in the decay distribution. For the present analysis, we use the same tapes. However, we have to take into account the differences between the two experiments. Firstly, the bubble chamber liquid in the two experiments is different and thus has different hadronic interaction lengths; secondly, the direction of the magnetic field is reversed in the present experiment; and, lastly the momentum distribution of the 'leaving' tracks is different, since the present experiment is done with higher energy neutrinos.

Appendix B contains the mathematical treatment of the procedure. It describes how the total number of background events is related to the information on the Monte Carlo tapes. Appendix B.1 explains how the above-mentioned tapes were produced. Appendix B.2 describes the correction to the background estimates for the different bubble chamber liquid.

The background is first corrected for the difference in interaction lengths. At this stage we assume that the momentum distribution of the 'leaving' tracks is the same in the two experiments. The results at this point are presented as a probability (per 'leaving' track) that a 'leaving' track can fake a muon and are displayed in Table 4.2. The probability is calculated as a function of the track momentum and track length. We then correct for the energy difference between the two experiments. This is done by taking the 'leaving' track distribution, binned according to momentum and length, from the present experiment and multiplying it by the probabilities calculated above. Appendix B.3 describes in detail the correction for the energy difference between the two experiments. The difference in the direction of the magnetic field is not a significant factor. It only changes the direction in which charged particles are bent as they travel through the bubble chamber to the EMI. The EMI detection probability and thus the probability of a 'leaving' track faking a muon is the same for negative as well as positive tracks.

Some of the tracks on the decay tapes can be ruled out as potential background by requiring them to pass two cuts. Firstly, the composite tracks have to have momentum $\geq$ 4 GeV/c, and secondly, both

the composite track and the decay muon have to be predicted to hit the EMI. It is possible in some cases that though the composite is predicted to hit the EMI the decay muon misses it. This is often the case for tracks which go near the edge of the EMI. In some instances, even though the incident pion/kaon and the composite track have momentum $>$ 4 GeV/c, the decay muon can have momentum less than the minimum amount ($\sim$ 2 - 3 GeV/c) required to traverse 10 hadronic interaction lengths (typical absorber thickness between the bubble chamber and EMIC). In such cases, the composite track will be predicted to hit the EMI, while the decay muon will lose all its energy before reaching EMIB and/or EMIC. These two factors are collectively referred to as the geometrical acceptance of the decaying track. Tracks which pass these cuts are processed through the EMI analysis program, PROB632. This program decides if the composite track and the decay muon will pass the cuts on 2-plane probability (as described previously).

Some of the decaying tracks which pass the EMI cuts can be removed by making cuts on the quality of the composite track. When the incident pion (or kaon) decays, the decay muon is produced at an angle and with a different momentum. These two effects change the curvature of part of the track, and this change can, at times, produce a large residual when the geometry program processes the incident hadron and the decay muon as a single track, whereas genuine muons are not affected by this problem. In charged current events, 99.6$\pm$0.2% of the muons have residuals $\leq$ 30 microns. We therefore demand that composite tracks which passed the EMI cuts have to have residuals $\leq$ 30

microns. For the case where all 'leaving' tracks are treated as pions this cut removes 8.3±1.3% of the tracks accepted by the EMI, whereas for the case where all tracks are treated as kaons it removes 22±1.7% of the tracks.

The fraction of undetected decays inside the bubble chamber, for pions and kaons, are 59±2% and 35±4% respectively, of the total background due to decays inside the bubble chamber. The background estimate, corresponding to the final event sample (13000 charged current events), is presented in Table 4.3 separately for all 'leaving' tracks being treated as pions and as kaons. The errors on these estimates are roughly 4%. They will be combined together with results from below in 4.2.1.3.

4.2.1.2 Decays outside the bubble chamber

The estimation of the background due to decays outside the bubble chamber is carried out in a slightly different manner than for the previous case. The first assumption made is that all decays take place just outside the bubble chamber. This is justified by the fact that the absorber (average interaction length for the zinc, magnet coils ~ 12 cm) is outside the chamber, and 90% of the 'leaving' pions and kaons interact within the first half of the absorber (roughly 30 cm). Secondly, it is assumed that the EMI detection efficiency and the geometrical acceptance for decays outside is the same as for decays inside which take place within 20 cm of the downstream bubble chamber wall.

With these assumptions and the Monte Carlo generated decay tapes, it is determined that when all 'leaving' tracks are treated as pions, 8.3% of the tracks are rejected because the composite track is predicted to hit the EMI while the decay muon does not, and the EMI 2-plane probability cut rejects 33.5% of the remaining decays. The corresponding numbers for the case when all 'leaving' tracks are treated as kaons are 50% and 66%, respectively. Therefore, the undetected decays are 61±10% and 17±12%, for pions and kaons respectively, of the total background due to decays outside the bubble chamber. Due to small statistics these numbers are obtained by averaging over all momenta and charges. This assumption introduces only a small error in the estimate.

The total background outside the chamber is estimated from a minimum bias sample of charged current events. Whenever each 'leaving' track is extrapolated to the EMI, by XTRAP, it also calculates the probability that the track will decay before reaching the EMI. This is done assuming the track is a pion. By adding up this probability for all the hadronic 'leaving' tracks, i.e., tracks other than the muon, we get a prediction for the total decay background. Using the detection efficiency calculated above we thus arrive at the undetected background estimate. The results are shown in Table 4.4. The errors in the estimate, in Table 4.4, due to the errors on the detection efficiencies are small.

4.2.1.3 Estimate of total decay background

To estimate the total decay background we need to know the fraction of pions and kaons in the 'leaving' track sample. We estimate the fraction of kaons by using the K^0 production rate in charged current events. According to isospin invariance, the number of charged kaons produced in these events is the same as the number of neutral kaons. We further make the assumption that number of positive kaons produced in charged current events is the same as the number of negative kaons. This assumption, leads to a 50% error in the estimate of the relative number of positive and negative kaons[2], however, it leads to only a 10-12% error in the background estimates. Also, all the kaons produced in charged current events are not potential background, because either they have momentum less than 4 GeV/c or when extrapolated they miss the EMI. The fraction of primary charged kaons which are potential background is determined from a neutrino Monte Carlo[3].

In a minimum bias sample of 831 completely measured charged current events 42 neutral kaons are observed. This observed rate must be corrected for losses due to poor detection efficiency within 1 cm of the primary vertex and within 20 cm of the downstream chamber wall[1,2] and for losses due to unseen decays and for losses due to interactions. The scanning efficiency[1,2] for K's within the detectable region is assumed to be 100%. The unseen decays include decays of K^0_S into neutral particles (br. ratio 31.4%), and all decays

of K^0_L. After correcting the raw rate for detection losses and unseen decays we obtain a neutral kaon production rate of 21±3% per charged current event. This then implies that the production rate of positive and negative kaons (each) is 10.5±5% per charged current event. From the neutrino Monte Carlo it is determined that only 11.4±2.1% of these kaons have momentum ≥ 4 GeV/c and are predicted to hit the EMI. This implies that the number of positive and negative kaons (each) which can contribute towards this background is 1.3±0.8% per charged current event.

In a minimum bias sample of 1434 charged current events (only the 'leaving' tracks were measured here) there are 331 positive and 254 negative hadronic 'leaving' tracks. Assuming that the fraction of protons[4] in the positive 'leaving' track sample is 5%, we obtain that the fraction of positive kaons is 6±3% and hence the pion fraction is 89±3%. The corresponding numbers for the negative 'leaving' tracks are 8±4% and 92±4%.

The decay estimates in tables 4.3 and 4.4 are combined and the total decay background is given in table 4.5. The last line in table 4.5 is obtained by multiplying the numbers of π and K decays by their respective fractions and adding them. There is a 10-12% error in the background estimate due to the uncertainty in the fraction of pions and kaons in the 'leaving' tracks, and there is another 10% error due to systematic measurement and geometrical reconstruction differences among the various groups in the collaboration.

4.2.2 Punch-through background

Hadrons which leave the bubble chamber can either decay outside or interact in the absorber or do neither. The background due to decays has been dealt with in the previous section. In the present section we will estimate the background due to hadrons interacting in the absorber and hadrons reaching the EMI without interacting or decaying. The two sources are collectively referred to as punch-through.

The probability that a hadron will reach both EMIB and EMIC without interacting or decaying is extremely small, $\sim 5*10^{-5}$, because of the presence of (typically) 10 interaction lengths of absorber. Therefore, the number of leaving hadrons, in the present data sample of 13000 charged current events, which can fake a muon is roughly 0.2; thus this source will be neglected.

The more important background is due to hadrons which interact in the absorber, giving rise to secondary and tertiary particles, some of which can hit the EMI. A hadron which is predicted to hit the EMI can at times be associated with these background hits to make a good EMI match, thus faking a muon. To estimate this background, we will use the actual hits in EMIC in the event timeslot. This method was developed for a previous experiment[5]. Although the method may seem approximate, it has been determined that it gives results which agree with a Monte Carlo calculation[1,6]. In the Monte Carlo, hadrons which leave the chamber, make a match in EMIB, and are predicted to hit EMIC, were followed as they traversed the absorber towards EMIC. The

hadrons were allowed to interact in the absorber until either they deposited all their energy in it or their secondary and tertiary products hit EMIC. Hadrons which made a good EMI match using these hits were thus able to fake a muon.

To estimate the background, we take only those hadrons which have momentum $\geq$ 4 GeV/c, a good match in EMIB (probability $\geq$ 0.5%) and are predicted to hit EMIC. These hadrons are taken from a minimum bias sample of charged current events and dimuon candidates. In charged current events, all 'leaving' tracks other than the muon are considered as hadrons. In the dimuon events, the primary muon is selected on the basis of its momentum. Also, in the event timeslot we use only those hits in EMIC which (a) cannot be associated with the primary muon, and (b) when compared with the hadron's predicted position result in a match worse than 0.05%. The second requirement is to reduce the number of hits due to the decay of hadrons. We then make the assumption, that all other hits in EMIC within a maximum cutoff distance from a hadron's predicted position (140 tubes for EMICV and 250 tubes for EMICH) are distributed uniformly along EMICH and EMICV. This can be justified by plotting $dN/d\chi^2$, where χ^2 is calculated using the hits selected as above and the predicted positions of hadrons, and comparing it with the theoretically expected result. In appendix C.1, we calculate the theoretical expression for $dN/d\chi^2$, and, in Figs. 4.4 (a) and (b), we show the plots for EMICV and EMICH, respectively. Comparing the two we see that the previous assumption is justified.

The procedure followed to estimate the background is quite straight-forward. Using the hits selected in the manner described above, a density of background hits (# hits/unit length) is calculated. This density is then used to calculate the expected number of hits in a region R, around the extrapolated position of the hadron, which corresponds to a 1% cut on the 2-plane probability. Appendix C.2 contains the necessary formulae. If we denote the expected number of hits as H, then the probability of observing no hits within region R (from Poisson statistics) is e^{-H}, and the probability of observing some hits within this region is $1 - e^{-H}$. Summing this probability over all hadrons gives us the total background. The background is calculated for, say, $\mu^-\mu^-$ by adding probabilities for negative hadrons in events where the primary muon is also negative. Similarly we can get the background for all the other event classes.

Hadrons are divided into three momentum bins. While calculating a density of hits, two cases are considered depending upon the number of extra hits in EMICV (and EMICH). If the number of extra hits ≤ 3, then an average density is calculated by summing over all such cases, whereas if the number of extra hits > 3, then the actual number of hits is used event by event to calculate the density. Table 4.6 shows the various steps during the calculation of this background. The punch-through background for the various event classes is shown in Table 4.7. The error in the background calculation is estimated to be roughly 40%. The punch-through background estimates are consistent

with the lower limits, calculated using the accidental 'in-time' background Monte Carlo, in 4.1.3.

One expects the punch-through probability per leaving track to be roughly constant (as a function of momentum), although we do not observe that in the present case. We expect a constant probability because the amount of punch-through increases with track momentum, whereas the region corresponding to a 1% cut on 2-plane probability decreases with momentum, thereby roughly cancelling each other out. The reason we do not observe this is due to a few events, with a somewhat noisy EMIC, which have a large background probability. In the results presented in tables 4.6 and 4.7, we have assumed that the punch-through probability for π^- and π^+ are the same. The 40% error on these estimates takes into account these noisy events.

4.2.3 Accidental associations

At times, 'leaving' tracks can be associated with random, background hits in the EMI and be falsely labeled as muons. This background is estimated using a 'wrong-frame' analysis - EMI information from a frame which is different from the one where an event is found is added to the event's data structure. We then compare the predicted positions of the tracks (in the event) with hits in the EMI data and look for fake multimuon events. Only those events are considered which have at least two 'leaving' tracks, including the muon. To improve statistics each event is used with EMI information from many different frames. This background contributes a negligible

amount (0.16±0.1% of the 64 dimuon events) to the final multimuon event sample. Using events with at least one 'leaving' track, the accidental contribution to the charged current sample is roughly 0.2±0.1%, which, again, is negligible.

4.3 Discussion of results

The minimum bias event samples, used in calculating the punch-through and decay backgrounds, have to be selected by the same cuts as those made while obtaining the multi-muon event sample (in 4.1.4). The same cuts have been made to select the event sample used in the punch-through background calculation, but not the event sample used in the decay background calculation. We correct for this by decreasing the decay background by a factor, which takes into account the effect of cuts which were made only for the punch-through sample. Specifically, the cuts on IPFB activity, matches in EMIBU, and independent hits in EMICV and EMICH are to be accounted for. Using numbers determined in 4.1, we estimate that the decay background has to be decreased by 17±1.5%. With this, we can combine the punch-through and decay backgrounds, and the result is presented in Table 4.8.

The net signal can be obtained by subtracting the total background from the event sample determined in 4.1.4. However, before we calculate dimuon production rates we have to correct the signal for

the various cuts which have been made and the detection efficiencies. The latter will be calculated in Chapter 5 and rates will be calculated in Chapter 6.

References

1) J.L. Orthel, Ph.D. thesis, LBL-10035, Lawrence Berkeley Laboratory, University of California, Berkeley, 1979 (unpublished);
C. Ballagh et al., Phys. Rev. D 21, 569 (1980)

2) C. Ballagh et al., Phys. Rev. D 24, 7 (1981). Using the method described in 4.2.1.3, to calculate the K^- and K^+ rate from the K^0 rate in this reference leads to a 50% error in the estimate, when compared with the explicit calculation of K^- and K^+ rates (in this reference).

3) The neutrino Monte Carlo is based on the TUBES program by C. Day. Details can be found in M.D. Sokoloff, Ph.D. thesis, University of California, Berkeley, 1983 (unpublished).

4) Yeager et al., Phys. Rev. D 16, 1294 (1977);
Burnett et al., Phys. Lett., 77B, 443 (1978).

5) F.A. Harris, Internal Report, University of Hawaii, Manoa, IR-43-78, 1978 (unpublished).

6) A. Grant, CERN/D.Ph.II/PHYS 75-42, 1975 (unpublished).

Table 4.1. Effect of various cuts on the raw event sample.

	Opposite Sign Dimuons	Like Sign Dimuons	Trimuons
Events in raw sample	67	31	8
Events lost due to:			
1) Requiring a match in EMIBU	4	5	2†
2) Requiring activity in IPFB	0	5	0
3) Requiring independent hits in EMICV and EMICH	17	8	6 (4†)
4) Residual on track ≤ 30 μ	0	1	0
Final Event Sample	52	12	0

† indicates number of events which were counted as dimuon events (all as opposite sign events).

Table 4.2. Probability (% per LT) of a 'leaving' track faking a muon.

P (GeV/c)	4 - 6	6 - 8	8 - 12	12 - 20	20 - 28	28 -
L (cm)						
70 - 90	0.180	0.219	0.200	0.060	0.056	0.022
90 - 130	0.549	0.319	0.282	0.149	0.097	0.062
130 - 170	0.655	0.504	0.230	0.222	0.094	0.073
170 - 230	1.121	0.697	0.572	0.314	0.211	0.149
230 -	1.935	1.362	0.842	0.533	0.328	0.226
Decays outside B.C.	0.140	0.093	0.065	0.040	0.024	0.013

Table 4.3. Background due to decays inside bubble chamber.

Event Class	$\mu^-\mu^-$	$\mu^-\mu^+$	$\mu^+\mu^-$	$\mu^+\mu^+$
Decay Mode				
π - μ	5.4	6.1	1.2	0.5
K - μ	23.5	24.1	5.4	2.1

Table 4.4. Background due to decays outside bubble chamber.

Event Class	$\mu^-\mu^-$	$\mu^-\mu^+$	$\mu^+\mu^-$	$\mu^+\mu^+$
Decay Mode				
π - μ	1.0	1.2	0.29	0.09
K - μ	2.1	2.4	0.64	0.19

Table 4.5. Total Decay background

Event Class	$\mu^-\mu^-$	$\mu^-\mu^+$	$\mu^-\mu^+$	$\mu^+\mu^+$
Decay Mode				
π - μ	6.4	7.4	1.4	0.60
K - μ	25.6	26.5	6.0	2.29
Total	8.0	8.1	1.9	0.6

Table 4.6. Punch-through calculation.

Momentum (GeV/c)		4 - 12	12 - 20	20 -
# Tracks with EMIB match ≥ 0.5%, and a match in EMIBU		58	37	68
# extra hits within maximum cutoff distance in	CV	77	47	180
	CH	112	54	183
# extra hits when match in EMIC < 0.05%	CV	36	32	147
	CH	85	34	161
# extra hits when match in EMIC < 0.05% and # extra hits < 3	CV	26	23	39
	CH	52	25	37
Average density when # extra hits < 3	CV	2.6	3.6	3.7
($X10^{-3}$) hits/cm	CH	1.4	2.3	2.1
Punch-through probability per 'leaving' track (%)		0.12	0.043	0.66

Table 4.7. Total Punch-through background.

Event Class	$\mu^-\mu^-$	$\mu^-\mu^+$	$\mu^+\mu^-$	$\mu^+\mu^+$
Punch-through background	3.0	5.3	0.5	0.3

Table 4.8. Total Punch-through and Decay background

Event Class	$\mu^-\mu^-$	$\mu^-\mu^+$	$\mu^+\mu^-$	$\mu^+\mu^+$
Punch-through background	3.0	5.3	0.5	0.3
Corrected decay background	6.6	6.7	1.6	0.5
Total background	9.6	12.0	2.1	0.8

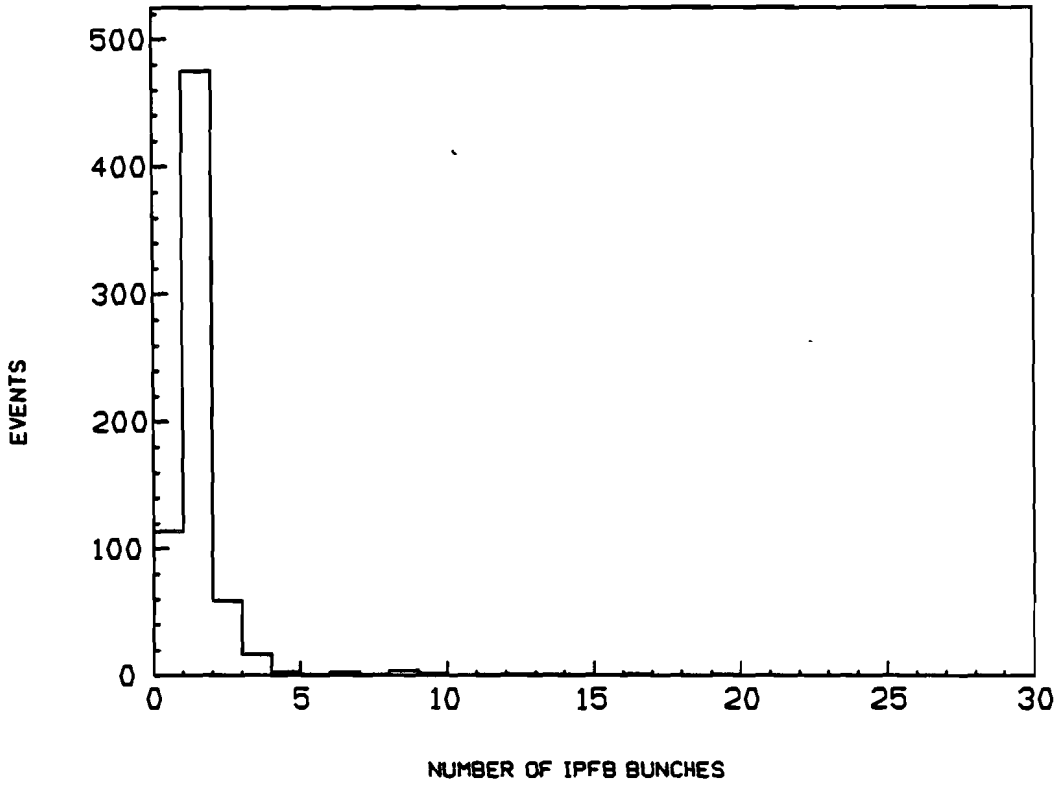

Fig. 4.1a. Number of bunches in IPFB in timeslots associated with 'beamtracks'.

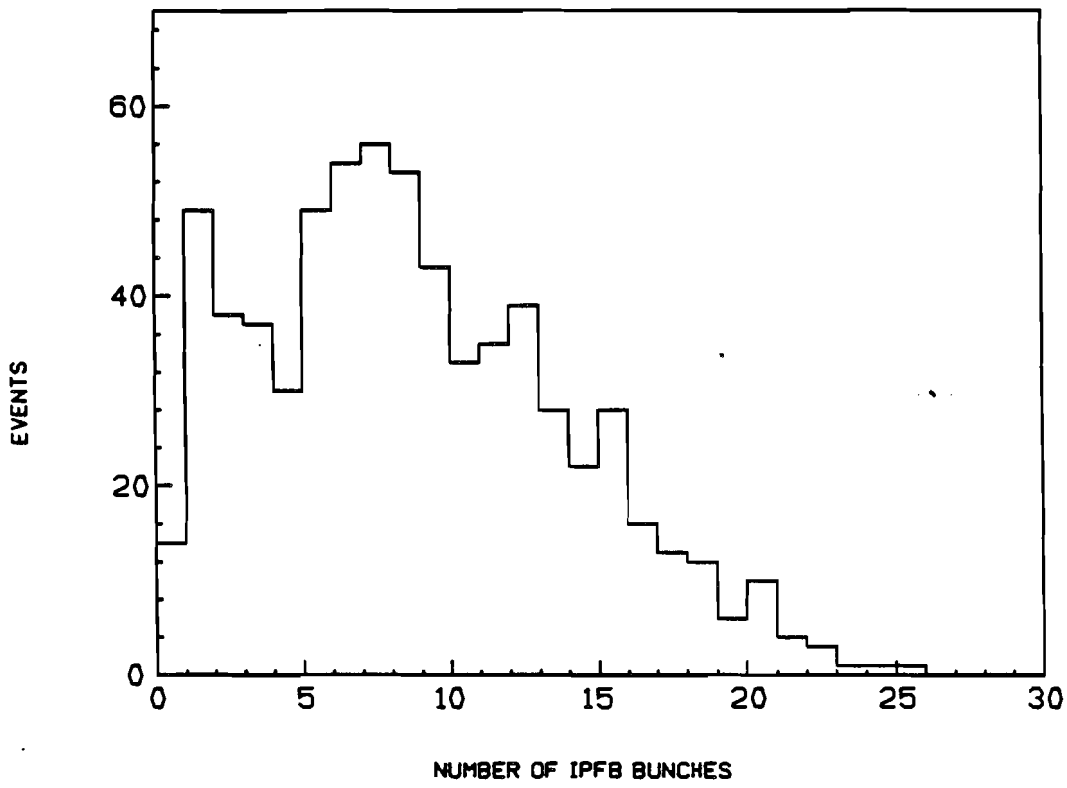

Fig. 4.1b. Number of bunches in IPFB in timeslots associated with neutrino events inside the bubble chamber.

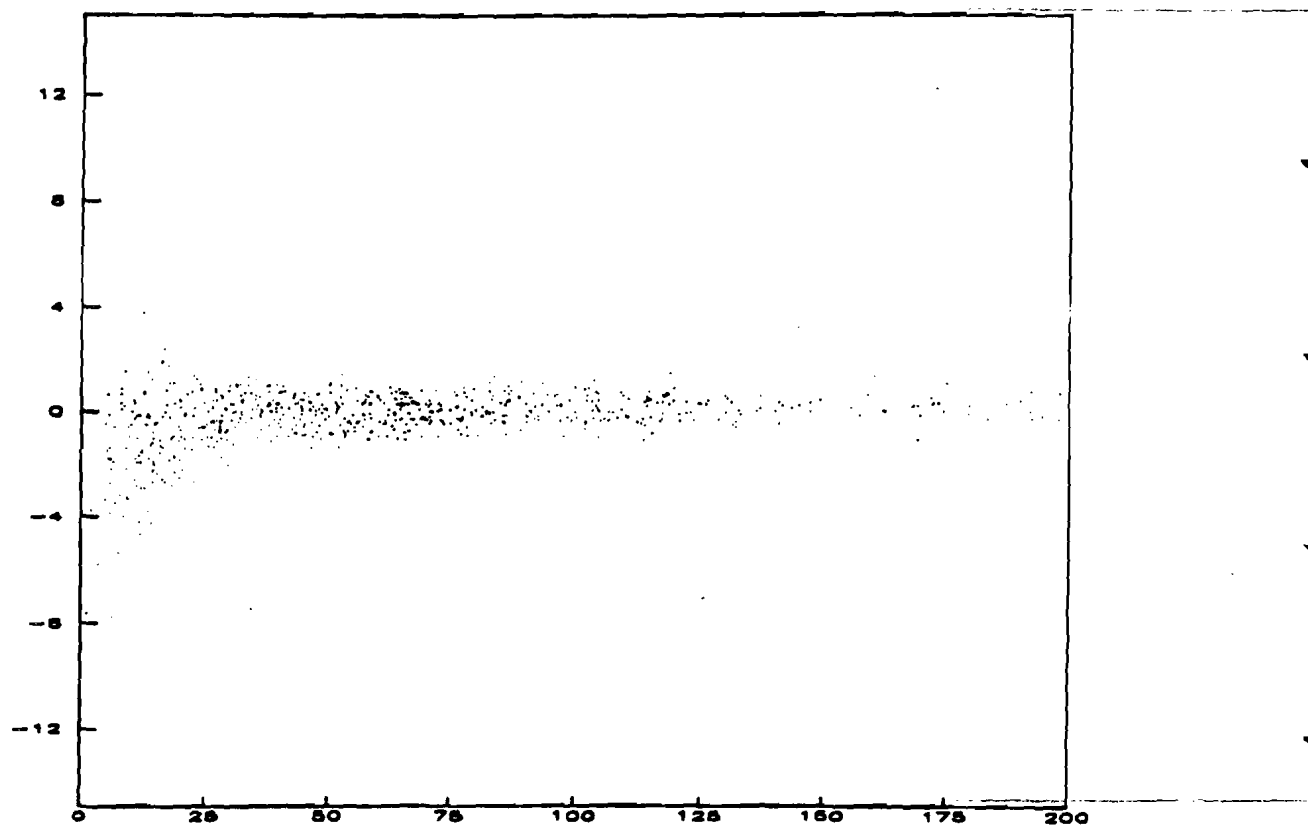

Fig. 4.2. Plot showing the dependence of the difference in U tube number calculated using EMIBV and EMIBH tubes predicted by XTRAP and the U tube predicted by XTRAP vs. track momentum. The Y axis is in units of cm and the X axis is in units of GeV/c.

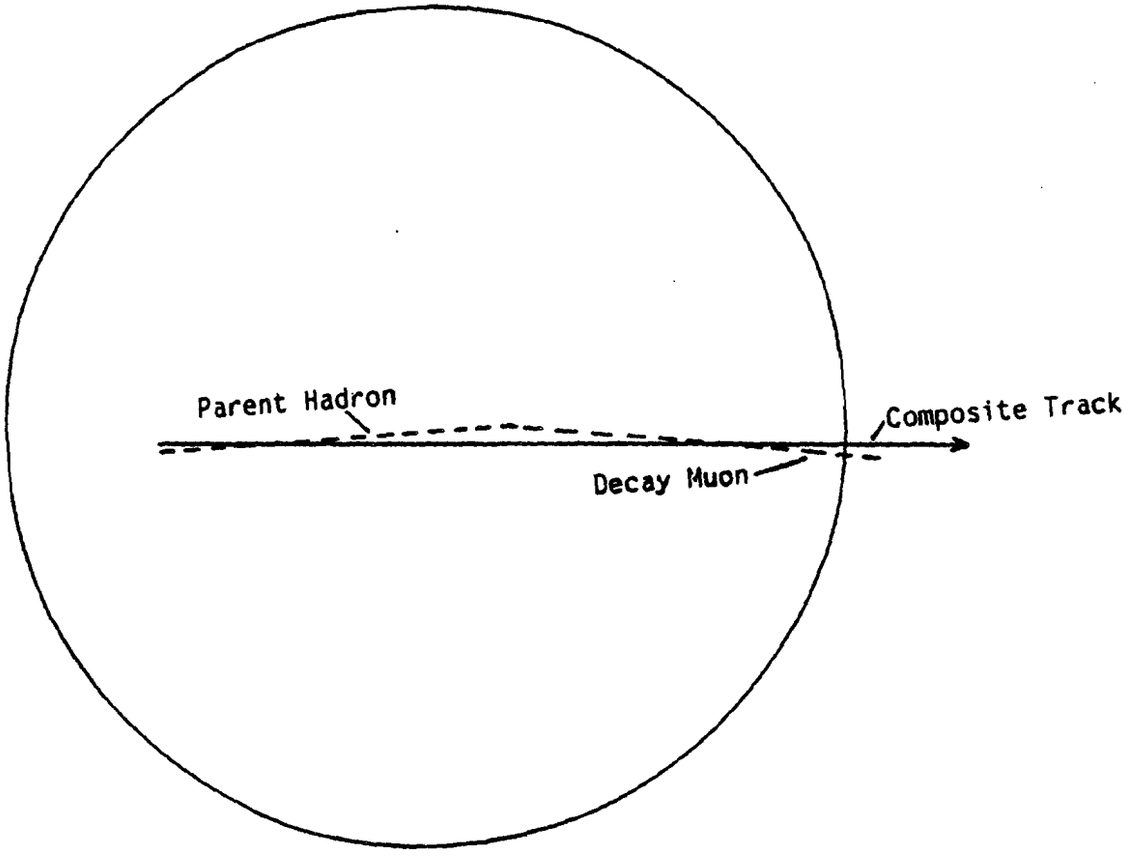

Fig. 4.3. Geometrical representation of the composite track which is fitted to the combination of the parent hadron and the decay muon.

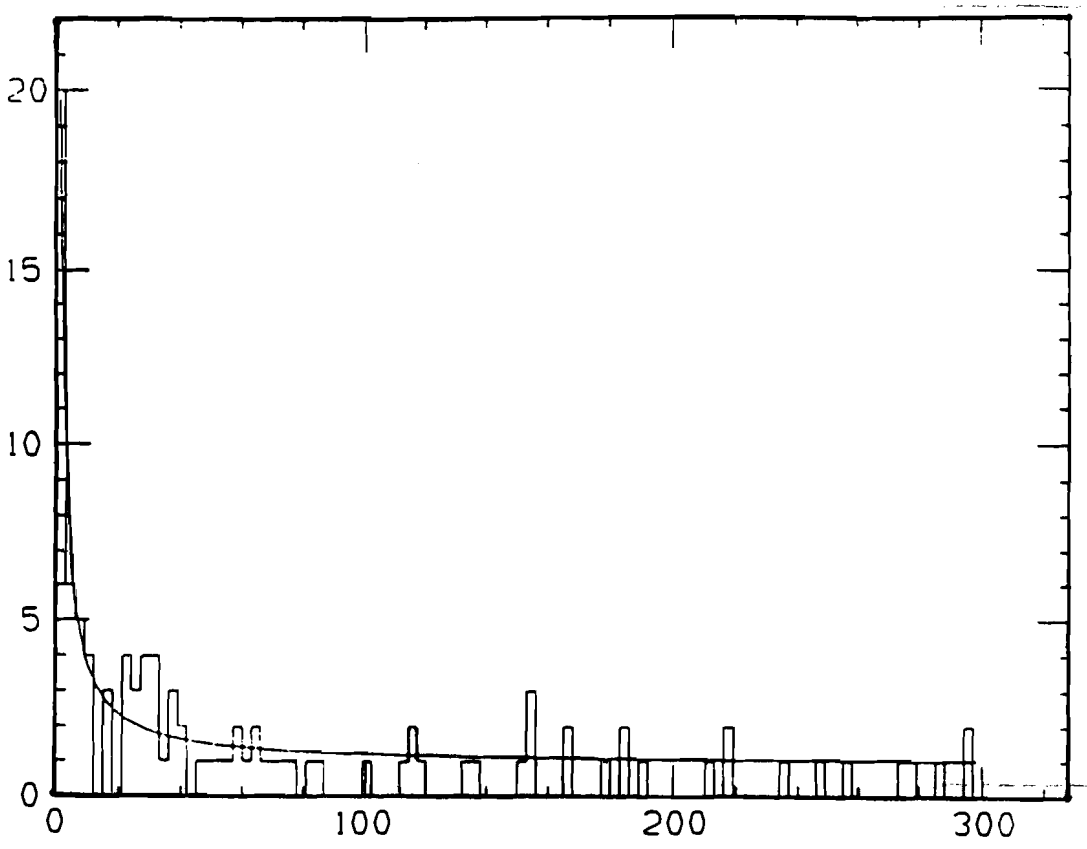

Fig. 4.4a. A plot of $dN/d\chi^2$ vs. χ^2 for EMICV. The X axis is the value of χ^2. The solid line is a fit to the data using a $1/\chi$ fit.

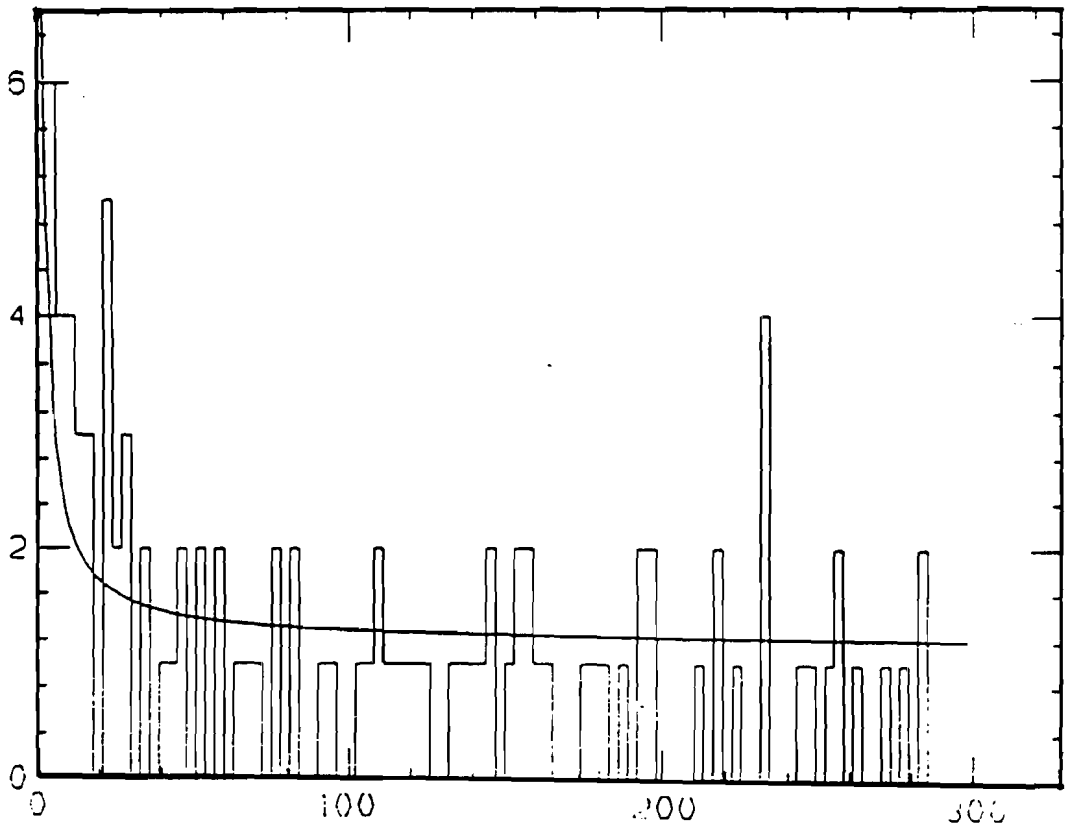

Fig. 4.4b. A plot of $dN/d\chi^2$ vs. χ^2 for EMICH. The X axis is the value of χ^2. The solid line is a fit to the data using a $1/\chi$ fit.

Chapter 5

Detection Efficiency

Not all multimuons that are produced in the data sample are detected, because of various losses and cuts made in the analysis. Therefore, the detected event sample has to be corrected to obtain the true production rate. Actually, we correct the net signal, which is obtained by subtracting the background from the event sample. The factors which have to be corrected for are, (a) losses at the scanning and measuring stage, (b) geometric and electronic acceptance of the EMI, and (c) the cuts made to reduce backgrounds (see Chapter 4.1). Apart from correcting the multimuon signal, we also have to correct the unbiased charged current sample, so that we can calculate multimuon production rates normalized to the charged current production rate.

5.1 Losses in scanning and measuring

5.1.1 Scanning efficiency

In the first step of the analysis chain (Chapter 3.1) all frames were scanned and event vertices noted down. A second scan was done on a smaller sample to determine a scan efficiency. The average scan

efficiency for finding events which have at least two 'leaving' tracks is found to be 99±0.5%. To correct the charged current sample we use the scan efficiency for finding events which have at least one 'leaving' track, which is 97±0.5%.

5.1.2 Faint or complicated events

After program DIMUON (Chapter 3.2) had been run on event vertices and the EMI data, events were tagged as possible multimuons. At this stage 'leaving' tracks had to measured in all such events which had at least two 'leaving' tracks. However, some events were extremely faint or had a very complicated topology and thus could not be measured. The fraction of missed events varied between the different groups, ranging from 2% to 17%. Averaging over all the groups yields a loss of 6±1%. The charged current rate for the entire data sample is obtained by extrapolating results from a sub-sample (14% of the entire data). The groups which contributed to this sub-sample had small losses and the average loss was 3±1.2%.

5.1.3 Overlooked tracks

In the events which were measured, there were losses due to 'leaving' tracks being overlooked by the scanners. This leads to a loss of dimuon events. This loss also varied between the different groups. To estimate the loss of dimuon events the following procedure is used. We first do a second scan on a subset of the events, which

have at least two 'leaving tracks', and determine how many 'leaving' tracks were missed in the first scan, as a function of the number of 'leaving' tracks in the event (this is done for only those tracks which have momentum $\geq$ 4 GeV/c and are predicted to hit the EMI). This is necessary because the greater the number of 'leaving' tracks in an event the smaller is the effect of randomly missing one or more of them. We then calculate the probability that both muons of a dimuon event are detected, assuming that the losses in unbiased events with a given number of leaving tracks are the same as those in true dimuon events with the same number of leaving tracks. Because true dimuon events have more leaving tracks on the average, we have to multiply the above efficiency by a factor which gives the probability that a dimuon event will have, say, N 'leaving' tracks. This is obtained from the Charm Monte Carlo (described in Chapter 6). All non-interacting tracks in the Monte Carlo events are extrapolated to the EMI, and the number of tracks, satisfying all criteria to be 'leaving' tracks, are binned. The calculation estimating the loss of dimuon events is presented in Table 5.1 (the result shown here is only for one lab). The total loss of dimuons is obtained by averaging over all the groups in the collaboration, and is estimated to be $9\pm2\%$. The loss for charged current events is estimated to be $1\pm0.1\%$ (using the procedure outlined above).

5.1.4 Reconstruction Losses

Some of the tracks measured cannot be reconstructed by the geometry program because they may in regions where the optical constants are not well determined, or they are badly measured. After remeasurements are done, this loss of 'leaving' tracks is extremely small and will be neglected.

The total loss of dimuon events due to faint or complicated events, overlooked tracks and reconstruction losses is 15±2%.

5.2 Geometrical and electronic acceptance of the EMI

5.2.1 Geometrical acceptance

Some non-interacting tracks, produced in events in the fiducial volume, and leaving the bubble chamber, are predicted to miss the EMI. This can be because they have low momentum, and thus they bend too much and end up missing the EMI. The events can also take place near the edge of the fiducial volume and if the tracks are produced at large angles then again they miss the EMI. The geometric acceptance has a very strong dependence on track momentum. The geometric acceptance for charged current events and dimuon events is calculated using the same algorithm (developed for a previous experiment). We use an unbiased sample for charged current events, Monte Carlo

generated events for opposite sign dimuons, and the event sample for like-sign dimuons. There are three steps in this method,

1) Each event is simulated to occur at different points in the bubble chamber. This is done by first rotating the event about the neutrino axis, while keeping the radial distance from it fixed. The rotation about the neutrino axis is a bit approximate, because the center of the neutrino beam does not pass through the center of the bubble chamber but is laterally displaced slightly (~ 6% of the chamber radius), and we end up rotating the event about an axis parallel to it. The radial distance is kept fixed to account for correlation between it and the event energy (this correlation is very strong for a di-chromatic beam but not as strong for a quad-triplet beam). The event is then moved randomly along the beam direction (or event axis). Finally, the muon is rotated about the event axis (in case of dimuon events both muons are rotated about the event axis). The event has to be in the fiducial volume. Each event is used 15 times, and each copy is treated as a separate event.

2) The events generated above are run through XTRAP.

3) Finally, these events are run through an analysis program which calculates, after looking at the results of XTRAP, the EMI's geometric acceptance. Each copy of the event is checked to see if the muon(s) is predicted to hit the EMI and from the fraction hitting we derive the detection efficiency. All events are combined using weights (1/efficiency) to determine the total sample weight or the average geometric efficiency. It is important to use weights since events don't occur in the minimum bias sample with equal probabilities, i.e.,

fewer lower momentum muons are detected compared to higher momentum muons relative to what is produced. However, for opposite sign dimuons we use Monte Carlo generated events, which have no bias in muon momentum due to detector acceptance. Therefore, for these dimuons we simply average the efficiency of all events to get a total sample efficiency. The like-sign events are treated similarly to charged current events. Weights calculated for all the dimuon events in the event sample are also used while histogramming various kinematical quantities (described in Chapter 6).

The geometric acceptance for charged current events is presented in Table 5.2. The acceptance for ν events was also checked using events from a ν Monte Carlo, and the results were found to be in excellent agreement with those of the minimum bias sample. The average geometric efficiency for (muons with momentum $>$ 4 GeV/c) opposite sign dimuon events is 83$\pm$2%, and 98$\pm$1% for like sign events. The reason for the different geometric acceptance for opposite and like sign events is that the acceptance for μ^+'s is smaller than for μ^-'s, and since the like sign is mainly $\mu^-\mu^-$ their overall acceptance is higher.

5.2.2 Electronic efficiency

Some muons that are predicted to hit the EMI are not detected. This is because the EMI has some inactive channels ($\sim$ 4%) and some channels which are not very sensitive. The main reason for inactive channels was that some wires produced too many spurious hits and were

disconnected. Also, the algorithm (Chapter 3.4.2 and 3.4.3) used to tag muons has inherent inefficiencies, leading to a further loss of muons. We will combine the inefficiencies due to inactive and less sensitive channels with those of the analysis program and refer to the result as the electronic inefficiency of the EMI.

We will use 'beamtracks' for the purpose of calculating the electronic efficiency. We require the 'beamtracks' to have momentum $\geq$ 20 GeV/c to reduce hadron contamination. We only consider those 'beamtracks' which are predicted to hit the EMI. As mentioned in Chapter 3.4.1 and 3.4.2 we have to calculate the efficiency separately for groups who used Jeremy Lys's version of the minimum χ^2 method, and for those who used Peter Kasper's.

Of all the 'beamtracks' predicted to hit the EMI, Jeremy Lys' version labelled 95.4% as muons. For 'beamtracks' which have 3 view measurements the 1% cut (based on Bayes' theorem in 3.4.3) removed an additional 5.6%, leading to a total efficiency of 89.8$\pm$0.8%, whereas the efficiency for 'beamtracks' with 2 view measurements is momentum dependent. For tracks with momentum $<$ 150 GeV/c the total efficiency is 78.3% and for tracks with momentum $\geq$ 150 GeV/c the corresponding efficiency is 64.4%. Peter Kasper's version tagged 92.7% of the 'beamtracks' as muons, and the 1% cut removed only 1.3% of these, giving a total efficiency of 91.4$\pm$0.8%. The latter 'beamtracks' do not have a momentum dependent efficiency. Averaging the two efficiencies over the fraction of data analyzed by each version gives an average electronic efficiency of 89.0$\pm$0.6%.

The efficiency of tagging a single muon is 89.0±0.6% and so the electronic efficiency for tagging dimuon events is 80.6±0.8%.

5.3 Cuts made to 'clean' the event sample

We require dimuon events to pass three criteria described in Chapter 4.1, (1) minimum activity in IPFB, (2) matches for the muons in EMIBU, and (3) independent hits in EMICH and EMICV. All three cuts lead to a loss of genuine dimuons. The loss of events by requiring activity in IPFB is 4±1%, by demanding matches in EMIBU 7.0±1.6%, and by requiring independent hits in EMICH and EMICV 5.6±0.5%. Therefore, the total loss is 16.0±1.8%. None of these cuts were made on the charged current sample and thus no correction is required for them.

5.4 Discussion

Using the efficiencies calculated above, the detection efficiency for opposite sign events is 47.6±2%, for like-sign events 56.3±1.5%. The detection efficiency for ν induced charged current events is 82±1% and for $\bar{\nu}$ induced events is 77±2.2%.

Table 5.1. Number of dimuon events missed because of overlooked tracks.

# of 'LT' in event	2			3			4			5			6			≥7		
# 'leaving' tracks detected	0	1	2	1	2	3	2	3	4	3	4	5	4	5	6	5	6	≥7
# events in sample	0	1	101	0	2	40	0	1	15	0	0	10	1	0	3	0	0	5
Prob. evt. is dimuon if m out of n tracks are measd	0.0	0.0	1.0	0.0	0.33	1.0	0.2	0.5	1.0	0.3	0.6	1.0	0.4	0.67	1.0			1.0
Eff. of picking dimuon events	101.0/102.0			40.66/42.0			15.5/16.0			10.0/10.0			3.4/4.0			5.0/5.0		
Prob. that dimuon evt. has n 'LT'	0.36			0.36			0.19			0.05			0.03			0.01		

Total efficiency of picking dimuon events

101.0*0.36/102. + 40.66*0.36/42.0 + 15.5*0.19/16.0 + 10.0*0.05/10.0 +
3.4*0.03/4.0 + 5.0*0.01/5.0
= 97.5%

Table 5.2. Geometric acceptance of an unbiased sample of charged current events.

Momentum (GeV/c)	Geometric acceptance for charged current data			
	ν		$\bar{\nu}$	
	Efficiency	(# events in sample)	Efficiency	(# events)
$P \geq 4.0$	96.6±0.6 %	(866)	91.9±2.3 %	(152)
$4.0 < P \leq 20.0$	84.6±2.5 %	(146)	66.8±7.3 %	(25)
$20.0 < P \leq 50.0$	99.7±0.2 %	(259)	98.4±0.8 %	(37)
$P > 50.0$	100.0±0.1 %	(461)	100.0±0.4 %	(90)

Chapter 6

Comparison of data sample with Monte Carlo predictions

In the previous three chapters, we extracted the multi-muon sample, estimated the backgrounds and calculated the detection efficiencies. We are now in a position to calculate multi-muon production rates, which are normalized to the single muon (i.e., charged current) production rate. We compare kinematic distributions for the opposite sign dimuon event sample with the predictions of a (charm) Monte Carlo. The like-sign event sample is compared with distributions from a π/K background calculation.

We first describe the Monte Carlo which generates opposite sign dimuons, and then the π/K background calculation. The latter is also used to generate kinematic distributions which describe the background events in the opposite sign sample.

6.1 Charm Monte Carlo

The Monte Carlo was written for a previous experiment[1], and it only generates the shape of the various kinematic quantities (thus it does not provide a check on the absolute opposite sign production rate). To compare these predictions with the event sample, we normalize the output of the Monte Carlo to the total dimuon signal (i.e, data - background). Kinematic distributions for background

events are generated, as mentioned above, by the π/K background calculation, and are normalized to the total number of background events (decay + punchthrough) in the event sample.

The charm Monte Carlo has three distinct stages, (a) production of a charm quark in a charged current neutrino event, (b) hadronization of the quark as a charm meson, and (c) decay of the meson to produce the second muon. We will briefly describe each step.

6.1.1 Production of a charm quark

In the Monte Carlo, we use the four quark model, described in Chapter 1.4, to describe charm production. We can ignore the presence of the b quark due to a small mixing angle between it and the u quark. We ignore any intrinsic charm component in the nucleon (which could produce a b quark, since c → b coupling is large). The t quark is ignored due to lack of phase space. Therefore, we can describe the mixing between d (s) and c quarks using only the Cabibo angle (ignoring the Kobayashi-Maskawa matrix), and in equations 1.7 - 1.10 (Chapter 1.6.1) we equate $V_{cd} = 0.228$ and $V_{cs} = 0.973$.

The nucleon structure functions[2] are obtained by using the form $x^{0.5}*(1-x)^{3.5}$ for valence quark distributions, and $(1-x)^7$ for the sea quark distributions. We take the quark (anti-quark) sea to be asymmetric, and the ratio of the strange to non-strange sea[2] is taken to be 0.52. With these assumptions, and the fraction of the nucleon momentum carried by various quarks[2], the explicit form for the quark density functions can be written as

$$xu(x) = 2.503*\sqrt{x}*(1.0-x)^{7/2} + 0.185*(1.0-x)^{7}$$

$$xd(x) = 1.246*\sqrt{x}*(1.0-x)^{7/2} + 0.185*(1.0-x)^{7}$$

$$xs(x) = x\bar{s}(x) = 0.096*(1.0-x)^{7}$$

$$x\bar{u}(x) = x\bar{d}(x) = 0.185*(1.0-x)^{7}$$

The kinematic effect of the large charm quark mass is taken into account by using the slow re-scaling procedure, and the corrected cross-sections for charm production in ν (and $\bar{\nu}$) interactions are in Equations 1.9 and 1.10 (Chapter 1.6.1). The large quark mass also introduces a threshold into the interaction, and we require that $W \geq W_{th}$ ($= 2.81$ GeV/$c^2 = M_D + M_N$). We write $W^2 = M_N^2 - Q^2 + 2M_N Ey = M_N^2 + 2M_N Ey(1-x)$ (where all variables have the same meanings as defined in Chapter 1.6.1), and using W_{th} as the lower limit for W we derive the allowed range for x, y and E. For instance, the minimum allowed value for E is $(W^2_{th} - M_N^2)/2M_N$ and the maximum is determined from the energy of the incident beam. We choose values for x, y and E, within their allowed range, so as to simulate the correct shape of the charm production cross-section (the energy spectrum of the beam[3] is taken into account). We also require the momentum of the primary muon to be greater than a specified value (e.g., ≥ 4 GeV/c).

We choose the incident lepton, ν or $\bar{\nu}$, according to the fraction of $\bar{\nu}$'s in the beam (which is a function of the lepton energy). We choose the target type, i.e., a neutron or a proton, according to the fraction n/p in present Ne-H_2 mix and the ratio $\sigma_{\nu n}/\sigma_{\nu p}$ (or for $\bar{\nu}$). We choose the target type for two reasons: (1) The density functions are defined such that xu(x) refers to the more abundant (valence)

quark and xd(x) to the less (valence) abundant quark, and since there are two d quarks in a neutron and one d quark in a proton (reverse for u quark), we use the density function xd(x) for νp interactions and xu(x) for νn interactions. Similarly for $\bar{\nu}$ interactions with a proton (neutron) we use $x\bar{d}(x)$ ($x\bar{u}(x)$). The cross-sections used for the various different cases are

$$\nu p \rightarrow \sin^2\theta_C \, d(\xi) + \cos^2\theta_C \, s(\xi)$$

$$\nu n \rightarrow \sin^2\theta_C \, u(\xi) + \cos^2\theta_C \, s(\xi)$$

$$\bar{\nu} p \rightarrow \sin^2\theta_C \, \bar{d}(\xi) + \cos^2\theta_C \, \bar{s}(\xi)$$

$$\bar{\nu} n \rightarrow \sin^2\theta_C \, \bar{u}(\xi) + \cos^2\theta_C \, \bar{s}(\xi)$$

In addition to the above terms there is also an overall multiplicative factor, which is defined in equations 1.9 and 1.10. (2) We require that the electric charge (and baryon number) in the initial and final state are the same, and thus the total charge of the hadronic system is determined from these constraints. For instance in $\nu p \rightarrow \mu^- X$, where X represents the hadronic system, X has charge +2, whereas in the interaction $\nu n \rightarrow \mu^- X$, X has charge +1.

The event vertex is chosen according to the spatial distribution of the neutrino beam and the geometry of the bubble chamber, and is required to lie within the fiducial volume. This is necessary because we use the Monte Carlo generated dimuon events to calculate their geometric acceptance by the EMI (described in Chapter 5.2.1).

6.1.2 Fragmentation of the charm quark

After a charm quark is produced in a ν ($\bar{\nu}$) interaction it fragments to produce a charmed meson or baryon. There is evidence[4] that charmed baryon production is suppressed for $E_\nu > 30$ GeV, and since in the present experiment the $\langle E_\nu \rangle \sim 90$ GeV we ignore charmed baryon production. We therefore assume that the charm quark fragments to produce D and D^* mesons. For $W < 2.95$ GeV only D mesons are produced, and for $W \geq 2.95$ GeV D and D^* mesons are produced (in the ratio 3:2)[5]. In case a D^* is produced we allow it to decay to $D\pi$ or $D\gamma$ (in the ratio 2:1). The fragmentation process is described by the Peterson[6] function

$$D_c(z) = \frac{1}{z\left[1 - \frac{1}{z} - \frac{\epsilon}{(1-z)}\right]^2}$$

where ϵ is a factor dependent on the quark mass, and z is the ratio of the meson and the quark energy. Theoretically, one expects $\epsilon \simeq 1/m_c^2$, and experimentally[7] its value varies from 0.14 to 0.79. The fragmentation function depends weakly on ϵ, and the large variation (0.14 to 0.79) in its value does not produce a significant change in the shape of $D_c(z)$[7]. For our Monte Carlo we use $\epsilon = 0.16$ (no error is reported on 0.79, and hence it is not used in calculating an average value of ϵ). In the fragmentation process, the charm meson gets a fraction, z, of the charm quark energy.

The charm meson is also given a momentum in a direction transverse to the hadronic system, where the latter's 4-momentum is

$P_{hs} = P_\nu + P_N - P_{\mu 1}$. The transverse momentum is chosen according to the function

$$\frac{dN}{dp_t^2} \propto e^{-6(p_t^2 + M_D^2)^{0.5}}$$

Since the charm meson gets only a fraction, z, of the charm quark energy, the remaining fraction, 1-z, goes into producing a hadron shower. The hadron shower consists of one baryon (to conserve baryon number) and a mixture of pions (π^0, π^- and π^+). The charge of the hadronic shower depends on the incoming lepton and the target nucleon. The particles in the hadronic shower are produced according to a flat rapidity distribution, and have energy and momentum (P_L and P_t) satisfying constraints on the hadronic shower.

6.1.3 Decay of the charm meson

At this stage we produce the second muon by allowing the charm meson to decay. We deal only with 3-body decays, $D \to \pi\mu\nu_\mu$, $K\mu\nu_\mu$ and $K^*\mu\nu_\mu$. The branching ratios for these decay modes[8] are 0.06/0.47/0.47. The matrix element for the decay, $Y \to \mu^+\nu_\mu X$, is[9]

$$M = \bar{u}_\nu \gamma_\alpha (1+\gamma_5) u_\mu \langle X | J_\alpha^+ | Y \rangle$$

Using this expression we can determine the energy spectrum of the final state particles. The functional form of the muon spectrum is the same for the $D \to \pi$ and $D \to K$ case since both are examples of spin

0 → spin 0 decay, whereas the $D \to K^*$ has a different form since it is a spin 0 → spin 1 decay mode[9]. We first choose the muon momentum according to the appropriate spectrum, and then generate the neutrino and strange meson momenta. We require the muon momentum to be greater than a specified value (4 GeV/c in the present case). In case the decay mode is $D \to K^* \mu \nu$, we allow the K^* to decay to $K\pi$.

This completes the chain of events, which starts with the production of a charm quark and ends with the semi-leptonic decay of the charm meson. With the information generated we can plot various kinematical quantities and compare with data.

6.2 π/K background program

The charm Monte Carlo is used to simulate genuine opposite sign dimuon events, whereas the background calculation uses ν and $\bar{\nu}$ induced (minimum bias) charged current events to generate fake dimuon events (both opposite and like sign). Only those charged current events are considered which have at least one 'leaving' track ($P \geq 4$ GeV/c and predicted to hit EMIB and EMIC) in addition to the muon.

The procedure to simulate background is quite straight forward. Each hadronic track in a charged current event is assigned a weight, which corresponds to the probability that it can fake a muon, either by decaying in flight or by "punching through" to the EMI. These weights are calculated in Chapter 4.2, and the probability (per 'leaving' track) of a hadronic track faking a muon is presented in tables 4.2 and 4.6. We calculate the same kinematical quantities here

as for the event sample (and for the Monte Carlo generated events), and while histogramming, each entry is weighted by the background weight of that particular hadronic track and the geometrical and instrumental weight of the charged current event it belongs to. The geometrical weight of a charged current event is parametrized in terms of the muon momentum and the angle it makes with the neutrino direction. We sum over all hadronic tracks in the charged current sample. Since we use a small sub-sample of events to generate the background, all distributions are normalized to the total background (see table 4.8). To simulate the like-sign background, we use negative hadronic tracks in ν induced events and positive hadronic tracks in $\bar{\nu}$ events, and for the opposite sign background, we use positive tracks in ν events and negative tracks in $\bar{\nu}$ events.

We now turn to the event sample to calculate multi-muon production rates and plot kinematic quantities.

6.3 Energy reconstruction of the dimuon and unbiased event sample

Since we do not detect all the neutral particles that are produced in an event, we have to correct for this inefficiency to avoid underestimating the energy of the hadronic shower and thus the energy of the incoming neutrino (or $\bar{\nu}$), the latter being reconstructed by adding the momenta of all particles along the neutrino direction. The unbiased event sample needed a larger correction, compared to the dimuon event sample, because not all of the converted neutral particles were measured in the former sample. For instance, only the

five closest γ's associated with the charged current event were measured, and none of the N^*'s were measured. On the other hand, every dimuon event was measured as completely as possible.

We use a method which had been developed for previous bubble chamber experiments[12] (SCOTT method). In this method we assume that (a) we know the neutrino direction, (b) we know the momentum of the leading muon, (c) the momentum of the detected hadrons is along the momentum vector of the total hadronic system ($= \vec{P}_\nu - \vec{P}_{\mu 1}$), and (d) the target nucleon is at rest, hence the muon momentum perpendicular to the neutrino direction in the μ-ν plane exactly balances the total hadronic transverse momentum (in the same plane). The correction is parametrized in terms of the visible hadronic momentum (P_x), parallel to the neutrino direction. This is done separately for dimuon events (the secondary muon is treated as part of the hadronic shower) and charged current events. The corrected hadronic momentum can be written as,

$$P_{x\ \text{corrected}} = b + aP_x$$

where,

$a = 1.30 \pm 0.02$ and $b = 2.5 \pm 0.3$ for charged current events

$a = 1.20 \pm 0.06$ and $b = 4.8 \pm 2.0$ for dimuon events

Therefore,

$$E_{\nu(\bar{\nu})} = P_{\mu\text{-}x} + P_{x\ \text{corrected}}$$

To determine the effectiveness of the SCOTT method for the present experimental conditions, we studied its effect on charged current Monte Carlo events (only ν induced events)[15]. We assume that $\bar{\nu}$ events are affected in a similar fashion. Only those Monte Carlo events are considered which have a muon with momentum $\geq$ 4 Gev/c that is predicted to hit the EMI. We also simulated the present experimental condition by including only the closest five γ's in the visible energy. These studies show that the SCOTT method is not capable of reconstructing the missing energy completely. The ratio $\langle E_{recon.}\rangle/\langle E_{true}\rangle$, for Monte Carlo events is only 0.93, implying a short fall of 7%. We introduced a second correction to account for this deficit. The 7% correction was split into two parts: (a) The muon momentum was increased by 4.3%. In our analysis programs, track momenta are 'fixed' up to reflect the fact that the curvature of a track is normally distributed (which is what is measured in bubble chambers), whereas momentum (1/curvature) is not. This 'fix' decreases the average muon momentum, and the 4.3% correction is used to correct this. (b) The visible hadronic energy is corrected by 10.2%. The individual corrections to the muon and visible hadronic momentum add up to a 7% increase in the total energy of the event. The two corrections (SCOTT and the 7% increase) brought the reconstructed energy close to the true value (the above ratio now becomes 0.99).

Also, the reconstructed energy spectrum, after the second correction (the 7% increase), is closer to the true energy spectrum.

To estimate the true energy spectrum of the unbiased event sample, we used three methods: (1) SCOTT method as described above, with the additional (7% increase) correction factor. (2) Scaling E_{vis} for the data sample according to the ratio E_{true}/E_{vis} as determined from Monte Carlo events. (3) Using the true energy distribution generated by the neutrino Monte Carlo. We divide the data in three energy bins (0-100 GeV, 100-200 GeV, $\geq$ 200 GeV), and calculate the fraction of events in these bins according to the three methods. The spread in the value of the fraction of events reflects the systematic uncertainty in the energy estimation. Our final result takes the mean of the extreme values as the central value, and the spread about this value as the systematic error.

We believe that the neutrino Monte Carlo uses the correct neutrino flux and reasonably accurate quark structure functions. This can be seen by comparing the muon spectrum from the data and the Monte Carlo, as shown in Fig. 6.1. The data includes muon from both the unbiased event sample and the unbiased leaving track sample, and corresponds to 1790 negatively charged muons. The agreement is good. However, the energy of the (visible) hadronic shower for the fully measured data sample (~ 500 events) is in some disagreement with the Monte Carlo, as shown in Fig. 6.2. At present we are not certain about the reasons for this disagreement, i.e., whether the problem is in the event sample or in the way the visible hadronic shower is being simulated by the Monte Carlo. Therefore, to reduce the error in the

final result due to relying solely on the unbiased data sample or the Monte Carlo, we follow the procedure outlined in the preceding paragraph.

The background events (charged current events which contain at least one hadronic track with momentum $\geq$ 4 GeV/c and predicted to hit the EMI) are treated similarly, by considering only those (neutrino) Monte Carlo events which had at least one hadronic track with momentum $\geq$ 4 GeV/c and which were predicted to hit the EMI. The spread in the fractions of events in the three energy bins is small in this case (compared to the error due to the background estimation techniques, as described in Chapter 4), and the resulting systematic error in the background is combined with the error due to the above mentioned techniques.

The dimuon event sample is corrected according to the SCOTT method only (without the additional correction factor of 7%). We believe that this is adequate, because, firstly, each dimuon event is measured more carefully than the unbiased sample, and secondly, the data corrected by the SCOTT method alone (without the additional 7% correction) agrees with the opposite sign dimuon Monte Carlo. The average event (data) energy and the fraction of events (data) in the various energy bins agree with the Monte Carlo results. We assume that the like-sign candidates are corrected adequately by the SCOTT method alone.

The unbiased event sample corrected as above is used in calculating multi-muon rates as a function of energy, and in obtaining the kinematic distributions for the background.

6.4 Multi-muon Production rates

6.4.1 Opposite Sign Dimuons (OSD)

6.4.1.1 Rates

Opposite sign dimuons are classified as either ν or $\bar{\nu}$ induced, on the basis of the transverse momentum of each of the two muons with respect to all the other particles in the event. The muon with the larger value of P_T is taken to be the primary muon, thus deciding the origin of the event, i.e., due to a ν or a $\bar{\nu}$. According to the charm Monte Carlo, in 97.0±0.6% of ν induced OSD, the μ^- has the larger P_T, whereas this fraction is 95.0±0.8% for $\bar{\nu}$ induced OSD. The events in the data sample are shown in Fig. 6.3, and using the above criteria we have 44 $\mu^-\mu^+$ and 8 $\mu^+\mu^-$ events. The squares indicate events where μ^- has the higher P_T, and crosses indicate events where μ^+ has the higher P_T. We correct these numbers for the inefficiency of the selection procedure (on the basis of P_T), subtract decay and punch-through backgrounds (from table 4.8), and use the detection efficiency for detecting OSD (from Chapter 5) to estimate their total production. The OSD rate (normalized to single muon events) for E ≥ 10 GeV and P_μ ≥ 4 GeV/c for both muons, is 0.64±0.14% for $\mu^-\mu^+$ events, and 0.47±0.25% for $\mu^+\mu^-$ events. Combining the two numbers, we calculate the total OSD rate to be 0.56±0.12%. These results are presented in table 6.1. The OSD rate is in agreement with result of previous

experiments[10]. We also divide the data into three energy bins, and the $\mu^-\mu^+/\mu^-$ rate (ν induced) as a function of energy is $0.28\pm0.13\pm0.02\%$ for $E_\nu < 100$ GeV, $0.76\pm0.27\pm0.14\%$ for $100 \leq E_\nu < 200$ GeV, and $1.1\pm0.34\pm0.2\%$ for $E_\nu \geq 200$ GeV. The first error includes both the statistical error and error due to uncertainties in the background estimation (the latter is roughly 1/5 of the statistical error), whereas the second error is the systematic error due to the uncertainty in the number of charged current events in the three energy bins (see Chapter 6.3 for the origin of the second error). See Figs. 6.4 (a) and (b) for a comparison of our results with those of other experiments.

We observe 8 neutral strange particles in 52 opposite sign events, however, to calculate rates we only use 48 events since 4 events were faint and could not be reliably scanned for V^0's. All V^0's are kinematically fit by program SQUAW. The characteristics of the 8 V^0's are shown in table 6.2. All K/Λ ambiguities are treated as Λ's, except for the ambiguity in event 23271207 (this V^0 has no 3-C fit) which is assigned a 80% probability[11] of being a K. The raw $\mu\mu V^0X/\mu\mu X$ rate is $15\pm5\%$. The raw V^0 rate in charged current events is $8.5\pm1\%$, and the fraction of background events containing V^0's is $8.7\pm1.5\%$. We thus see that the neutral strange particle production rate is higher in opposite sign dimuons. We now correct this rate for detection efficiency of the V^0 and decays into neutral particles. We weight each V^0 by the (inverse of the) probability that it will decay inside the bubble chamber (instead of interacting before decaying or leaving the bubble chamber without decaying or interacting). A weight

of 0.0 is assigned to the V^0 if it decays within 1 cm of the primary vertex (poor detection efficiency), or within 20 cm of the downstream wall (poor momentum determination of the decay tracks). Since each dimuon event was scanned very carefully, we assume that the scan efficiency for V^0's which convert at least 1 cm from the primary vertex is a 100%. The weight for the V^0 also includes the probability (geometrical and instrumental) of detecting the event in which it is found. The latter were calculated in Chapter 5.2.1 and 5.2.2. The corrected V^0 rate per dimuon event, after subtracting background, is found to be 0.50 ± 0.21. If we assume, from isospin invariance, that equal numbers of neutral and charged strange particles are produced, then we find that the strange particle production per dimuon event is 1.0 ± 0.42, which is consistent with the charm hypothesis (see Chapter 1.6.1 for a discussion of this point).

In the present sample we have a large number of K/Λ ambiguities. This could possibly be due to poor momentum determination since the interaction length is small, hence the decay tracks interact more quickly precluding a good measurement of the track momenta. One option is to remeasure some of the V^0's where there are large errors on the momentum of the decay tracks.

6.4.1.2 Kinematic distributions

We now plot various kinematic variables, used to describe deep inelastic scattering and dimuon events, and compare the results for the data sample with the charm Monte Carlo predictions and background events, as described earlier on. Some of these variables have already been defined in Chapter 1.6.1. Out of 52 opposite sign events we use only 48 events for the present purpose, because 4 events were faint and could not be reliably measured.

For the purpose of making these plots, we require that for an event to be classified as $\mu^+\mu^-$ the P_T (with respect to all non-muon particles in the event) of the μ^+ has to be greater than that of the μ^- by at least 1.414 GeV/c. The motivation behind this is to have a cleaner separation of ν and $\bar{\nu}$ events. However, in the present sample we find that after making this cut we are left with only 4 $\mu^+\mu^-$ events instead of 6, as predicted by the charm Monte Carlo. The probability of such a fluctuation is 13%. In the following plots the $\bar{\nu}$ induced events are shown shaded. The smooth dotted curve represents the Monte Carlo predictions normalized to the net dimuon signal (event sample - background), and the dotted-dashed curve represents the sum of the Monte Carlo predictions and the background calculation predictions (unless otherwise specified), where the latter have been normalized to the total background in the sample. The events have been weighted by their instrumental and geometric weights (as calculated in Chapter 5.2.1 and 5.2.2.)

The averages for the various kinematic variables are presented in table 6.3, and one can compare the dimuon event sample with the background predictions, Monte Carlo predictions and the unbiased charged current sample. The variables, for the unbiased sample, denoted by * are obtained by using hadrons which have momentum $\geq$ 4 GeV/c. The dimuon means are calculated from the sample means and the background means. The agreement between the dimuon means and the Monte Carlo predictions is very good.

In Figs. 6.5, 6.6 and 6.7 we present the plots for the energy of the primary muon, the secondary muon and the event energy. The agreement is reasonable. Figs. 6.8 and 6.9 show the distributions for the mass of the hadronic system recoiling against the primary muon and the 4-momentum transfer squared. The agreement is very good.

In Fig. 6.10 we present the Bjorken x distribution. The small peak, at x= 0.3, is due to one event with a high weight (3.8). The Bjorken y distribution is shown in Fig. 6.11. The excess in the high y bin (0.85 to 0.9) is mainly due to two low energy events with relatively high weights (2 and 3.8). The lack of events at low y is due to the charm threshold suppression and the slight depletion of events at high y (if one ignores the effect of the two high weight events) is due to the requirement that the primary muon momentum be $\geq$ 4 GeV/c.

The plots for the variable measuring the asymmetry in the energies of the two muons, $\gamma = (E_{\mu 1}-E_{\mu 2})/(E_{\mu 1}+E_{\mu 2})$, is shown in Fig. 6.12. The peak in the bin (-0.2,-0.3) is due to the high weight (3.8) event. The ratio of the muon energies, β, is shown in Fig. 6.13. The

momentum of the second muon perpendicular to the μ_1-ν plane is shown in Fig. 6.14. The solid line corresponds to hadrons with momentum $\geq$ 4 GeV/c in the charged current minimum bias sample, whereas the broken lines have their usual meanings. The peak in the 0.8-0.9 GeV/c bin is due to the high weight event.

In Fig. 6.15 we present the charged particle multiplicity distribution. The solid line is obtained from the charged current sample. Fig. 6.16 shows the angle, ϕ, between the two muons projected on a plane perpendicular to the neutrino direction. The agreement with data is very good.

In Fig. 6.17 we present the fraction of the hadronic energy carried off by the secondary muon, $z_{\mu 2} = E_{\mu 2}/(E_\nu - E_{\mu 1})$. This variable measures the charm fragmentation function indirectly, since the second muon carries only a part of the charmed hadron momentum. For comparison, three different fragmentation function are plotted in the figure. The dot-dash is the sum of the charm Monte Carlo and background predictions using the Peterson function, ϵ = 0.16 (as described in Chapter 6.1.2), the dotted line is the Monte Carlo predictions only using the same function, the solid line is the sum of Monte Carlo and background predictions where a uniform z distribution is used in the Monte Carlo, and the dashed line is obtained using a delta function for the fragmentation, $\delta(z-0.68)$.

In Figs. 6.18 (a) - (c) we plot the z distributions for V^0's, negative tracks and positive tracks in $\mu^-\mu^+$ events only. The solid lines represent the corresponding distributions obtained for charged current events. The distribution for K^0's falls more rapidly for

charged current events, implying a softer source. In charged current events K^0's are produced mainly via associated production and hence have a lower fraction of the hadronic energy, whereas in dimuon events they are produced by the decay of the charmed hadron which carries a large portion of the hadronic energy. The distribution for negative tracks is similar for both charged current and dimuon events. The shaded portion of the plot for positive tracks represents the secondary muon. It seems that the distribution for charged current events falls off faster than for dimuon events, however, the 4 GeV/c cut on the second muon complicates the comparison.

In Fig. 6.19 we present the invariant mass, $M_{\mu\mu}$, plot for the two muons. The small peak at 10 GeV/c^2 is due to a relatively high weight (3.0) event. The larger peak at 6.4 GeV/c^2 is more interesting, since it contains 7 events with roughly the same weight (~ 1.2 - 1.3), whereas we expect 1.4 events. The probability for a fluctuation in this bin is $1*10^{-4}$. If, however, we take into account the number of bins in this plot, and the fact that we have made many different plots (since a peak in any one of them would have been interesting), the significance of this peak becomes small. Also, the error on the invariant mass for most of the muon pairs is large. We note that the fraction of events with $M_{\mu\mu} \geq 5$ GeV/c^2 in the data is 0.31 ± 0.08, whereas the charm Monte Carlo predicts 0.14 ± 0.01. This represents a 2σ effect.

The characteristics of the 8 events with $6 < M_{\mu\mu} \leq 6.7$ GeV/c^2 are shown in table 6.4. We see that all these events typically occur at large values of ϕ (angle between the muons), correspond to large

values of Q^2 and neutrino energy. The mean momentum of the second muon is also larger. All the other kinematic variables have roughly the same values as for the rest of the events. If we look at all events with large values of $M_{\mu\mu}$, say $\geq$ 5 GeV/c^2, we notice that they all have similar characteristics. In table 6.5 we present the average values of the kinematic variables for the events in the peak, all events with $M_{\mu\mu} \geq 5$ GeV/c^2 but not in the peak, and the charm Monte Carlo predictions for events with $M_{\mu\mu} \geq 5$ GeV/c^2 (only statistical errors are shown). We see that all three categories have large values of ϕ, Q^2, E_ν and $P_{\mu 2}$. This leads us to believe that the enhancement at large $M_{\mu\mu}$ is a kinematic effect, rather than a signal for the decay of a new particle. The transverse momenta of the primary muon, with respect to all the non-muon particles in the event i.e., the hadronic shower, is much larger than that of the secondary muon, suggesting that the latter is associated with the hadronic shower, whereas the former is not. In high energy collisions one would expect events with large Q^2 which could lead to the hadronic system coming off at a sharp angle with respect to the neutrino direction, thus producing a large angle between the two muons. One must, however, point out that a large value of ϕ could also be obtained in the decay of a single particle, which is travelling almost parallel to the neutrino direction.

As argued above, the excess of events in the $M_{\mu\mu}$ plot is probably a statistical fluctuation. The data from a high statistics counter experiment[13] in the same neutrino beam is being analyzed currently, and their results will provide an independent check. None of the

previous neutrino experiments (at lower energies), studying opposite sign dimuons, have reported any such excess.

In summary, we conclude that the opposite sign data is in reasonable agreement with the charm hypothesis and with results from previous experiments.

6.4.2 Like-Sign Dimuons (LSD)

6.4.2.1 Rates

We now turn to the like-sign data. The results are presented in table 6.6. The background is taken from Table 4.8, and the detection efficiency is taken from Chapter 5. The data is consistent with background at all energies . The 90% confidence level upper limit for $\mu^-\mu^-/\mu^-$ is $1.2*10^{-3}$, and on the basis of 1 $\mu^+\mu^+$ event we set the 90% C.L. upper limit for $\mu^+\mu^+/\mu^+$ at $2.5*10^{-3}$. We divide the $\mu^-\mu^-/\mu^-$ result into two bins, and the 90% C.L. upper limit for $E_\nu < 200$ GeV is $6.4*10^{-4}$, whereas this limit for $E_\nu \geq 200$ GeV/c is $5.0*10^{-3}$. Since we have 7 $\mu^-\mu^-$ events with $E \geq 200$ GeV, with an expected background of 4.3 ± 1.3 we also quote a rate for this energy bin. The corresponding rate for $\mu^-\mu^-/\mu^-$ for $E_\nu \geq 200$ GeV is $(1.7\pm1.9\pm0.3)*10^{-3}$. The first error includes the statistical error and the error due to background estimation techniques (the latter being 1/2 of the statistical error), whereas the second is the systematic error due to the uncertainty in the number of charged current events in various energy bins (see Chapter 6.3 for the origin of the second error). One

must remember that both the upper limit and the rate in the highest energy bin are consistent with zero. These results are consistent with previous upper limits[14]. See Fig. 6.20 for a comparison with other experiments. Even though our upper limits are higher than the results from counter experiments, one must point out that the counter experiment results have often been wrong in the past (see Chapter 1.6.2 for a discussion).

We observe one neutral strange particle (K^0) in the like-sign sample. The raw V^0 rate per dimuon event is 8.3±8.3%, which is consistent with the raw V^0 rate in charged current events (8.5±1%), and with the rate in background events (6.7±1.5%).

6.4.2.2 Kinematic Distributions

As mentioned earlier, we will compare the kinematic distributions for the like sign data with background predictions. We use the same factors as before, to correct for the missing neutrals in the data sample and background events. In the following plots the full histogram corresponds to the data, and the solid line corresponds to the background predictions. As before, the primary and secondary muons are chosen on the basis of their momentum, transverse to all the non-muon particles in the event. In all but one case the primary muon's transverse momentum is greater than that of the secondary muon by at least 2 GeV/c.

The mean of the kinematic distributions is shown in table 6.7, and some of the kinematical quantities for each event are displayed in

table 6.8. The data seems to have slightly higher mean values for $E_{\mu 1}$, E_{ν} and the mass of the hadronic system recoiling against the primary muon. All other variables show very good agreement with background predictions.

In Figs. 6.21 and 6.22 we show the plots for energy of the primary and the secondary lepton. The agreement with background is very good. In Fig. 6.23 we present the distribution of the neutrino energy. One should notice that there are no events with $E_{\nu} < 100$ GeV, whereas the background calculation predicts that we should see 3.0 ± 1 events. The probability of such an occurrence is 2-14% (the range reflects the uncertainty in the background).

Fig. 6.24 shows the distribution for Q^2. The agreement with background is very good. In Fig. 6.25 we show the distribution of the invariant mass, W, of the hadronic system. We notice that there is a lack of events for $W < 10$ GeV/c^2. In Figs. 6.26 and 6.27 we show the distributions for Bjorken x and Bjorken y. The data is consistent with background. In Figs. 6.28, 6.29, 6.30 and 6.31 we show the distributions for transverse momentum of the secondary muon perpendicular to the μ_1-ν plane, angle between the two muons projected on a plane perpendicular to the neutrino direction, fraction of the hadronic energy carried off by the second muon, and the invariant mass of the two muons. All the distributions are in remarkable agreement with background predictions.

6.4.3 Trimuons

We do not observe any trimuons in our event sample. This corresponds to a raw 90% confidence level upper limit (on the $\mu^-\mu^-\mu^+/\mu^-$ rate) of $2.1*10^{-4}$, for $P_\mu \geq 4$ GeV/c. The raw limit is consistent with the results of previous experiments (see Chapter 1.6.3. for a discussion of this point), and after taking into account the detection efficiencies and the effect of various cuts, this limit will only increase. Thus, our results are compatible with previous experiments.

References

1) John Wills, Internal Report IR-47-79, University of Hawaii at Manoa, March 1979 (unpublished).
C. Ballagh et al., 1981, Ref. 27, Chapter 1.

2) H. Abramowicz et al., 1982, Ref. 26, Chapter 1.

3) D.C. Carey, 1975, Ref. 1, Chapter 2.

4) H.E. Fisk, Proc. of the Intl. Symposium on Lepton and Photon Interactions at High Energies, Bonn, August 24 - 29, 1981.

5) J. Blietshceau et al., Phys. Lett. 86B, 108 (1979).

6) C. Peterson et al., Phys. Rev. D27, 105, (1983).

7) J. Dorfan, Proc. of the Intl. Symposium on Lepton and Photon Interactions at High Energies, Cornell, August 4 - 9, 1983.

8) H. Abramowicz et al., 1982, Ref. 26, Chapter 1;
E. Thorndike, Proc. of the Intl. Symposium on Lepton and Photon Interactions at High Energies, Kyoto, August 19 - 24, 1985.

9) V. Barger and R.J.N. Phillips, Phys. Rev. D14, 14 (1976).

10) Refs. 26 and 27 in Chapter 1.

11) In C. Ballagh et al., 1981, Ref. 27 Chapter 1, 8 K^0's and 2 Λ's were observed, thus, a 80% probability is assigned to the ambiguous V^0.

12) C. Ballagh et al., 1980, Ref. 26 Chapter 1;
M.D. Sokoloff, 1983, Ref. 9 Chapter 1.

13) F. Merritt, Univ. of Rochester preprint, 1987, Ref. 39 Chapter 1.

14) Ref. 39 in Chapter 1.

15) Ref. 3 in chapter 4.

Table 6.1. Opposite sign dimuon results.

	$\mu^-\mu^+$	$\mu^+\mu^-$
Event Sample	44	8
Background	12.0±2.5	2.1±0.4
Net Signal	32.0±7.2	5.9±2.6
Signal corrected for detection efficiencies & selection procedure	71.2±15.1	10.3±5.5
Corrected number of charged current events	11130	2172
Dimuon rate per charged current event	0.64±0.14%	0.47±0.25%

Table 6.2. Characteristics of V^0's

Event	Type	V^0 type	χ^2 for K (3-C)	χ^2 for Λ (3-C) hypothesis	Wt. Fitted Mom. (GeV/c)		M $\mu 2V$ (GeV/c^2)	No. of life-times
2242 320	$\mu^- \mu^+$	Λ		1.7	0.00	2.5	2.86	0.02
2256 104	$\mu^+ \mu^-$	K^0	2.3		2.36	20.3	1.21	0.10
2277 578	$\mu^+ \mu^-$	Λ	14.3	1.1	1.46	2.8	3.30	0.36
2283 11	$\mu^- \mu^+$	K^0	3.3		1.55	6.0	1.31	0.19
2313 871	$\mu^+ \mu^-$	Λ	6.0	0.4	4.59	3.1	2.70	0.14
23161895	$\mu^- \mu^+$	Λ	3.3	2.9	4.34	39.2	1.83	0.12
23271207	$\mu^- \mu^+$	K/Λ	0.4/1-C	0.3/1-C	1.57/ 1.64	4.3	2.20	1.51/ 1.1
23321255	$\mu^- \mu^+$	Λ		6.7	1.76	0.6	3.40	1.4

Table 6.3. Characteristics of opposite sign events.

Sample (weighted)	Dimuon	Background (Wt)	Dimuon Mean (Wt)	Dimuon Monte Carlo	Charged Current Mean (Wt)
$E_{\mu 1}$ (GeV)	69.8±9.5	73.3±6.3	68.9±11.0	75.0±2.2	74.8±2.8
$E_{\mu 2}$ (GeV)	20.6±2.9	21.9±2.0	20.2±3.5	20.2±0.7	
E_{ν} (GeV)	168±13	187±10	162±14	172±3	141±4
γ	0.36±0.06	0.44±0.03	0.33±0.07	0.45±0.01	
β	0.75±0.16	0.68±0.10	0.77±0.18	0.64±0.03	
x	0.19±0.02	0.17±0.01	0.20±0.02	0.16±0.01	0.17±0.01
y	0.62±0.03	0.60±0.02	0.63±0.03	0.57±0.01	0.49±0.01
W (Gev/c^2)	11.6±0.6	12.4±0.3	11.3±0.6	11.6±0.2	9.6±0.2
Q^2 (GeV/c)^2	33.2±5.2	30.8±3.5	34.0±5.8	28.9±1.3	20.6±1.1
$M_{\mu\mu}$ (GeV/c^2)	3.6±0.4	3.2±0.2	3.7±0.4	3.0±0.1	
Φ (deg)	128±6.5	134±4	126±7	135±2.0	135±1*
$P^{\mu 2}_{\mu 1-\nu}$	0.36±0.04	0.34±0.02	0.37±0.05	0.30±0.0	0.31±0.1*
Charged Mult.	8±0.5	7.9±0.3	8±0.6		6.7±0.1
$z_{\mu 2}$ [Peterson] [fn]	0.23±0.02	0.24±0.01	0.23±0.02	0.23±0.00	

Table 6.4. Characteristics of events with 6 $\leq_{\mu\mu}$ $\leq$6.7 GeV/c^2.

Roll/ → Frame	2231/ 957	2279/ 420	2310/ 1606	2311/ 484	2316/ 1895	2322/ 1112	2323/ 765	2327/ 418
$E_{\mu 1}$ (GeV)	109±19	210±21	19±0.5	135±49	34±3	15±1	52±1	53±12
$E_{\mu 2}$ (GeV)	19±1.4	24±0.5	31±1.4	18±1	65±14	124±30	20±0.3	43±9
$M_{\mu\mu}$	6.1±2.3	6.4±1.2	6.1±0.4	6.0±4	6.3±3	6.5±2.6	6.7±0.3	6.1±4
E_{ν} (GeV)	200±20	362±23	117±6	258±49	263±14	337±19	103±3	118±12
Q^2(GeV/c)^2	7.2	98.0	90.0	27.0	112	98.0	44.0	14.6
W (GeV/c^2)	12.8	13.7	9.7	14.0	17.8	17.8	7.1	10.4
Φ (deg)	175	175	176	157	158	179	173	173
x	0.04	0.34	0.49	0.12	0.26	0.16	0.47	0.12
$P_{T(\text{non-muon})}^{\mu 1}$	1.54	16.0	4.80	6.96	4.2	2.20	9.7	13.9
$P_{T(\text{non-muon})}^{\mu 2}$	1.23	0.50	0.31	1.45	1.3	0.35	1.0	6.7
$P_{T\ (\mu 1-\nu)}^{\mu 2}$	0.20	0.12	0.12	0.67	0.57	0.02	0.27	0.45
$z_{\mu 2}$	0.21	0.16	0.31	0.12	0.38	0.38	0.39	0.66

Table 6.5. Comparison of opposite sign events with Monte Carlo for events with $M_{\mu\mu} \geq 5$ GeV/c^2.

	Events with $6 \leq M_{\mu\mu} \leq 6.7$ (Wt. mean)	Events with $M_{\mu\mu} \geq 5$ GeV/c^2 but not in peak (Wt. mean)	Monte Carlo predictions for events with $M_{\mu\mu} \geq 5$ Gev/c^2
$E_{\mu 1}$ (GeV)	80±24	138±32	117±7
$E_{\mu 2}$ (GeV)	41±13	43±10	36±2
$M_{\mu\mu}$ (GeV/c^2)	6.3±0.2	7.4±0.7	6.4±0.1
E_{ν} (GeV)	218±35	260±40	241±8
Q^2 (GeV/c)^2	61±15	63±20	60±4
Φ (deg)	171±3	169±5	167±1
$z_{\mu 2}$	0.32±0.06	0.39±0.06	0.31±0.01
$P_{T\mu 1-\nu}^{\mu 2}$	0.30±0.08	0.31±0.11	0.33±0.02
x	0.25±0.06	0.30±0.06	0.30±0.01
y	0.63±0.08	0.46±0.09	0.50±0.02
W (GeV/c^2	13.4±1.6	11.9±1.9	11.6±0.4

Table 6.6. Like-sign dimuon results.

	$\mu^-\mu^-$	$\mu^+\mu^+$
Event sample	11	1
Background	9.6±1.8	0.8±0.2
Net sample	1.4±3.8	0.2±1.0
Corrected number of charged current events	11130	2172
90% confidence level upper limits (per charged current event)	$1.2*10^{-3}$	$2.5*10^{-3}$

Table. 6.7. Characteristics of like-sign events.

	Event Sample (weighted)	Background sample (weighted)
$E_{\mu 1}$ (GeV)	103±19	77±7
$E_{\mu 2}$ (GeV)	16.4±3.2	17.4±2.2
E_{ν} (GeV)	235±25	189±11
Q^2 $(GeV/c)^2$	34.9±10	39.1±3.7
W (GeV/c^2)	14.1±1.0	12.2±0.5
$M_{\mu\mu}$ (GeV/c^2)	2.9±0.5	3.2±0.2
x	0.16±0.05	0.20±0.02
y	0.58±0.05	0.59±0.02
Φ (deg)	126±14	136±5
$P_{T\ \mu 1-\nu}^{\mu 2}$ (GeV/c)	0.33±0.08	0.28±0.03
Charged multiplicity	9.8±1.7	9.1±0.4
$z_{\mu 2}$	0.14±0.03	0.17±0.01

Table 6.8. Details of individual like-sign events.

Event	Potential length (cm)	$P_{\mu 1}$ (GeV/c)	$P_{\mu 2}$ (GeV/c)	E_{vis} (GeV)	$P^{T}_{\mu 1}$ * (GeV/c)	$P^{T}_{\mu 2}$ * (GeV/c)
2237076601	200	104.0	34.1	238.0	5.4	0.4
2239030102	117	19.0	17.2	100.0	3.5	0.8
2243021401†	192	112.0	18.9	225.0	2.5	0.3
2255084201	116	125.0	5.0	191.0	9.6	0.2
2260076701	256	170.0	10.5	278.0	3.3	0.4
2270089301	170	103.0	36.5	225.0	10.6	0.8
2271104701	294	99.0	8.4	266.0	2.8	0.5
2281098801	130	28.0	8.6	94.0	3.1	0.5
2300123201	253	209.0	7.8	308.0	20.2	0.6
2327119501	201	177.0	36.8	348.0	5.9	2.2
2333006802	121	77.0	23.5	125.0	7.9	2.6
2333087201	107	8.8	5.8	135.0	1.8	0.8

* momentum transverse to all other tracks in event

† $\mu^+\mu^+$ event

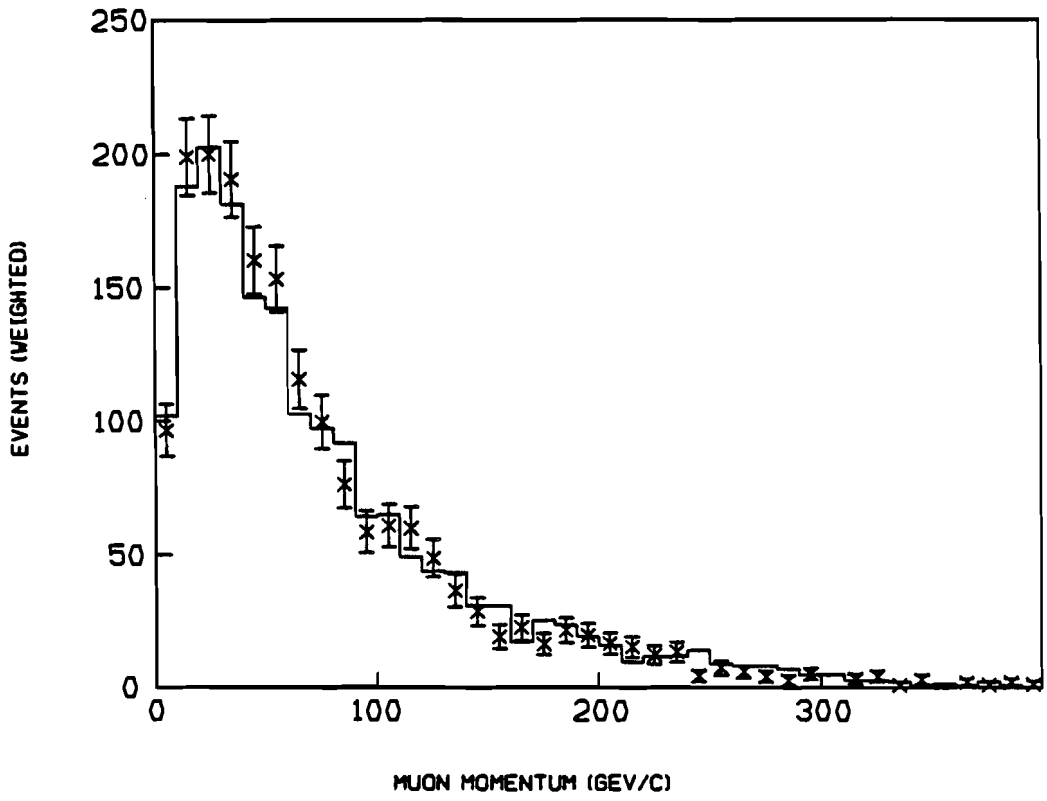

Fig. 6.1. μ^- momentum (GeV/c) for data (crosses) and neutrino Monte Carlo (histogram). The data corresponds to 1790 μ^- in an unbiased event and leaving track sample. The data is weighted by its electronic acceptance.

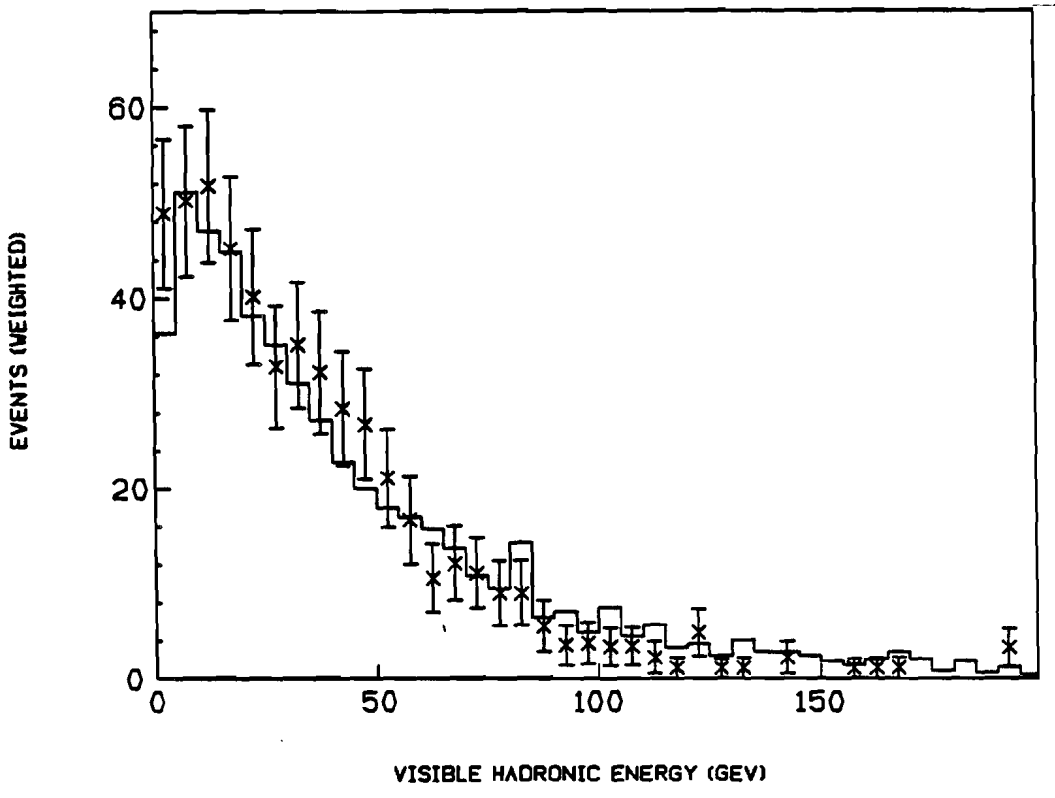

Fig. 6.2. Visible hadronic energy (GeV) in ν induced events for data (crosses) and the neutrino Monte Carlo (histogram). Data corresponds to 500 ν events, taken from an unbiased event sample. The data is weighted by its electronic acceptance.

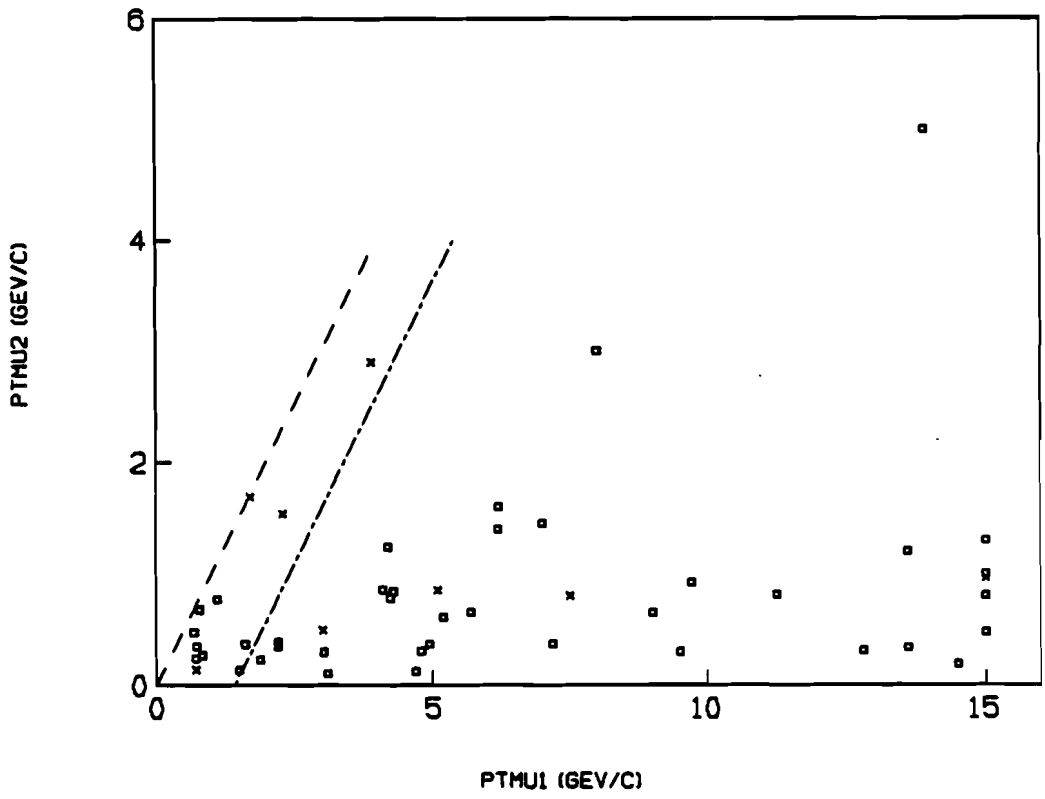

Fig. 6.3. Transverse momentum (GeV/c) of the two muons in opposite sign events with respect to all other particles in the event. The muon with the larger value of P_T is chosen as the primary muon. Squares indicate $\mu^-\mu^+$ events, and crosses $\mu^+\mu^-$ events. Primary muon momentum is along X - axis.

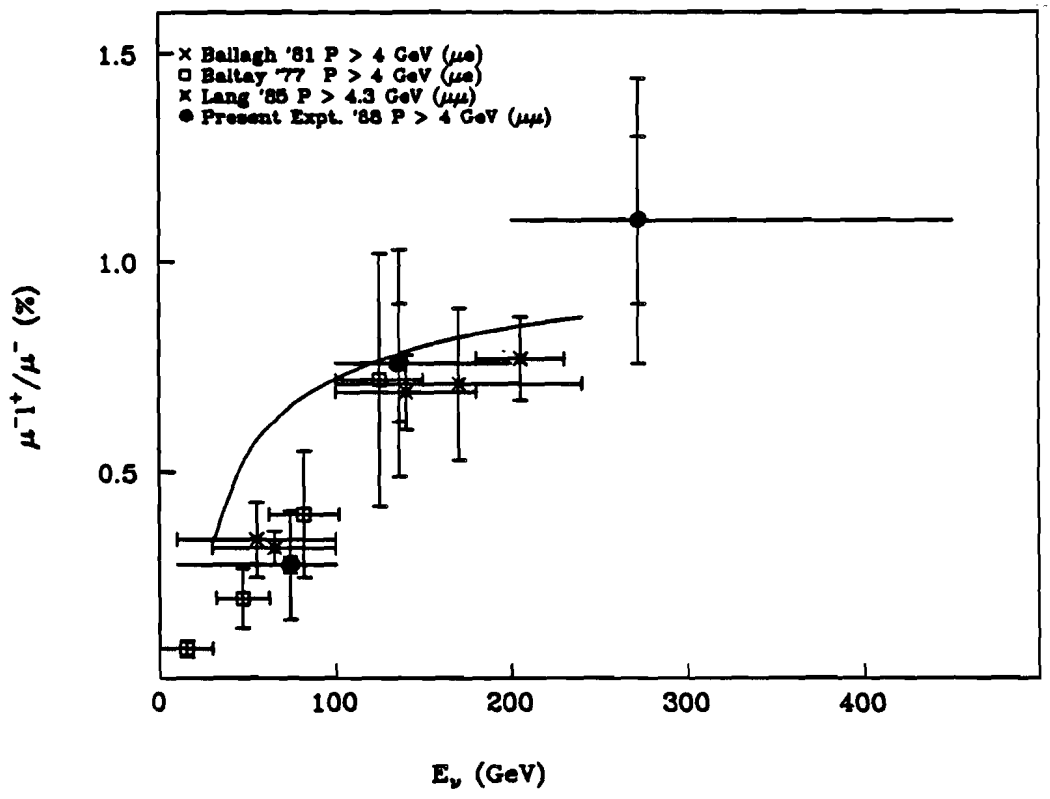

Fig. 6.4a. $\mu^- l^+/\mu^-$ rate as a function of neutrino energy (Gev).

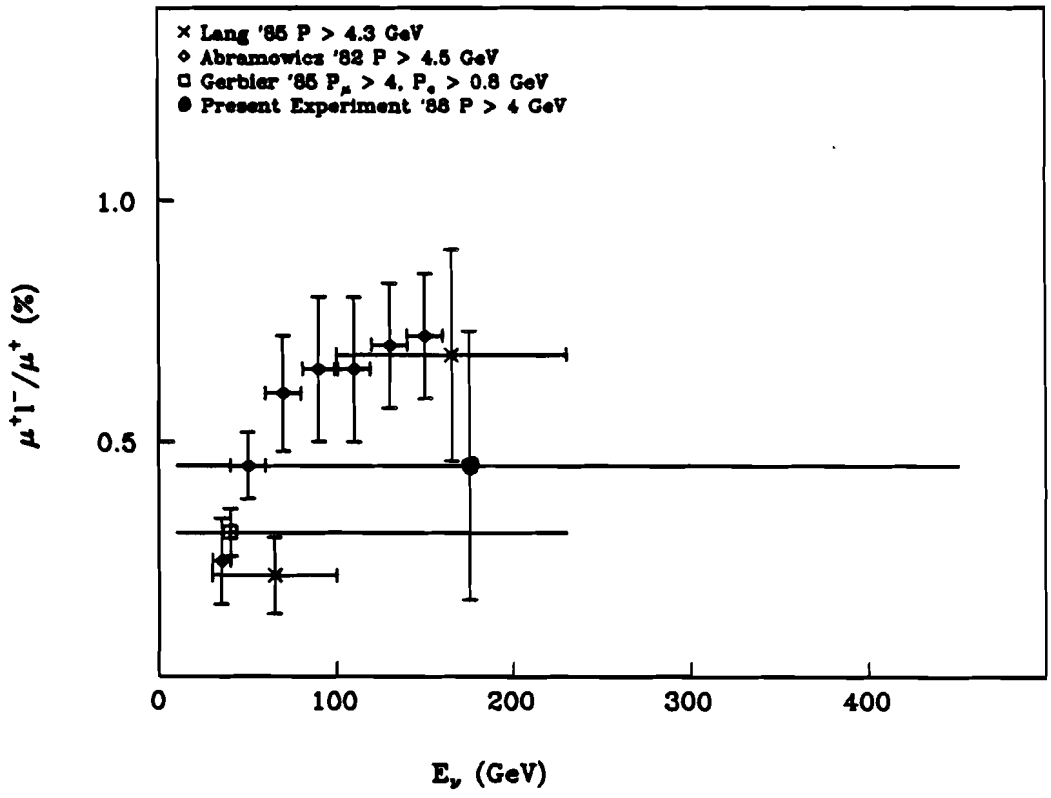

Fig. 6.4b. μ^+l^-/μ^+ rate as a function of anti-neutrino energy(GeV).

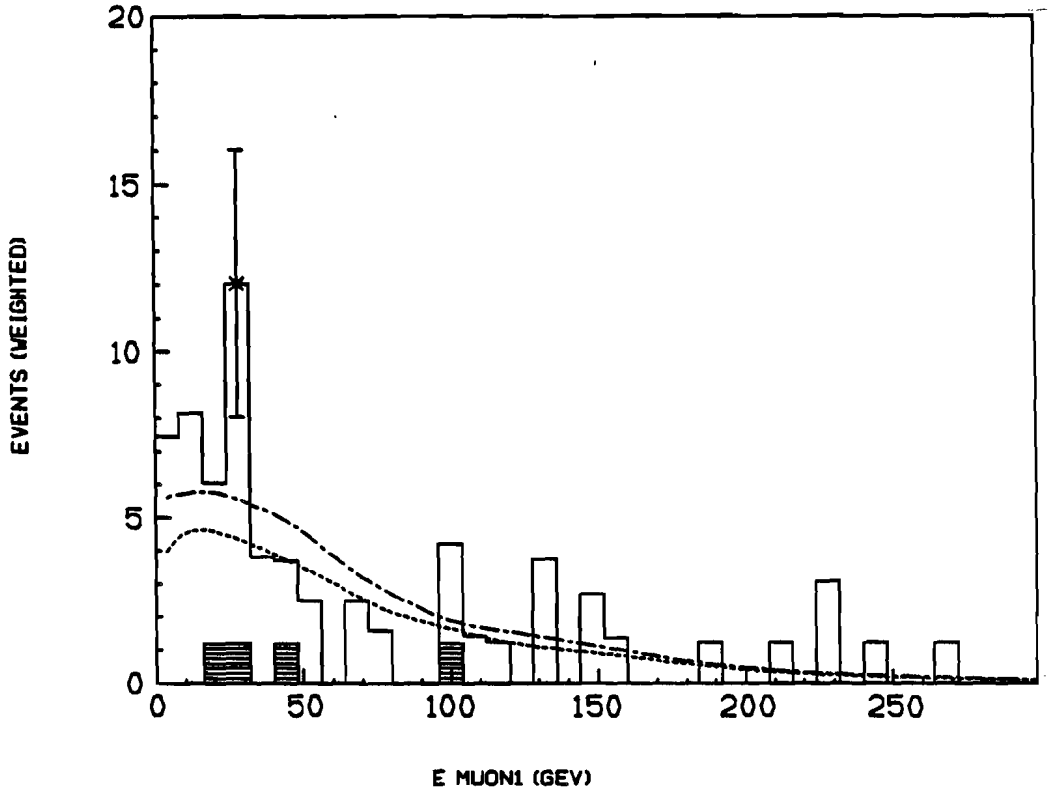

Fig. 6.5. Energy (GeV) of the primary muon in opposite sign events. The Y axis corresponds to the number of opposite sign events (wieghted for geometrical and instrumental acceptance). The dotted curve is the Monte Carlo predictions for opposite sign events (normalized to the netdimuon signal), and the dot-dash curve is the sum of Monte Carlo and background predictions (the latter normalized to the total number of background events in the sample). The anti-neutrino events are shown shaded. The same convention is followed in Figs. 6.5 through 6.19.

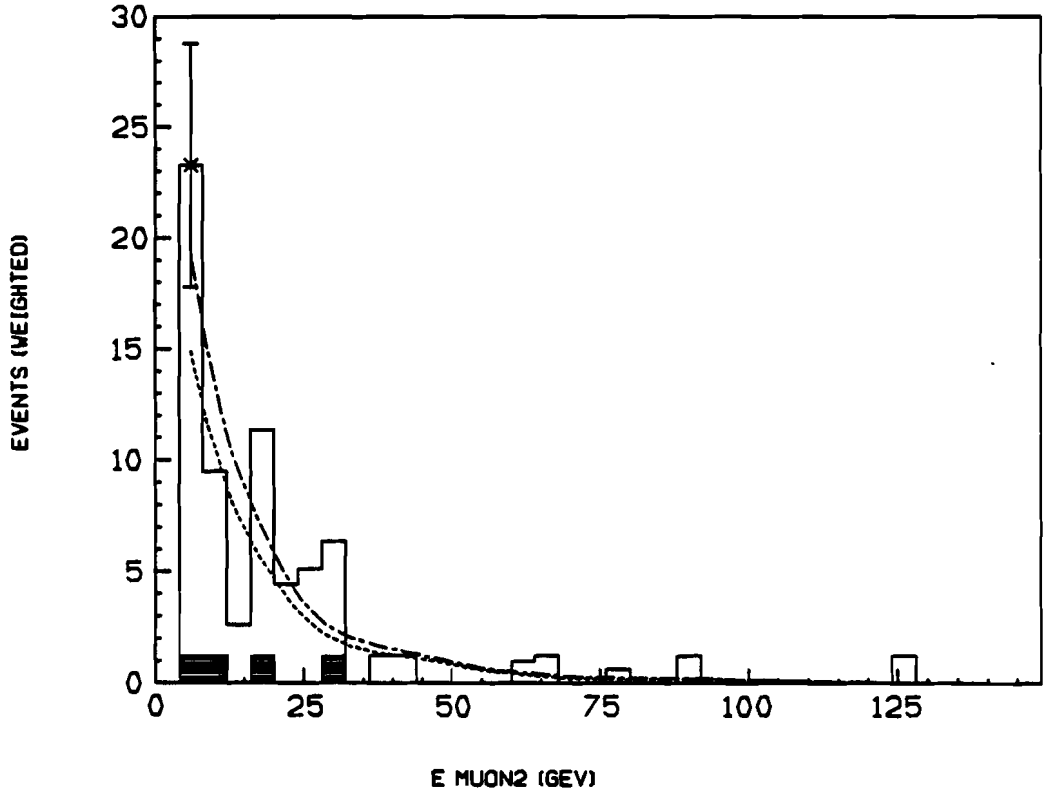

Fig. 6.6. Energy (GeV) of the secondary muon in opposite sign events.

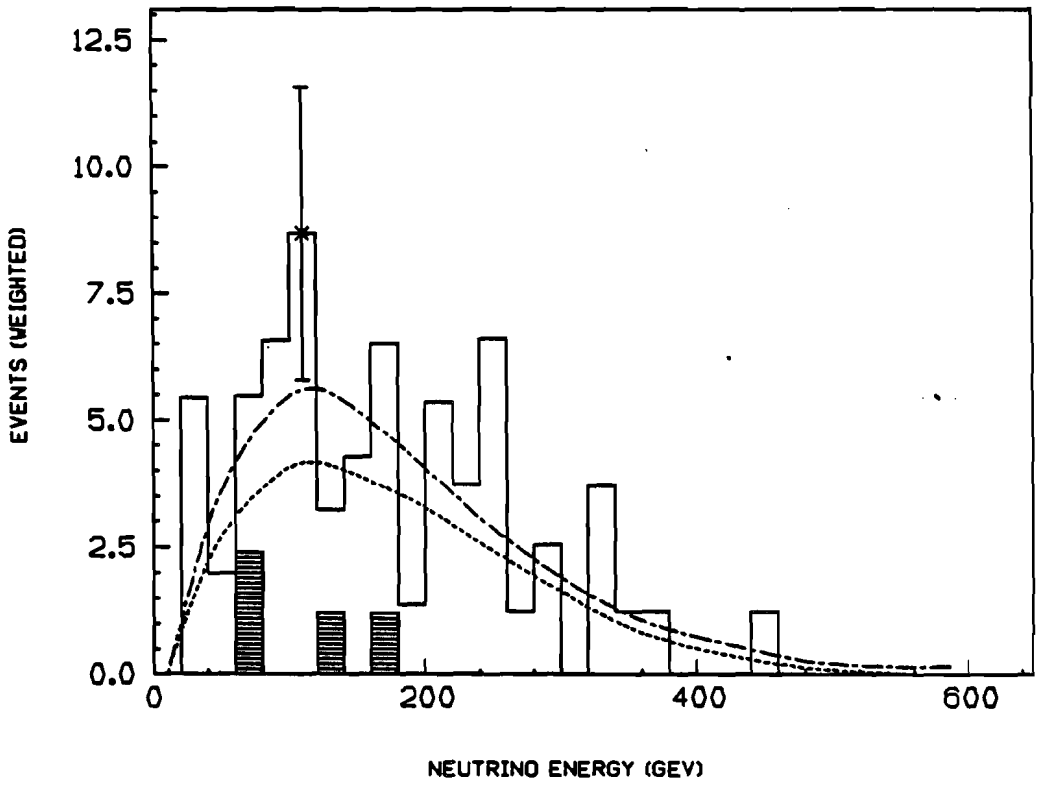

Fig. 6.7. Neutrino energy (GeV) for opposite sign events.

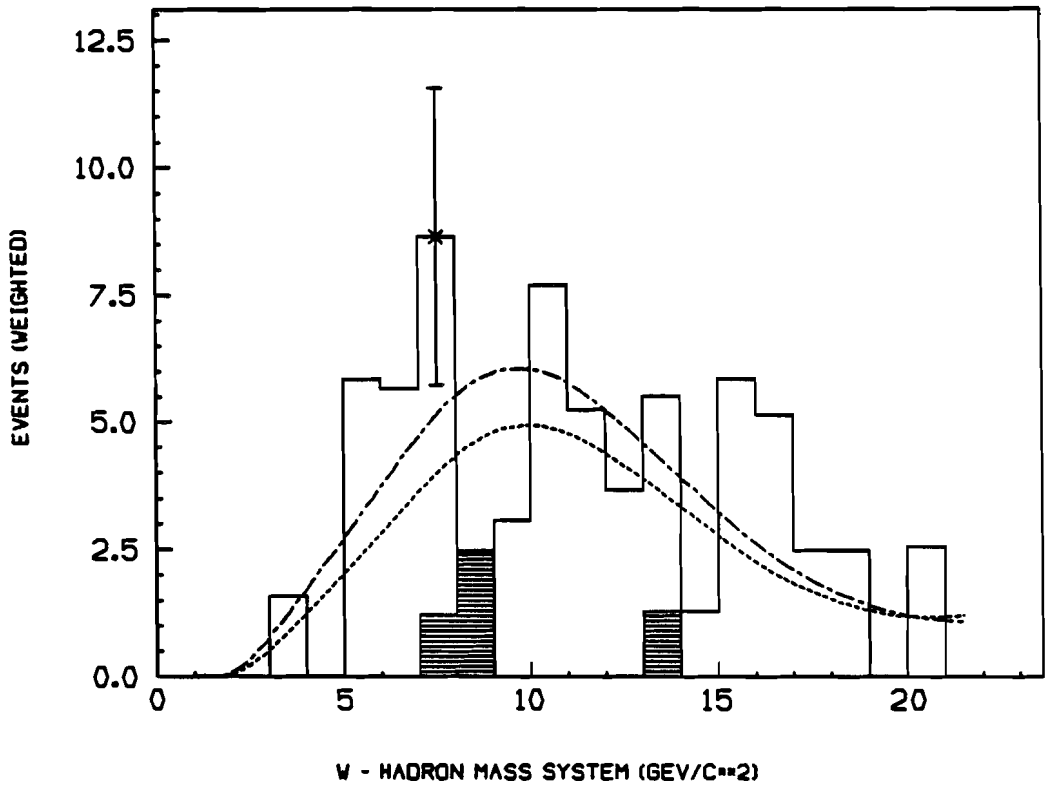

Fig. 6.8. The invariant mass (GeV/c^2) of the hadronic system recoiling against the primary muon, in opposite sign events.

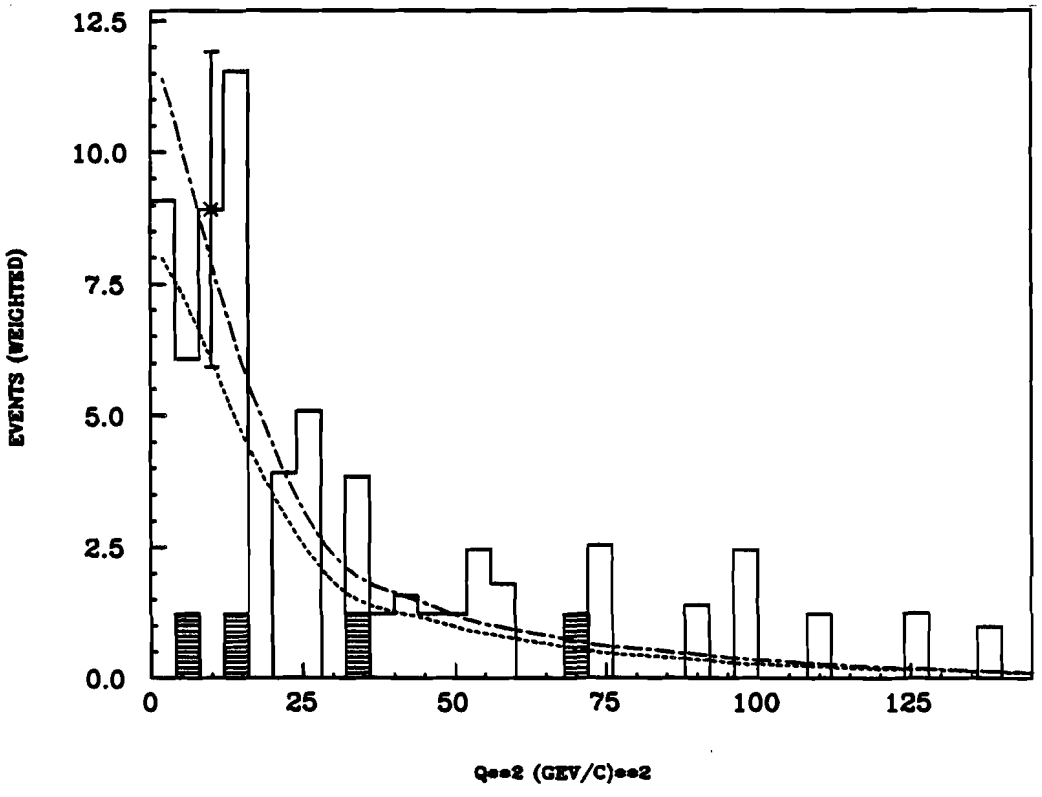

Fig. 6.9. The 4-momentum transfer squared $(GeV/c)^2$ in opposite sign dimuon events.

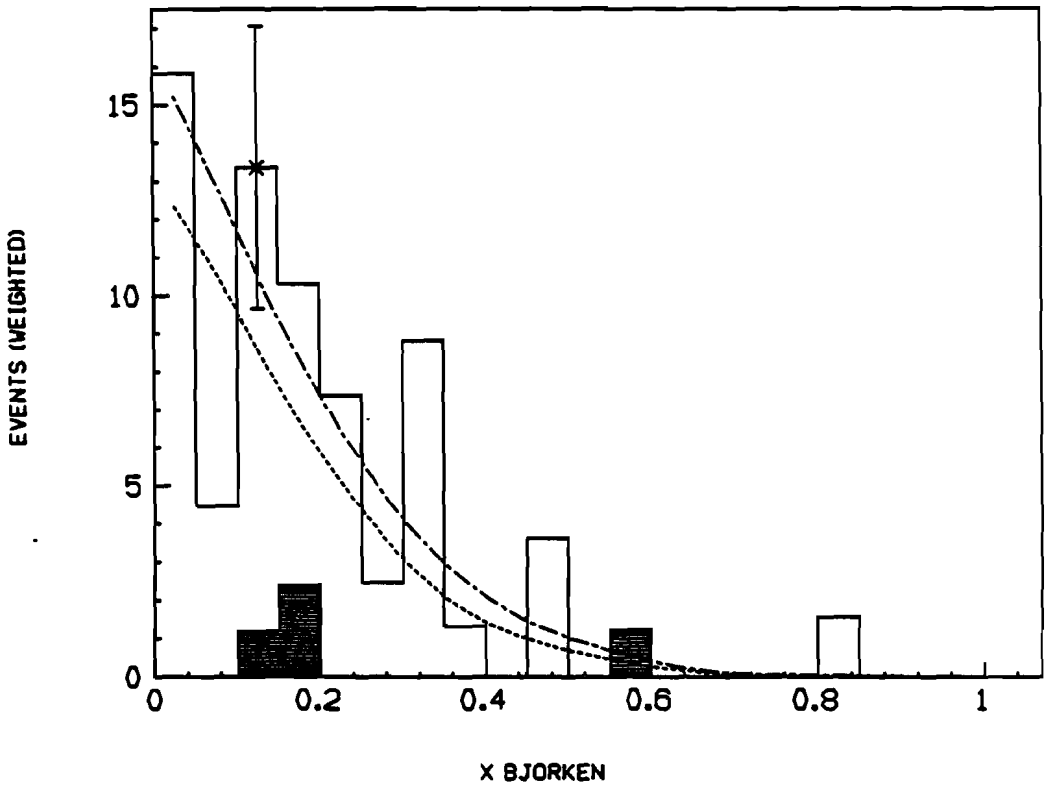

Fig. 6.10. Bjorken x distribution for opposite sign dimuon events.

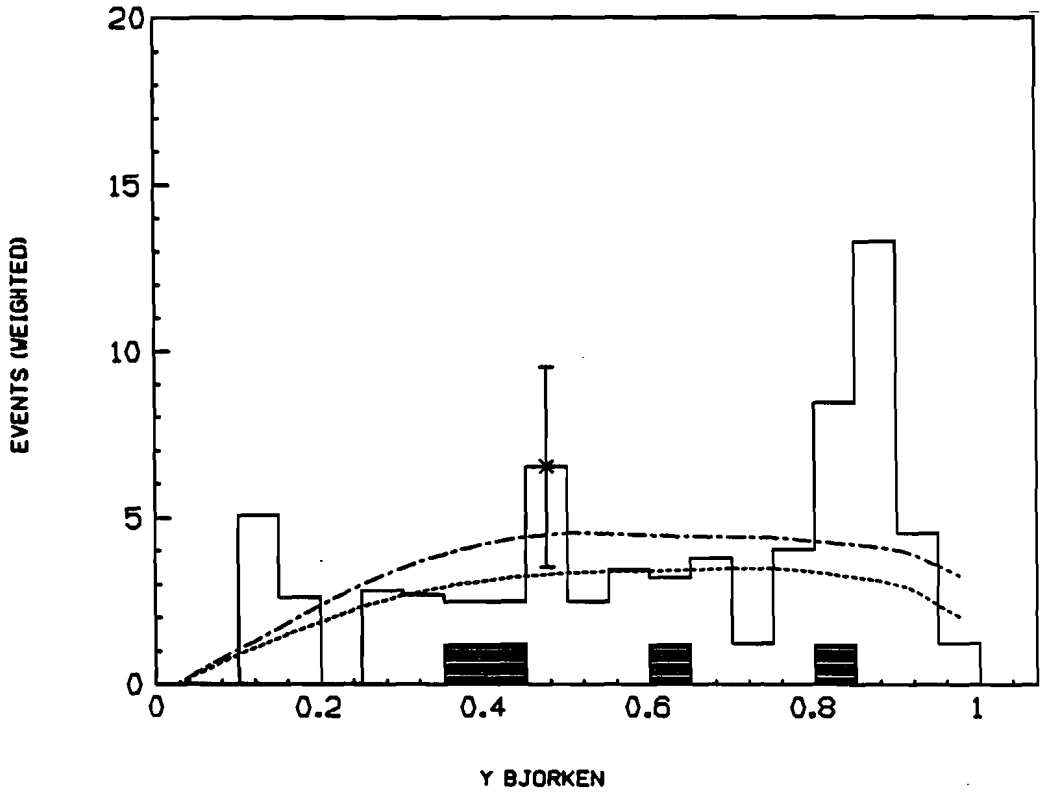

Fig. 6.11. Bjorken y distribution for opposite sign dimuon events.

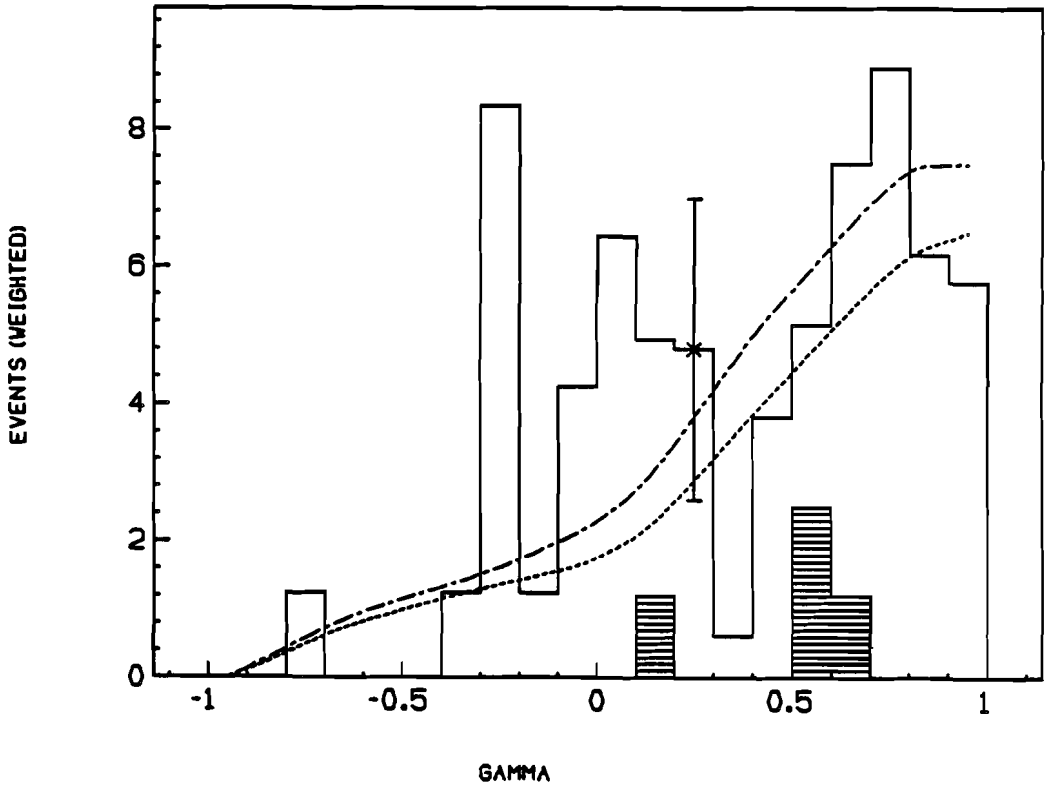

Fig. 6.12. The assymetry, $\gamma = (E_{\mu 1}-E_{\mu 2})/(E_{\mu 1}+E_{\mu 2})$, for opposite sign dimuon events.

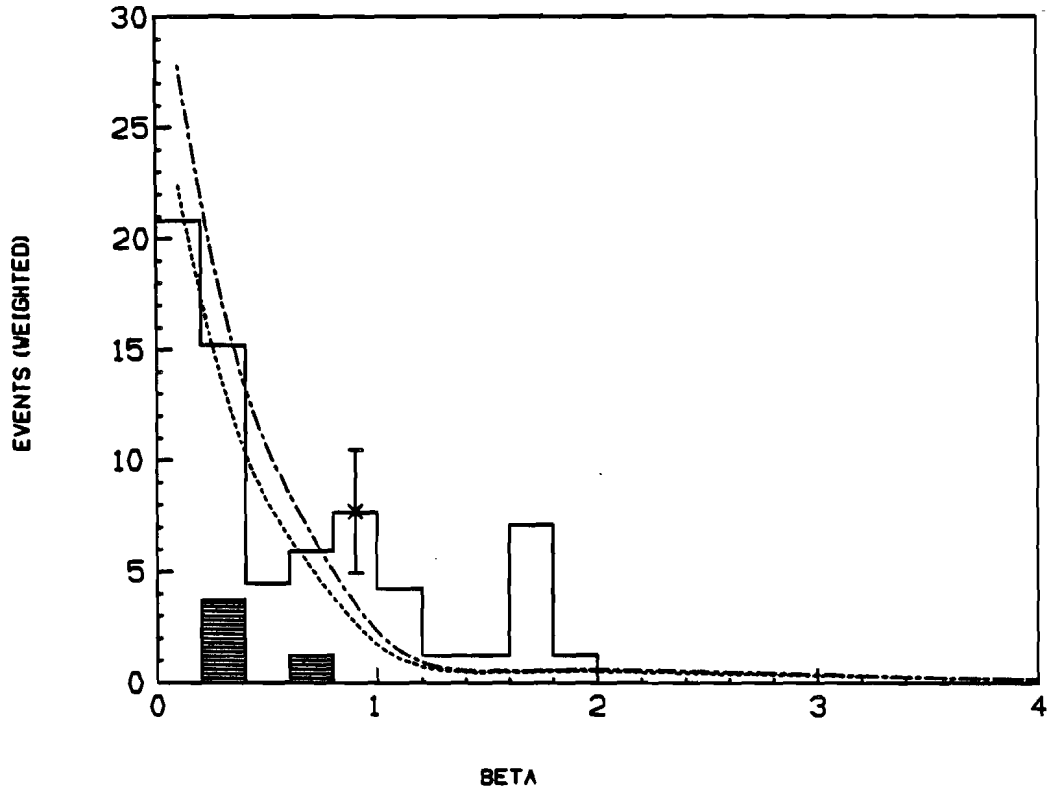

Fig. 6.13. The ratio, $\beta = E_{\mu 2}/E_{\mu 1}$, for opposite sign dimuon events.

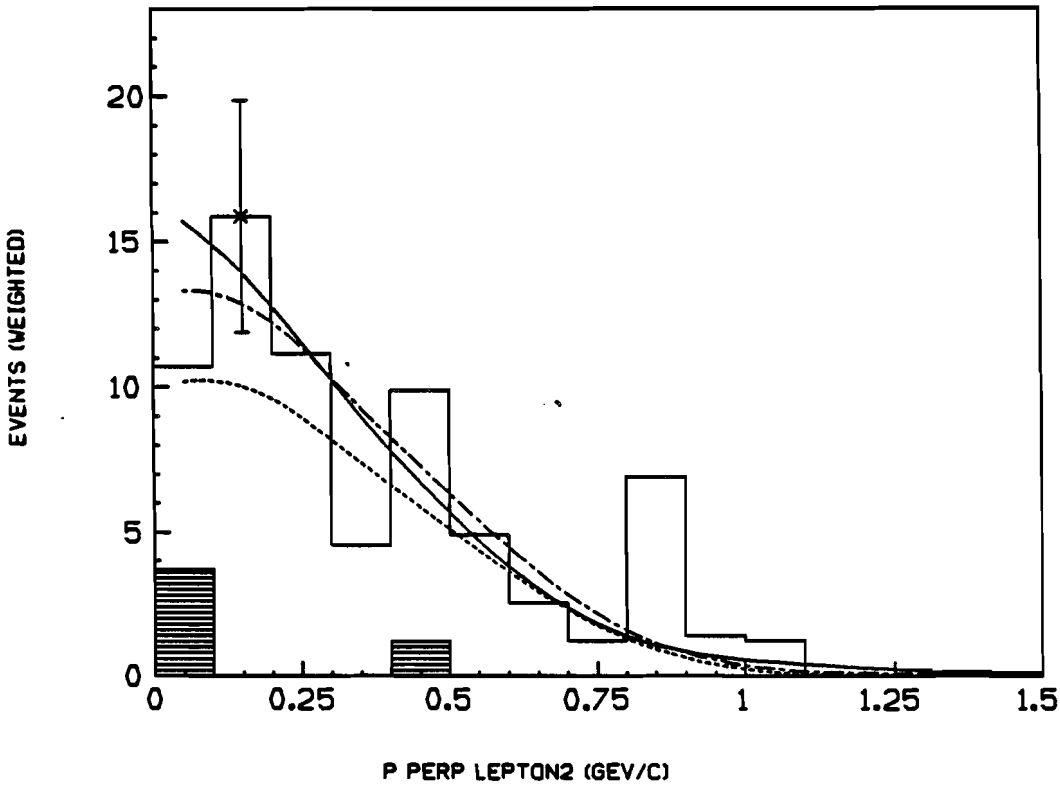

Fig. 6.14. The momentum (GeV/c) of the second muon in a direction perpendicular to the plane formed by μ_1 and the incident ν (for opposite sign dimuon events).

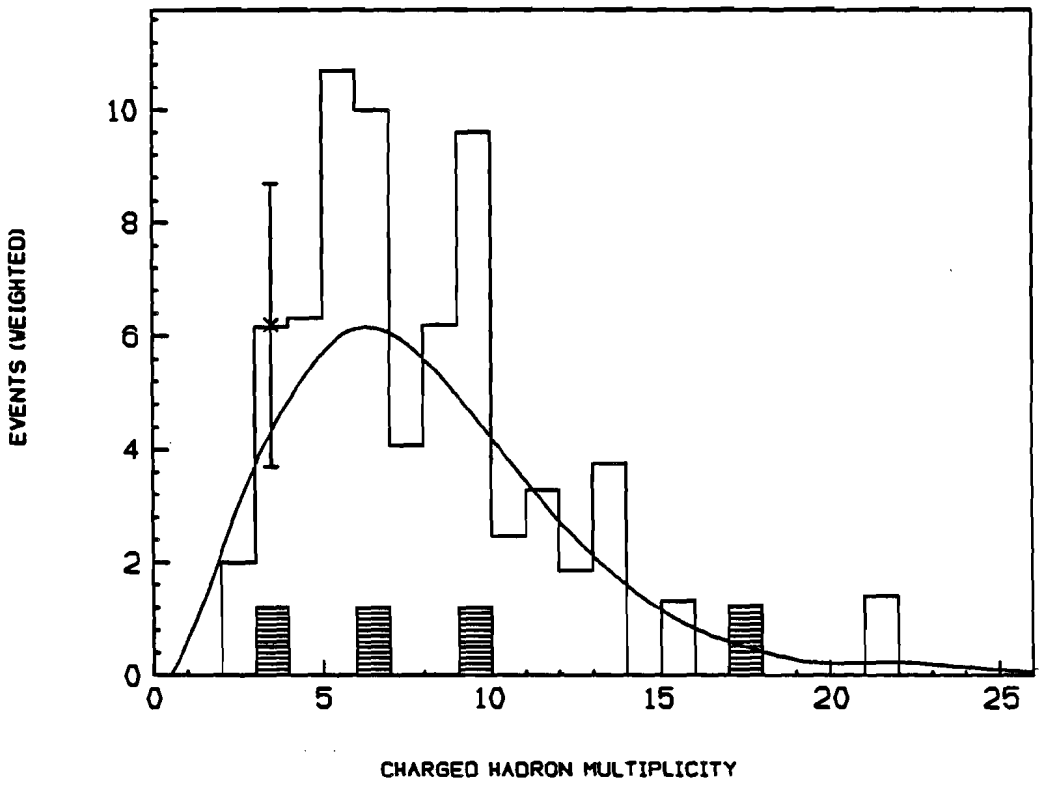

Fig. 6.15. The charged hadron multiplicity in opposite sign events. The solid line correponds to the unbiased charged current sample.

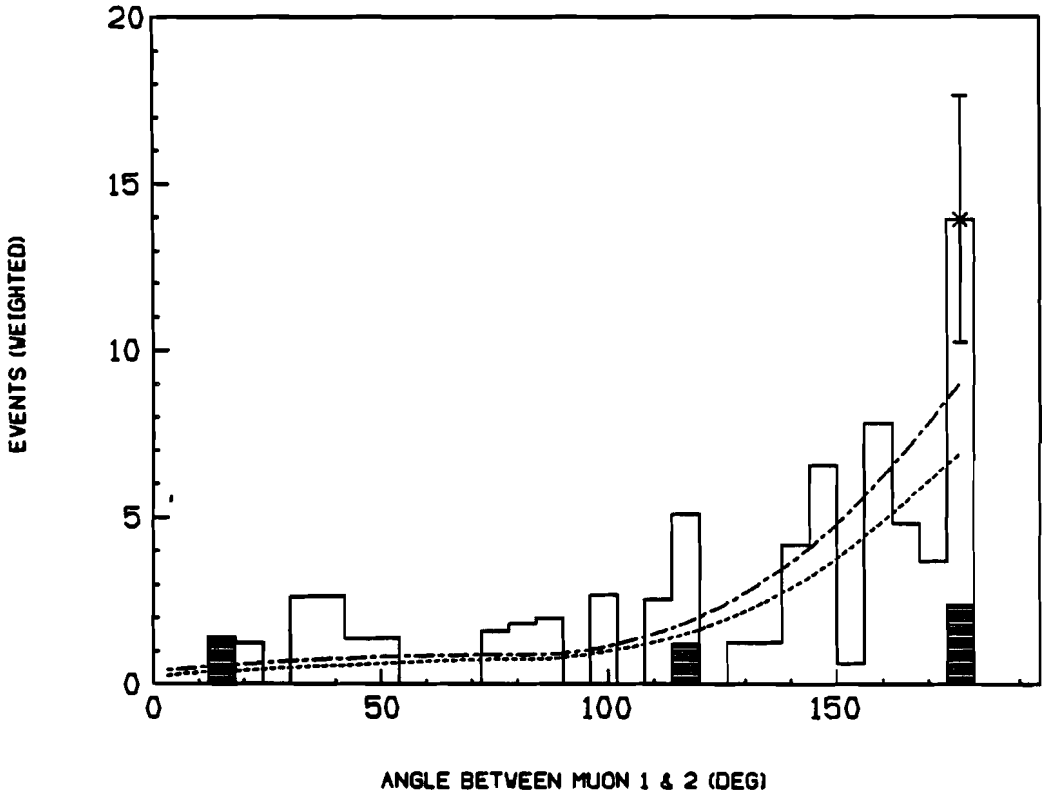

Fig. 6.16. The angle, Φ (deg), between the two muons, projected on a plane perpendicular to the neutrino direction (for opposite sign dimuon events).

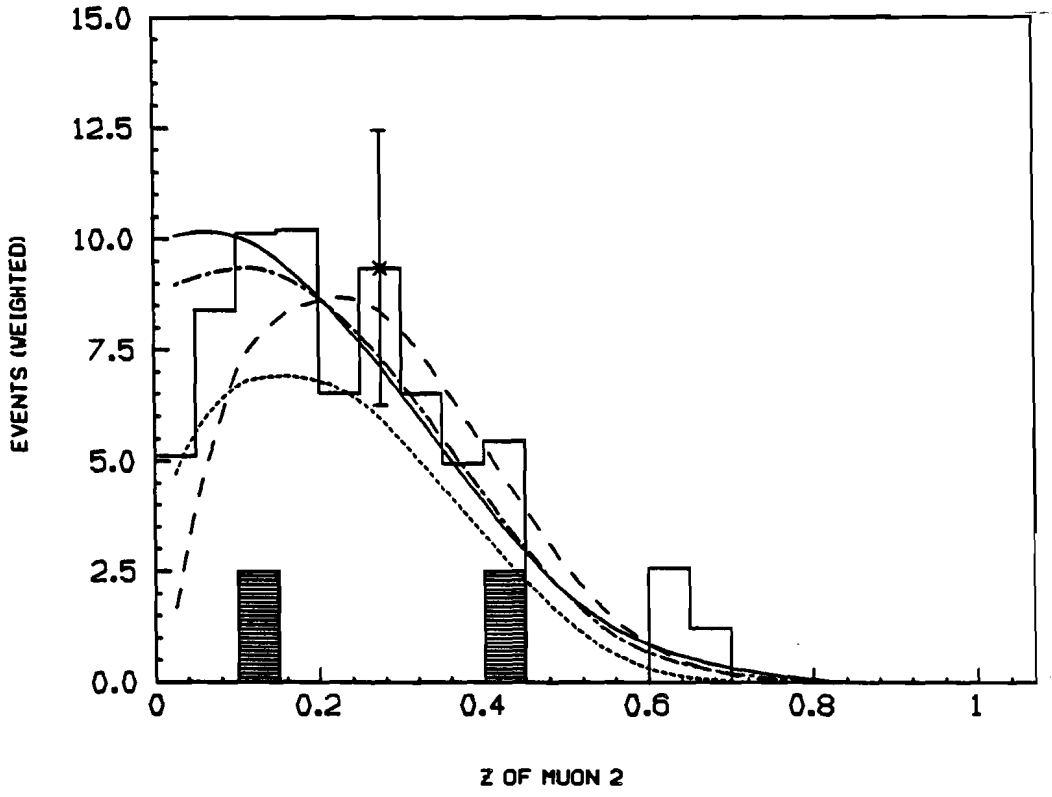

Fig. 6.17. The fraction, $z_{\mu 2}$, of the hadronic energy carried by the second muon, in opposite sign events. $z_{\mu 2} = E_{\mu 2}/(E_{\mu}-E_{\mu 1})$. The dot and dot-dash correpond to the Peterson function for the charm fragmentation function, whereas the solid line corresponds to the sum of Monte Carlo and background predictions for a uniform z distribution, and the dashed line corresponds to Monte Carlo plus background for a delta function, $\delta(z-0.68)$.

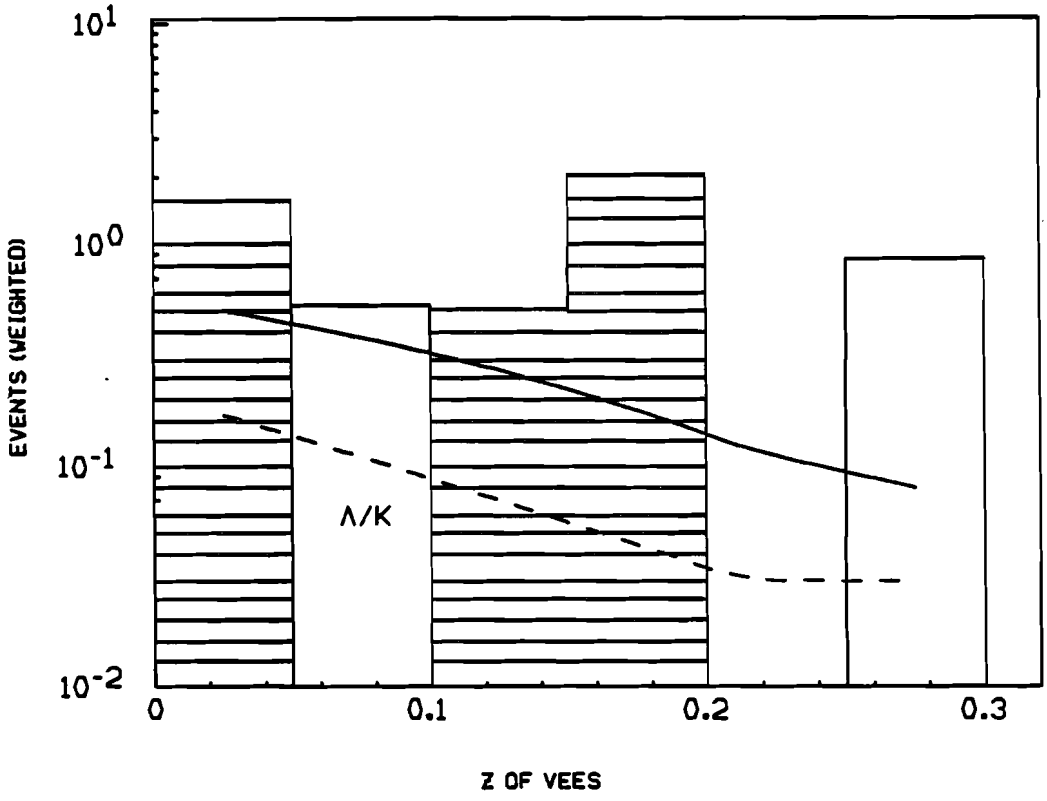

Fig. 6.18a. On the Y axis we plot the number of tracks/unit z/event, where z is the fraction of the hadronic energy carried off by V^0's in opposite sign dimuon events. The shaded portion represents Λ in the dimuon sample. The solid line refers to K^0's and the dashed line refers to Λ's in the unbiased charged current sample.

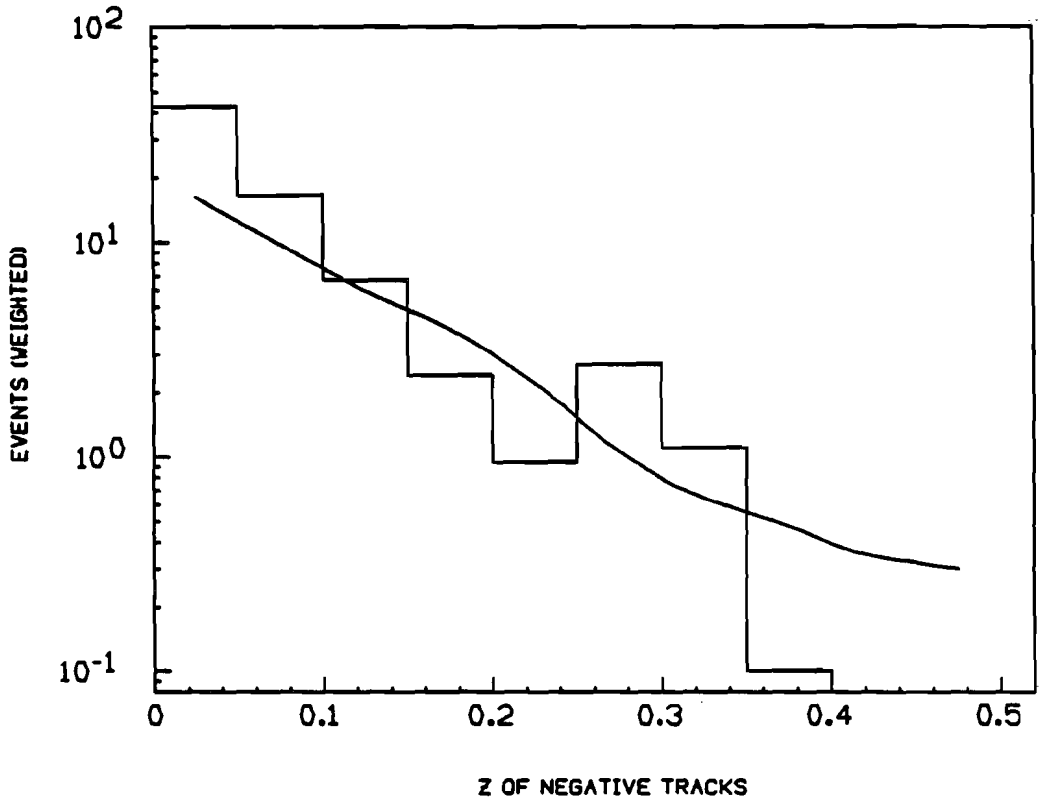

Fig. 6.18b. On the Y axis we plot the number of tracks/unit z/event, where z is the fraction of the hadronic energy carried off by negative tracks in opposite sign dimuon events. The solid line is for hadrons in the unbiased charged current sample.

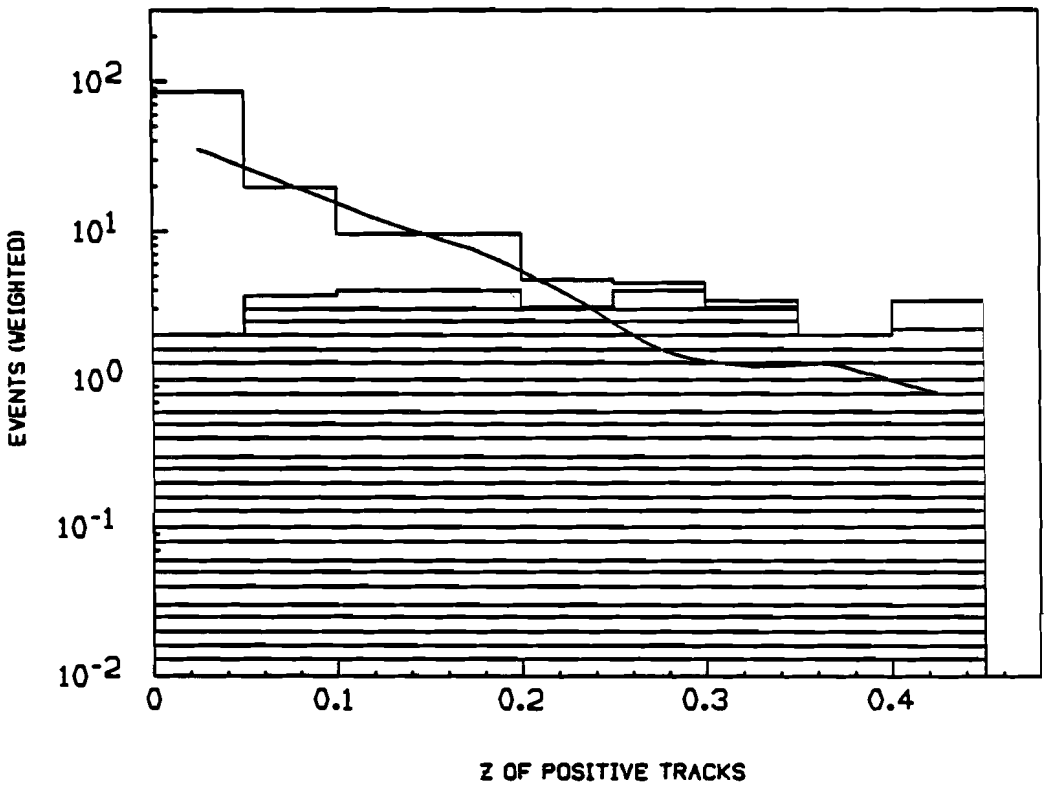

Fig. 6.18c. On the Y axis we plot the number of tracks/unit z/event, where z is the fraction of the hadronic energy carried by positive tracks in opposite sign dimuon events. The contribution of the second muon is the shaded region. The solid line is for hadrons in the unbiased charged current sample.

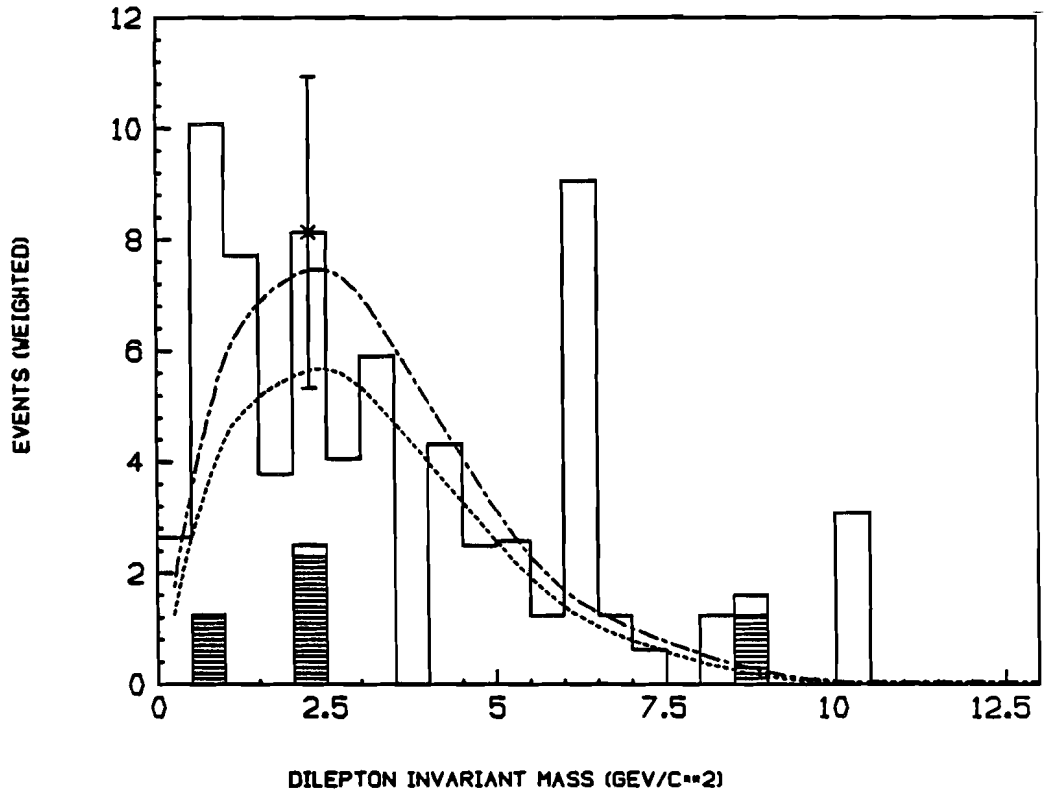

Fig. 6.19. The invariant mass (GeV/c^2) for the two muons in opposite sign dimuon events.

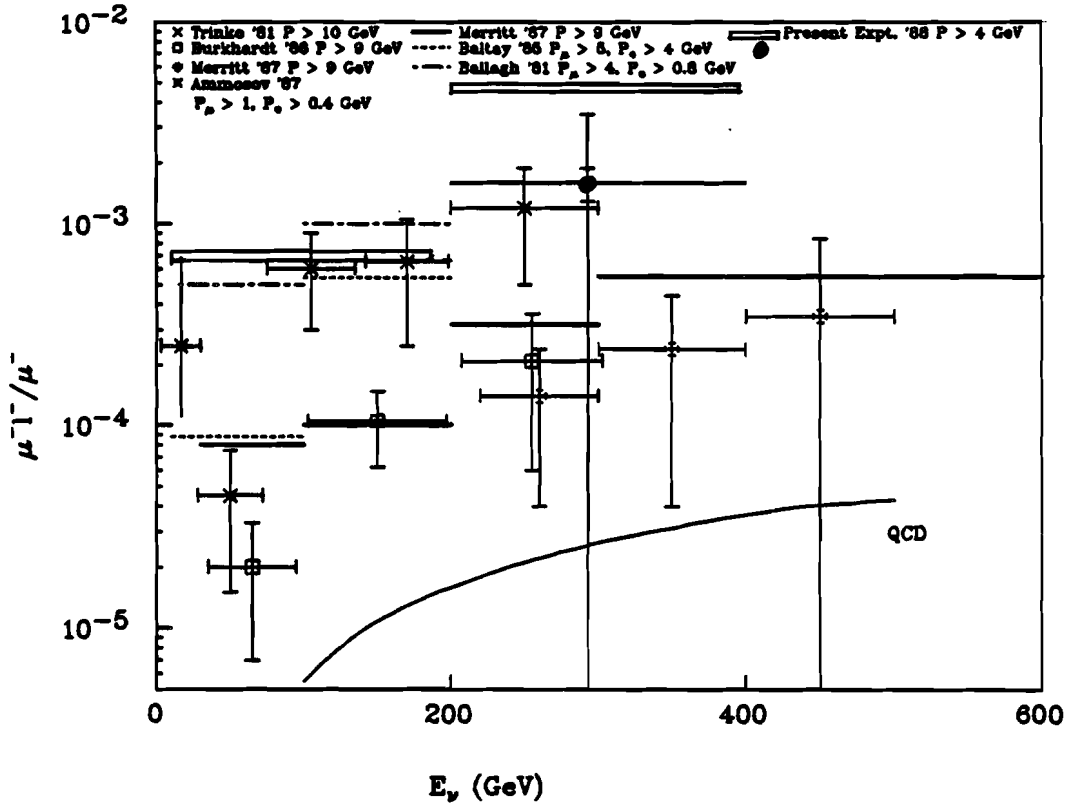

Fig. 6.20. μ^-l^-/μ^- rate as a function of neutrino energy (GeV).

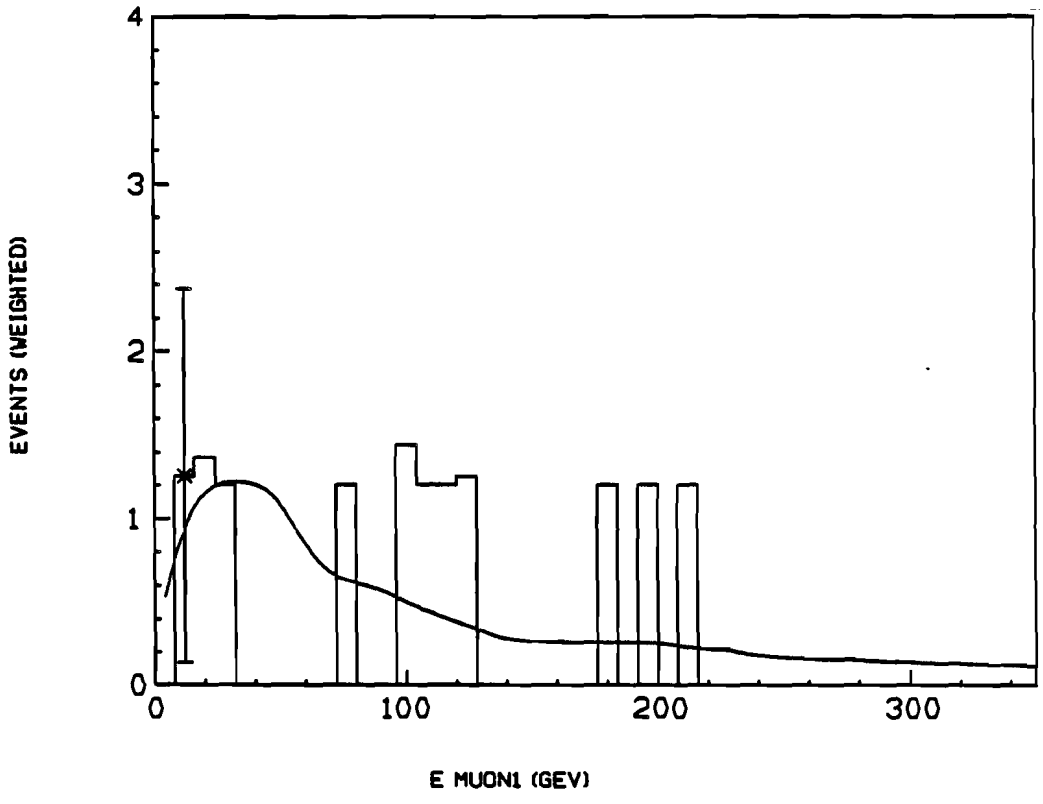

Fig. 6.21. The energy (GeV) of the primary muon in like-sign dimuon events. The Y axis corresponds to the number of events (weighted for geometrical and electronic acceptance) in the dimuon sample. The solid line is the background prediction, normalized to the total number of background events. The same convention is followed in Figs. 6.21 through 6.31.

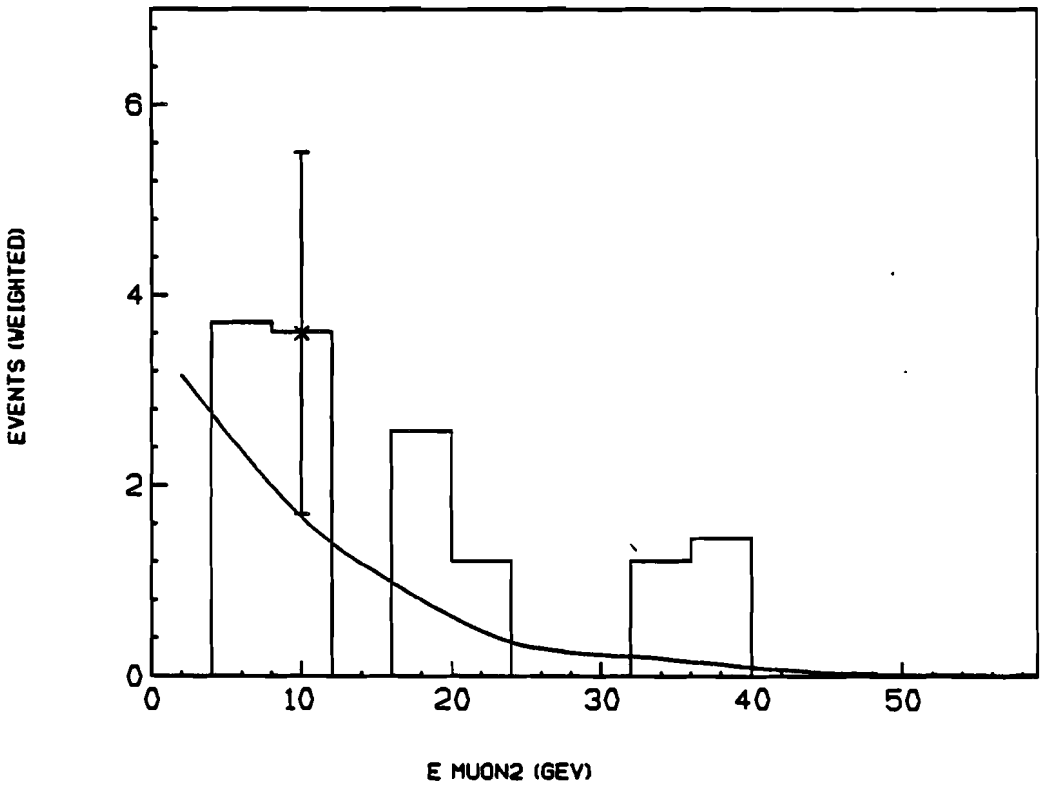

Fig. 6.22. The energy (GeV) of the second muon in like-sign dimuon events.

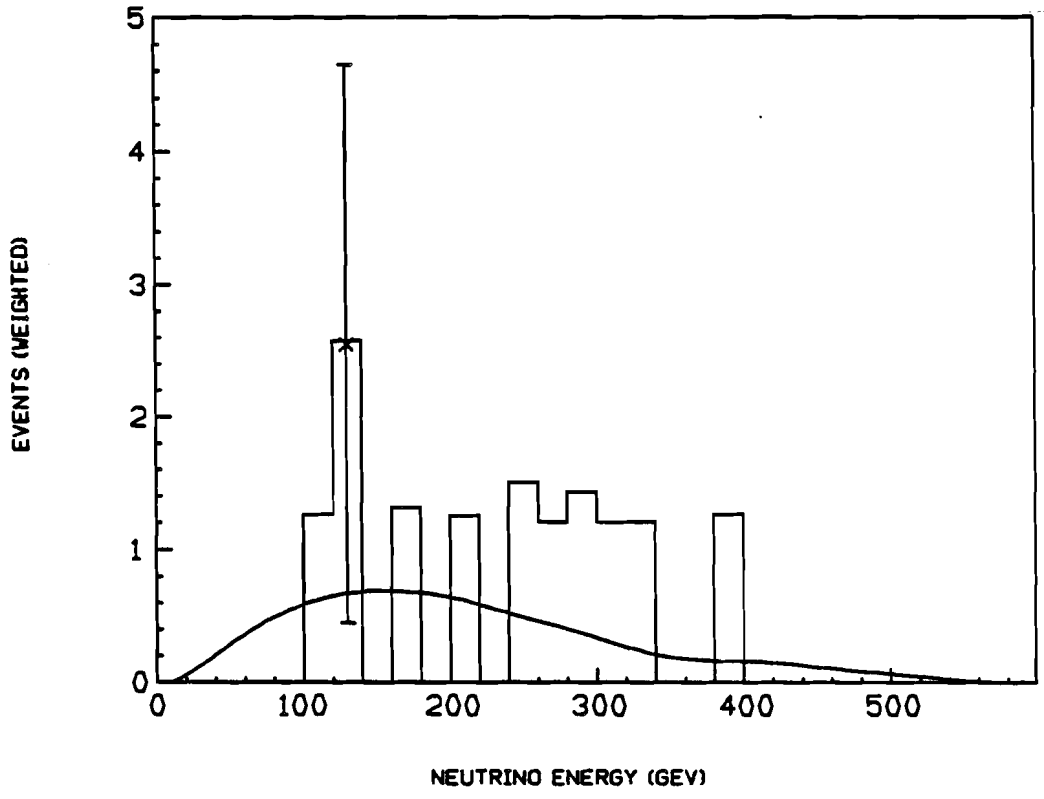

Fig. 6.23. Neutrino energy (GeV) for like-sign dimuon events.

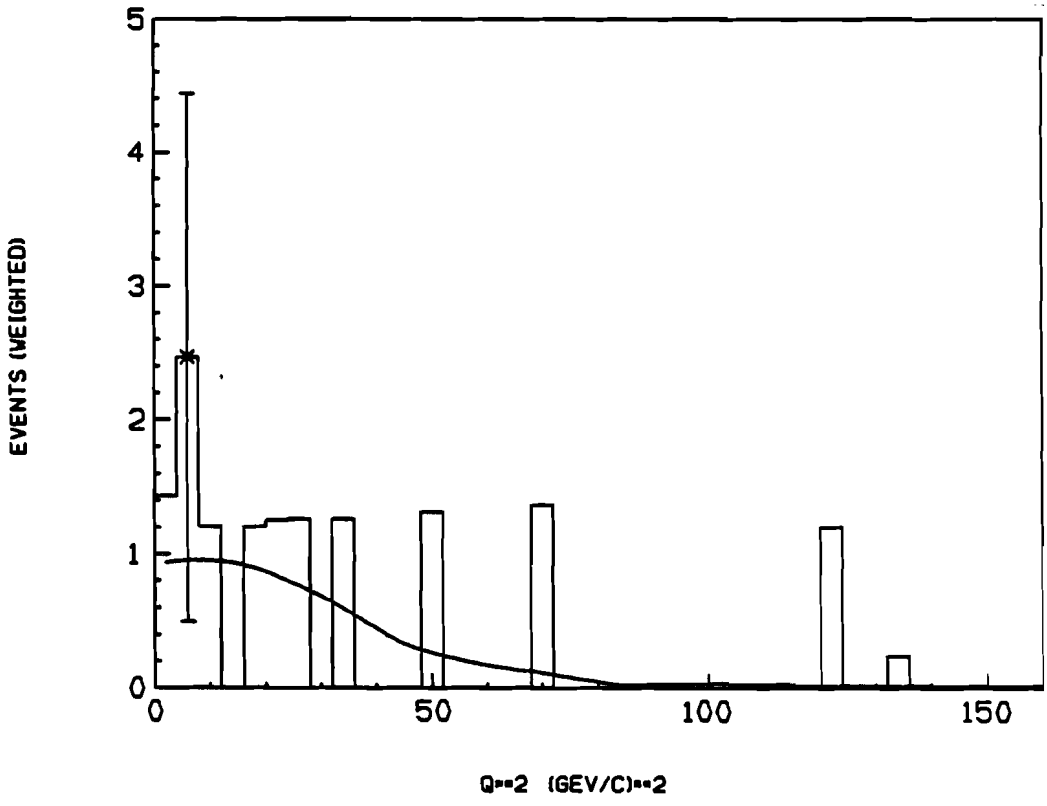

Fig. 6.24. 4-momentum transfer squared $(GeV/c)^2$ for like-sign dimuon events.

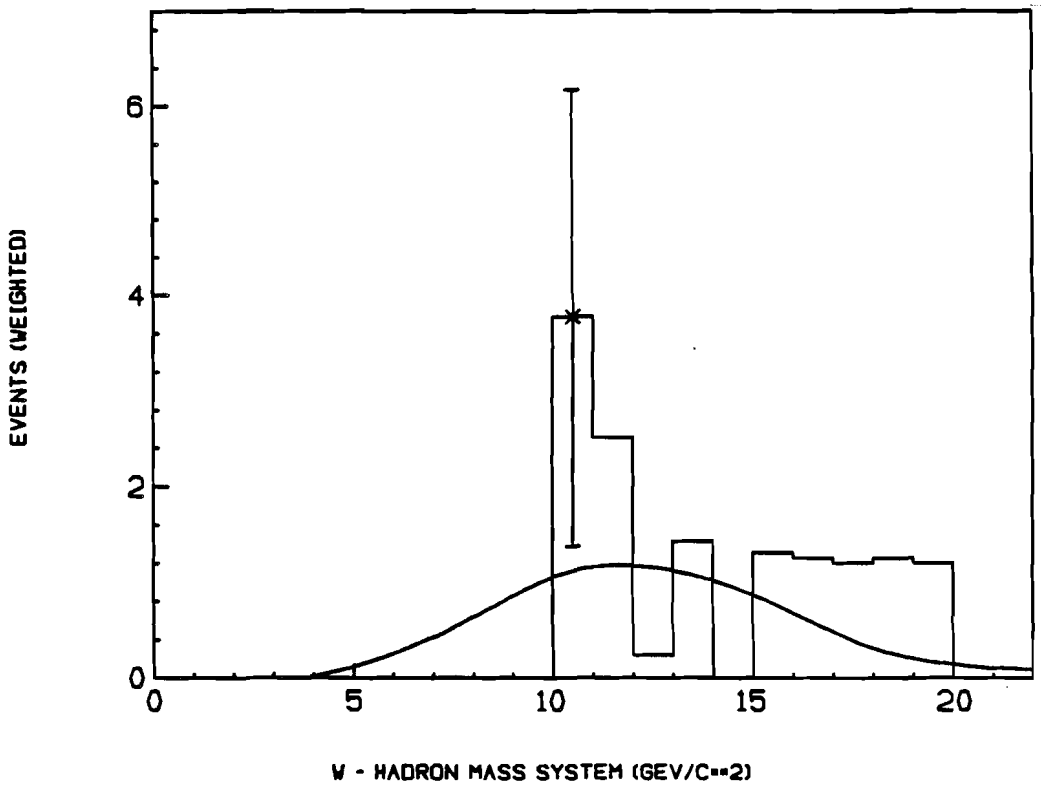

Fig. 6.25. The invariant mass (GeV/c^2) of the hadronic system recoiling against the primary muon, for like-sign dimuon events.

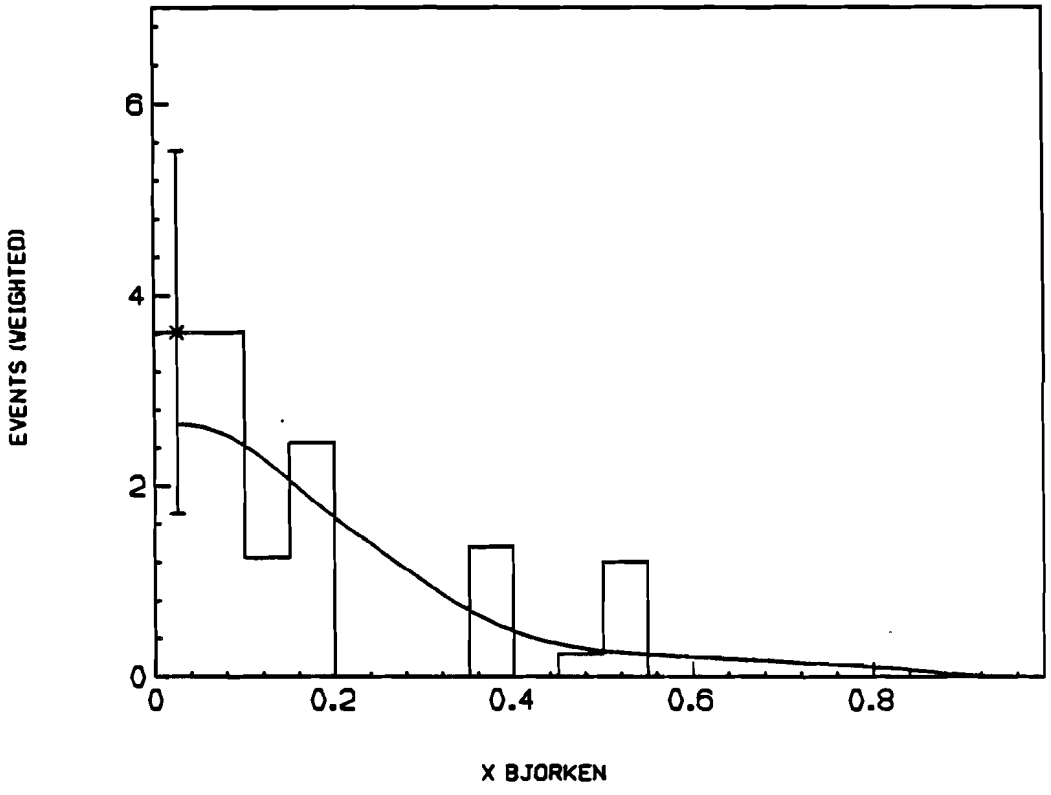

Fig. 6.26. Bjorken x distribution for like-sign dimuon events.

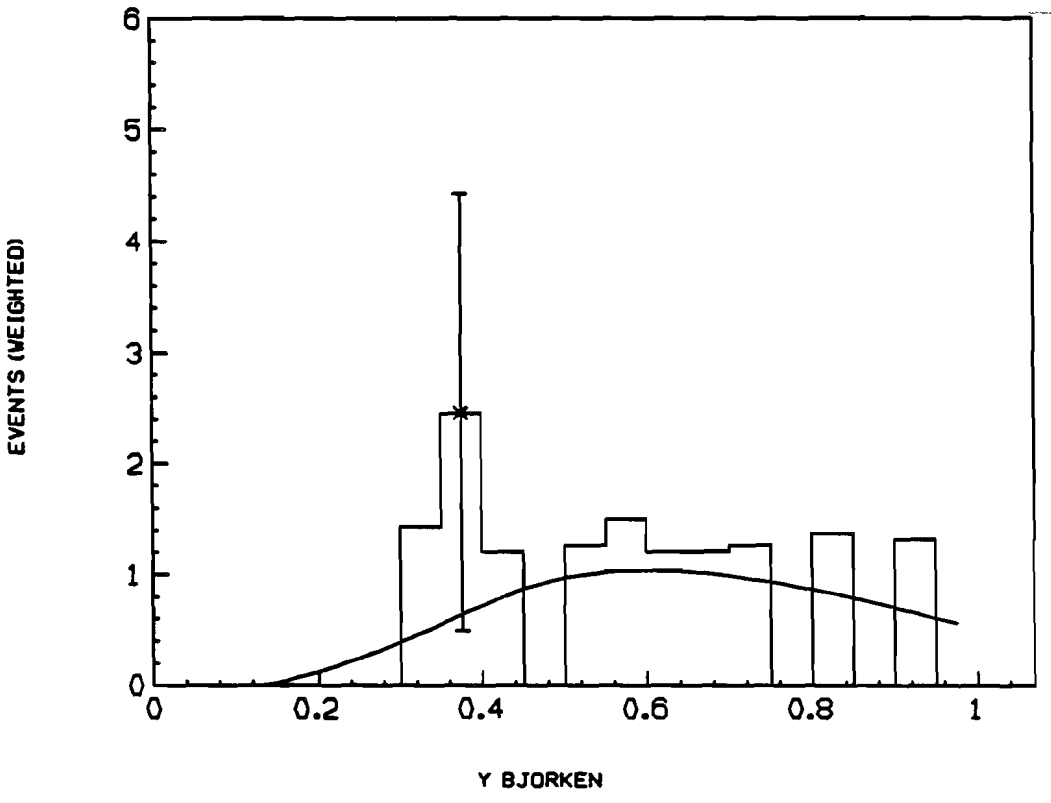

Fig. 6.27. Bjorken y distribution for like-sign dimuon events.

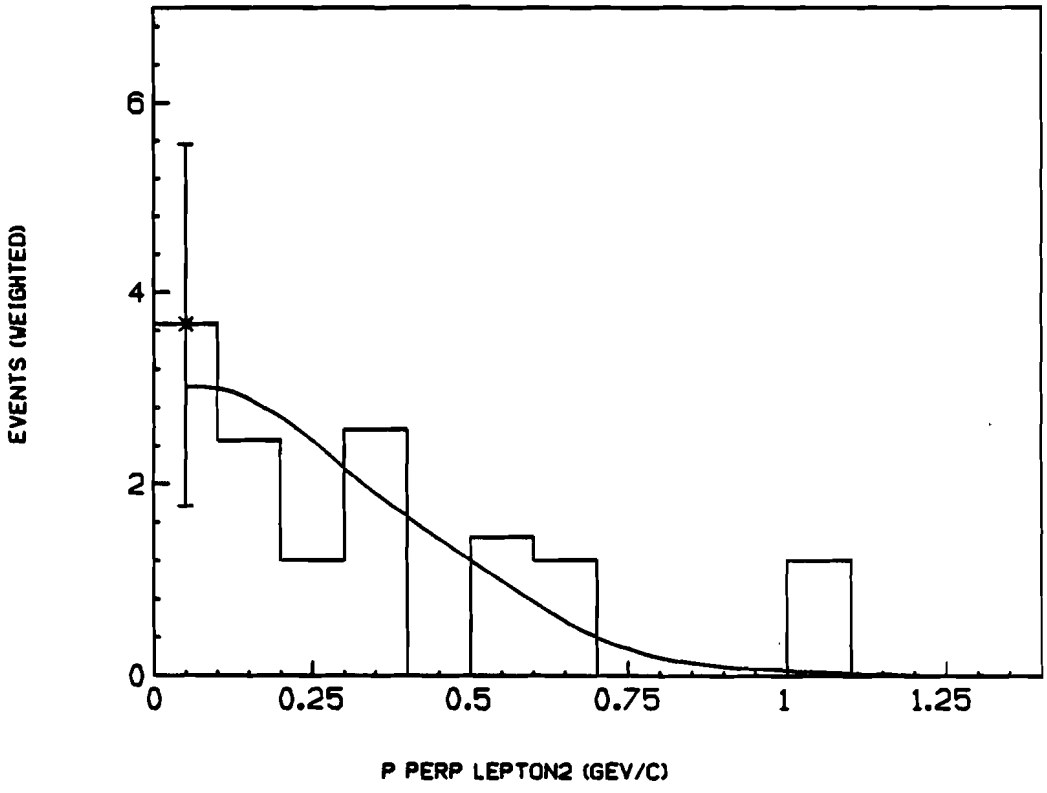

Fig. 6.28. Momentum (GeV/c) of the second muon perpendicular to the plane formed by μ_1 and ν (for like-sign dimuon events).

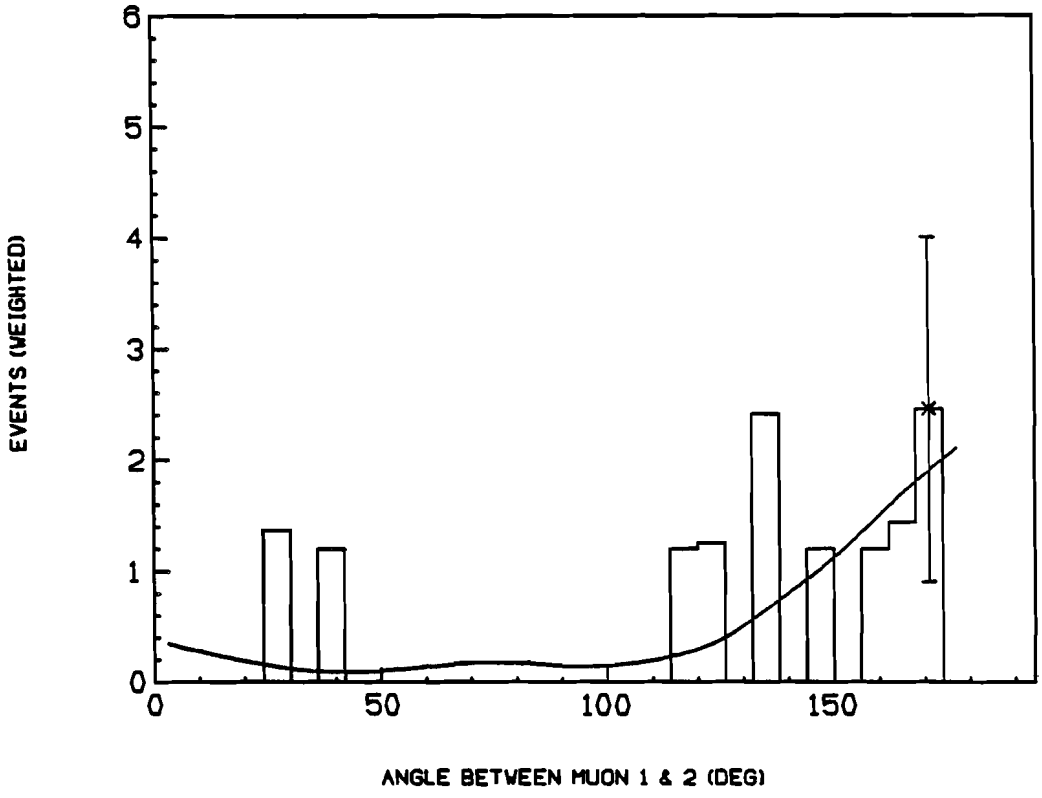

Fig. 6.29. The angle, Φ (deg), between the two muons projected on a plane perpendicular to the neutrino direction (for like-sign dimuon events).

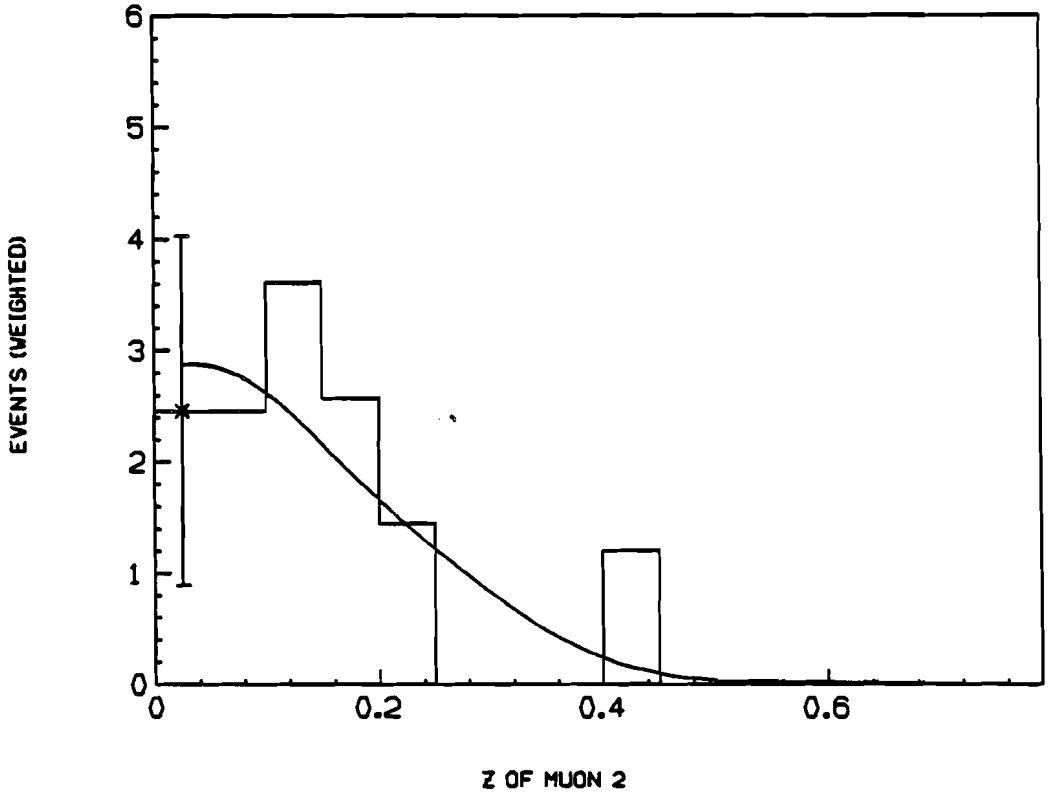

Fig. 6.30. The fraction, $z_{\mu 2}$, of the hadronic energy carried away by the second muon in like-sign events.

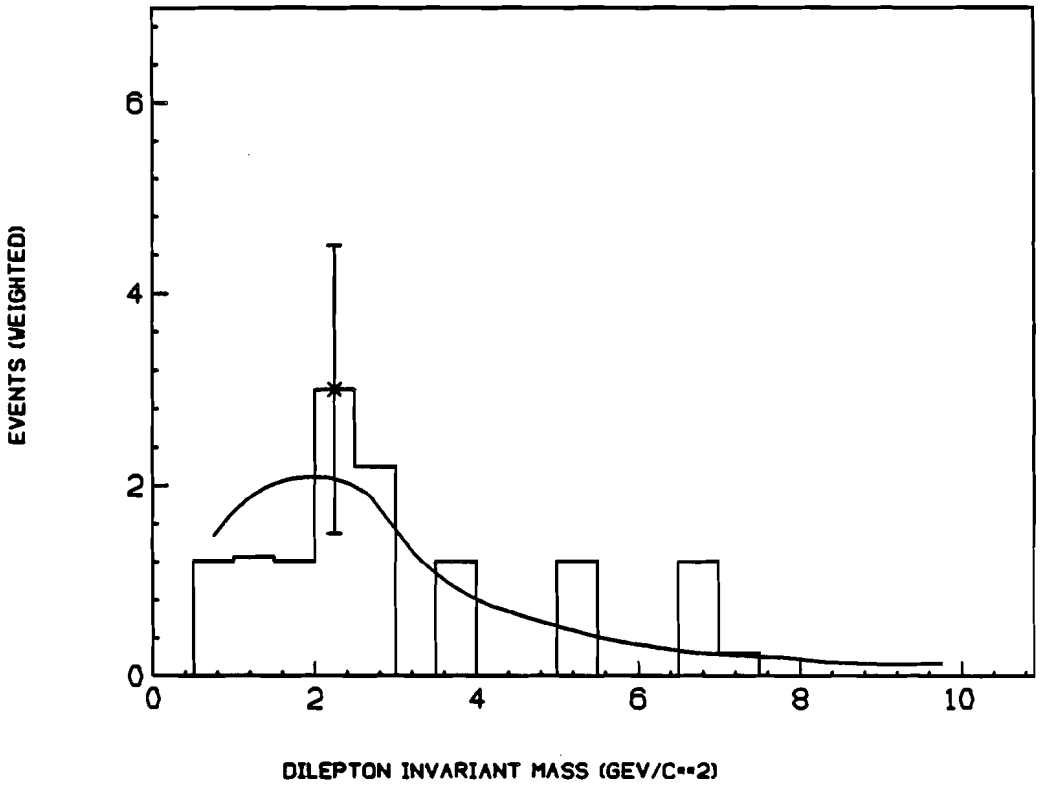

Fig. 6.31. The invariant mass (GeV/c^2) of the two muons in like-sign dimuon events.

Chapter 7

Conclusions

We observe opposite sign dimuons, with the $\mu^-\mu^+/\mu^-$ rate being $0.64\pm0.14\%$ and $\mu^+\mu^-/\mu^+$ being $0.47\pm0.25\%$ for muons with momentum $\geq$ 4 GeV/c. We determine the rate for $\mu^-\mu^+/\mu^-$, where the event energy $\geq$ 200 GeV, to be $1.1\pm0.34\pm0.2\%$. This rate is consistent with those from previous experiments. The kinematic distributions of the opposite sign sample agree well with the sum of the charm and background predictions. We did observe a peak in the distribution of the invariant mass of the two muons, but most likely it is a statistical fluctuation rather than a signal for a new particle. The neutral strange particle production rate agrees well with the charm hypothesis. We do not observe any two prong opposite sign dimuons, which could be a signal for the decay of a heavy neutral lepton.

The like-sign event sample is consistent with being entirely background. The 90% C.L. upper limit set by us, $1.2*10^{-3}$ for $\mu^-\mu^-/\mu^-$ (muon momenta $\geq$ 4 GeV/c), is consistent with upper limits set by other experiments. The corresponding 90% C.L. upper limit for events above 200 GeV is $5*10^{-3}$, the corresponding rate is $(1.7\pm1.9\pm0.3)*10^{-3}$. The kinematic distributions for the event sample agree reasonably well with the predictions from background calculations. We observe one neutral strange particle in the like-sign event sample, which

corresponds to the rate at which they are seen in charged current events.

We do not observe any trimuons. We set the 90% C.L. upper limit (not corrected for detection efficiency and backgrounds) on $\mu^-\mu^+\mu^-/\mu^-$ to be $2.1*10^{-4}$ for muon momenta $\geq$ 4 GeV/c. This is consistent with rates observed by other experiments.

In addition, we scanned in great detail the vertex area for each dimuon event in both conventional and high resolution (wherever available) photographs, to search for short-lived particles. We did not observe any unambiguous candidates.

In summary, we see no conclusive evidence for new phenomena; the "standard model" can explain all observations in the present experiment.

Appendix A

Formulae for χ^2 and Bayes' Theorem

A.1 Calculation of χ^2

If Δ_H (Δ_V) is the difference between the extrapolated position and hit position for a track, in the H and V layers, and the error in the extrapolated positions are σ_H and σ_V, then the single layer chi-square is given by,

$$\chi^2_{H,1} = \left[\frac{\Delta_{H,1}}{\sigma_{H,1}}\right]^2 \qquad \text{A.1.1}$$

where 1 refers to EMIB and 2 refers to EMIC. A similar expression holds for the V layer. Combining χ^2's for H and V layers in one plane leads to an expression for a 2 degree of freedom χ^2

$$\chi^2_1 = \chi^2_{H,1} + \chi^2_{V,1} \qquad \text{A.1.2}$$

and

$$\chi^2_2 = \chi^2_{H,2} + \chi^2_{V,2} \qquad \text{A.1.3}$$

The expression for the four degree of freedom χ^2, which includes EMIBH, EMICH, EMIBV and EMICV, is

$$\chi^2_{12} = \frac{\chi^2_{H,1} - 2\rho_H\chi_{H,1}\chi_{H,2} + \chi^2_{H,2}}{1 - \rho^2_H} + \frac{\chi^2_{V,1} - 2\rho_V\chi_{V,1}\chi_{V,2} + \chi^2_{V,2}}{1 - \rho^2_V} \qquad \text{A.1.4}$$

ρ_H (ρ_V) is the correlation between hits in EMIBH(V) and EMICH(V).

The probability used in the analysis is the probability for getting a χ^2 worse than the one observed and is given by

$$\frac{1}{2^h \Gamma(h)} \int_{\chi_0^2}^{\infty} (\chi^2)^{h-1} e^{-\chi^2/2} d\chi^2 \qquad \text{A.1.5}$$

where h is half the number of degrees of freedom ($n_D/2$) for which the expression is being evaluated. This expression is also known as the confidence level associated with a given value of n_D and an observed value of χ^2_0.

A.2 Bayes' Theorem

Bayes' theorem allows one to use the a priori knowledge about an event to make the best estimate for any measured quantity related to the event. The a priori knowledge about a track is known in terms of its extrapolated position, x_0, and Gaussian error distribution, of width σ. If a tube, of width b-a, is hit by the track, then using Bayes' Theorem, the above Gaussian distribution is modified to:

$$f(x)dx = \frac{\frac{1}{\sqrt{2\pi\sigma^2}} e^{-\frac{(x - x_0)^2}{2\sigma^2}} dx}{\frac{1}{\sqrt{2\pi\sigma^2}} \int_a^b e^{-\frac{(x - x_0)^2}{2\sigma^2}} dx} \qquad \text{for } a \leq x \leq b \qquad \text{A.2.1}$$

$$= 0 \qquad \text{for } x \geq b \text{ or } x \leq a$$

The above expression reduces to,

$$f(x)dx = \frac{1}{\sqrt{2\sigma^2}} \frac{e^{-\frac{(x - x_0)^2}{2\sigma^2}}}{A} \qquad A.2.2$$

$$\text{where } A = \frac{1}{2} \left[\text{erf}(t_1) - \text{erf}(t_2) \right] \qquad A.2.3$$

$$\text{and} \quad t_1 = \frac{a - x_0}{\sigma\sqrt{2}} \quad , \quad t_2 = \frac{b - x_0}{\sigma\sqrt{2}} \quad . \qquad A.2.4$$

where erf(t1) is the error function with t1 as the argument. The expression for the mean of this distribution, in the region between a and b is

$$\begin{aligned} \langle x \rangle &= \int_a^b x f(x) dx \\ &= x_0 + \frac{\sigma}{A\sqrt{2\pi}} \left[e^{-t_1^2} - e^{-t_2^2} \right] \end{aligned} \qquad A.2.5$$

$\langle x \rangle$ is used as the estimate for the position of a track, which hits a tube of width b-a. We compare this value, $\langle x \rangle$, with the results of XTRAP to calculate a χ^2 for one degree of freedom.

Appendix B

Formulae for π/K decay background

B.1 Production of tapes with simulated decays

Each leaving track was allowed to decay according to the distribution

$$(1 - e^{-\alpha L}) \qquad \text{B.1.1}$$

where

$$\alpha = \frac{1}{\lambda} = \frac{1}{\lambda_I} + \frac{1}{\lambda_D} \qquad \text{B.1.2}$$

L is the length of the leaving track, λ_I is the hadronic interaction length and λ_D is the decay length. $\lambda_D = \eta c\tau$, where $\eta = P/m$, P being the particle momentum and m the mass assigned to the particle, τ is the proper decay time of the particle. Therefore, the total number of tracks which decay and are fitted as composite tracks is given by N_{DT}, where

$$N_{DT}(P,L) = N_{LT}(P,L)\ (1 - e^{-\alpha L}) \qquad \text{B.1.3}$$

where N_{LT} is the total number of leaving tracks in the event sample used to generate the simulated decays.

The next step is to relate N_{DT} to the actual number of decays, N_D, in the event sample.

$$N_D(P,L) = \epsilon\, N_0(P)\, (1 - e^{-\alpha L}), \qquad \epsilon = \frac{\lambda}{\lambda_D} \qquad \text{B.1.4}$$

$$N_{LT}(P,L) = N_0(P) \left[e^{-\alpha L} + \epsilon\, (1 - e^{-\alpha L}) \right] \qquad \text{B.1.5}$$

where N_0 is the number of charged pions (or kaons) produced at the primary vertex. The leaving track sample is contaminated by some decays of the longer length tracks, and that contribution is given by the second term in the expression for N_{LT}. With the above expressions it is easy to see that

$$N_D(P,L) = \frac{\epsilon}{e^{-\alpha L} + \epsilon\, (1 - e^{-\alpha L})}\, N_{DT}(P,L) \qquad \text{B.1.6}$$

Each track on the decay tape was used 15 times and each time the track passed the cuts on momentum, geometric acceptance and the EMI 2-plane probability, the weight, WT, was summed, where

$$WT(P,L) = \frac{1}{15} * \frac{\epsilon}{e^{-\alpha L} + \epsilon\, (1 - e^{-\alpha L})} \qquad \text{B.1.7}$$

WT gives the probability that one track on the decay tape will fake a muon and thus produce a fake dimuon event. Looping over all the tracks on the decay tape will thus give the total decay background. It is evident from the expression of WT that it is only a function of the track momentum and length. Two tapes were made, one where all the

leaving tracks were treated as pions and one where all the tracks were treated as kaons.

B.2 Correction for different bubble chamber liquid

One cannot apply the expressions in B.1 to the present experiment for two reasons. Firstly, the interaction length has changed and secondly, N_{LT}, the number of leaving tracks used in making the decay tapes was taken from the event sample of the experiment done with lower energy neutrinos. In this section we will correct for the different interaction length, assuming that neutrino energy is the same. The expression for WT will be recalculated and results will be presented as a probability per leaving track that a leaving track can fake a muon.

Since the interaction length is different, the distribution of the tracks as a function of the decay distance, as measured from the primary vertex to the decay point is different. Correcting for this change requires us to express the above expressions in terms of another variable, X, which is the decay distance defined above. The subscripts 1, 2 in the following expressions refer to the two experiments with different interaction lengths, with 2 referring to the present experiment. The expressions in B.1 can be rewritten in differential form in terms of P,L and X as follows

$$N_{DT}(P,L,X) = N_{LT_1}(P,L)\ \alpha_1\ e^{-\alpha_1 X} \qquad \text{B.2.1}$$

$$N_{D_1}(P,X) = \epsilon_1\ N_{0_1}(P)\ \alpha_1\ e^{-\alpha_1 X} \qquad \text{B.2.2}$$

The expressions B.1.3 and B.2.1 are identical. This can be seen by integrating B.2.1 between the limits X = 0 and X = L. Similarly, B.1.4 and B.2.2 are identical. The expression B.1.5 does not change since neither N_{LT} nor N_0 depend on X. The expression for WT does not change either, because terms containing X cancel out.

Now we write the expressions to relate N_{D2} to N_{DT}. As stated previously we assume $N_{01} = N_{02} = N_0$. With this we have

$$N_{D_2}(P,X) = \epsilon_2\ N_0(P)\ \alpha_2\ e^{-\alpha_2 X} \qquad \text{B.2.3}$$

Writing N_0 (P) in terms of N_{LT1}, from expression B.1.5 we have

$$N_{D_2}(P,L,X) = \epsilon_2\ \frac{N_{LT_1}(P,L)}{e^{-\alpha_1 L} + \epsilon_1\ (1 - e^{-\alpha_1 L})}\ \alpha_2\ e^{-\alpha_2 X} \qquad \text{B.2.4}$$

$$= \frac{\epsilon_2}{e^{-\alpha_1 L} + \epsilon_1 (1 - e^{-\alpha_1 L})} * \frac{N_{DT}(P,L,X)}{\alpha_1 e^{-\alpha_1 X}}\ \alpha_2\ e^{-\alpha_2 X} \qquad \text{B.2.5}$$

The expression for N_{DT} is taken from B.2.1. Rearranging B.2.5 and using each track on the decay tape 15 times gives us the expression for WT_2

$$WT_2(P,L,X) = \frac{1}{15} * \frac{\epsilon_2 \ \alpha_2 \ e^{-\alpha_2 X}}{e^{-\alpha_1 L} + \left[\epsilon_1 (1 - e^{-\alpha_2 L}) \right] \alpha_1 e^{-\alpha_2 X}} \qquad \text{B.2.6}$$

As before WT_2 is summed for every track which passes the EMI cuts. The probability F(P,L) (per leaving track) that a leaving track can fake a muon is given by calculating WT_2 for every (P,L) bin and dividing by the total number of leaving tracks in that bin. The expression for F(P,L) is

$$F(P,L) = \frac{\sum_X WT_2(P,L,X)}{N_{LT_1}(P,L)} \qquad \text{B.2.7}$$

The probability F(P,L) is only a function of track momentum and length and is independent of the neutrino energy and thus can be used for the present experiment. Table 3 in chapter 4 shows the values of F(P,L).

B.3 Correction for higher energy

The correction to account for the higher energy neutrinos is simple. If the leaving track distribution, in the present experiment,

is expressed as N_{LT2} (P,L), then the total decay background is given by

$$N_{D_2} = \sum_P \sum_L F(P,L) * N_{LT_2}(P,L)$$

This is done separately for the different event classes, μ^-h^- etc., and the results are shown in Table 4.3.

Appendix C

Formulae for Punch-through background

C.1 Calculation of $dN/d\chi^2$

We assume that the number of extra hits (defined in Chapter 4.2) is uniformly distributed along EMICH (and EMICV), i.e., $dN/dX = K$. To relate this to $dN/d\chi^2$ we need the relationship between X and χ^2. The expression for χ^2 for two independent degrees of freedom (as in CH and CV) is

$$\chi^2 = \left[\frac{\Delta X}{\sigma_X}\right]^2 + \left[\frac{\Delta Y}{\sigma_Y}\right]^2 \qquad \text{C.1.1}$$

or

$$1 = \left[\frac{\Delta X}{\sigma_X \chi}\right]^2 + \left[\frac{\Delta Y}{\sigma_Y \chi}\right]^2 \qquad \text{C.1.2}$$

C.1.2 is an ellipse with $\sigma_X\chi$ and $\sigma_Y\chi$ as the semi-major and semi-minor axes. The projection of this ellipse along the X and Y axes is $2\sigma_X\chi$ and $2\sigma_Y\chi$, respectively. We can thus write,

$$X = 2\sigma_X \chi \qquad \text{C.1.3}$$

now $$\frac{dN}{d\chi^2} = \frac{dN}{dX} * \frac{dX}{d\chi^2} \qquad \text{C.1.4}$$

$$d(\chi^2) = 4\sigma_X^2 \, d\chi^2$$

or $$dX = \sigma_X \, d(\chi^2)/\chi \qquad \text{C.1.5}$$

Substituting C.1.5 in C.1.4 we get,

$$\frac{dN}{d\chi^2} = \frac{K \sigma_X}{\chi} = \frac{K_1}{\sqrt{\chi^2}} \qquad \text{C.1.6}$$

C.2 Determination of Punch-through Background

If d is the density of extra hits along an axis (either EMICH or CV) and R is the region around the hadron's extrapolated position which corresponds to a 1% cut in 2-plane probability then the expected number of hits in that region is H = dR. According to Poisson statistics e^{-H} is the probability of observing no hits in R, and $1 - e^{-H}$ is the probability of observing some hits within that region. We will now calculate an expression for R, along both EMICH and EMICV.

The expression for χ^2 corresponding to 4 degrees of freedom, with the coordinates in EMIB and EMIC correlated, is

$$\chi_4^2 = \frac{\chi_{2X}^2 - 2\rho_X \chi_{2X} \chi_{1X} + \chi_{1X}^2}{1 - \rho_X^2} + \frac{\chi_{2Y}^2 - 2\rho_Y \chi_{2Y} \chi_{1Y} + \chi_{1Y}^2}{1 - \rho_Y^2} \qquad \text{C.2.1}$$

ρ_X and ρ_Y are the correlations between EMIBH and EMICH, and EMIBV and EMICV, respectively. The above equation can be rewritten as,

$$\chi_4^2 = K_1\chi_{2X}^2 - K_2\chi_{2X} + K_3 + K_4\chi_{2Y}^2 - K_5\chi_{2Y} + K_6 \qquad \text{C.2.2}$$

where, $K_1 = \frac{1}{1 - \rho_X^2}$ $\quad K_2 = \frac{2\rho_X\chi_{1X}}{1 - \rho_X^2}$ $\quad K_3 = \frac{\chi_{1X}^2}{1 - \rho_X^2}$

$K_4 = \frac{1}{1 - \rho_Y^2}$ $\quad K_5 = \frac{2\rho_Y\chi_{1Y}}{1 - \rho_Y^2}$ $\quad K_6 = \frac{\chi_{1Y}^2}{1 - \rho_Y^2}$

By completing squares we can write C.2.2 as

$$\chi_4^2 = K_1 \left[\chi_{2X}^2 - \frac{K_2}{K_1}\chi_{2X} + \frac{K_3}{K_1} + \frac{K_2^2}{4K_1^2} - \frac{K_2^2}{4K_1^2} \right] + \text{term for } \chi_{2Y}$$

$$\chi_4^2 = K_1 \left[\left(\chi_{2X} - \frac{K_2}{2K_1}\right)^2 + \left(\frac{K_3}{K_1} - \frac{K_2^2}{4K_1^2}\right) \right] +$$

$$K_4 \left[\left(\chi_{2Y} - \frac{K_5}{2K_4}\right)^2 + \left(\frac{K_6}{K_4} - \frac{K_5}{4K^2}\right)^2 \right]$$

Since K_1, K_2, K_4 and K_5 are independent of χ_{2X} and χ_{2Y} we can redefine the latter two quantities and write the previous equation as

$$\chi_4^2 = K_1 \chi_{2X}^{'2} + \left[K_3 - \frac{K_2^2}{4K_1} \right] + K_3 \chi_{2Y}^{'2} + \left[K_6 - \frac{K_5^2}{4K_4} \right]$$

$$K_1 \chi_{2X}^{'2} + K_4 \chi_{2Y}^{'2} = \chi_4^2 - K_3 - K_6 + \frac{K_2^2}{4K_1} + \frac{K_5^2}{4K_4}$$

$$= \chi_4^2 - \chi_{1X}^2 - \chi_{1Y}^2 = K_7$$

The previous equation can also be written as

$$K_1 \left[\frac{\Delta_{2X}'}{\sigma_2^X} \right]^2 + K_4 \left[\frac{\Delta_{2Y}'}{\sigma_2^Y} \right]^2 = K_7$$

$$\left[\frac{\Delta_{2X}'}{\sigma_{2X} \sqrt{K_7/K_1}} \right]^2 + \left[\frac{\Delta_{2Y}'}{\sigma_{2Y} \sqrt{K_7/K_4}} \right]^2 = 1$$

The projection of the above ellipse along the X and Y axes will give the region which corresponds to a 1% on the 2-plane probability. This region will be denoted as R_X and R_Y, where

$$R_X = \sigma_X \sqrt{2K_7/K_1} \qquad \text{and} \qquad R_Y = \sigma_Y \sqrt{2K_7/K_1}$$

In the above equation all quantities are known. χ_{1X} and χ_{1Y} define the match in EMIB, and χ^2 corresponding to a 1% cut for 4 degrees of freedom is 13.4. The punch-through probability can be easily calculated and is given by

$$P = \left[1 - e^{-d_X R_X} \right] * \left[1 - e^{-d_Y R_Y} \right] \qquad \text{C.2.3}$$

where, d_X and d_Y are the density of extra hits along EMICH and EMICV.